Optical Supercavity
and
Precision Ring Laser Measurements

A THESIS

SUBMITTED IN PARTIAL FULFILMENT

OF THE REQUIREMENTS FOR THE DEGREE

OF

DOCTOR OF PHILOSOPHY IN PHYSICS

IN THE

UNIVERSITY OF CANTERBURY

BY

Ziyuan Li

University of Canterbury

1993

Acknowledgements

I wish to dedicate this thesis to my parents who have always put the needs of their children ahead of their own, my wife Huaying, my son Ben for all family consistent encouragement, support and enjoyment to my work.

My most sincere thanks go to my supervisor Professor Geoff Stedman and family. Your academic attainments, kind help in all aspects of my work, thesis and life have been invaluable to me. I have not only gained a knowledge of ring laser but a new insight into values of life as well. I also appreciate your offer for a post-doctoral position.

The excellent guidance and generous help of Professor Hans Bilger are greatly appreciated. Your expertise and spirit of devotion to science is invaluable to my work and thesis as well as to the ring laser project.

My sincere thanks go to Professor B. G. Wybourne and Dr. Rod Syme for most generous help and financial support by a Teaching Assistantship from the Department of Physics & Astronomy and research bursary from the University of Canterbury, and for financial support which assisted my attendance of the National Physics Conference 1990 in Massey.

My special thanks go to Clive Rowe, Peter Wells and Morrie Poulton for their tremendous and most kind help and support in all aspects of my work.

Special thanks also go to Dr. R. G. T. Bennett and Professor F. V. Kowalski for their valuable suggestions and references.

I would like to thank the members of the staff and students of the Physics and Astronomy Department who have helped me, particularly:

Gill Evans, Mary Kinnaird, Beverley Bristowe and Dr. William Tobin for their very kind help and care in my work and life;

Bruce Bradshaw, Stephen Hemmingsen and Ross Ritchie for their support in mechanical and electronics aspects;

Andrew McGregor for help in data processing;

Derek Smithies, Cindy Lienert and their parents for their very kind hosts;

Qingsheng Wang for many valuable discussions and help in my life.

It has been really a pleasure living in this beautiful country and working with such kind people. I will always remember the one and half year correspondence, which I have kept as a memento in my life, with Professors Wybourne and Stedman, and remember the midnight four year ago, when Professor Stedman and his son, Tim met me in airport, ...

Finally, I would like to thank my colleagues and friends in Tainjin University for their encouragement in my study and their care to my family after my leaving.

Thank you to all.

Contents

List of Figures

List of Tables

Abstract

A variety of discoveries, inventions and new experimental and theoretical results characteristic of high-precision devices are discussed in connection with the Canterbury ring laser and with optical supercavities in general.

Cavity losses of a few ppm define one fundamental limit for precision measurements. We report a ringing phenomenon in the responses both of the Canterbury ring cavity and of commercial (Newport SR-130) supercavities under excitation by an external laser, whenever the laser frequency and the cavity resonance cross in time. The temporal waveform or ringing profile for any cavity is defined by two parameters. We invent an efficient, inexpensive and competitive "ringing" method for measuring losses of supercavities, and demonstrate its accuracy of 1 ppm. It was found that the asymmetry in the output profile of a scanning Fabry-Perot interferometer is much more significant than formerly realised, despite the long history of such interferometers. For the output profile of a scanning Fabry-Perot cavity to have an asymmetry of less than 5%, for instance, the cavity resonance scanning time should be more than 100 times the cavity decay time. Another method for measuring the cavity loss by simply scanning the cavity is presented with a resolution of and system bias of 1 ppm and 4 ppm respectively.

Backscattering of a few ppm at the supermirrors induces significant beat frequency pulling in a cavity. A totally novel method based on the measurement and Fourier analysis of the instantaneous beat frequency is presented to determine the frequency pulling and related fundamental parameters for our ring laser.

The origins of the beat frequency shifts induced by the dispersion of the laser medium and by mode competition are discussed. A new method is presented to stabilize the beat frequency by using a transverse magnetic field, in view of the empirical observation of such an effect. Its theoretical origin is shown here to be a significant puzzle, since such an effect seems to be forbidden by time-reversal and parity selection rules for any matter-radiation interaction effect for any polarisation state of the ring, in any multipole of interaction and even with allowance for the possible partial orientation of the plasma by the applied field.

A detailed account of the construction and operation of the Canterbury ring laser facility is given. Our results from the Canterbury ring laser itself demonstrate a precision of frequency resolution of 11 μHz (a fraction 2.32×10^{-20} of the He-Ne laser frequency, corresponding to a sensitivity of $1.6 \times 10^{-7}\ \Omega_E$ in earth rotation measurement). This is of the same order as the quantum limit for beat frequency linewidths, given the present losses of our ring laser, and is at least two orders of magnitude greater than the sensitivities of existing laser gyroscopes.

Chapter 1

Introduction

Commercial and military applications of ring lasers have advanced supermirror and ring laser gyroscope technology. Devices a few square centimetres in area are already in commercial use for inertial guidance of aircraft for the measurement of the absolute rotation rate (Chow *et al.* 1985, Stedman 1985). These advances have not been reflected in a corresponding advance in pure scientific research. Commercial applications have outstripped fundamental research, partly because of commercial and military secrecy. The Canterbury ring laser project aims to redress the imbalance by developing non-military scientific applications of this technology. The ring laser constructed at Canterbury has attained, as we shall report, a fractional frequency resolution of 2.32×10^{-20} (11 μHz in 474 THz). This opens a new window of precision measurement for any effect which results in a different optical path length for counterpropagating beams around a ring. This includes, but is not limited to, the detection of rotation as in a gyroscope, and has a number of potential applications in applied sciences as well as in fundamental experiments in physics. For example, such a laser could be used as a seismometer and would sense microseisms as they affect the observed earth rotation rate, at a precision better than 1 ppm. Exploiting this possibility clearly assumes, as for a standard seismometer, a highly stable mechanical environment for the device. Again, nonreciprocal optical effects giving absolute phase shifts of 10^{-10} rad between counterrotating beams would be detectable (Stedman *et al.* 1993). This would allow sensitive tests of nonlinear optical effects in gases associated with the chiral effects of electric and magnetic fields. Field-induced magnetic linear dichroism in gases is one obvious candidate. A popular application of the precision of a ring laser is in tests of special relativistic effects in the dragging of light in moving

media. Detailed discussions about the potential applications of the Canterbury ring laser are presented in appendix C.

Not surprisingly, the struggle to produce a ring laser with such high resolution itself has uncovered new physics and offers novel challenges. There is a number of factors each of which appreciably would change the scale factor, or alter the bias of the beat frequency, in such precision measurements. These challenges make the ring laser a doubly interesting device.

1.1 Canterbury ring laser

Professor Stedman of the Physics Department, in cooperation with Professor Hans Bilger of Oklahoma State University's School of Electrical and Computer Engineering, has initiated over recent years a new experimental research project: the construction of a 1 metre square high-precision ring laser. This permits a wide variety of basic experiments in physics. Lasers of different sorts and at different frequencies currently hold the record for frequency stability and resolution because of the enormous difference between the frequency of the relevant electromagnetic radiation (in our case the helium-neon laser line at a frequency of 4.74×10^{14} Hz) and the frequency stability achievable for this optical frequency. Ring lasers permit a certain characteristic class of measurements, in which minute non-reciprocal optical effects in media can be detected with high accuracy.

The combination of large area and supercavity mirrors in the Canterbury ring is believed to be unique. We have been most fortunate in securing at almost nominal cost some state-of-the-art cavity supermirrors from the firm (Ojai Research) who supply the world's best supermirrors. These have a measured reflectance of 99.9985%. In return the Canterbury group including Professor Bilger has been able to offer collaboration by way of theoretical investigation of mirror design technology, and have suggested ways of improving mirrors further which Ojai Research has been able to implement in practice. The major component of this improvement is to suggest ways of reducing birefringence (polarisation anisotropy in the phase shift of reflected beams) by etching the uppermost layer of the multidielectric mirror coating. This method was the basis of a New Zealand Patent Application No 235614, lodged on 7 October 1990. This matter is the topic of another student's research, and is not otherwise discussed in this thesis; see Bilger *et al.* (1990) for the first publication of details.

One of the major expenses in this ring laser project is the mounting of the laser on a block of Zerodur, or very low-expansion ceramic glass with a thermal

expansion coefficient of the order of 10^{-8}, to reduce thermal fluctuations. With Zerodur, a one-degree temperature change will affect the length of the big ring by a sizeable fraction of a wavelength. Maximum sensitivity therefore requires a site with thermal as well as mechanical stability.

When the ring laser research group was searching for a suitable site in the South Island of New Zealand, New Zealand Television Network made public the existence of a bunker (Fig. 1.1) under the Cashmere Hill which had been built in 1940s as a High Command retreat in the event of invasion. The site was ideal, and negotiations with the owners of the cavern site and access areas secured the use of this cavern to the ring laser project; both the private family and the Hospital Board (part owners of the cavern area) have been generous in their cooperation, to the point of a legal agreement. This has given the University as a whole access to a uniquely suitable site for a high-stability laboratory. Geology students also regularly conduct studies of the rock structure in the cavern.

Fig. 1.1. The cavern is 30 m under the Cashmere Hill of Christchurch, whose floor has dimension 23 m × 34 m and whose height is 5 m.

The ring laser group then built a double room (Figs. 1.2 and 1.3) including simple clean room facilities, dehumidifier etc., so as to make the cavern habitable for man and machine. The design has been kept to minimal size and cost. The clean room design, drawn up after inspection of some far more expensive facilities in the Royal New Zealand Air Force and after discussion with our US ring laser consultant, is again a judicious compromise.

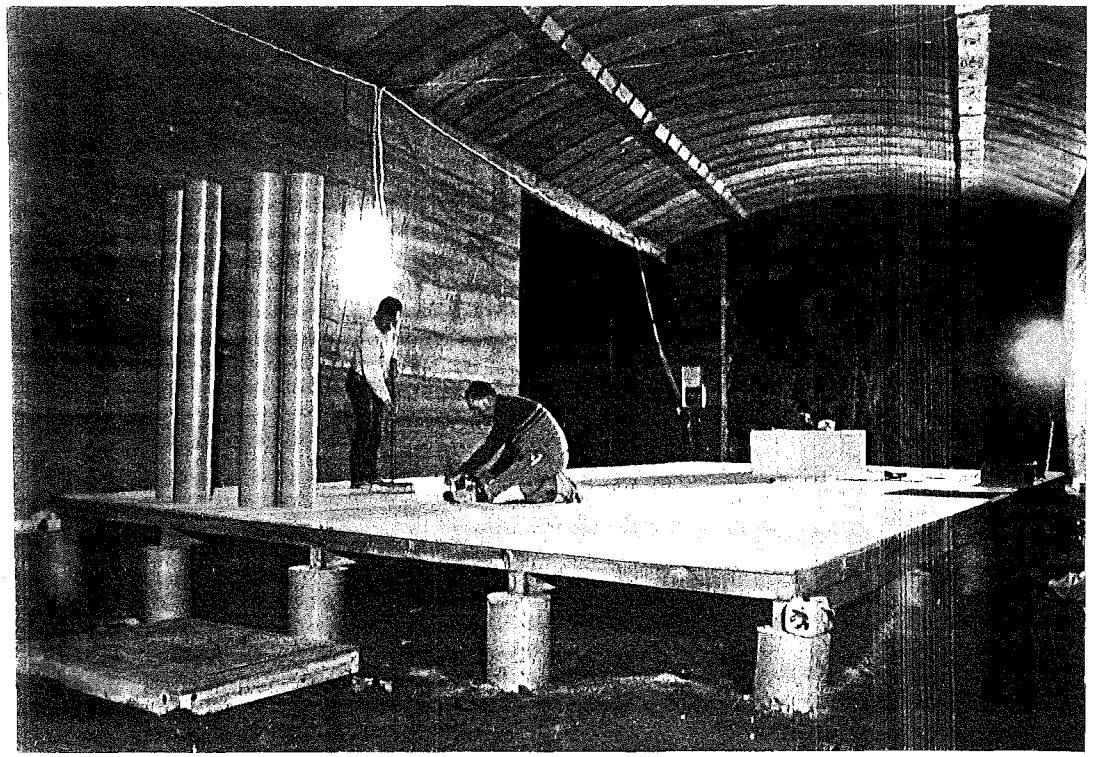

Fig. 1.2. The ring laser room under construction in the Cashmere cavern.

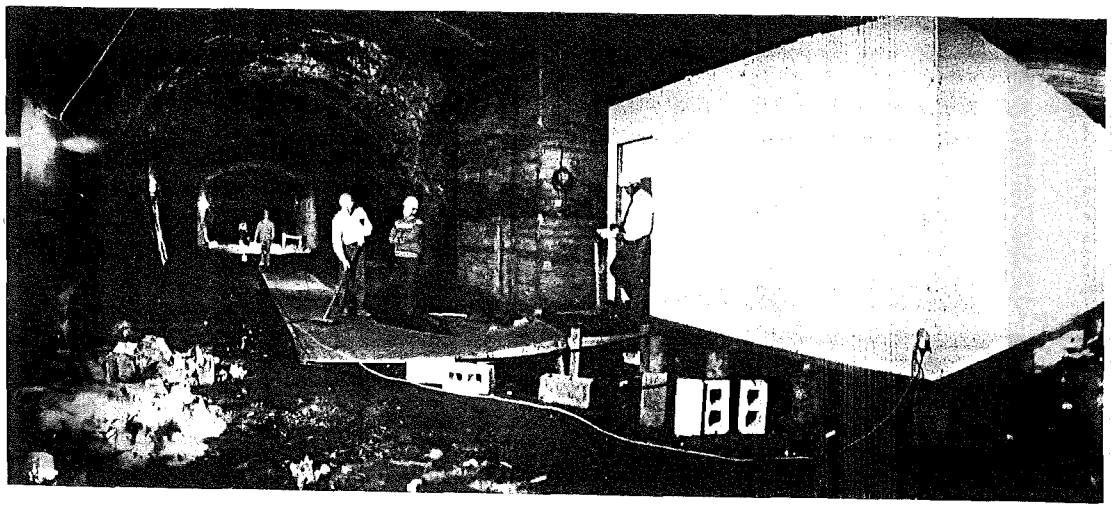

Fig. 1.3. Overview of the Cashmere cavern and the ring laser room (right).

The use of Zerodur for thermal stability, together with the cavern sitting (the temperature should vary by less than a millidegree when the cavern is thoroughly sealed), should ensure thermal stability as well for data collection over long periods. Now the Canterbury ring laser is successfully operating in the Cashmere cavern (Figs. 1.4) and the ring laser team is smiling (Fig. 1.5)!

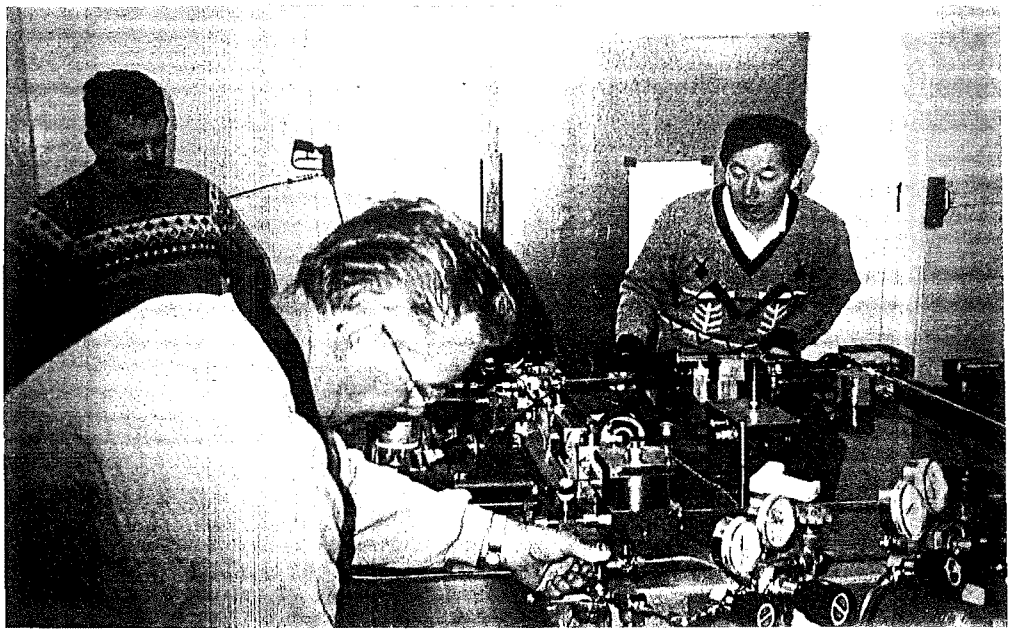

Fig. 1.4. The Canterbury ring laser is under testing in the Cashmere cavern.

Fig. 1.5. The ring laser team (the Canterbury part) in the Rutherford building . From left Morrie Poulton, Professor Geoff Stedman, Peter Wells, Ziyuan Li and Clive Rowe. Professors Hans Bilger, Frank Kowalski and Brian Wybourne are absent.

1.2 Thesis layout

My Ph.D project was defined initially as that of participating with the ring laser major project and in particular establishing techniques and applications for measuring the finesse of the ring, and more generally the finesse of an optical super-cavity, itself a function of the losses in the probe cavity.

The major discoveries and contributions I made to the Canterbury ring laser research group are listed as follows:

a. The invention of the ringing profile method for the measurement of the supercavity finesse;
b. The discovery of the asymmetric response profile of a scanning Fabry-Perot interferometer;
c. A new method for determination of the frequency locking parameters of the ring laser by studying the instantaneous beat frequency of the ring laser as a function of time;
d. The effects of a transverse magnetic field on the beat frequency of the ring laser;
e. An analysis of the origins of frequency pulling and pushing in the Canterbury ring laser;
f. Development of appropriate strategies for aligning the elements of the large ring.

This work, in addition to some minor contributions of mine to the development and implementation of the ring laser project, is described in detail in this thesis. Sufficient extra material is included at parts to make the whole a reasonably cohesive summary of the principles and practice of the construction and operation of this facility, although a more detailed manual on many practical points is available separately as an in-house report (Stedman 1993a).

Some of this research has already been presented in four papers which have been published through the duration of my thesis work. These four papers are presented in appendices A to D and are, in order of publication:

Appendix A. Ziyuan Li, R.G.T. Bennett and G.E. Stedman (1991); Swept-frequency induced optical cavity ringing, *Opt. Commun.*, **86,** 51-57.

Appendix B. H.R. Bilger, G.E. Stedman, M.P. Poulton, C.H. Rowe, Ziyuan Li, P.V. Wells (1993); Ring laser for precision measurement of nonreciprocal phenomena, *IEEE Transactions, Instrumentation and measurements*, **42**, 407-411.

Appendix C. G.E. Stedman, H.R. Bilger, Li Ziyuan, M.P. Poulton, C.H. Rowe, I. Vetharaniam and P.V. Wells (1993), Canterbury ring laser and test for nonreciprocal phenomena, *Aust. J. Phys.*, **46**, 87-101.

Appendix D. Ziyuan Li, G.E. Stedman and H.R. Bilger (1993), Asymmetric response profile of a scanning Fabry-Perot interferometer, *Opt. Commun.*, **100**, 240-246.

In chapter 2, I will review the various measurement techniques used until now for determining the overall reflection power losses of supermirrors. This is important because the quality of cavity mirrors is one of the most critical elements in the active ring laser gyroscopes, and the newest generation of high-accuracy ring laser gyroscopes requires state-of-the-art optical coatings (Thomas 1978, Kalb 1986). The optical properties of the mirrors in the ring laser affect gyroscope performance in a number of different ways. Two effects whose limitations are of importance in practice are backscattering-induced locking and quantum noise.

First and foremost, non-specular scattering of the incident laser light by the coating causes a phenomenon known as lock-in (Aronowitz 1965, 1971). A proportion of the scattered light admixes with the counterrotating beam, and so causes the clockwise and counterclockwise beams of the ring laser to couple together. At low rotation rates the two beams become locked in frequency, and the ring laser ceases to produce meaningful output. Furthermore, near the lock band, severe scale factor variations occur; the scale factor is defined simply as the gyroscope output frequency for a given rotational rate. For high accuracy ring laser applications the scatter coefficient ($I_{scattered}/I_{incident}$) must be less than a few ppm, i.e. a few parts in 10^6. Backscattering from the mirrors largely determines the lock band and so the useful rotation range of the ring laser for detection of rotation.

The total power losses (transmission, scattering and absorption) at the mirrors determine the quality factor Q of the cavity, and so the level of quantum noise of the ring laser and the limit of the sensitivity of the system to small changes in any nonreciprocal effect, or an effective rotation rate. All of these loss mechanisms for the incident radiation in the multilayer stack affect the cavity

quality factor, and so broaden the laser linewidth. The effect on gyroscope performance is an increase in white noise. Typical requirements for high accuracy ring laser gyroscopes set absorption below 20 ppm (Kalb 1986).

Therefore, the development of fast, sensitive optical measurement techniques to determine the cavity quality factor and the associated performance factors is of prime importance in the development of the mirror coatings for ring laser gyroscope applications. Before the advent of this new measurement technology, only the visible spectrophotomenter was available for the measurement of absorption loss and transmission. While it is a good tool in the development of low-quality coatings, the spectrophotometer has an intensity resolution only of approximately 0.05% (Kalb 1986). Since ring laser gyroscope coatings have transmissions below 0.01%, this is clearly inadequate.

In chapter 3, I will present an analysis for a "ringing" method (Li *et al.* 1991) for determination of cavity quality factors. We have successfully demonstrated this new method for the measurement of cavity losses. Development of this method is based on the observation of a ringing, or beating, phenomenon in the output of both a ring cavity and Newport SR-130 interferometer when excited by an external laser source. The ringing profile of the output is caused by the beating between the laser frequency and the cavity resonant frequency when either is swept in a time comparable to the decay time of the cavity. The standard phase shift method (Herbelin *et al.* 1980, 1981, Kwok, Herbelin, and Ueunten 1982, Elleaume *et al.* 1985) of measuring quality factor is severely limited in precision because of the effect of the random vibrations which detune the laser cavity and the test cavity during the time of the measurement. The ringing profile method which we discuss does not suffer from the noise problem inherent in the phase shift method, since the detuning is automatically utilised in performance of a measurement. The detuning noise is also avoided in another standard method, the so-called ringdown measurement (Anderson, Frisch, and Masser 1984) in which the exponential decay of an optical pulse is monitored. However, the ringing profile method presented here avoids the very considerable cost of the ringdown technique since fast optical switching and electronics are not required.

In chapter 4, I discuss the asymmetry of the temporal response profile of a Fabry-Perot interferometer (FPI) under a frequency-scanned input or with cavity scanning. This is discussed also in Li *et al.* (1993). This constitutes another novel part of our research on supercavity mirrors, despite the fact that the FPI was invented about a century ago. In high resolution spectroscopy using a FPI the extraction of the real input spectrum from the output is of great importance. Most of the literature on this subject uses the symmetric Airy function in the

deconvolution algorithm. However, the Airy function for the intensity distribution in the fringe pattern is strictly valid only for a source of constant brightness and spectral distribution and for a nonscanning FPI. For a scanning FPI, the limitations on scanning speed were discussed by Greig and Cooper (1968). They estimated a time to establish the interference pattern as approximately 1.4 $F\tau$ (= 2.8 πt_c), where F is the finesse, τ is the round trip time of the FPI and t_c its power decay time. However, their analysis was based on the Lummer-Gehrcke plate (Born and Wolf, 1964), and is relevant only for the steady-state multiple beam interferometer. The profile of FPI output is still symmetric in that case.

The analysis given in this thesis shows that the asymmetry in the output profile of an FPI is inherent to its character. We find that significant asymmetry appears in a fringe profile for a scanning FPI even when the time interval which is required for scanning over the probe frequency was as large as $100t_c$. This is particularly important for spectral measurement using a supercavity FPI. In using the Newport SR-130 supercavity (whose free spectral range is 6 GHz and finesse ~ 60,000) to measure the mode spectrum in our 1 m^2 ring laser, we can see the asymmetry of the fringe profile of the interferometer output over a large range of the FPI scanning rates, from 3 GHz/s -50 GHz/s.

In chapter 5, I will review recent progress in the use of various ring laser devices and associated techniques. Since our ring laser is designed for precision measurements of inertial rotation, the sensitivity of the ring laser is a major factor to be consider in the project. Therefore, in this review, I will, in particular, compare the sensitivity of various optical rotation sensors in Sec. 5.11.

In chapter 6, I describe the facilities of the Canterbury ring laser system and present our major experimental results for beat frequency determinations.

In chapter 7, I discuss the effects of backscattering on the beat frequency of the ring laser, which is one of the most important error sources in ring laser measurement. The backscattering in a ring laser is caused by imperfections of the dielectric mirrors (Thomas 1978, Haus 1985) or by impurities (dust etc.) on their surfaces. In general, backscattering can give rise to frequency locking and pulling phenomena in ring lasers (Aronowitz and Collins 1966, Aronowitz 1971, Aronowitz and Lim 1977, Statz *et al.* 1985, Chow *et al.* 1985). In this case, the average beat frequency f_b is given by $f_b = (f^2 - f_l^2)^{1/2}$, where f is the nominal frequency difference of the counterpropagating beams in the ring laser and f_l is the frequency locking threshold caused by the backscattering. f_l is the function of the resultant backscattering which are not only dependent on the amplitudes but also the phases of the each individual backscattering center (Statz *et al.* 1985). Since the phases of these backscattering vary with the lengths of each arm of the ring

laser, the phase of the resultant backscattering is variable even if the total path length of the ring is controlled by a servo system.

Therefore, for precision measurements, the effect of the frequency pulling on the beat frequency must be determined accurately. We invent and implement an entirely new method to determine the parameters of this frequency pulling. Unlike the method of counting the average beat frequency (Aronowitz 1971), we collect data on the profile of the interference fringes, and explore from the derived Fourier spectrum or instantaneous beat frequency the most important parameters, including the frequency pulling in our ring laser.

In chapter 8, I give an analysis for dispersion effects, with or without the saturation, of the gain medium on the laser beat frequency. This is another very important error source for the ring laser measurements. The different cases, such as, natural neon mixture, single neon isotope and equal isotope mixtures are discussed. Our discovery of the effect of transverse magnetic field effects on the stabilization of the frequency splitting is presented in this chapter.

Brief conclusions from my analysis and experimental research are presented in chapter 9.

Chapter 2

Review of measurement techniques

We will review the techniques for measuring the losses in an optical supercavity, i.e. a cavity incorporating supermirrors, in this chapter. In our context, "supermirror" is a traditional term associated with the development of mirrors whose reflectance is enhanced to the level of say 99.998% or more by a sequence of quite recent technical developments. This has greatly enhanced the capabilities of Fabry-Perot instruments, and of ring laser gyroscopes, as we shall demonstrate in an instrument of uniquely large area and quality factor. Unlike the standard methods (e.g. cathode sputtering, E-beam sputtering) for making mirrors (e.g. metallic coatings, conventional dielectric coatings) used until recently in all standard lasers, a special mirror coating technique - the ion-beam deposition process - has been developed independently by a number of ring laser gyroscope manufacturers (Kalb 1986). The supermirror technique takes advantage of advanced polishing techniques and ion-beam coating technology to provide the highest reflectivity and lowest loss of any commercially available mirrors. When used in etalons or optical cavities, these mirrors can provide finesses in excess of 30,000, approximately 30 times better than mirrors manufactured by standard techniques. A selection of ion beam deposited coating covers the spectral range of 558 - 1705 nm.

The supermirrors used in the Canterbury ring laser have 0.016 nm rms surface microroughness (i.e. the substrates are smooth to atomic dimensions), achieved through ion beam milling with argon and nitrogen beams. The ion-beam sputter coated SiO_2/TiO_2 $\lambda/4$ layers give losses of ~ 4 ppm due to scattering (TIS), 4 ppm from transmission, and absorption of 7 ppm, approaching the losses of the bulk materials. The observed total reduction in reflection is then 15 ppm,

corresponding to a reflectivity of 99.9985% (Stedman *et al.* 1993).

We will explain why such low losses in the supercavity are necessary for the high performance of ring laser gyroscopes in Sec. 2.1, following the discussions of various techniques for measuring the losses of the supercavity in Sec. 2.2 - 2.7. A comparison of the different measurement schemes will be presented in Sec. 2.8. In Sec. 2.9 we shall highlight the competitive performance of a new method which we analyse and demonstrate, in which the temporal waveform or profile of the cavity response to a chirped input is used to determine the supercavity loss and decay time.

2.1 Laser gyroscope quantum limit

In general, the uncertainty principle of quantum mechanics imposes limits on all measurements performed on an atomic scale. Macroscopic measurements, on the other hand, suffer from measurement uncertainties that mostly are not quantum mechanical in nature. However, the multioscillator ring laser gyroscope is one exception. Dorschner *et al.* (1980) have reported that the multioscillator ring laser gyroscope can operate at the quantum limit. In contrast, optical rotation sensors which suffer from extraneous noise, such as that induced by dither in a two-frequency ring laser gyroscope or by mode coupling effects in passive sensors, cannot attain this ultimate fundamental limit. Dorschner *et al.* (1980) have proved that the fundamental uncertainty in the measurement of the rotation rate of a laser ring gyroscope can be derived from a general quantum mechanical uncertainty principle. Also, the same relationship can be obtained from a spontaneous emission noise formulation as shown in the following derivation (Dorschner *et al.* 1980, Statz *et al.* 1985):

In a ring laser where each mode is occupied by, on the average, $\langle n \rangle$ photons, the ratio of the spontaneous to the stimulated transition emission rate $\dot{n}_{sp}/\dot{n}_{st}$ is $1/\langle n \rangle$. In the steady state, the stimulated emission rate is $\langle n \rangle / t_c$, where t_c is the ring cavity photon lifetime (or cavity decay time). Therefore, the spontaneous emission rate is $1/t_c$ per mode. Consider a particular polarisation component in the following. The electric field E_1 of each spontaneously emitted photon, unlike that of the stimulated photons, adds randomly in phase or in quadrature (with equal probability) to the pre-existing optical frequency electric field E_n. Let E_{1q} be the quadrature part of E_1. We have then for the small phase perturbation $\langle \Delta\phi_1^2 \rangle = \langle (E_{1q}/E_n)^2 \rangle = \frac{1}{2}E_1^2/E_n^2 = 1/2\langle n \rangle$. These perturbing phase jumps add to give a random walk in phase that amounts to (rms measure)

$\Delta\phi(t)_{rms} \equiv \langle\Delta\phi(t)^2\rangle^{1/2} = [(t/t_c)\langle\Delta\phi_1^2\rangle]^{1/2}$ after a time t. In the steady state, the power loss of each mode $P_{loss} = h\nu\langle n\rangle/t_c$, where ν is the frequency of the laser. Considering the two modes in the ring laser are independent, we then find the uncertainty in the beat frequency of the ring laser gyroscope by adding the uncertainties in the frequencies of the two modes,

$$\Delta f_{rms} = (1/\pi t)\Delta\phi(t)_{rms} = (1/\pi t_c)(h\nu/2P_{loss}t)^{1/2}. \tag{2.1}$$

The beat frequency resolution of the Canterbury ring laser, which we will discuss in chapter 6, indeed reaches the quantum noise limit calculated by Eq. (2.1).

Eq. (2.1) shows that the rms frequency fluctuation, Δf_{rms}, of the beat frequency of a ring laser is inversely proportional to the photon lifetime t_c. For an optical cavity, the quality factor Q, the linewidth (or FWHM) $L_{1/2}$, the finesse F, the round trip losses in the cavity Γ, the mirror reflectivity R and the cavity decay time t_c are related as follows:

$$Q = 2\pi\nu t_c = \nu/L_{1/2} \tag{2.2a}$$
$$F = \Delta\nu_{FSR}/L_{1/2} = \pi\sqrt{R}/(1-R) \tag{2.2b}$$
$$t_c = 1/(\Delta\nu_{FSR}\,\Gamma) = 1/(2\pi L_{1/2}) \tag{2.2c}$$

where $\Delta\nu_{FSR} = c/P$ is the free spectral range of the cavity, c is the speed of light and P is the optical path of the cavity. This stimulates the development of the various measurement techniques.

Eq. (2.2c) shows that the beat frequency fluctuation Δf_{rms} will be proportional to the losses Γ in the cavity. This is why a ring laser gyroscope requires low losses (or high Q, long t_c, high R, high F, narrow $L_{1/2}$) in the ring cavity. Since the losses (absorption plus transmission plus scattering) in the cavity are proportional to $1 - R$, the development of accurate measurement techniques for determining the mirror reflectivity is very important in the development of ring laser gyroscopes (Sanders 1977). By measuring any one of these parameters, the other parameters can be calculated through the Eqs. (2.2).

2.2 Linewidth measurement

The simplest technique to determine an optical cavity quality factor is directly to measure the linewidth (or fringe width) $L_{1/2}$ of the cavity as in a scanning Fabry-Perot interferometer. The test mirror is made part of a two (or more)

mirror cavity, with the other mirrors being of known reflectivity. A probe laser beam is injected and transversely mode matched into the cavity, and swept in frequency through the test cavity resonance. The output of the test cavity is recorded, and fringe width (or linewidth) of the cavity output is determined. This fringe width can be converted to any other related parameters by using Eqs. (2.2). This technique works well with high loss cavities, where the linewidth is very broad. Kalb (1986) mentioned that as the mirror deposition process was further developed, and cavity losses decreased, the technique began to be plagued by errors associated with thermal noise, as well as the speed and repeatability of the frequency scan. Kalb (1986) points out that this technique will require improvements if it is to remain useful in the future, since lower loss coatings decrease the sensitivity and resolution of the measurement results. Because this method is very simple, it still is utilized somewhat today. For example, this method is used for the measurement of finesse of the supercavity optical spectrum analyzer SR-130 developed by Newport Corporation.

However, there are some problems in this finesse measurement as used by Newport. For example, as we will show in chapter 4, the fringe width of a scanning cavity will increase with the scanning rate of the cavity, so that the measured fringe width will be larger than that of the nonscanning cavity. Again, the profile of the output of a scanning cavity can not be described by the Airy function. In chapter 4 we will present a theoretical analysis and experimental results, as well as an improvement of this method.

2.3 Loss comparison technique

Early in the development of ion-beam sputter deposition process for ring laser gyroscope applications, Sanders (1977) claimed that most of the established vendors of multilayer dielectric mirror coatings had some means of measuring transmittance to ± 0.0001, but none had the means, with the equivalent high degree of accuracy, to measure reflectivity. Thus, when specifying reflection parameters to a laser mirror vendor one specified a particular transmittance and could only hope for minimum loss to absorption and scattering. Sanders invented a method to directly measure the reflectivity of mirrors. His experiment setup is shown in Fig. (2.1).

The technique involves two intralaser cavity measurements, one with the sample mirror in the cavity and one without. Fig. (2.1) indicates two laser geometry configurations: first without the sample mirror; second with the sample

mirror. Mirror #2 remains fixed for both configurations, and mirror #1 is removed to position #2 for the second measurement and configuration. The rotatable window serves as a measurable loss or calibrated leak for the cavity. The window is first oriented nominally at Brewster's angle relative to the laser beam axis and then rotated until laser action is quenched as a result of the induced reflection loss. This measurement is made twice: first without the sample mirror (configuration #1) using only mirrors #1 and #2, then with the sample mirror. The difference in the measured losses required to quench laser action is the amount of loss introduced by the sample mirror.

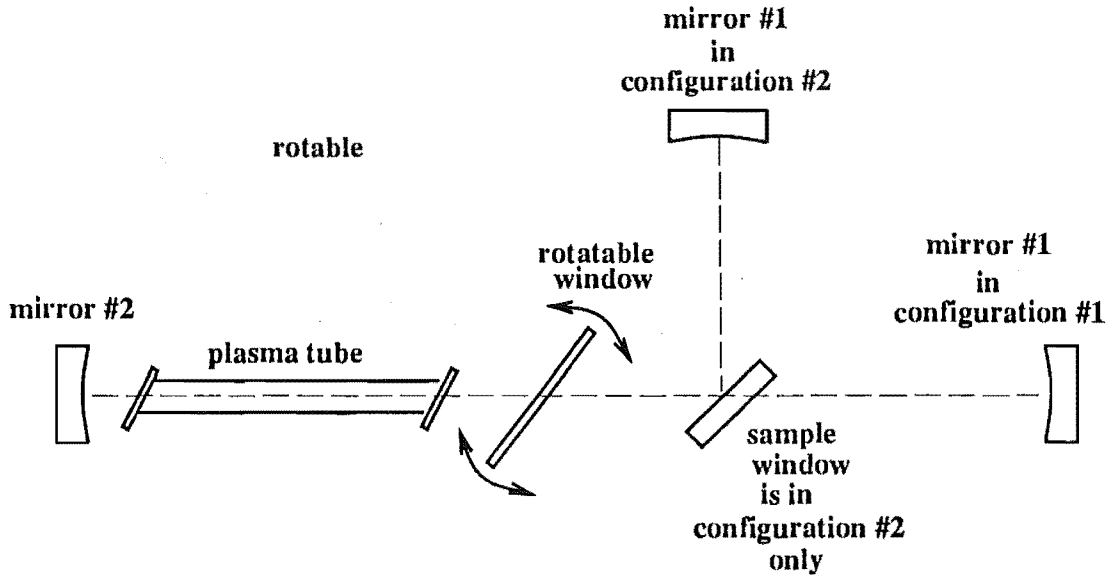

Fig. 2.1. Reflectance measurement apparatus (two laser cavity configurations) . From Sanders 1977.

There are two necessary restrictions associated with the geometry of the laser cavities and sample mirror which ensure equivalent gain and loss to the two lasers - the over-all laser cavity length of the two configurations must be the same, and the sample mirror must be plane. This ensures the same mode geometry and thus the same gain and diffraction losses associated with the plasma tube.

In this method, the accuracy and repeatability of the measurement is a function of the sharpness and stability of the lasing threshold. An effort must be made to hold the gain and losses constant from one measurement to the next. The reproducibility is limited by the quality of the optics, stability of the current flowing through the plasma discharge, precision angle reading associated with the

rotatable window, dust that might fall unnoticed on a piece of the optics, and to some extent mechanical and thermal stability of the setup. The accuracy of the reflectivity measurement in Sanders's device was ± 100 ppm.

2.4 Phase shift method.

Herbelin *et al.* (1980, 1981) developed a phase shift method to determine the reflectivity by measuring the cavity decay time of an optical resonator. This approach uses a continuous laser beam with intensity modulation. This modulated beam is matched transversely into the probe cavity and then passed through this cavity. The light beam that emerges from the resonator is also modulated but is shifted in phase by an angle α, related to the time the photon spends in the cavity t_c by an expression given by Herbelin *et al.* (1980).

$$\tan \alpha = 2\pi f_m t_c \tag{2.3}$$

where f_m is the frequency of the intensity modulation of the laser beam. We should mention here that Eq. (2.3) was derived by the summation of the intensities, rather than of the amplitudes, of the subwave components which are bouncing in the cavity. In principle, this is not correct for a coherent laser source. The phase difference α between the input and output beams was measured by a lock-in amplifier. Herbelin *et al.* (1981) claimed that the reflectivity resolution of 50 ppm was achieved at wavelength in the visible-to-near-infrared, where the mirror reflectivity was 99.975%. This method was also used at mid-infrared (from 2.7 to 4.0 μm)(Kwok, Herbelin, and Ueunten 1983), and a reflectivity resolution of 500 ppm was obtained, where the mirror reflectivity was not so high (99.20%). They predict that if the mirror reflectivity is 99.9% or better, this method can achieve an accuracy of 100 ppm at mid-infrared wavelength.

Elleaume *et al.* (1985) have used this phase shift method for the measurement of the degradation of mirrors used in a ring free-electron laser where the total round trip gain of laser is quite low (~0.1%). Due to its low gain, the ring free-electron laser necessitates the use of high reflectivity mirrors. The reflectivity measurements obtained by using a laser were compared with those obtainable by using the synchrotron radiation, as well as with the results of directly measuring the cavity decay time by simply switching off the ring free-electron laser itself, which we will discuss in Sec. 2.7. For new or weakly degraded mirrors, the three techniques gave similar results when operated one after the other in exactly

the same experimental conditions. For highly degraded mirrors discrepancies appeared with a spread of estimated losses as high as 100%.

There are two problems in this phase shift method. One of them, as we mentioned previously, is the noisy character of the transmitted laser intensity. The accuracy of the determination of the phase of the transmitted beam is limited by this noise. The noise present in the transmitted beam is intrinsic to this technique. Fabry-Perot analysis shows that transmission will occur only when one of laser modes (which occur at integer multiple frequencies of c/P) matches the frequency of the one of the cavity modes. The noise in the transmitted beam results from the independent vibration of the two cavity lengths. Let us assume we can solve this problem by mechanical and thermal stabilization of the cavity lengths, and lock the laser frequency to the cavity resonance. The second problem still exists in this method, because this phase shift is dependent on the detuning of the cavity resonance (Billardon *et al.* 1991). As a solution of this problem, Billardon *et al.* (1991) demonstrate that the best measurement results are obtained using an incoherent or moderated coherent light source (coherent length is low with respect to the cavity length) to avoid this problem. However for the measurement of He-Ne laser mirrors, the incoherent source with appropriate wavelength is not available.

2.5 Ring-down technique

Anderson, Frisch, and Masser (1984) developed a technique to determine the losses in the cavity by directly measuring the decay time. This method relies on the fact that, with no light incident on the cavity, its output is determined only by its transient response which is characterized by an exponential decay of the intensity with a time constant which in turn is determined only by the round trip losses in the cavity, the round trip path length of the cavity, and the speed of light. Therefore if light is injected into the cavity and then the source is quickly shut off, the decay time can be measured directly. As the cavity losses decrease, the cavity decay time increases, increasing measurement sensitivity and resolution.

This technique measures the cavity decay time directly in a straightforward manner using relatively simple instrumentation. In this approach, a continuous laser beam is injected into the probe cavity. When the cavity is clearly in resonance for a reasonable amount of time, light will build inside the cavity and be transmitted throughout the mirrors of the cavity. A detector senses the intensity of the light transmitted through one of the mirrors; when the transmitted light

reaches a predetermined level, the laser light is switched off via a Pockels cell or an acousto-optic modulator. The decaying light level is monitored by the detector and recorded by a digital storage oscilloscope.

The optical switch is the most critical part of this method simply because it must be fast. Typical decay times of low loss cavities may be from 0.1 to 50 μs. The precision of the measurement is directly determined by the speed of the optical switch. Anderson *et al.* (1984) report that their apparatus has a decay time resolution of 10 ns and has demonstrated a total cavity loss resolution of 5 ppm.

This method was used for probing a standing electromagnetic wave in a laser ring cavity by Abromson and Bickel (1990). They inserted a quartz fibre with a diameter of 0.4 μm into an optical cavity. The losses in the cavity induced by the fibre varied with its position in the cavity. By observing variations in the cavity's irradiance decay time, they observed the longitudinal shape of the laser standing wave.

One problem remains in this technique. Anderson *et al.* (1984) argue that motions of the mirrors due, for example, to mechanical vibrations are usually small over time scale of the cavity decay time. Once the light is switched off, motion of the mirrors cannot significantly change the decay time since the fractional change in cavity length is negligible. Indeed, the noise level of the transmitted beam is greatly reduced compared with the phase shift method. However, occasional nonexponential decays of the cavity output exist on the measurements (O'Keefe and Deacon 1988). This problem results from the mirror motion during the cavity decay time. Billardon *et al.* (1991) have proved and demonstrated that the mirror velocity in certain range has an influence on the exponential decay of the cavity. This is because the light intensity in the cavity and so the output will depend on the summation of all components of the amplitudes which have different frequencies arising from multiple internal reflection on the moving mirrors of the cavity. In this case, the transmitted intensity can be expressed as the product of the normal exponential decay R^{2n} and a time dependent function F(n). i.e. $I_n = R^{2n} F(n)$ (Billardon *et al.* 1991), where R is the reflectivity of the mirror and n is an integer. The properties of $F(n)$ are dependent on several parameters: the laser linewidth, velocity of the mirror motion, mirror reflectivity and cavity length.

2.6 Pulse ring-down scheme

A pulse ring-down approach is developed to measure low losses in the cavity (O'Keefe and Deacon 1988, Ramponi *et al.* 1988). In this scheme, a short pulse

(10 ns) is used to replace the continuous laser beam. This short light pulse is coupled into a linear or ring cavity from which a small (a few parts per million) portion is output in each transit cycle. The rate of decrease in the output signal is determined by the total cavity loss. The loss measurement is then based upon the measurement of a signal decay and a numerical fitting to the loss rate.

This technique avoids the problem associated with the requirement of achieving longitudinal mode coincidences in matching a continuous input signal by using short pulses so that every pulse of the probe laser enters the cavity with no additional intensity fluctuation or time delay. As a result, the sensitivity and data rate are improved, and technical requirements of the system are greatly relaxed.

Since the coherence length of the laser pulse is so short that no interference can become established in the test cavity. In this short pulse regime, the Fabry-Perot theory breaks down, permitting any frequency to be injected into the test cavity. Therefore continuous frequency scanning becomes possible without jumping from mode to mode as the frequency is scanned. The detailed analysis of this short pulse approach has been presented by O'Keefe and Deacon (1988).

With this advantage, a frequency tunable dye laser configured in an oscillator-amplifier arrangement, which is pumped by a frequency-doubled Nd:YAG laser or nitrogen pulse laser, is used to combine a test cavity for measuring the absorption spectra of water vapour near 1.1 μm by Ramponi *et al.* (1988) and gaseous molecular oxygen around 0.68 μm by O'Keefe and Deacon (1988).

This technique can also be used to distinguish surface contamination and bulk loss of mirrors (O'Keefe and Deacon 1988). The reflection bandwidth of a multilayer dielectric mirror is narrowed by surface or interlayer contamination. Bulk losses, on the other hand, are independent of wavelength. The contribution of surface (e.g. pollution-related) and bulk (defect-related) losses can be separated by a measurement of the spectrum of the loss.

The pulse ring-down technique is also used to measure the reflectance of multilayer high reflectance mirrors directly deposited on fibre ends by Stone and Stulz (1990). The pulse source used in this experiment was a pulsed diode laser operating at a wavelength of 1.53 μm. There are two requirements on the laser. One is that it must have sufficient power to make it possible to resolve the output pulse above the noise. Second, the pulses must be short enough to be resolvable in time. They use a mirrored fibre length of 5 m, so that the spacing of output pulses is about 33 ns and the probe laser pulse width is 25 ns. The measured results demonstrated by Stone and Stulz (1990) are in excellent agreement with theoretical expectations.

A cavity lossmeter based on this technique has been developed commercially by Deacon Research, Palo Alto, Calif. The fractional precision and the absolute accuracy of the loss measurement in their instrument are 1% and 1 ppm.

2.7 Laser ring-down measurement

When the mirrors have been installed in a laser, it is often important as well as convenient to measure directly the decay time of the cavity by using the laser itself. For most lasers operating in TEM_{00} mode, an aperture in the cavity is required to prevent the higher order modes from oscillating. For a He-Ne laser, the discharge tube with a diameter of a few millimetres has the same effect as an iris in achieving TEM_{00} mode operation. In this case, it is difficult to use an external laser source to measure accurately the decay time of the cavity because the aperture will induce an extra loss for the probing laser injected into the cavity owing to any mismatching of the transverse mode. For a ring laser cavity, the effective radius of curvature of a mirror for horizontal and vertical axes are different (Verdeyen 1989). This results in astigmatism and so an elliptical laser beam spot and, in general, different positions of the waists of the laser beam in these two orthogonal axes of the cavity. Baxter *et al.* (1982) have demonstrated that two cylindrical lenses with different radii of curvature are necessary to accomplish mode matching in a ring laser. Any mismatching of the external laser beam into the cavity caused by mechanical displacement or thermal fluctuation will induce an extra loss for the measurement of the cavity losses due to the aperture effect of the discharge tube in the cavity. This requirement makes the cavity loss measurement very difficult for a He-Ne ring laser when using an external light source.

However, this cavity decay time can be measured by directly using the oscillating laser itself. When a laser is operating, the oscillating mode is exactly matched with its cavity. By quickly ceasing pumping, one can reduce the gain essentially to zero in a time shorter than the cavity decay time. Then the laser detection system records an exponential decay which can be used to estimate the cavity decay time. For the Canterbury ring laser, the cavity decay time is expected to be greater than 15 μs, which is much longer than the lifetime of the metastable state of Ne (about 10^{-7} s). Therefore the accuracy of the measurement is mainly limited by the quenching time of the plasma discharge. This time depends on the speed of the electronic system and the characteristics of the gaseous discharge.

Elleaume *et al.* (1985) used this method to measure the cavity losses, where

the free-electron laser oscillation was switched off by changing the rf frequency. The measurements agree with the phase shift method when the cavity loss is less than approximately 600 ppm.

2.8 Comparison of measurement techniques

In principle, then, the reflectivity of the supermirrors can be determined by any one of three approaches: directly measuring the losses in the cavity, measuring the linewidth of the cavity and measuring the cavity decay time, we assume that the effect of the mirror flatness can be ignored. For convenience in the discussion, we summarise the precision of different measurement techniques published prior to this thesis in Table 2.1.

Table 2.1 Comparison of measurement methods

Parameter of Measurement	Precision	Reference
losses	100 ppm	Sanders (1977)
Phase shift	50 ppm	Herbelin *et al.* (1980)
Cavity decay time (by external cw source)	5 ppm	Anderson *et al.* (1984)
Cavity decay time (by external pulse source)	1 ppm	O'Keefe & Deacon (1988)
Cavity decay time (by laser itself)	10 ppm	Elleaume *et al.* (1985)

Table 2.1 shows that recent techniques developed for determining the high reflectivity of the supermirrors are mainly based upon the measurement of the cavity decay time. This is because the cavity decay time increases with the reflectivity of the mirrors and becomes progressively easier to measure.

The precision of the cavity loss of 1 ppm is obtained by using the pulse ring-down technique (O'Keefe and Deacon 1988). However, this device is too expensive (NZ$200,000) to be used in our research. The ring-down technique with a precision of 5 ppm in cavity loss measurement by using an external continuous

laser source is also a practical method, but this scheme need a fast optical modulator (rise time of 10 ns). An acousto-optic modulator with such fast speed costs about NZ$18,000 (e.g. Newport N17440 ultra-fast digital modulator), and an electro-optic modulator with a bandwidth of 100 MHz is still about NZ$8,000.

The phase shift method (Herbelin 1980) is also based on the cavity decay time but by measuring the phase shift of an intensity modulated beam. The major problems are the noise characteristic in the output signal and the dependence of the phase shift on the detuning of the test cavity. Owing to these two problems, the scheme only achieved a precision of 50 ppm in cavity loss measurement.

As for the approach of directly measuring the cavity loss (Sanders 1977), since the parameter of the measurement is the cavity loss itself, the precision of the measurement is determined by the sharpness and stability of the lasing threshold. This in turn is a function of the discharge current through the laser tube, and losses caused by several optical elements in the cavity, such as the two windows on the laser tube and the rotatable window for measuring the loss in the cavity. It is difficult to maintain the same condition during the measurements. Therefore, the accuracy of the cavity loss measurement of this scheme is limited to 100 ppm. This method is therefore no longer used; the resolution and repeatability are both poorer than those achieved by the ring-down technique.

Although the method of measuring the linewidth of a cavity recommended by Newport is valid for low finesse cavities, it is not suitable for supermirror cavities without improvements (Kalb 1986), and it has not been used by any manufacturers of the supermirrors so far.

2.9 Introduction to our methods

To perform the cavity loss measurement, we invented the ringing profile method (Li, Bennett and Stedman 1991), which we will discuss in this chapter, and modified the method for directly measuring the linewidth by scanning the probe cavity, which will be discussed in chapter 4. Our experiment results demonstrate that these two techniques are simple, reliable, sensitive and less expensive for the measurement of the reflectivity of the supermirrors. The equipment required for these two techniques are similar to a simple scanning Fabry-Perot interferometer system. The accuracy of the cavity loss measurements achieved by ringing profile method is 1 ppm. For the improved linewidth measurement, the resolution of the measurement is 1 ppm, but with the system error of 4 ppm, which is mainly caused by the broadening effect of the laser linewidth on the cavity output profiles.

To explain why the cavity loss measurement techniques based upon the measurement of the linewidth of the test cavity can also achieve the same precision as those obtained by the measurement techniques based on the cavity decay time, let us examine more closely their sensitivities.

From Eq. (2.2c), we obtain relations between changes in the decay time and in the linewidth of a cavity resulting from a small change of the round trip losses in the cavity of the form

$$\delta t_c = (P/c\ \Gamma^2)\ \delta\Gamma \tag{2.4a}$$

$$\delta L_{1/2} = (c/2\pi P)\ \delta\Gamma \tag{2.4b}$$

or

$$\delta t_c/t_c = \delta L_{1/2}/L_{1/2} = \delta\Gamma/\Gamma \tag{2.4c}$$

where δt_c, $\delta L_{1/2}$ and $\delta\Gamma$ represent the changes of the cavity decay time, the linewidth of the cavity and the losses in the cavity, respectively. Eq. (2.4c) shows that the requirements of the fractional uncertainties for the cavity decay time and the linewidth measurements are the same. For the cavity with a loss of 100 ppm, for instance, to achieve a precision of 1 ppm in this loss estimate, the fractional uncertainties $\delta t_c/t_c$ and $\delta L_{1/2}/L_{1/2}$ should be within 1% for the two methods, respectively. Therefore, the key point for a successful measurement is that the measurement device should be very sensitive to the small change of the cavity loss when this loss is itself very small.

Eq. (2.4a) shows that in the cavity decay time measurement, the sensitivity of the device will be proportional to the cavity path length P. This is because the decay time lengthens with the cavity path. The sensitivity of the measurement also depends on the total losses in the cavity; the cavity decay time will increase with the decrease of the losses in the cavity. A longer cavity is therefore preferable in cavity loss measurements when using the ring-down technique. On the other hand, any fluctuations of the test cavity length during the decay measurement will induce nonexponential decay, in turn giving new errors in the loss measurement (Billardon *et al.* 1991). This problem limits the measurement precision for a long cavity decay time. Therefore, a balance has to be struck between the sensitivity and stability by choosing a suitable cavity length. For example, Anderson *et al.* (1984) used a cavity of length 10 m and a fast optical modulator (with a turn-off time of 10 ns) in the experiment. For a low loss case (180 ppm), the measured cavity decay time was 185 μs ± 1.4%, where the error was the rms deviation from the mean of twenty consecutive measurements. For the high loss case (1270 ppm), the cavity decay time was measured as 26.24 μs ± 0.2%. In the latter case, the

sensitivity of the measurement is lower, but the fractional uncertainty is better than the former case.

For the linewidth measurement of the cavity, the sensitivity of the device is inversely proportional to the cavity optical length. This is because the free spectral range of the test cavity increases with the decrease of the cavity path. Eq. (2.2b) shows that the finesse is independent of the change of the cavity path length, but the linewidth of the cavity increases with the free spectral range of the cavity. Therefore, for the linewidth measurement of the cavity, a short cavity path length is more suitable. For example, the Newport supercavity has a total cavity loss of about 100 ppm. and the cavity length is 25.3 mm (corresponding to a free spectral range of 6 GHz). By using Eq. (2.2c), $L_{1/2} = \Delta\nu_{FSR}\,\Gamma/2\pi$, we obtain the linewidth of the cavity is about 100 kHz. From Eq. (2.4c), we can see that the resolution required to detect a cavity loss change of 1 ppm using the linewidth measurement is about 1 kHz, whereas the linewidth of the cavity measured in our experiments is 96.5 ± 1.0 kHz. For a Newport SR-200 series supercavity, whose length is 20 μm and free spectral range is 7.6 THz, and under the same condition on the mirrors, the resolution required to detect a cavity loss change of 1 ppm is 1.3 GHz. This confers an advantage, as we see below, for precision measurements of supercavity loss.

The probe laser frequency jitter (owing to the phase fluctuation of the laser field) also adds significant error to the cavity linewidth measurement. In chapter 4, we will deal with this problem. Our analysis there shows that the measured linewidth of the test cavity will depend on the scanning rate of the cavity. To reduce the error of the measurement to within 1%, a very low scanning rate is required. The time required to scan over the resonance of the cavity should be at least 100 times the cavity decay time. However, it is in the case of such a low scanning rate that the probe laser frequency jitter becomes large compared with the linewidth of the test cavity and gives a noisy output signal. We encountered this problem in our experiments. A solution is given in chapter 4. In principle, the linewidth measurement of the cavity requires a coherent light source. The coherent time of the laser source should be longer than the cavity decay time to achieve a good ratio of signal to noise in the cavity output. This coherent time of the probe laser is related with its spectral linewidth, which is proportional to the mean square phase jitter of the laser (see appendix A). Therefore, the upshot is that laser frequency stability considerations also suggest a preference for short cavities in linewidth measurement techniques.

In our experiment, we used a Newport NL-1 frequency-stabilised He-Ne laser as a probe light source in the ringing profile method. It has a linewidth of

about 4 kHz over a time interval of 0.1 ms. When this was used for the measurement of loss in a Newport SR-130 supercavity, the linewidth of the cavity output profile has been broaden about 4%. For a Newport SR-200 series supercavity (which is not available to us), a fractional uncertainty in the loss of less than 0.4% or absolute accuracy less than 0.4 ppm, are predicted for this technique. This is because the laser frequency fluctuation is far smaller than the required resolution, of 1.3 GHz, for achieving a precision of 1 ppm when the cavity loss is 100 ppm.

In the ringing profile measurement technique, the most important single parameter for defining the profile is $a_1 = \frac{1}{2}\beta/\gamma_c^2$, where β is the scanning rate of the cavity, and γ_c is the amplitude decay rate of the cavity and is defined by $2\gamma_c = 1/t_c$ (see chapter 3). By using Eq. (2.2c), we obtain the fractional change of this parameter with the losses in the test cavity in the form

$$\delta a_1/a_1 = 2\delta\Gamma/\Gamma. \tag{2.5}$$

Eq. (2.5) shows that the tolerance in the measurement of the cavity losses for the ringing profile method is twice as much as that of the ring-down techniques or the linewidth measurement. For instance, for a test cavity with the losses of 100 ppm, the fractional uncertainties in the loss measurement of the cavity required for achieving a precision of 1 ppm are 2% for the ringing profile method and 1% for either the ring-down techniques or the linewidth measurement.

The second advantage of the ringing profile method is that the time interval required for the probe laser frequency to scan over the resonance of the cavity is the order of tens of microseconds. In this short time, the effect of the laser frequency jitter on the precision of the measurement makes an extra contribution to the rate of frequency scanning. The composed rate of frequency scanning can be calibrated in our experiment by the intensity modulation of the laser source, which provides a scale for the relative frequency scanning. Therefore the laser frequency jitter does not affect the precision of the measurement of the cavity losses in the ringing profile technique. This has been demonstrated in our experiment (see chapter 3).

In practice, the normalised scanning parameter a_1 should be chosen in the range 1-10 to maximise the characteristic effects of cavity loss on the profile and so minimise errors in data analysis. This can be achieved easily by adjusting the cavity scanning rate β. With this adjustment, the length of the test cavity, and so in turn the cavity decay time do not affect the fractional precision of the

measurement. Hence the ringing profile method measures the losses in a long or short cavity with the same relative precision.

In summary, we have discussed the advantages and problems of each supercavity loss measurement method. For a long cavity, ring-down techniques are suitable. The longer cavity in turn means a longer decay time, making the ring-down measurement easier. For the linewidth measurement approach, a short cavity is preferable since it reduces the coherence length requirements for the probe laser. This choice also makes the measurement device more compact. The ringing profile method can be used in a wide range of the test cavity lengths. Each of these two methods is less expensive than the ring-down technique. Measurement of the loss in an active laser cavity is conveniently done by measuring the ringdown time directly on stopping pumping; otherwise matching problems with an external light source induce extra loss in the laser discharge tube or in cavity apertures by incipient vignetting. This extra loss will add to the total cavity losses and can not be allowed for in the measurement.

In our experiments, the ringing profile method is used to measure losses both in the Newport SR-130 supercavity and in our 4 m passive ring supercavity. An improved linewidth method is also used for the Newport SR-130 supercavity for comparison with the ringing profile method. The results from the two methods are in excellent agreement. The laser ring-down technique is also used to measure the cavity loss of our ring laser (Stedman *et al.* 1993), and the measurement result is consistent with the result from the ringing profile approach and with the precision attained for measuring the laser beat frequency in gyroscope mode.

Chapter 3

Ringing Response of a Scanned Resonator

We discuss in this chapter an optical ringing phenomenon when a high finesse cavity is excited by an external laser source which is not frequency-locked to the cavity, and so has a time-varying or swept relative frequency shift. Our early report (Li *et al.* 1991) gave results whose precision is greatly improved by the results of this thesis. We find that this simple and inexpensive technique is capable of yielding supercavity finesses or quality factors with the very competitive accuracy of 1 part per million. Some variations on this theme are discussed in this and in later chapters. In particular, application is made to the ring laser cavity, so determining quality factors which may be compared with other and somewhat crude ringdown estimates. Also, the presence of significant asymmetry in the profile at relative frequency scanning speeds which are too low to generate significant ringing is discussed in chapter 4.

In Sec. 3.1, we will give a brief introduction to ringing phenomena in various fields and to our observations in the high finesse cavities. A theoretical analysis applying to the general case is given in Sec. 3.2. The description of the experiments are presented in Sec. 3.3. Finally, the comparison between the experimental results and theoretical fitting is shown in Sec. 3.4.

3.1 Ringing phenomena and applications

The ringing of a resonant system under swept frequency excitation has been investigated and applied in a wide variety of problems, whenever the frequency of a signal and the resonant frequency of the system cross over in time. Observations of such phenomena have been used to perform a frequency analysis of ocean

waves by Barber and Ursell (1948), Barber (1849) and Storey (1958), and to measure the quality factor of a superconducting cavity by Bennett (1970). They have been noted in acoustic waves by Avenel *et* al. (1983). Rothenberg and Grischkowsky (1985) and Rotherbery (1986) sent a frequency-swept ultrashort optical pulse through a resonant vapor, determining from the observed ringing the time-dependent phase of the ultrashort pulse. Loy (1977) observed ringing in a Stark-switching optical experiment when the resonant frequency of the medium was swept rather than the pulse frequency. Ioannidis *et al.* (1988a, 1988b) observed ringing in an optical fibre ring resonator, phase modulation being induced by a piezoelectric cylinder around which is wrapped a length of optical fibre.

In any experiment displaying these phenomena, the system must be linear, the input frequency must sweep through the system resonance within a time which is smaller than the decay time of the resonant system, and the coherent length of the source must be long compared to the temporal width of the ringing pulse.

We first observed this ringing phenomenon for optical cavities by chance in our mode-matching experiment. A He-Ne laser (Melles Griot 05LLR 831, with an output beam power of 5 mW, unpolarized and without frequency-stabilization) was matched transversely by a conventional lens and injected into the main ring. The latter is a square cavity with a perimeter of 4 m and with supermirrors whose reflectivities were approximately 99.9985%, giving a free spectral range of 75 MHz and a finesse $\sim 10^4$. The output of the cavity was detected by a photomultiplier (PMT) and recorded by a digital storage oscilloscope. There were no locking loops between the laser cavity and the test cavity, so that the relative frequency variations arise from independent variations of the two cavity lengths caused by mechanical and thermal fluctuations, including atmospheric microturbulence in the (unsealed) ring cavity.

The output of the cavity appeared as a series of the pulses with irregular shapes as a consequence of the relative frequency variations between the two cavities. We noticed an interesting phenomenon with these pulses: the leading edges of some pulses rose smoothly, but the trailing edges have pronounced oscillatory envelopes with the characteristic of a chirp with ascending frequency. The origin of this ringing phenomenon was confirmed in discussions with Dr. R.G.T. Bennett (University of Canterbury) and Professor F.V. Kowalski (Colorado School of Mines, Boulder, Colorado, USA), who provided some valuable references and suggestions.

A further experiment was performed using a Newport SR-130 supercavity or scanning Fabry-Pérot interferometer in place of the square ring resonator, and a

Newport NL-1 frequency-stabilized He-Ne laser in place of the Melles-Griot general laboratory laser. We observed very stable, highly repeatable ringing profiles from the output of this interferometer (Li *et al.* 1991). The ringing waveform depends significantly and characteristically on each of three considerations: the quality factor of the probe cavity, the functional form of the relative frequency scanning, and the laser linewidth. Oversimplifying somewhat, we can separate the role of each parameter as follows. The ratio of the cavity resonance width to the (linear part of the) scanning rate determines, and so can be estimated from, the overall ringing pulse width. Several orders of the nonlinear terms in the scanning rate may be estimated from the temporal distribution of the interference maxima; the random variations in the nonlinear coefficient cause the difference in waveform between pulses. The linewidth of the laser line can be estimated from the visibility of the ringing oscillations.

3.2 Theory of the ringing profile

Although the Airy formulae $I_t/I_i = T^2/[(1-R)^2 + 4R\sin^2(\delta/2)]$ and $I_r/I_i = 4R\sin^2(\delta/2)/[(1-R)^2 + 4R\sin^2(\delta/2)]$, or filter functions for intensities, are used in standard theoretical studies of the scanning Fabry-Perot interferometer (e.g. Cooper 1971, Zipoy 1979), they are inadequate for the analysis of ringing. It is vital to include the phase shift information in the amplitude response, since ringing is a consequence of interference between the instantaneous laser amplitude and the cavity amplitude response function. Our analysis therefore avoids the Airy function description of an optical response.

Let $A_i(t)$ be the incident complex wave amplitude for one choice of linear polarisation of the beam incident in an optical cavity. Its Fourier transform will be written as $\mathcal{A}_i(\omega)$.

In the simplest approximation of a wave with constant amplitude, $A_i(t) = A_0\exp[i\phi(t)]$. The effect of residual laser jitter needs inclusion; we use a stochastic model for phase noise and write the input field at time t as

$$A_i(t) = A_0 \exp[i\phi(t)] \exp(-|t|/\tau_s), \tag{3.1}$$

where τ_s is an effective decay time, and $\phi(t) = \int\omega(t)dt$. $\omega(t)$ is the instantaneous angular frequency. A derivation is given in appendix A. The angular frequency can be expanded in a Taylor series: $\omega(t) = \omega_0 + \omega_0't + \frac{1}{2}\omega_0''t^2 + (1/6)\omega_0'''t^3$, where the expansion coefficients are ω_0, the injected frequency at $t=0$, ω_0', the (linear

approximation to the) relative scanning rate, and where ω_0'', ω_0''' represent nonlinearities in the relative scanning rate. $\omega(t) - \omega_0$ is to be interpreted as the instantaneous difference between the laser frequency and the cavity resonance, arising from scanning of the SR-130 and from microturbulence of the air and motion of the cavity mirrors for the ring cavity, after taking a short-time (sub-millisecond) average over jitter. Over the microsecond time scale of the experiment we may expect the linear term ω_0' to dominate, so that the response of either the SR-130 scanning Fabry-Perot cavity or the 1 m^2 ring cavity to a monochromatic wave will be similar to the response of a stable cavity to a wave with linear FM. We shall determine the quadratic and cubic terms ω_0'', ω_0''' as well as the linear term ω_0' applicable in any particular run, together with the effective laser linewidth and the cavity finesse, from the profile of the system response.

The amplitude transfer function of the optical cavity is $H(\omega) = T/[(1 - R\exp(-i\delta_c)]$. T is the power transmissivity of the cavity mirrors, and R their reflectance; typically $T \sim 4$ ppm, while $1 - R \sim 15$ ppm, the difference representing the effects of absorption and scattering in the multilayer dielectric coatings (Bilger *et al.* 1990). The round-trip optical phase shift $\delta_c = (\omega - \omega_c) P/c$ where ω_c is the resonant frequency of the cavity, P is the optical path of the cavity and c is the speed of light.

In such a supercavity with finesse F of order 10^4, δ_c will be of order 10^{-4} modulo 2π when the transmitted field $\mathcal{A}_t(\omega) = \mathcal{A}_i(\omega)\ H(\omega)$ is significant. Hence (Anderson *et al.* 1984) we may expand the exponential in $H(\omega)$, and retain only the linear term: $H(\omega) = B/[\gamma_c + i(\omega - \omega_c)]$ where $B \equiv cT/RP$ and the amplitude decay rate of the cavity $\gamma_c \equiv c(1 - R)/RP$. We work in the time domain, where the transmitted amplitude $A_t(t)$ is the convolution of $A_i(t)$ and the impulse response $h(t)$, the inverse Fourier transform of $H(\omega)$, so that

$$h(t) = BS(t)\ \exp(-\gamma_c t)\ \exp(i\omega_c t) \tag{3.2}$$

where $S(t)$ is Heaviside's unit step function (Bracewell 1965): $S(t) = 0$ for $t \leqslant 0$ and $S(t) = 1$ for $t > 0$. Then:

$$A_t(t) = \int_0^\infty dt'\ A_i(t')h(t - t'). \tag{3.3}$$

We choose the origin of time so that $\omega_0 = \omega_c$ and obtain from the above equations, with the change of variables $\tau \equiv \gamma_c t'$, $\bar{t} \equiv \gamma_c t$, $b \equiv 1/(\gamma_c \tau_s)$, $a_1 \equiv \frac{1}{2}\omega_0'/\gamma_c^2$,

$a_2 \equiv (1/6)\omega_0''/\gamma_c^3$, $a_3 \equiv (1/24)\omega_0'''/\gamma_c^4$, $C = A_0B/\gamma_c$:

$$A_t(t) = C\exp(-\bar{t})\exp(i\omega_c t)\int_{-\infty}^{t} d\tau \exp(\tau - b|\tau|)\exp\{i[\tau^2(a_1 + a_2\tau + a_3\tau^2)]\}. \qquad (3.4)$$

This equation encapsulates the ringing phenomenon. The final complex exponential (sinusoidal) factor represents the beating of the amplitudes (particularly for $\tau > 0$, i.e. $t > 0$; and so for the decay of the pulse, since the accompanying exponential factor then enhances the contribution), its nonlinear form characterising the spacing of interference maxima; the resulting oscillations are damped by the term involving b, and the overall envelope is provided by the remaining real exponential pulse terms. The parameter b represents the ratio of the laser linewidth to the probe cavity width since $b \equiv 1/(\gamma_c\tau_s) \equiv \gamma_s/\gamma_c \equiv \Delta\nu_L/L_{1/2}$, where γ_s, γ_c are the amplitude decay rates of the laser and the cavity, and $\gamma_s/2\pi = \frac{1}{2}\Delta\nu_L$, $\gamma_c/2\pi = \frac{1}{2}L_{/2}$, $\Delta\nu_L$ is the laser linewidth and $L_{1/2}$ is the cavity full width at half maximum.

We perform a least squares fit of the model parameters a_1, b, a_2 and a_3 to the our preliminary experimental pulse waveform, and in doing so find this parameterisation to be both adequate and informative. This is demonstrated by the curves (a), (b), (c) of Fig. (3.1), which give the predictions of Eq. (3.4) when each of b, a_2 and a_3 respectively are varied over a certain range.

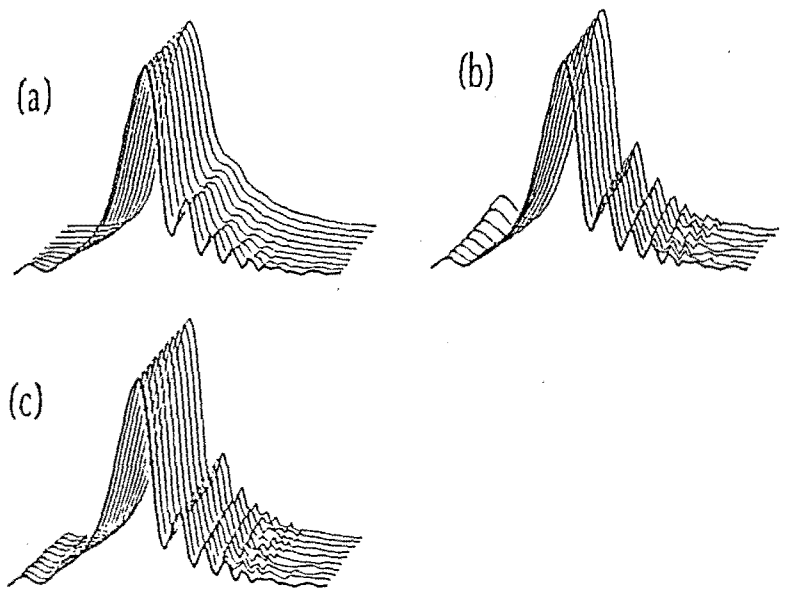

Fig. 3.1 (a), (b) and (c): the predictions of Eq. (3.4) when each of the laser linewidth parameter b, and the nonlinear scanning rate parameters a_2 and a_3 respectively are varied.

A comparison of these figures gives further emphasis to our earlier qualitative discussion. The major effect of the (renormalised) effective laser width parameter b is on the visibility of the ringing. The nonlinear coefficients a_2, a_3 squeeze the oscillations on the tail, as observed experimentally, but their variation affects ringing in the precursor (i.e. the profile for times prior to the main peak), some evidence of which can be seen in the experimental profile.

In our more recent experiment for SR-130 supercavity, the averaging function of a digital storage oscilloscope has been used, so that the distortion and noise, causing by the random frequency vibrations between the laser and cavity resonance, on the ringing profiles are greatly reduced. In this case, the ringing profile is basically dominated by the linear frequency scanning parameter a_1.

The dependence of the ringing profile on the parameter a_1 is shown in Fig. (3.2), where we assume the parameters b, a_2 and a_3 to be zero. The extent of the ringing on a cavity output profile is visible from the solid lines in the diagrams. In (b) and (c) of the Fig. (3.2), the dashed and dotted lines represent the real and imaginary parts respectively of the amplitude of the cavity output.

3.3 Experimental description

3.3.1 Preliminary experiment

We have already reported preliminary experimental results of this ringing phenomenon in optical cavities (Li *et al.* 1991). A copy of the paper is presented as appendix A. In fact, the preliminary experiment was completed on our 1 m^2 ring cavity and the Newport SR-130 supercavity in a limited time (two weeks), owing to the very restricted period at that stage over which we were given the loan of a suitable digital storage oscilloscope.

The experiment setup is a standard arrangement of scanning interferometers as shown in Fig. (1) in appendix A. A He-Ne laser (Melles Griot 05LLR 831 or Newport NL-1) is used as an external light source. The TEM_{00} mode of this laser is injected through an acousto-optic modulator (AOM) as isolator and a matching lens (focal length of 300 mm) into probe supercavities: 1 m^2 ring cavity with a finesse of $\sim 10^4$ and Newport SR-130 interferometer with a free spectral range of 6 GHz and with a finesse which quoted as greater than 20000. The output of the probe cavity is detected by a photomultiplier (PMT) and recorded by a digital storage oscilloscope (Hitachi Denshi Model VC-6275) an item we were later able to purchase.

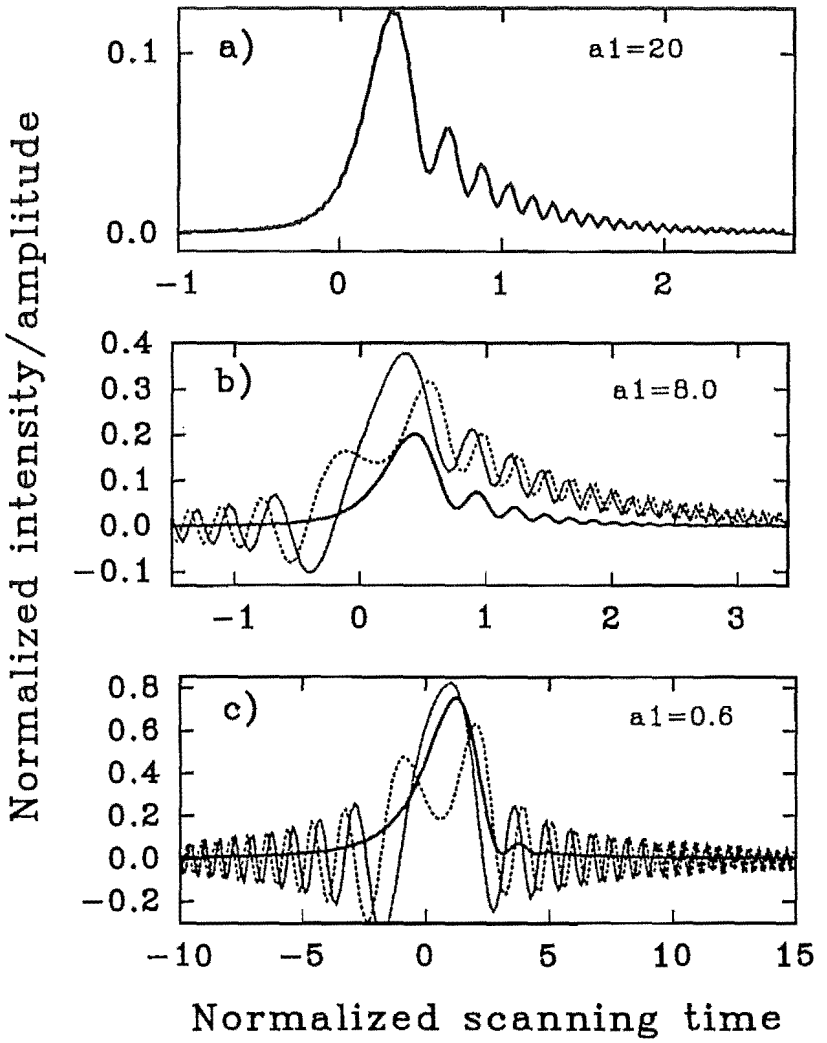

Fig. 3.2. Dependence of the ringing profile on the parameter a_1. a_1 = 20, 8.0 and 0.6 in (a), (b) and (c), respectively. The solid lines in the diagrams are the intensity of the cavity output. The dashed and dotted lines represent the real and imaginary parts respectively of the amplitude of the cavity output.

Some aspects of our preliminary experiment needed improvement. At first, the data processing was rather complicated: the ringing profiles of the cavity output were recorded by a digital storage oscilloscope, the screen then being photographed; the pulse profile on the photographic print was scanned and transferred into a computer; the profiles were digitized using specially written software and the computer mouse; finally, another specially written program in TurboPascal carried out the data fitting. Each step contributed an error to the measurement. The second source of error came from the detector noise. The photomultiplier we used in the preliminary experiment had an efficiency of 0.1% at the wavelength of 633 nm, and we had to adjust the signal/noise ratio and its sensitivity to the detection scheme by adjusting the time constant in the PMT detector circuit. Owing to the above error sources, measurement of the cavity loss had a systematic bias of 30 ppm in our preliminary experiment.

3.3.2 Improvements in experiment

We have now made some significant improvements in our more recent experiments:

- the ringing profile recorded by the digital storage oscilloscope is directly transferred into a computer to perform the data fitting;
- the calibration of the scanning rate of the cavity is provided by the frequency of the intensity modulation with a fractional frequency precision of 10^{-7};
- the output signal is monitored by a more efficient (~3% at wavelength of 633 nm) PMT with a bandwidth of 100 MHz.

The experiment setup is shown in Fig. (3.3). The intensity of the Newport NL-1 frequency-stabilized He-Ne laser is modulated by the acousto-optic modulator (Newport N24080) inserted between the He-Ne laser and the supercavity to supply a calibration for the frequency scan which is useful since the relation between voltage and expansion of the piezoelectric material is in general not exactly linear (Aschauer, Asenbaum, and Gerl 1990). In principle, we could use an AM or FM calibration of the scanning rate. Since the nonlinearity of the frequency sweep provided by the driver of the acousto-optic modulation signal in this AOM is 15% (as quoted by Newport), we chose AM modulation in our experiment. A modulation signal of 2 MHz is used as input to the modulator driver and a frequency counter is used to monitor the modulation frequency. When the intensity of the laser beam is modulated through the acousto-optic modulator, two side bands will appear on the output of the probe cavity. The

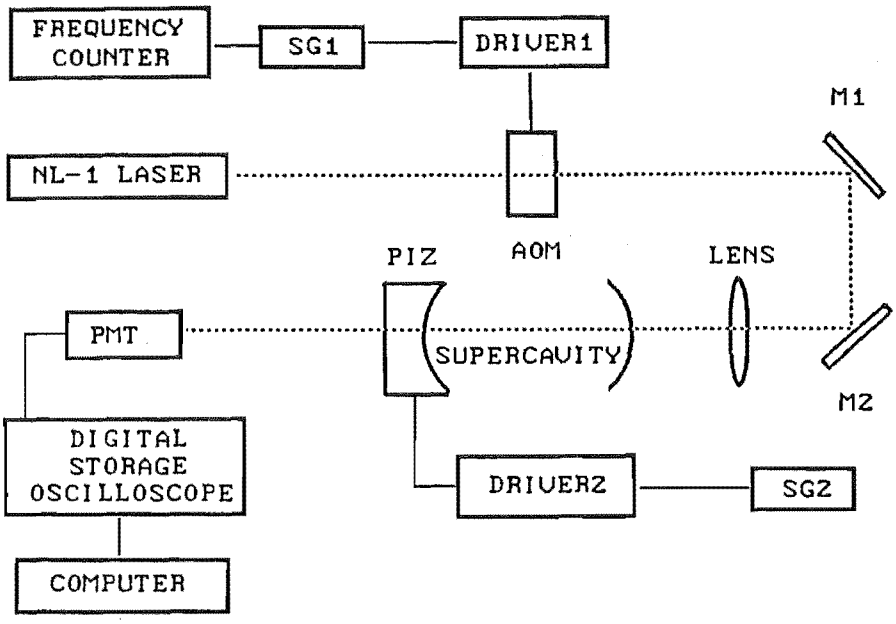

Fig. 3.3. Experiment setup for the ringing profile measurement

separation of these two side bands is exactly twice the modulation frequency. This provides a precise frequency scanning calibration for our measurement.

The SR-130 supercavity is scanned at 25 Hz and its frequency scanning rate is controlled by adjusting its frequency scanning range. For example, when its frequency scanning range equals its free spectral range (6 GHz), the frequency scanning rate of the SR-130 supercavity $\beta/2\pi$ = 150 GHz/s. The output of the scanning cavity is detected by a photomultiplier (Thorn EMI Type 9214) with a nominal bandwidth of 100 MHz, and its output is sent to a digital storage oscilloscope (Hitachi Denshi Model VC-6275) with a maximum sampling rate of 200 million samples per second and a fractional precision of time scale reading of 10^{-4}. Some details about the NL-1 frequency-stabilised laser and the acousto-optic modulator are given as follows.

3.3.3 NL-1 frequency-stabilised laser

The principle of this stabilized laser is described by Niebauer *et al.* (1988). The laser has internal mirrors. Adjacent longitudinal modes are separated in frequency by $c/2L$ where L is the length of the laser tube and c is the speed of light; for the NL-1 laser (where $L \simeq 21$ cm) this frequency difference is ~ 700 MHz. Adjacent longitudinal modes have orthogonal polarizations (Balhorn, Kunzmann, and

Lebowsky 1972). Near the symmetric tuning position, only two such adjacent longitudinal modes fit within the Doppler width (1.5 GHz) of the neon emission line at 474 THz (633 nm). Thus, as the cavity is tuned, the intensity of one polarization increases while the intensity of the orthogonal polarization decreases. High frequency stability is obtained by locking the cavity length to keep the ratio of the intensities constant as suggested originally by Balhorn *et al.* (1972). There are two possible locking points, which differ by interchanging their polarization. Since one polarization is selected for the output beam (using a polarizing beam splitter), the frequency of the laser output changes by ~700 MHz when the locking position is switched. The output polarization mode can be locked either on red side (lower frequency) or the blue side (higher frequency) of the centre frequency of the neon emission line.

The fractional frequency drift of the Newport NL-1 He-Ne laser is less than 2×10^{-9} per day. For our experiment, the short term (microsecond) frequency stability is more important for the cavity loss measurement. The rms frequency fluctuations of NL-1 laser are quoted as 100 kHz in the short term (5 ms), 5 KHz in the medium term (100 sec) and 20 KHz for long term (1 hr). In our measurement, the time for the laser frequency to be scanned through the probe cavity is the order of a few microseconds. For such short periods, information on the laser stability has not been provided by Newport.

In our experiment, we have observed the effect of the laser frequency jitter on the ringing profile of the output of the probe cavity. The results of data fitting in next section shows that the experimental data are in excellent agreement with our theoretical prediction. This provided a novel method to determine the frequency fluctuation of the probe laser over such short periods.

3.3.4 Optical isolation

In our experiment, a Newport N24080 acousto-optic modulator (AOM) is used to provide the isolation of the NL-1 laser from the feedback arising from the laser beam reflection at the probe cavity mirror. Feedback among optical elements must be minimized for a frequency stabilized laser. Feedback amplitudes will coherently add to and subtract from the laser field, so as to induce frequency fluctuations of the laser. Salomon, Hill, and Hall (1988) point out that for a frequency-stabilized laser to reach 1 Hz locking accuracy, an isolation of $\sim 10^{-5}$ in intensity (100–dB isolation) is needed.

There are several methods for achieving adequate optical isolation. A simple

isolator can be constructed from a polarizing beam-splitter cube and a quarter wave plate (e.g. Chartier *et al.* 1989). Light in a forward direction is polarized by the cube, then circularly polarized by the quarter wave plate. Back reflections will change left-circular polarized light to right-circular (or vice versa). Upon passing through the quarter wave plate, the returning beam is linearly polarized and is blocked by the polarizing cube. In practice, this type of isolator can attenuate the returning beam by 30 dB (as quoted by Newport). Magneto-optical (Faraday-effect) devices (e.g. Carlisle and Cooper 1989) are also popular tools for achieving optical isolation. This method utilizes crystals that rotate the plane of polarization by 45^0 when they are placed in a magnetic field. The rotation is independent of direction. Thus, returning light will be rotated by 90^0 with respect to the input. If input and output polarizers are oriented at 45^0 to each other, the returning beam will be strongly attenuated. For example, a series optical isolator made by Newport is based on this method. For critical applications, Newport's H series isolators deliver either 60 dB or 90 dB isolation, and are designed for diode laser wavelengths, at a cost of ~ NZ$10,000. Isolators available at the He-Ne laser wavelength have multi-wavelength tunability and provide isolation better than 35 dB (as quoted by Newport).

The optical isolation achieved by means of the acousto-optic modulator (Smith 1973) is different from the beamsplitter/waveplate and magneto-optical isolators. The isolation properties of the acoustooptic modulator are based upon the fact that the light deflected by an acoustooptic modulator is shifted in frequency by an amount equal to the acoustic frequency (Gordon 1966, Korpel 1981). Further, the reflected beam passing through the modulator a second time is again shifted in frequency by the same amount and in the same sense, if the modulator is operating in the Bragg mode, and hence the reflected light returned to the laser is shifted in frequency by an amount $2\nu_a$, where ν_a is the frequency of the acoustic wave. Provided the frequency of the light returned to the laser is not close to any resonant frequency of the laser cavity, it will not pull the laser and will simply be reflected from the output mirror of the laser. Salomon, Hils and Hall (1988) also use an acousto-optic modulator as an isolator for the 632.8 nm laser frequency stability and an isolation of ~ 70 dB is achieved. Chartier *et al.* (1989) also use this technique for the frequency stabilization of the 543 nm He-Ne laser.

The acoustic frequency of the Newport N24080 AOM used in our experiment is 70 MHz. The frequency of the reflected light from the cavity mirror is then shifted by 140 MHz, which is far outside of the cavity resonant profile (of width ~1 MHz) of the NL-1 laser, so that the frequency stability of the NL-1 laser

is not affected by the optical feedback.

The deflection angle θ of the incident laser beam in an acousto-optic modulator is given by (e.g. Korpel 1981)

$$\theta = \lambda f_a / v_a \tag{3.5}$$

where λ is the wavelength of the incident laser, f_a and v_a are the frequency and velocity of the acoustic wave, respectively. The Newport N24080 acousto-optic modulator is made from flint glass. The acoustic velocity and frequency are 3.51 km/sec and 70 MHz in the modulator respectively. At the He-Ne wavelength, the deflection angle of the incident laser beam is approximately 12.4 mrad.

Eq. (3.5) shows that the deflection angle is dependent on the frequency of acoustic wave. When a sine voltage modulates the acoustic wave to perform an intensity modulation of the laser beam, the frequency, f_a, of the acoustic wave splits three components: f_a, $f_a + f_m$ and $f_a - f_m$ where f_m is the modulation frequency. Therefore, when the laser beam is modulated in intensity, two sidebands appear with a differential frequency shift $\pm f_m$ with respect to the carrier frequency of the laser beam. The change $\Delta\theta$ in the deflection angle of the sidebands can be calculated from Eq. (3.5) as $\Delta\theta = \pm \lambda f_m / v_a$. Assuming f_m = 1.5 MHz, we get $\Delta\theta \simeq \pm$ 0.27 mrad. This small amount of change in the deflection angle is detectable in our experiment: the sideband magnitudes in the output of the supercavity are very sensitive to the deflection angle of the sidebands, which is proportional to the modulation frequency of the acousto-optic modulator, owing to the angular misalignment of the sidebands respect to the probe cavity (We aligned the carrier component of the laser beam to be normal to the probe cavity, which is nonfocal cavity and has a preferred axis.). We find that the sideband components in the cavity output disappear when the modulation frequency f_m is greater than 6 MHz. In this case, the deviation angle, $\Delta\theta$, of the sidebands from the carrier is about 1 mrad and this indeed corresponds to the order of magnitude of the precision necessary to align the SR-130 Fabry-Perot interferometer.

3.4 Experimental results

New and more accurate experimental observations of the ringing profiles for the SR-130 supercavity than those we published earlier (appendix A) and at different scanning speeds are presented in appendix E. The main task for determining the

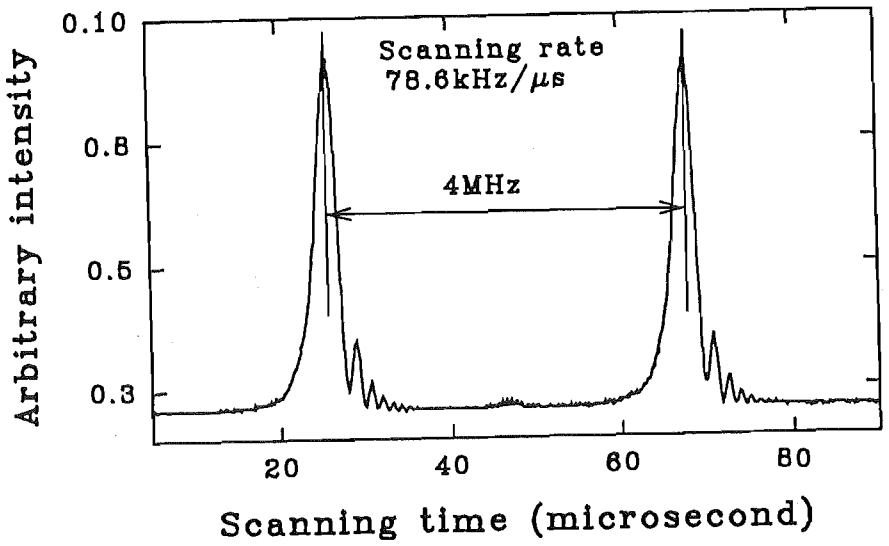

Fig. 3.4. Illustration of the calibration of the frequency scanning rate. Only two side bands of a AM laser beam are shown in this picture and the central component is suppressed by adjusting the dc offset of the AOM driver.

probe cavity losses is that of fitting the experiment data of the ringing profile to the theoretical model governed by Eq. (3.4). We developed a program in Turbo Pascal, which is attached in the thesis as appendix F, to perform the fitting. While the numerical techniques used are unsophisticated, this program is particularly well adapted to the task in hand, given the very different effects (some linear and some nonlinear) of changes in the fitting parameters.

Fig. (3.4) illustrates the calibration of the frequency scanning rate of ringing profiles. In our experiment, the frequency f_m of the laser intensity modulation provided by the AOM is 2.00232 MHz, so that the frequency interval between the two sidebands is 4.00464 MHz. We can read the time interval Δt between the two side bands with a fractional uncertainty of 10^{-4}. Then the frequency scanning speed is given by $f' = 2f_m/\Delta t$.

We noticed that the carrier magnitude of the modulated laser beam in the output of the Fabry-Perot cavity was dependent on the DC offset of the AOM driver in our experiment. For a AOM, no ultrasound, no Bragg reflection. The intensity of light reflection is therefore a function of the ultrasound wave amplitude which however nonlinear goes zero. AM of the ultrasound amplitude translates into AM of the light intensity. If the DC level is nonzero, and the AM a small fraction, the intensity is $C + A\cos 2\pi f_m t$, and (as an amplitude for the optical

carrier $\cos 2\pi ft$) so give central carrier and sidebands. If the DC level is zero, the optical intensity falls to zero each half cycle of the AM, when the latter passes through zero, and so its FFT harmonics have double the frequency spacing. In this case, the light amplitude-V curve is linear through the origin, so that the phase of the AM variation of the optical frequency is correlated and changes by 180 degrees as the input voltage of AOM driver changes sign. Hence the pure AM variation in the amplitude of the light beam gives no carrier at the optical frequency for the amplitude in principle. While the detector only measures an intensity, the Fabry-Perot cavity has the function of detecting frequency components of the amplitudes, which do not include the carrier as shown in Fig. 3.4.

In the following theoretical fitting, we assume the parameters a_2 and a_3 to be zero. Fig. (3.5) shows typical fittings of the experimental data to three ringing profiles with different frequency scanning rates, where each ringing profile is the average of 64 runs for averaging out the noise on the profiles. In the diagrams, the solid lines are the theoretical fits using Eq. (3.4) and the broken lines present the experimental data of the ringing profiles. The theoretical curves are so close to coincidence with the experimental profiles that the differences between these profiles is often not apparent. Suppose that we take, for each ringing profile, 600 experimental data I_{ei}, and the corresponding numerically calculated predictions I_{ti}, where i = 1 to 600. The typical residual error in the least square fitting $s = [1/(n\text{-}2)\ \sum_{i=1}^{n} (I_{ti} - I_{ei})^2]^{1/2}$ is 0.004, in units where the maximum of the ringing profile is unity. For example, for the ringing profile of Fig 3.5(b), taken with a frequency scanning rate of 50.2 GHz/s, the maximum is 300 scale units and s = 1.09 units. To further distinguish the tiny differences in the fittings of the ringing profiles, we have magnified the five experimental ringing profiles with their theoretical fits in appendix G, Figs. G(1) - (5).

From this fitting procedure we determine the parameters a_1 and b for each run of the experimental ringing profiles. Then we can calculate the cavity FWHM by

$$L_{1/2} = (f'/\pi a_1)^{1/2}, \tag{3.6}$$

since $a_1 \equiv \frac{1}{2}\beta/\gamma_c^2$ using the definitions in which the angular frequency scanning rate $\beta = 2\pi f'$ and the cavity intensity decay rate $2\gamma_c = 2\pi L_{1/2}$.

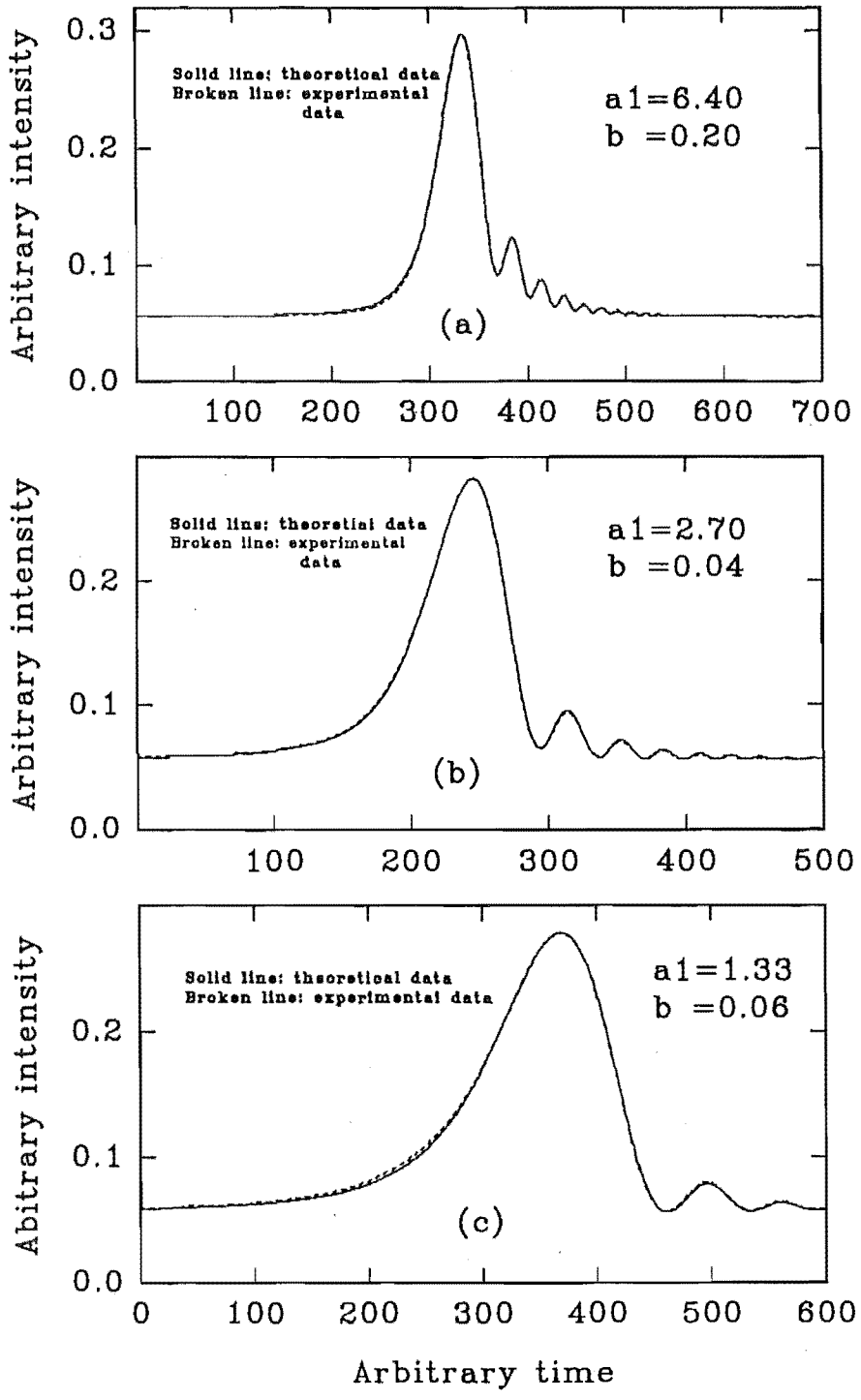

Fig. 3.5 Experimental results and theoretical fits for three runs on the SR-130 supercavity with different frequency scanning rates. The solid and broken lines are the experimental data and the theoretical fits from using Eq. (3.4).

The one round trip loss Γ in the cavity is obtained by $\Gamma = 2\gamma_c\tau = 2\pi L_{1/2}\tau$, where $\tau = P/c$, and is the round trip time of the cavity. The finesse F of the cavity is given by $F = \Delta\nu_{FSR}/L_{1/2} = 1/(\tau L_{1/2})$ and the quality factor of the cavity is $Q = \nu/L_{1/2} = (\nu/\Delta\nu_{FSR})F$, where $\Delta\nu_{FSR}$ is the free spectral range of the cavity and ν is the laser frequency of 474 THz. The laser line width $\Delta\nu_L$ can be obtained by $\Delta\nu_L = bL_{1/2}$.

The fitting results of five ringing profiles for SR-130 supercavity, which are shown in Figs. G(1)-(5) in appendix G, with the frequency scanning rate range from 38.36 to 185.8 GHz/s, and derived constants are listed in table 3.1. The cavity mirrors have a separation of 25.3 mm, give a free spectral range $\Delta\nu_{FSR}$ equal to 6.0 GHz

Table 3.1 Fitting & calculating results

Parameters	(1)	(2)	(3)	(4)	(5)	Units
f'	185.8	115.6	79.77	58.89	38.36	GHz/s
a_1	6.40	3.95	2.70	2.10	1.33	dimensionless
b	0.20	0.10	0.04	0.04	0.05	dimensionless
$L_{1/2}$	96.2	96.5	97.0	96.5	96.4	kHz
$\Delta\nu_L$	19.3	9.65	3.88	3.86	4.82	kHz
F	6.24	6.22	6.19	6.22	6.22	10^4
Q	4.93	4.92	4.89	4.92	4.92	10^{12}
Γ	100	100	101	100	100	10^{-6}

From table 3.1, we can see that the fractional uncertainty of the measurement of the round trip losses Γ (100 ppm) in the SR-130 supercavity is less than 1%, and the absolute uncertainty of the measurement is 1 ppm.

Chapter 4

Asymmetric scanning profile measurement of cavity linewidth

Through the long history of the scanning Fabry-Pérot cavity, it has been assumed that its response to a monochromatic wave is a symmetrical peak corresponding to the Airy function or spectral response. This has been widely used to describe the characteristic of a Fabry-Pérot cavity as a spectrometer. As mentioned in the previous chapter, the method for directly measuring a Fabry-Pérot cavity linewidth by scanning the cavity through a monochromatic source has also been used for a long time (Kalb 1986). However we show in this chapter that the finite scanning speed of a Fabry-Perot interferometer induces significant asymmetry in the shape of the peak, that is its temporal response profile when subjected to a monochromatic input beam. The amplitude of this profile is mathematically equivalent to that of a fixed interferometer subjected to an input beam which is chirped in frequency at an appropriate rate. In each case, the response is related to the complex error function. The extent of the asymmetry then depends on a single parameter, $\eta = \beta t_c^2$, where β is the frequency scanning rate and t_c is the power decay time of the interferometer. We show that obtaining an asymmetry of less than 5% in the profile obtained from scanning a monochromatic beam requires a scanning time as much as 100 times of the decay time t_c of the interferometer. This is a much more stringent requirement than has been contemplated previously in the literature. Since the width of the peak as well as its shape is dependent on the parameter η and by a commensurate amount, corresponding care must be taken in the measurement of the source spectrum or the cavity linewidth from scanning Fabry-Pérot data.

In the previous chapter, we discussed a ringing phenomenon in the output of an optical cavity, that is, oscillations in intensity at times later than that of the

peak of the profile. These intensity oscillations depend for their existence on the finite scanning rate of the optical cavity. In this chapter, we will show theoretically and experimentally that asymmetry in the output of a scanning optical cavity is significant even at scanning rates which are too low to generate significant ringing. The symmetric Airy function describes only the limiting case where the scanning speed of an optical cavity is zero. In Sec. 4.1, we will briefly discuss the previous problem and our findings. In Sec. 4.2 and 4.3, we will prove the formal equivalence of the two physical problems: we relate the response of a scanning optical cavity to a monochromatic wave to that for a fixed cavity with a frequency scanned, or chirped, input beam. This turns out to be very useful in our analysis of peak asymmetry. In Sec. 4.4, we derive a general expression for the output of a scanning optical cavity, and then in Sec. 4.5 an analytic solution within a reasonable approximation for determining the asymmetry in the profile. The experimental results and discussions are given in Sec. 4.6.

4.1 Limitation of the Airy function

In high resolution spectroscopy with a Fabry-Pérot interferometer, the extraction of the input spectrum from the output profile is of great importance. Most of the literature on this subject uses the symmetric Airy function in the deconvolution algorithm (Ballik 1966, Hernandez 1966, Day 1970, Cooper 1971, Zipoy 1979, Vaughan 1989). However, the Airy function for the intensity distribution in the fringe pattern is strictly valid only for a source of constant brightness and spectral distribution and for a non-scanning interferometer. For a scanning interferometer, the limitations on rapid scanning were discussed by Greig and Cooper (1968). They estimated the observation time for establishing the interference pattern to be approximately 1.4 $F\tau$, where F is the finesse and τ is the round trip time of the interferometer. We can rewrite this expression as $1.4F\tau = 2.8\pi t_c$ since $F = \Delta\nu_{FSR}/L_{\frac{1}{2}}$ and $\tau = 1/\Delta\nu_{FSR}$, where $\Delta\nu_{FSR}$ is the free spectral range of the interferometer and $L_{\frac{1}{2}}$ is its power FWHM (full width at half maximum) in frequency; $L_{\frac{1}{2}} = 1/2\pi t_c$ where t_c is the decay time of the power in the cavity. However, their analysis was based on the Lummer-Gehrcke plate (Born and Wolf 1980), and is relevant only for the steady-state multiple-beam interferometer.

We find that asymmetry in the temporal response profile of a scanning Fabry-Pérot cavity can be significant even when the time interval which is required for scanning over the probe frequency is as large as $100t_c$; the cavity linewidth also increases with the scanning speed. This is particularly important for both the

spectral measurements using a supercavity interferometer and the determination of a supercavity linewidth. In using the Newport SR-130 supercavity to measure the mode spectrum in our 1 m^2 ring laser, we can see the asymmetry of the fringe profiles of the interferometer output over a large range of interferometer scanning rates, from 3 GHz/s - 50 GHz/s. The output FWHM of the SR-130 supercavity increases from 106 KHz to 302 KHz in the above range. When we further increase the scanning rate of the interferometer, the ringing profile discussed in the previous chapter becomes conspicuous.

The response of a scanning interferometer can be expressed as a series of field amplitudes corresponding to various intracavity components. The asymmetry of the fringe profiles might be expected to depend on the three parameters: the reflectivity R of the mirrors, the round trip optical path P of the reflected beams in the interferometer and the scanning rate of the interferometer. While the influences of these three parameters on the asymmetric line profile could be determined by numerical calculations, its physical significance would be obscured. We will prove that the response of a scanning interferometer to a signal of constant frequency is equivalent to the response of a fixed interferometer to a frequency which is scanned in a certain linear manner. This allows an analytic development and solution to the point of relating the response to an error function, and shows that in general the asymmetry of the profiles depend on the single parameter η where $\eta \equiv \beta t_c^2$.

4.2. Response of scanning cavity to monochromatic field

Let us consider a monochromatic wave $A_{in}(t, z) = A_0 \exp i(k_0 z - \omega_0 t)$ to be injected into a scanning interferometer. The mirrors are separated by a length l; one of these mirrors is moving at a constant speed v so as to increase l. The frequency of the transmitted wavelet $A_n(t, z)$ will be Doppler shifted on each reflection; after the nth reflection, the wave has a frequency $\omega_n = \omega_0(1 - 2nv/c)$ and wavevector $k_n = \omega_n/c$ to first order, where c is the speed of light. The output of the scanning interferometer is the sum of the waves $A_n(t, z)$. Although the cavity length is modified by $\Delta l = v\tau$ within one round trip of a light pulse, we take a snapshot picture of the infinite wave trains at the given time t when the moving mirror is at $z = 0$, and demand only that the boundary conditions be satisfied at each reflection in order to determine the phases of the components. Applying the boundary conditions for reflection and transmission in each mirror rest frame, and Lorentz transforming where necessary to the laboratory frame, we

can obtain the transmitted field.

Assume the wave $A_{in}(t, z)$ is incident on the back, stationary mirror of a scanning Fabry-Perot interferometer (Fig. 4.1). Within the interferometer the waves reflected from the front (and moving) mirror gave the form $A_0' = A_0rq\exp\{-i[k_1z + \omega_1t]\}$, $A_1' = A_0r^3q\exp\{-i[k_2z + \omega_2t - 2k_1l]\}$, etc. The transmitted wave has the components $A_0'' = A_0q^2\exp\{i[k_0z - \omega_0t]\}$, $A_1'' = A_0r^2q^2\exp\{i[k_1z - \omega_1t + 2k_1l]\}$, $A_2'' = A_0r^4q^2\exp\{i[k_2z - \omega_2t + 2(k_1 + k_2)]\}$, etc., where q is the transmission coefficient of the wave amplitude at each reflection. These give rise to a total transmitted amplitude of

$$\begin{aligned} A_{out}(t, z) &= A_{in}(t, z)(1-R)\{1 + R\exp\{i[(k_1-k_0)z-(\omega_1-\omega_0)t + 2k_1l]\} \\ &\quad + R^2\exp\{i[(k_2-k_0)z-(\omega_2-\omega_0)t + 2k_1l + 2k_2l]\} + ...\} \\ &= A_{in}(t, z)(1-R)\sum_{n=0}^{\infty} R^n\exp(i\Phi_n) \end{aligned} \tag{4.1}$$

where

$$\Phi_n = \omega_0\{n[B_0 + (B_1t + B_2)v/c] + n^2Cv/c\}, \tag{4.2}$$

and $B_0 = -C = 2l/c \equiv \tau$, $B_1 = 2$, $B_2 = -2(z + l)/c$ and $R = r^2$.

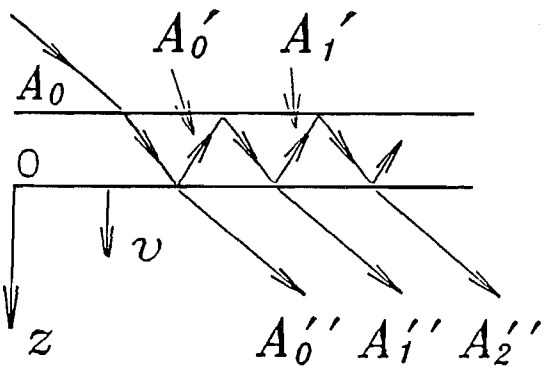

Fig. 4.1 A snapshot of a scanning FPI at time t. The incident wave $A_0\exp\ i[k_0z - \omega_0t]$ gives rise to transmitted waves $A_0'' = A_0q^2\exp\ i[k_0z - \omega_0t]$, $A_1'' = A_0r^2q^2\exp\ i[k_1z - \omega_1t + 2k_1l]$, $A_2'' = A_0r^4q^2\exp\ i[k_2z - \omega_2t + 2(k_1 + k_2)l]$, etc., where q is the transmission coefficient of the wave amplitude, and within the FPI the wave reflected from the moving mirror have the form $A_0' = A_0rq\exp\text{-}i[k_1z + \omega_1t]$, $A_1' = A_0r^3q\exp\text{-}i[k_2z + \omega_2t - 2k_1l]$, etc.

B_0 represents the phase shift from repeated internal reflections with a stationary mirror, and would in isolation lead to the Airy function. B_1 arises from a combination of effects associated with the Doppler shift, including both its direct effect on the phases of the emerging partial waves and its indirect effects on the phase shift accumulated in internal reflections. On its own B_1 simply modifies the effective cavity length by a velocity-dependent amount, without affecting the symmetry of the Airy profile. Part of the indirect effect of the Doppler shift is to induce a term in the exponent which is quadratic in n (the term C) since on the nth bounce the frequency is shifted by n steps; it is this term which will induce asymmetry in the interferometer profile.

4.3 Response of steady-state cavity to a FM field

Let us consider an input field which is ramped in frequency:

$$A_{in}(t, z) = A_0\exp\{-i[\omega_0 + \tfrac{1}{2}\beta(t-z/c)](t-z/c)\}. \tag{4.3}$$

β is the frequency scanning rate; the instantaneous frequency $\omega = \omega_0 + \beta(t - z/c)$ and is related to the time derivative of the phase (Siegman 1986), and because of the dependence on t and z through $(t - z/c)$ the above form satisfies the wave equation with $k = \omega/c$. The amplitude transfer function of a fixed interferometer may be written $H(\omega) = (1\text{-}R)\Sigma_n R''\exp in\omega\tau$, and its Fourier transform is given by $h(t) = (1\text{-}R)\ \Sigma_n R''\delta(t\text{-}n\tau)$ where δ is the Dirac delta function (Olesen and Jacobsen 1982). The output of the interferometer is given by the convolution of the input field and the impulse response of the cavity:

$$\begin{aligned} A_{out}(t, z) &= (1 - R)\Sigma_n R'' A_{in}(t\text{-}n\tau) \\ &= (1\text{-}R)A_0\exp\, i(k_0 z\text{-}\omega_0 t + \beta tz/c - \tfrac{1}{2}\beta t^2 - \beta z^2/2c^2)\ \Sigma_n R''\exp\, i\Phi_n \end{aligned} \tag{4.4}$$

where

$$\Phi_n = \omega_0(n[B_0 + (\beta\tau/2\omega_0)(B_1 t + B_2)] + n^2\beta\tau C/2\omega_0). \tag{4.5}$$

Apart from the complex factor, which does not affect the magnitude of the temporal profile, this has the form of Eq. (4.1) for the scanning interferometer under constant excitation, where $(\beta\tau/2\omega_0)$ now plays the role of v/c and as before the parameters $B_0 = -C = \tau$, $B_1 = 2$. $B_2 = -2z/c$ and is now different to that for the scanning interferometer case; however this difference amounts merely to a change in the origin of time. Hence the cases of a linearly scanned interferometer

with fixed input frequency and a fixed interferometer with a linearly ramped input frequency give indistinguishable intensity profiles at the output.

4.4 Intensity profile of cavity

We have proved the formal equivalence of the two problems: we can express the output of a scanning interferometer as that for a interferometer with a frequency scanned input beam. Neither equation 4.1 nor its counterpart (equation 4.4) for the fixed interferometer is easily solved; a series of the form $\Sigma_n a^n b^{n^2}$ is involved. Instead, we use the equivalence described above to derive an alternative solution.

We can rewrite the amplitude transfer function of an optical cavity as $H(\omega) = (1-R)/(1-R\exp i\delta_c)$, where $\delta_c = (\omega-\omega_0)\tau$ is the phase delay in a round trip of the injected wave in the interferometer relative to that (a multiple of 2π: $\omega_0 = 2\pi N/\tau$, $N\lambda = 2l$) for exact resonance, and as before $\tau = 2l/c$. For small detuning: $\omega \simeq \omega_0$, this may be approximated by $H(\omega) = 1/[1 - 2i(\omega-\omega_0)/\Gamma_c]$, where the power rate of decay in the cavity is $\Gamma_c = 1/t_c = 2\pi L_{\frac{1}{2}}$; note that Γ_c is twice the amplitude rate of decay γ_c. The quality factor $Q = \omega t_c$, the free spectral range (FSR) is $c/2l$, the finesse is $F = \pi R/(1-R) = Q\lambda/2l$, and the power full width at half maximum $L_{\frac{1}{2}} = \nu_0/Q = c(1-R)/2\pi lR$.

The input field $A_{in}(t, z)$ defined by Eq. (4.3) has the Fourier transform:

$$A_{in}(\omega, z) = A_0 \exp[i(k_0 z - \beta z^2/c^2)] \times \int_{-\infty}^{\infty} dt \exp\{i[(\omega - \omega_0 + \beta z/c)t - \tfrac{1}{2}\beta t^2]\} \tag{4.6}$$

and with the change of variable $t \to u = (\beta/2)^{\frac{1}{2}}[t - (\omega-\omega_0)/\beta - z/c]$, this gives

$$A_{in}(\omega, z) = A_0(2/\beta)^{\frac{1}{2}} \exp i[k_0 z + (\omega-\omega_0)^2/2\beta + (\omega-\omega_0)z/c]\, I \tag{4.7}$$

where $I = \int_{-\infty}^{\infty} du \exp(-iu^2) = \pi^{\frac{1}{2}} \exp(-i\pi/4)$. Multiplying this by the response function of the fixed interferometer and Fourier transforming, we obtain

$$\begin{aligned} A_{out}(t, z) &= \frac{1}{2\pi}\int_{-\infty}^{\infty} d\omega \exp(-i\omega t)\, A_{in}(\omega, z)\, H(\omega) \\ &= A_0/(2\pi\beta)^{\frac{1}{2}} \int_{-\infty}^{\infty} d\omega \frac{1}{1 - 2i(\omega-\omega_0)/\Gamma_c} \times \\ &\times \exp i[(\omega-\omega_0)^2/2\beta + (\omega-\omega_0)(z/c - t) - \omega_0 t + k_0 z - \pi/4]. \end{aligned} \tag{4.8}$$

This can be cast into closed form using the complex error function in the form (Abramowitz and Stegun 1965)

$$w(\zeta) = \frac{i}{\pi}\int_{-\infty}^{\infty} d\nu \frac{\exp(-\nu^2)}{\zeta - \nu} = \exp(-\zeta^2)\ \mathrm{erfc}(-i\zeta) \quad (\mathrm{Im}\ \zeta > 0). \tag{4.9}$$

To this end we now change variable $\omega \rightarrow \nu$ where

$$\nu \equiv G\ \exp(-i\pi/4)[(\omega-\omega_0)/(2\beta)^{\frac{1}{2}} + (\beta/2)^{\frac{1}{2}}(z'/c-t')], \tag{4.10}$$

and the sign factor $G \equiv -\mathrm{sgn}[1 + \left[\frac{\eta}{2}\right]^{\frac{1}{2}}(z'/c - t')]$, where $z' = \Gamma_c z$, $t' = \Gamma_c t$, $\eta = \beta/\Gamma_c^2$; this is chosen so that the expression

$$\zeta \equiv G\ (1/8\eta)^{\frac{1}{2}}\{-\exp(i\pi/4) + \exp(-i\pi/4)[\eta/2]^{\frac{1}{2}}[z/c - t]\} \tag{4.11}$$

always has a positive imaginary part. We then have the closed form for the resultant amplitude:

$$A_{out}(t, z) = -Ge^{-i\pi/4}\left[\frac{\pi}{8\eta}\right]^{\frac{1}{2}} A_0 \exp i[k_0 z-\omega_0 t-\tfrac{1}{2}\beta(z/c-t)^2]\ w(\zeta). \tag{4.12}$$

Hence the corresponding intensity ratio I_{out} ($|A_{out}|^2$), I_0 ($|A_0|^2$) of the outgoing and incoming beams is then given by

$$I_{out}/I_0 = \frac{\pi}{8\eta}|w(\zeta)|^2. \tag{4.13}$$

Fig. (4.2) shows this calculated intensity response (solid line) of a scanning interferometer for three values of the normalized scanning rate: η = 0.5, 0.1, and 0.01. The dashed line and the dotted line in Fig. 4.2(a) represent the real and imaginary parts respectively of the transmitted amplitude. The definitions of the characteristic parameters of an asymmetric transmission profile are shown in Fig. 4.2(b); δ_D is the deviation of the profile peak from the ideal case. Δ_l and Δ_r describe the half-width of the intensity profile on the left and right side respectively. For convenience of discussion, we define the deviation parameter $\Delta_d = 2\delta_D/L_{\frac{1}{2}}$ and the asymmetry parameter in the frequency domain of $\Delta_a = 2(\Delta_l - \Delta_r)/L_{\frac{1}{2}}$. For the case η = 1% as shown in Fig. 4.2(c), the corresponding scanning time over the probe frequency is 100 times the decay time of the interferometer, and the asymmetry parameter Δ_a is less than 5%.

As the normalized scanning rate increases, the profile of the transmitted intensity of the scanning interferometer varies in four ways: the asymmetry and the peak shift of the profile change, the relative FWHM increases, and the transmitted intensity decreases.

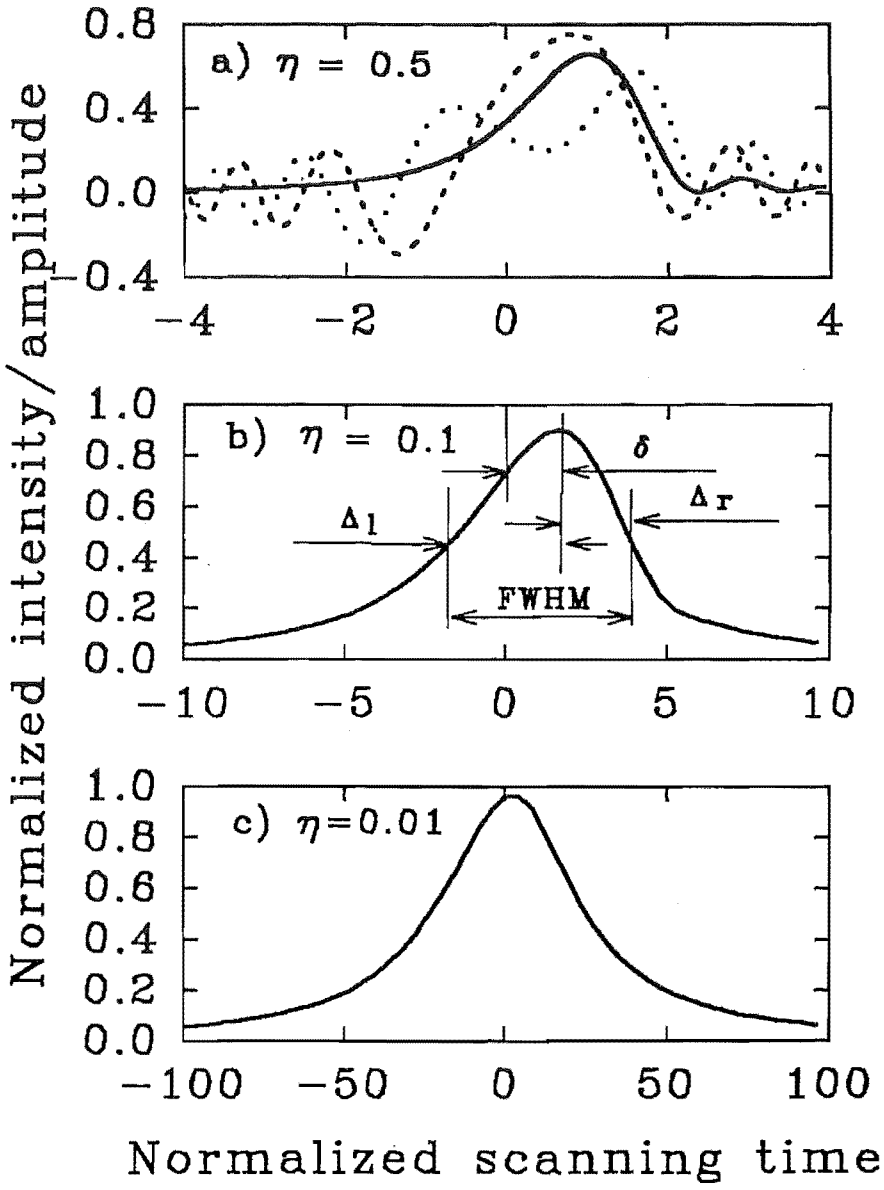

Fig. 4.2 Amplitude and intensity profiles from numerical evaluation of Eqs. (4.12) and (4.13) at various normalised scanning rates η: (a) η = 0.5, (b) η = 0.1 and (c) η = 0.01. Throughout, the solid line represents the intensity profile, and in (a) the broken and dotted lies represent the real and imaginary parts of the amplitude. Here and in following figures the normalised time $t' = \Gamma_d t$.

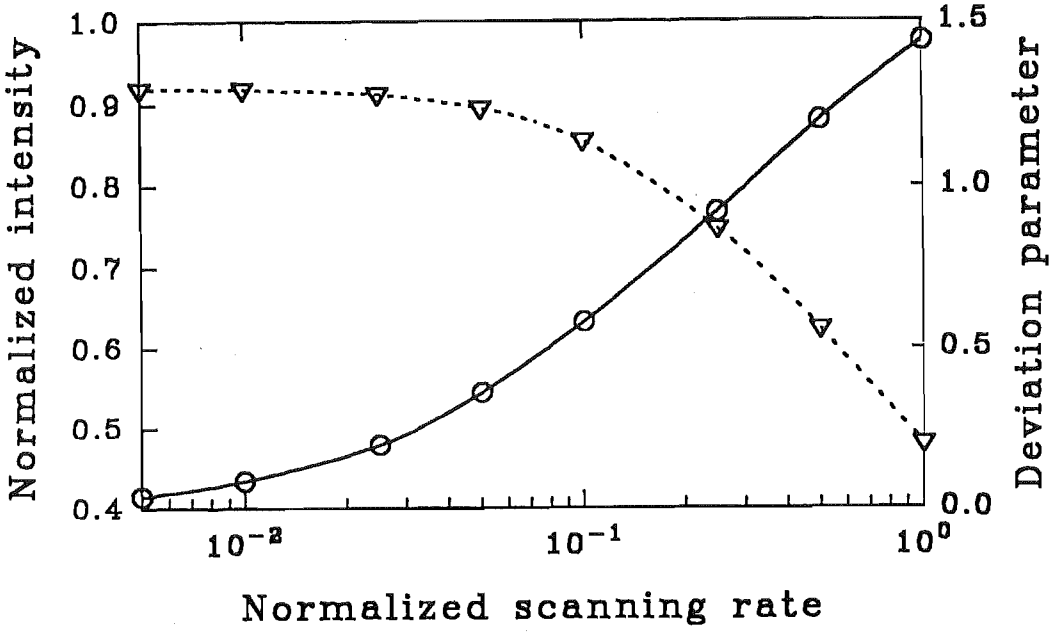

Fig. 4.3. Variation of the output intensity ratio I_{out}/I_0 and the peak deviation δ with the normalised scanning rate η from numerical calculation of Eq. (4.13).

Fig. 4.3 shows numerical calculations of the variations in the intensity ratio I_{out}/I_0 at the peak shown the dotted line and the peak deviation δ_D via the noralised scanning rate η. For η = 0.01 and 1, the I_{out}/I_o = 0.93 and 0.48, respectively. On the other hand, the peak deviation δ_D increases with the normalized scanning rate η. The deviation parameter Δ_d is changed from 0.04 to 1.42 when η is changed from 0.01 to 1.

4.5 Analytical formulae for limiting case

We expand Eq. (4.13) for low values of the normalized scanning speed η. In the limit that the scanning rate β (and therefore η) tends to zero, and omitting an unobservable overall phase, we find

$$A_{out}/A_0 = \left[\frac{\pi}{8\eta}\right]^{\frac{1}{2}} w(\zeta) = = \frac{i}{\sqrt{(8\pi)}} \int_{-\infty}^{\infty} \frac{dv e^{-v^2}}{\xi - \sqrt{\eta}\, v} \tag{4.14}$$

where $\xi = \sqrt{\eta}\,\zeta$. The denominator factor may be rewritten as $\exp(\sqrt{\eta}\, v/\xi + \frac{1}{2}\eta v^2/\xi^2)$ to $O(\eta v^2)$, and on completing the square of the Gaussian

integral and expanding the result to $O(\eta v^2)$ we obtain $A_{out}/A_0 = \frac{i}{\sqrt{(8a)\xi}} e^{b^2/a}$, $a = 1 - \eta/2\xi^2$, $b = \sqrt{\eta}/\xi$;

$$I_{out}/I_0 = |A_{out}/A_0|^2 = \exp[-(2\eta)^{\frac{3}{2}}t']/[1 + \tfrac{1}{4}\eta t'^2 + \sqrt{8}\, t'\eta^{\frac{3}{2}}]. \qquad (4.15)$$

A comparison (in the case that $\eta = 1\%$) of the results of eqs. 4.13 and 4.15 shows that even for this relatively large parameter value the approximation is good to ~ 10%. In the time domain the asymmetry parameter $\Delta_a = 2(2T_0 - T_+ - T_-)/(T_+ - T_-)$, where the maximum of I_{out} is at $t' = T_0 \equiv -8\sqrt{(2\eta)}$, and the half-power points are the solutions $T_\pm$ of $I_{out} = \frac{1}{2}I_0$, giving $\frac{1}{4}\eta T_\pm^2 + 3(2\eta)^{\frac{3}{2}}T_\pm - 1 = 0$. Hence $T_+ + T_- = -12\sqrt{(8\eta)}$, $(2T_0 - T_+ - T_-) = 8\sqrt{(2\eta)}$, and $T_+ - T_- = 4\sqrt{(72\eta^3+\eta)}/\eta$. We obtain

$$\Delta_a = 4\sqrt{(2\eta^3/[72\eta^3 + \eta])}. \qquad (4.16)$$

This equation (to be plotted in Fig. 4.4) shows that η values of 1%, 5% and 10% translate into asymmetry parameters of approximately 6%, 26% and 43% respectively.

4.6. Comparison with experiment

All experimental cases discussed in the previous chapter are in the fast scanning rate range, so that the output of the cavity has a ringing profile. The experimental results to be presented in this section are obtained at low scanning speed; the moralised scanning rate η of a cavity is less than 4. The experimental setup is the same as shown in Fig. (3.3). The emphases of our experiments are on the measurements of the asymmetry in the output profile and of the FWHM of the cavity when the scanning speed of the cavity varies.

4.6.1 Asymmetry in profile

We use the deviation parameter Δ_d defined in section 4.4 to define the asymmetry in the peak of the temporal output profile of a scanning cavity. First, the output of the cavity (Newport SR-130) is detected by a photomultiplier (Thorn EMI 9214). It is averaged and recorded in a digital storage oscilloscope (Hitachi Denshi VC-6275). Then the data for the profile intensity so digitized is transferred into a

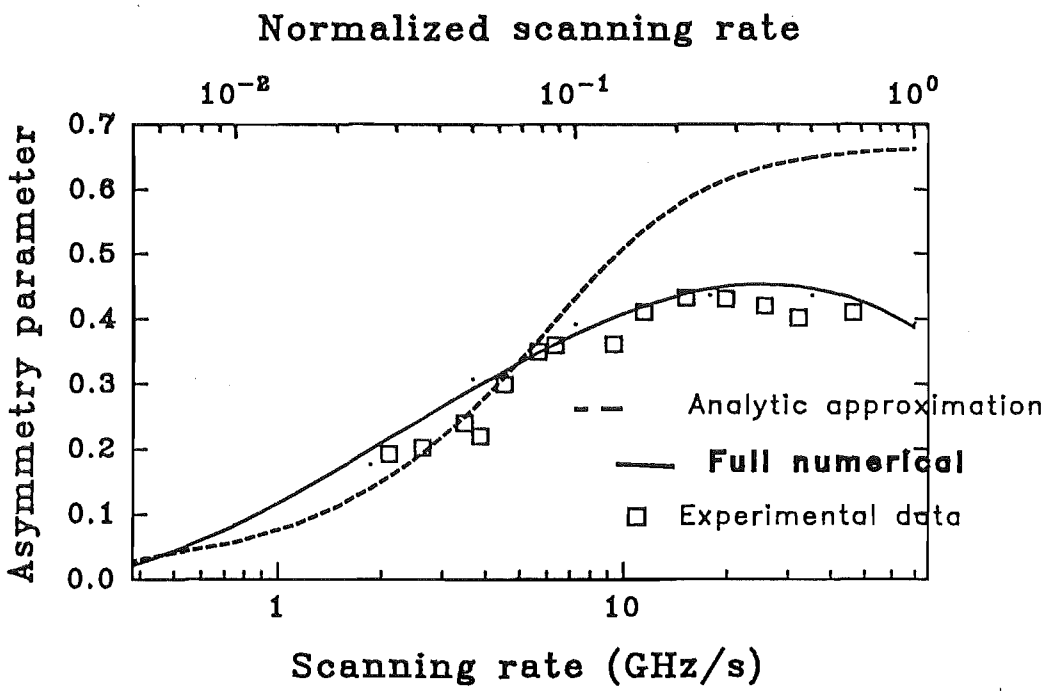

Fig. 4.4. Variation of the asymmetry Δ_a of the profile with the scanning rate (the normalized rate η used in the calculation being plotted on the upper axis, and the absolute value β for the experiment on the lower). The solid (broken) line is the numerical prediction from the full (approximate) theory (Eqs. 4.13 and 4.16 respectively).

PC computer. We then measure the deviation, δ_D, of the profile peak from the ideal case, the right and left half-widths of the intensity profile, Δ_r and Δ_l, and finally the asymmetry Δ_a and the FWHM of the profile, by fitting η in Eq. (4.13) to the observations.

In Fig. (4.4), the experimental data for the asymmetry parameter Δ_a is represented by the squares, the full numerical calculation given by Eq. (4.13) is plotted as the solid line and the analytic approximation obtained by Eq. (4.16) is described by the broken line.

4.6.2. FWHM of scanning cavity

Kalb (1986) mentioned that while the technique of measuring the FWHM of an optical cavity by simply scanning over a laser source works well with a low finesse cavity, it was plagued by errors associated with thermal noise, as well as with the speed and repeatability of the frequency scan for cavities of higher finesse. Kalb (1986) pointed out that this technique will require improvements if it is to remain useful in the future.

In our experiment, we find that the main source of error is coming from the frequency jitter of the probe laser. Frequency jitter in the output of the NL-1 frequency-stabilized laser is evident when the resonance of the interferometer is scanned over this probe frequency. The effect of this frequency jitter on the calibration of the scanning rate increases as the scanning rate is decreased. Fig. (4.5) gives an extreme example of the effect of jitter for a very low scanning rate (0.93 GHz/s). Fig. 4.5(a) shows that the separations of the side bands from the central peak differ by more than 20%. Fig. 4.5(b) is a typically ragged shape of the output profile of the scanning cavity at such low scanning rate.

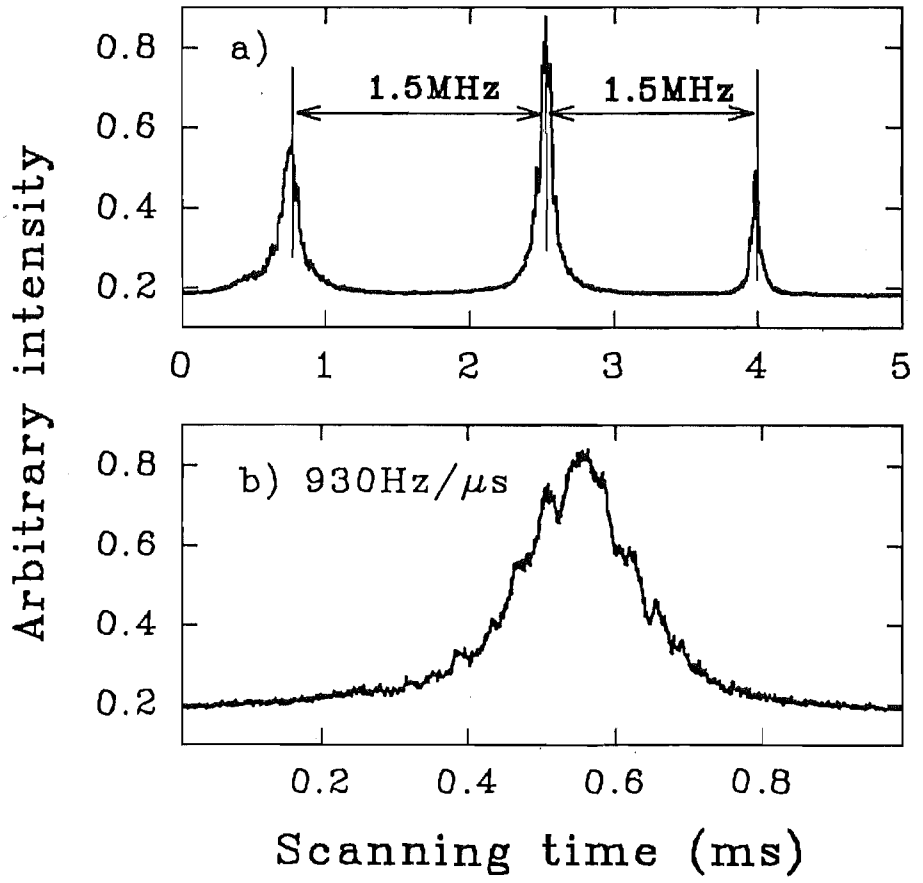

Fig. 4.5 A profile obtained at very low scanning rate (0.93 GHz/s). (a) Unequal spacing of sidebands caused by jitter during collection of the profile. (b) Ragged shape of the profile for one such peak, reflecting shorter-term frequency jitter of the NL-1 laser.

In our experiment, this problem is overcome by two means. First, we average over runs to reduce the effect of noise on the profile of the cavity output. Fig. 4.6(a) and (b) show profiles from the average of 64 runs with the scanning rates 9.29 GHz/s and 3.46 GHz/s. The variation of the FWHM of the sidebands reflects the frequency jitter of the NL-1 laser. The FWHM of the profile is dependent on the scanning speed. In Fig. 4.6(a), the FWHM of the profile is 123.2 kHz with the cavity scanning rate of 9.29 GHz/s. This FWHM reduces to 104.0 kHz when the scanning rate is lowered to 3.46 GHz/s (Fig. 4.6b). For even lower scanning speeds, the sideband profiles become more noisy even when averaging is performed; this increases the error on the calibration of the frequency scanning

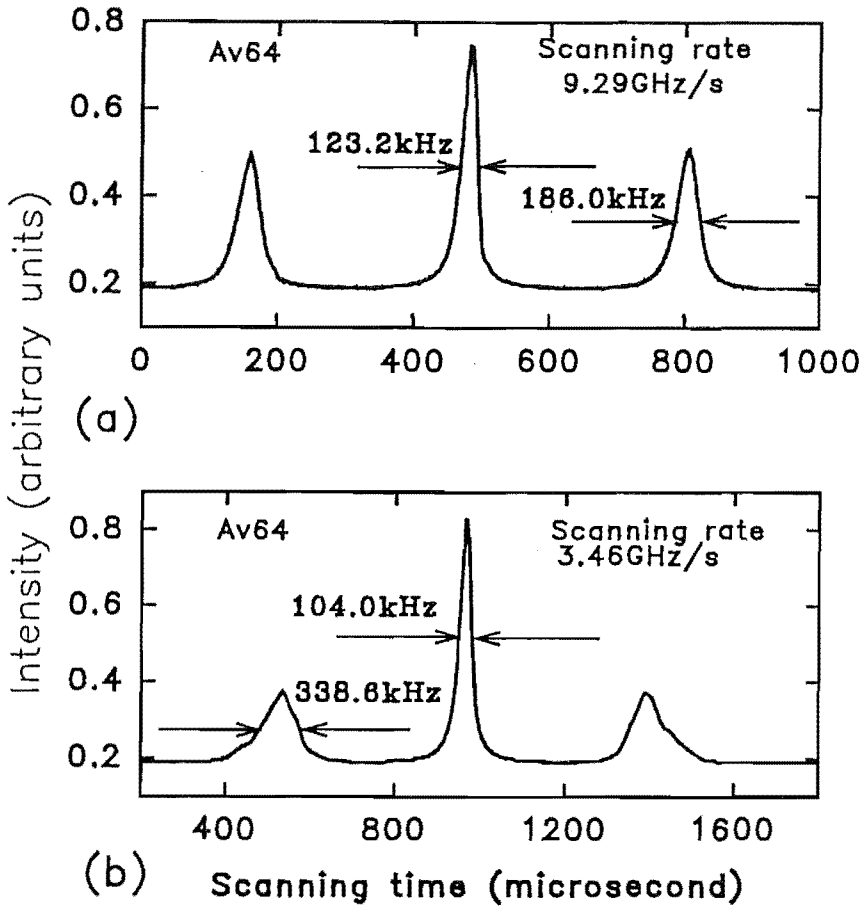

Fig. 4.6 Joint effect on the profile of probe frequency jitter and frequency scanning rate is shown in (a) and (b). The averages of 64 runs at scanning rates of 9.29 GHz/s and 3.46 GHz/s respectively, with the oscilloscope triggering on the central peak. The larger width of the side peaks reveals the variation in scanning rate and so averaging of non-coincident peaks.

Therefore we incorporate a second procedure, by fitting the measured values of the profile FWHM at different scanning speed to the theoretical curve predicted by Eq. (4.13) so as to determine the limiting value of FWHM of the cavity when the scanning speed tends to zero.

In Fig. (4.7), the scales have been chosen for best fit, and this choice together with the value of the known absolute frequency scanning rate β gives a FWHM $L_{\frac{1}{2}} = (1/2\pi)(\beta/\eta)^{\frac{1}{2}} = (\nu'/2\pi\eta)^{1/2}$, since $\eta = \beta t_c^2 = 2\pi\nu' t_c^2$, $t_c = 1/2\pi L_{\frac{1}{2}}$ for the SR-130 supercavity. The squares represent the experimental data. The FWHM is determined by $L_{\frac{1}{2}} = 2f_m \Delta t_{\frac{1}{2}}/\Delta t$, where f_m is the modulation frequency of the laser beam, Δt is the time interval between the two sidebands and $\Delta t_{\frac{1}{2}}$ is the FWHM in the time domain. The experimental data are in excellent agreement with the numerical calculation from equation (4.13).

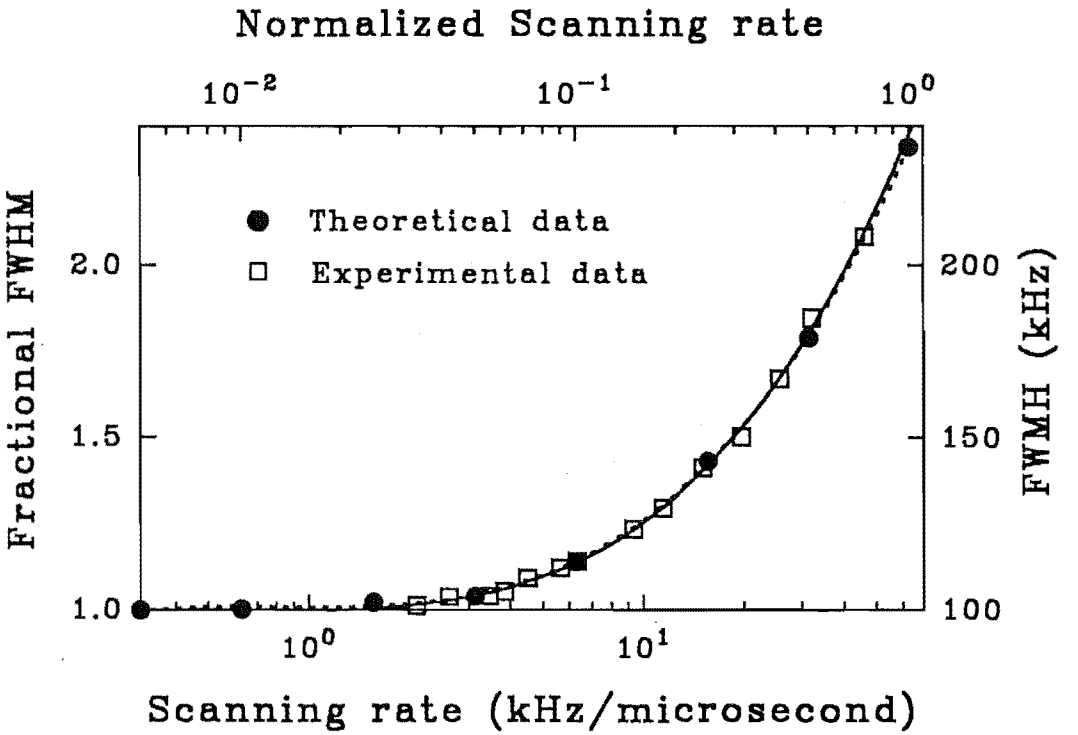

Fig. 4.7. Increase of the full width at half maximum (FWHM) of the profile with the scanning rate. The broken line is the theoretical prediction and the solid line is a fit to the experimental data.

From Fig. (4.7), we obtain that the FWHM of the Newport SR-130 supercavity is 100 ± 1 kHz. This result of the linewidth measurement is larger than that we determined by our ringing profile method by 3.5 kHz. The origin of this difference may come from that we did not take account for the effect of the laser linewidth on the measurement of the linewidth in this chapter.

In principle, the probe laser linewidth will increase the FWHM value of the cavity output profile. The ragged shape of the cavity output profile shown in Fig. (4.5b) reveals that when the SR-130 supercavity is working at low frequency scanning rates (e.g. 0.93 GHz/s in Fig. 4.5b), the coherence time of the NL-1 frequency-stabilized laser is already shorter than the time period which is required crossing over the FWHM of the cavity. The coherence time t_s of a laser is given by $t_s = 1/2\pi\Delta\nu_s$ where $\Delta\nu_s$ is the linewidth of the laser, as defined before. For NL-1 Laser, the coherence time t_s is about 37 μs, corresponding to the averaged linewidth of 4.2 kHz as we measured and given in Chapter 3. For SR-130 supercavity, the cavity decay time t_c = 1.6 μs (= $1/2\pi L_{1/2}$). In Fig. (4.5b) the FWHM of the cavity output profile in time domain is about 200 μs, which is more than 5 times longer than the coherence time of NL-1 laser. In this case, the laser linewidth will broaden the width of the cavity output profile.

Therefore, we can conclude that for precisely determining the linewidth of a cavity by directly measuring the cavity profile width, the both of laser linewidth and the frequency scanning rate should be carefully taken into account.

In our measurement, the laser linewidth is much less the cavity linewidth. In this case, the resolution of our measurement in linewidth is 1 KHz, corresponding the losses of 1 ppm in the cavity for SR-130 supercavity. The system error induced by the laser linewidth is 4 ppm.

Chapter 5

Summary of recent progress in ring laser technology

We will review the recent progress in laser ring gyroscopes in this chapter. Optical rotation sensors may be classified into two types: passive and active. The passive scheme includes the Sagnac interferometer, optical ring cavities, fibre-optic ring resonators, and fibre-optic coil interferometers. The active approach concerns the planar cavity ring lasers, nonplanar cavity or multimode ring lasers, and fibre ring lasers.

Each of these rotation sensors is discussed briefly in the following sections with the emphasis on their historical background and present status. Little emphasis is placed on their principles and theoretical description since these have been fully presented in the review literature (Post 1967, Aronowitz 1971, Chow *et al.* 1985).

5.1 Problem of Sagnac interferometer and its solutions

The basic priciple for understanding the operation of an optical rotation sensor is the so-called Sagnac effect, first discussed by G. Sagnac in 1913 when he demonstrated the feasibility of using an interferometer to sense rotation. The effect is a direct consequence of the finite speed of light. Classical physical optics consideration show that light propagating along the direction of rotation of a ring requires a slightly greater time to complete each full circuit, relative to the ring, than does light propagating along the same path but against the direction of ring rotation.

Post (1967) presented a good review of the Sagnac effect, in which historical and theoretical background information was presented, and various Sagnac-type experiments were described. Of these, a major optical achievement was the Michelson-Gale experiment (Post 1967). They succeeded in measuring the rotation rate of the earth by means of the Sagnac effect. To obtain the required sensitivity for detecting the earth rotation they had to choose an unusually large size for the surface area enclosed by the light beam. The interferometer was rectangular with sides 0.4 × 0.2 miles!

Obviously, an optical rotation sensor with such a large area is not practical for applications. The measurement of rotation is of considerable interest in a number of areas. For example, inertial navigation systems as used in aircraft and spacecraft depend critically on accurate inertial rotation sensors. The allowable errors in rotation sensor performance depend on the particular application. Typical requirements for aircraft navigation lie between 0.01 and 0.001 deg/h (Ezekiel 1984). In terms of the earth rotation rate with an angular frequency (Ω_E = 15 deg/h) this corresponds 10^{-3} to 10^{-4} Ω_E.

The difficulty in using a Sagnac-type passive interferometer as a practical device for these applications arises from its lack of sensitivity, since the phase difference for the two waves travelling in the two directions is too small to detect at such a rotation rate for rings of manageable area. Light in a ring interferometer with an area $\vec{A}$ rotated at an angular speed $\vec{\Omega}$ experiences a differential time delay $\Delta t = 4\,\vec{A}\cdot\vec{\Omega}/c^2$ (Aronowitz 1971), where c is the speed of light. The round trip optical path difference $\Delta L = c\,\Delta t = 4\vec{A}\cdot\vec{\Omega}/c$. The phase difference between the counterpropagating beams after one round trip is therefore given by

$$\begin{aligned}\Delta\Psi &= 8\pi\vec{A}\cdot\vec{\Omega}/(c\lambda)\\ &= S_p\Omega\end{aligned} \qquad (5.1)$$

where the scale factor $S_p = 8\pi A\cos(\theta)/c\lambda$, λ is the wavelength of the light beam and θ is the angle between the two axes of the ring cavity plane and the rotation. The effectiveness of the Sagnac interferometer is limited by the fact that this phase difference is just too small to be detectable. For instance, for a Sagnac interferometer with an area 1 m^2 rotating at 10^{-3} Ω_E, which is the sensitivity required for aviation applications as mentioned previously, the differential time delay $\Delta t = 3.23 \times 10^{-24}$ s, $\Delta L = 9.7 \times 10^{-16}$ m, and the phase difference, given by Eq. (5.1), $\Delta\Psi = 9.62 \times 10^{-9}$ rad, where we assume that the axis of the cavity

rotation is normal to the plane of the interferometer. The resolution of early Sagnac-type interferometers was no better than 0.001 of an interference fringe (Heer 1984), which corresponds a phase shift of 6×10^{-3} rad, and is about 6 orders of magnitude worse than the required sensitivity.

Therefore, although the Sagnac effect had been well understood for many years, the Sagnac interferometer was not even considered as an alternative to conventional mechanical gyroscopes until the development of the laser in the early 1960s. The sensitivity of optical rotation sensors is greatly increased by using lasers. Herr (1984) gives an interesting historical account of the ring laser gyroscope development. Laser ring gyroscopes allow two advances in increasing the sensitivity of optical rotation sensors.

The first of these is associated with the use of a resonant system in laser gyroscopes. Either an active laser medium is introduced into the ring resonator or a laser is used as an external source injected into the ring resonator. The advantage of using a resonant system in ring laser gyros is that the rotation-induced phase differences of counterpropagating beams in the ring interferometer are transmuted into a frequency difference between the beams. This frequency difference Δf is given by $2\pi\Delta f = \Delta\Phi/\tau$, where τ is the round trip time in the ring and is defined by $\tau = c/P$, c is the speed of light and P is the perimeter of the ring resonator.

The second advantage is the possibility of increasing the total round-trip path length by the use of a kilometre-long optical fibre as the cavity of the interferometer, which may be wrapped many times around a small cylinder. From Eq. (5.1) we see that the phase difference, $\Delta\Psi$, between the counterrotating beams is given by

$$\Delta\Psi = 4\pi L\varrho\Omega/(c\lambda), \tag{5.2}$$

where we assume the axis of the cavity rotation is normal to the plane of the cavity, ϱ is the radius of the fibre coil and L is the total optical fibre length. This represents the important result that the phase difference induced by the rotation of a multi-turn fibre coil increases linearly with the total length of the optical fibre. At the present time, a typical fibre-optic interferometer gyro contains an optical fibre of length 1 km with a loss of 2.3 dB/km (Moeller, burns and Frigo 1989), and a rotation sensitivity of 3.2×10^{-4} deg/h was obtained.

I will discuss various laser gyros of these two schemes in the following sections. Since the active ring laser design gave the first laser gyroscope in the

world and is still the only scheme used in the commercial optical gyroscopes for navigation applications, I start my discussion with the active ring laser.

5.2 Active ring laser gyroscope

Macek and Davis (1963) demonstrated the first ring laser, barely two years after the first helium-neon laser had been demonstrated at Bell Laboratories, and its unique potential as a rotation sensor via the Sagnac effect. The ring laser was 1 metre long on each side and had a helium-neon gain tube in each leg. The lowest frequency splitting they could measure in their ring laser was a few kHz, corresponding to the laser cavity rotation rate of the order of $10^2\ \Omega_E$.

Generally, in the stationary laser gyro, there are two oppositely directed travelling waves oscillating in a symmetric cavity. The optical paths are identical for both beams and the beams therefore oscillate at the same frequency f, which satisfies the condition $f = mc/P$, where m is an integer. When the cavity is rotated, the degeneracy of the optical path for each beam is removed. The clockwise (CW) and counter clockwise (CCW) modes in the cavity will have different frequencies because of the difference in the effective round-trip optical path lengths caused by the rotation of the cavity. Therefore the Sagnac phase shift is transmuted into a shift in the resonant frequencies proportional to the rotation rate for the counterpropagating modes of a ring laser. This frequency difference is measured by heterodyning counterpropagating beams and directly counting either the beat frequency or the motion of the interference fringes. The frequency difference between the CW and CCW beams is given by (Aronowitz 1971)

$$\begin{aligned} \Delta f &= 4\vec{A}\cdot\vec{\Omega}/(\lambda P) \\ &= S\Omega, \end{aligned} \tag{5.3}$$

where $S = 4A\cos(\theta)/\lambda P$ and θ is defined as the same as in Eq. 1. Note that the scale factor S is a factor of $c/(2\pi P)$ greater than S_p given by Eq. (5.1). For the Canterbury square ring cavity with perimeter $P = 3.4771$ m and the He-Ne wavelength, this factor is about $10^7\ s^{-1}$. The phase shift of 9.62×10^{-9} rad quoted in Sec. (5.1) corresponds to a differential frequency shift of the order of 0.1 Hz for an active ring laser with the same size as the above ring interferometer. This increased scale factor together with the relative experimental ease associated with small frequency difference measurements makes the active ring laser much more

attractive.

After 20 years of development, the first commercial optical gyroscope - the active ring laser gyroscope - is presently used for aviation inertial guidance systems in aircraft (e.g. the Airbus 320), also in various missiles (e.g. the Patriot system). A ring laser gyroscope with an area of the order of square decimetres has a sensitivity to rotation rates of order $10^{-4}\ \Omega_E$ (Chow *et al.* 1985). Martin (1986) gives an overview of commercial ring laser gyroscopes and their applications. The optical gyroscope's greater reliability, wide dynamic range, and ability to withstand high acceleration and harsh environments make it superior to mechanical gyroscopes, with their spinning rotors and complex gimballed mounts. Martin (1986) predicted that the complete replacement of mechanical gyroscopes in many applications seems inevitable.

Although the active ring laser is successful, it has problems associated with having the gain medium inside the cavity itself! For example, in an active ring laser, for small rotation rates, the counterpropagating beams tend to lock together, which is so-called frequency lock-in, as a result of the backscattering in the laser cavity, so that even for nonzero rotation rates the frequencies of the two beams are degenerate (Aronowitz 1965, 1971; Haus *et al.* 1985). Another problem associated with having the gain medium in the cavity is the variation in the refractive index of the gain medium, which causes the variation of the scale factor. These problems may be eliminated in a passive ring cavity.

5.3 Passive ring cavity

Ezekiel and Balsamo (1977) first reported on the operation of a passive ring cavity gyroscope as a means of avoiding the lock-in problem. The basic characteristic of a passive ring cavity is that the lasing medium is outside of the ring cavity so that the mode structure of the laser light in the cavity is determined by a cavity external to the ring cavity. The expression for the frequency difference of the counterpropagating beams given by Eq. (5.2) is also applicable to passive ring resonators. In their experiment, light from a laser of a single frequency f_0 is split into two beams, each of which is shifted in frequency by an acousto-optic shifter before entering the resonator. The polarization of the light is aligned with one of the polarization axes of the resonator. The beam propagating in the CW direction is shifted by a fixed frequency f_1 and the CCW beam is shifted by f_2. The CW resonance of the cavity is automatically locked to $f_0 + f_1$ by means of a primary

feedback loop driving a PZT controlled cavity mirror while another feedback loop is used to adjust f_2 so that $f_0 + f_2$ is locked to the CCW resonance. The presence of a rotation generates a difference Δf between the CW and CCW resonance frequencies of the cavity, which is determined by the difference between f_2 and f_1. The rms fluctuation in the output of their experimental setup was 10 deg/h in an integration time of 10 sec. A later report (Ezekiel *et al.* 1978) showed that with a square cavity of about 17 cm on a side, and a 1 mW external laser, the rms fluctuation in the measurement of rotation was 0.45 deg/h for an integration time of 1 sec.

For a passive cavity, the fundamental limitation to the measurement precision is derived by considering shot noise at the photodetector. The uncertainty in the rotational measurement is given by Ezekiel, Harrison and Sanders (1978) in the form

$$\Delta\Omega = (\lambda P/4A)(2/n\eta_D t)^{1/2} L_{1/2} \tag{5.4}$$

where the n is the number of photons per second at the detector, η_D is the photodetector quantum efficiency, t is the averaging time and $L_{1/2}$ is the linewidth of the passive cavity. For a cavity with given reflectivity of the mirrors, the linewidth and the area of the cavity will increase with the cavity path length. Therefore the uncertainty limitation in the measurement can be reduced by using a big ring. Sanders *et al.* (1981) further studied the performance of the passive cavity rotation sensor with a larger size (0.7 m × 0.7 m). As they expected, the sensitivity was improved. For an averaging time of 10 sec, the random drift was 1.1×10^{-2} deg/$\sqrt{\text{h}}$, which was consistent with the shot-noise limit for their experiment setup. For a longer averaging time (90 sec) the random drift was 5.6×10^{-3} deg/$\sqrt{\text{h}}$, this results an uncertainty of ring laser in the rotational measurement $3.7 \times 10^{-4}\ \Omega_E$.

In principle a passive ring cavity could be built of the order of 30 m × 30 m or even greater, and the sensitivity of the measurement of rotation rate could reach $3 \times 10^{-11}\ \Omega_E$ in an integration time of 1 hour (Sanders *et al.* 1981). However, such a development of a passive ring cavity faces a number of problems. For instance, the beam misalignment caused by thermal and mechanical stresses generates high-order transverse modes in the cavity that tend to pull the resonant frequency of the TEM_{00} mode that is used as a reference. In this way, unequal CW and CCW beam misalignment generate nonreciprocal frequency errors. So far, passive ring cavities have not become practical rotation sensors.

In fact, a program (Rotge *et al.* 1986) for the development of a passive resonant ring laser gyroscope with a area of 60 m^2 was initiated at Frank J. Seiler Research Lab., USAF Academy, in 1982. The predicted sensitivity of this large device was about 10^{-10} Ω_E. The resonant ring was supported by a 205,000 kg reinforced concrete isolation test platform. The platform was floated on pneumatic isolators on a seismic base and actively controlled to provide isolation from vibration in six degrees of freedom to about 10^{-8} g and two axis tilt attitude stabilization (with respect to local vertical) to better than 10^{-3} arc seconds. This was a large project and there were over 20 support projects performed by university researchers, USAF Academy faculty, Air Force reservists, USAF Academy cadets, and Air Force Institute of Technology students. In November 1985, after reviewing costs required to complete this ambitious project and near-term Air Force inertial sensing requirements, the Air Force Office of Scientific Research, the sponsoring organization, terminated the program.

5.4 Resonant fibre-optic gyroscopes

The first experiment using a resonant fibre-optic gyroscope was performed by Davis and Ezekiel (1981). The principles and techniques used in the resonant fibre-optic gyroscope are almost identical with those in a passive cavity. In addition, because the fibre used was not polarization conserving, several polarization controllers were used to compensate for fibre birefringence. In the Davis and Ezekiel experiment, the length of the fibre was 200 m, and the coil diameter was 19 cm. They achieved a sensitivity of 0.1 deg/h in measuring rotation rate.

In principle, the passive fibre-optic resonator gyroscope needs a high coherence optical source (Iwatsuki *et al.* 1984) because it consists of an optical ring resonator. From 1981 to 1986, experiments on the fibre-optic resonator gyroscope were limited to the use of highly stabilized He-Ne laser (e.g. Meyer *et al.* 1983) owning to the status of semiconductor lasers at that time. However, in a practical passive fibre-optic resonance gyroscope, a semiconductor laser must be coupled to a low loss optical fibre ring resonator if the system is to be adequately miniaturized and stabilized.

With the development of semiconductors, Ohtsu and Araki (1987) firstly used a semiconductor laser with a linewidth of 13 MHz as a coherent source in a passive ring fibre resonator with a area of 0.46 m^2. The rotational sensitivity they

obtained was 1.5 deg/h with the integration time for measurements of 100 sec.

The fibre-optic resonance gyroscope has the advantage of reducing a fibre length over a conventional fibre-optic interferometer gyroscope (which will be discussed in the next section) because it makes use of the sharp resonant characteristics of a fibre-optic ring resonator. However, this scheme has severe problems to be solved if it is to achieve highly sensitive detection of the rotation rate.

The first problem is the effect of backscattering due to splices in the fibre and to Rayleigh backscattering from the fibre itself on the drift characteristics of fibre-optic resonance gyroscope (Iwatsuki, Hotate and Higashiguchi 1984, 1986b; Carroll and Potter 1989, Takahashi, Tai and Kyuma 1990). Generally, the backscattering contributes to a nonreciprocal phase shift of the travelling beams in the fibre-optic resonator. For example, Rayleigh backscattering gives rise to an apparent rotation rate of (for circular loops) (Chow *et al.* 1985)

$$\Omega_{MAX} = (\lambda c s / 4\pi \varrho)(G\alpha_S / L) \tag{5.5}$$

where α_S is the Rayleigh scattering attenuation coefficient of the fibre, G is the scattering directivity along the fibre ($1 \leqslant G \leqslant 1.5$), and s is the acceptance angle of the fibre core. In order to obtain an order of magnitude estimate of Ω_{MAX} we choose λ = 633 nm, L = 100 m, ϱ = 1 m, s = 0.1 rad, G = 1.0, and α_S = 10^{-5}/m. Using these values in Eq. 6.5 yields an approximate upper limit to the apparent backscatter-induced rotation rate of 98 deg/h.

In order to reduce the effect of backscattering the optical phase modulation technique (Sanders *et al.* 1981) is widely employed (e.g. Takahashi *et al.* 1990). The principle of operation is based on the phase modulation of one beam (CW or CCW waves) with a frequency f_m and an appropriate amplitude so that the carrier is suppressed and the interference light between the signal and reflected lights has only alternating components $\pm f_m$, $\pm 2f_m$, $\cdots$. Since these alternating components can be decoupled at an electronic filter, the effect of reflections can be mitigated. By using this method, Takahashi *et al.* (1990) achieved a rotational detection sensitivity of 3×10^{-5} rad/s (6 deg/h) in a fibre-optic resonator gyroscope with a 10 cm fibre-ring diameter and an external-cavity laser diode as a high coherent light source.

The second problem is associated with the polarization and birefringence (Chow *et al.* 1985, Iwatsuki *et al.* 1986a) in an optical fibre. A single-mode fibre permits the transmission of modes of two orthogonal polarizations through the

fibre. Disturbances, such as temperature fluctuations and mechanical stresses, cause power to be transferred from one polarization mode to the other. Light in one polarization mode has a velocity different from the light which is being propagated in the other polarization mode. This energy transfer between the two polarization modes causes a drift of the beat frequency of a passive fibre-optic resonance gyroscope. To solve this problem, single polarization-maintaining fibres have been developed. One method to achieve this is the introduction of high birefringence into the fibre coil, far exceeding the birefringence induced by small temperature fluctuations and mechanical disturbances which are responsible for the undesirable energy transfer (Chow *et al.* 1985). Fibres with a high birefringence can be produced by drawing the fibres so that they have an elliptical core or by introducing a high anisotropic internal stress. Any resonator has two eigenstates of polarizations. In a polarization-maintaining fibre resonator, the eigenstates are identical to the linearly polarized modes of the fibre. Therefore, by setting the fibre polarizers at the lead portions of the resonator, one can excite only one eigenstate of polarization in the resonator. Takiguchi and Kazuo (1992) give a further discussion on the bias of an fibre-optic resonant gyroscope caused by the misalignment of the polarization axis in the polarization-maintaining fibre resonator.

The third problem is the optical Kerr effect in the optical fibre. Recently work has been done which indicates that a nonreciprocal phase shift due to the Kerr nature of the fibre resonator is a significant source of error in a fibre-optic resonant gyroscope (Iwatsuki *et al.* 1986c, Lamouroux *et al.* 1990). To understand why this is so, a brief discussion of the optical Kerr effect in the fibre-optic gyroscope will be given here. A Kerr medium is defined as one in which the susceptibility of the medium is given by $\varepsilon = \varepsilon_0 + \Delta\varepsilon^{NL}$, where in the simplest case $\Delta\varepsilon^{NL} = \varepsilon_2|E(x)|^2$, and $E(x)$ is the total electric field at location x. If the amplitudes E_1 and E_2 of the counterpropagating beams are different, $E(x) = E_1 e^{ikx} + E_2 e^{-ikx}$. Then the effect of this nonlinear law for susceptibility in the relation $P_E = \varepsilon E$ is to give unequal susceptibility coefficients A_+, A_- for the counterrotating waves:

$$P_E = \varepsilon_0 E(x) + A_+ E_1(x)e^{ikx} + A_- E_2(x)e^{-ikx} + \cdots \qquad (5.6)$$

where the terms are of higher order in e^{ikx} and correspond to the harmonic generation. Substituting these relations in the susceptibility law (Kaplan and Meystre 1981) gives that

$$A_+ = \varepsilon_2(|E_1|^2 + 2|E_2|^2), \tag{5.7a}$$

and

$$A_- = \varepsilon_2(|E_2|^2 + 2|E_1|^2). \tag{5.7b}$$

Hence, in the presence of two counterpropagating waves of different amplitude, the nonlinear components A_+ and A_- are different for opposite direction. If ε_2 is sufficiently different from zero and the beam splitter does not split the laser beam into equal parts then the nonreciprocal phase shift induced by the optical Kerr effect can become the limiting factor in the sensitivity of the fibre-optic gyroscopes. For example, in the experimental setup used by Bergh *et al.* (1981), if the ratio of the intensities of the two beams is maintained to 0.5 ± 10^{-4} the apparent rotation rate induced by the Kerr effect in the fibre is 10^{-3} deg/h.

The performance of the fibre-optic resonator gyroscope has been limited by the previous problems. Two types of passive fibre-optic gyroscopes currently under development: interferometers and resonators. To date, the published performance of interferometric fibre-optic gyroscopes has far exceeded that of resonant-ring fibre-optic gyroscopes.

5.5 Interferometric fibre-optic gyroscopes

The passive fibre-optic interferometer gyroscope uses Sagnac's original procedure of exciting an interferometer from an external optical source and directly measuring the light wave's phase shift after it traverses a closed path. But the path is an optical fibre instead of free space, and the effective sensitivity is multiplied by using many turns of fibre. The first demonstration of such a system was made by Vali and Shorthill (1977). This scheme is attractive because the fibre-optic gyroscopes can be very small and extremely rugged. They turn on instantly, have long shelf life, and are virtually maintenance-free. Fibre gyroscopes could use integrated-optic guide-wave circuits, which can be mass-produced. The resulting low cost would be a major advantage. Some predict more than an order of magnitude cost reduction compared with ring laser gyroscopes (Kim and Shaw, 1986).

Contrary to the fibre-optic resonator gyroscope, the interferometric fibre-optic gyroscope needs a laser with a broad line-width as the external light source to reduce the backscattering effect since a small portion of the backscattering light is capable of interfering with the primary beam. Bergh,

Lefevre, and Shaw (1981) demonstrated this technique of reduction of laser coherence length to reduce the Rayleigh backscattering effect. In their experiment, they used a 580 m coil, with a core radius of 2 μm wound on a 7 cm radius spool. It was found that the rms value of the phase error with a He-Ne laser as the source was 1×10^{-3} rad for a 1-sec integration time. This value was reduced to 5×10^{-5} rad for the same integration time when the He-Ne laser was replaced by a GaAs-diode laser (which has a small coherence length). This is equivalent to a rotation rate of 0.5 deg/h for the parameters given above. Using an integration time of 30 s, the minimum detectable rotation rate was found to be 0.2 deg/h.

Kim and Shaw (1986) presented an overview of the interferometric fibre-optic gyroscopes. They mentioned that the experimental fibre gyroscope had demonstrated a sensitivity equal to that of the active ring laser gyroscope. At the present, however, much of the commercial effort is addressing applications that can tolerate relatively low sensitivity and accuracy - of the order of 1 to 100 degrees an hour. For example, oil well logging, determining the direction and distance the drill bit travels, is one of several applications that require a significantly different set of gyroscope characteristics. High sensitivity and accuracy for small rotation rates are required, but not wide linear dynamic range or great scale factor stability. Well-logging gyroscopes measure the earth's rotation vector components with sensitivity up to 0.01 deg/h.

The passive fibre-optic interferometer gyroscope has some similar problems encountered in the resonant fiber-optic gyroscope. For example, the bias associated with birefringence in the fiber when the counterpropagating waves have different states of polarization, and the problem associated with backscattered waves in the fibre arising from Rayleigh scattering also reappear. Both of these phenomena lead to noise, instability, and drift in the beat signal in response to environmental effects such as vibration and thermal variation. To further increase the sensitivity to present levels, a number of other physical phenomena had to be identified and accommodated, including the Faraday effect in the fibre material in the presence of the earth's magnetic field and the nonlinear optical Kerr effect in the fibre material.

Much effort has been done to improve the performance of the interferometric fibre-optic gyroscopes. Mackintosh and Culshaw (1989) showed that the Rayleigh backscattering noise in a fibre-optic gyroscope can be nulled by adjustment of the coupling ratio of the loop coupler and the state of polarization in the gyroscope loop. They expected that the sensitivity of the rotation measurement by this method would be less than 10^{-2} deg/h. Ono, Nishiura, and Nishikawa (1991) presented a signal processing approach to a wide dynamic range

and linear scale factor rotation sensing based on the basic open-loop phase-modulated interferometric fibre-optic gyroscope. Contrary to the closed-loop one, the open loop configuration does not need a nonreciprocal phase shifter in the fibre coil to achieve a wide dynamic range (Kim and Shaw, 1986). A preliminary experiment showed that their approach provides good linearity over a wide dynamic range for rotational rates up to 10^{-3} deg/s. Moeller, Burns, and Grigo (1989) demonstrated an open-loop all-fibre gyroscope with polarization-holding fibre with a low insertion loss (14 dB) and good polarization extinction (20 dB) throughout the optical circuit. As a consequence, this gyroscope has low noise and low bias drift. They utilized a feedback circuit to control peak detected power and to stabilize the scale factor. Although the scale factor was found to depend on physical parameters of temperature and source current, these dependences could be modelled and the rms deviation of the scale factor was found to be 32 ppm or less over 12 days, for a maximum rate of 4 deg/s. They mentioned that this was the first time scale-factor stability approaching inertial quality had been achieved in interferometric fibre-optic gyroscopes.

Jin and Culshaw (1992a) presented a 2-D frequency-division multiplexed, interferometric fibre-optic gyroscope system since most applications of gyroscopes involve the use of a cluster of instruments measuring rotations along orthogonal axes. The system used a single light source and a single detector and had been successfully implemented in a laboratory demonstrating system as there are obvious potential economies in components when all the gyroscopes in a cluster are energized from a single source. However, the use of a single source for several gyroscopes does introduce the possibility of crosstalk between the signals detected from each of the gyroscopes. Jin and Culshaw (1992b) demonstrated that the crosstalk noise induced by backscattering was reduced from 5 deg/h to 0.2 deg/h by proper choice of modulation depth and frequency of the each modulator positioned in the coupled ends of the two fibre loops.

5.6 Active fibre laser technique

We have discussed the passive fibre-optic gyroscopes. One might think that an active all-fibre gyroscope would be interesting to further improve the performance of the fibre gyroscopes. Indeed, the possibility of an active fibre ring resonator gyroscope based on stimulated Brillouin scattering was first suggested in the literature by Thomas *at al.* (1980). The primary attraction of the optical fibre Brillouin scattering ring laser gyroscope is that a direct frequency read-out of the

rotation rate is obtained from an all-fibre system. It was further postulated that the gain medium is decoupled and some of the errors common to conventional ring laser gyroscopes, such as lock-in and mode pulling would not be readily observed. Kadiwar and Giles (1989) reported preliminary results on the observation of rotation rate sensitivity for the Brillouin scattering ring laser gyroscopes. In their experiment, a 1.4 mW single longitudinal mode He-Ne laser (λ = 633 nm) was used as the pump source. The pump light was coupled to both directions of the ring resonator by means of a 50/50 beam splitter. The resonator has a finesse of 240 and a loop length of 4.16 m. The frequency of the stimulated Brillouin scattering light was shifted about 26 GHz from the pump frequency. The output of the gyroscope passed a Fabry-Perot to filter out the pump light. Although the beat frequency was observed in the experiment, the sensitivity of the experimental setup was not mentioned by the authors. Huang *et al.* (1993) provided a synthetic heterodyne detection scheme for ring laser gyroscopes to sense both rotation rate and direction. This scheme is compatible with the sinusoidal push-pull phase modulation technique for suppressing frequency locking. The good experimental results show the potential of this detection scheme in applications.

5.7 Multioscillator ring laser gyroscope

So far, the active ring laser gyroscope we have discussed is assumed to have a pair of linearly polarized modes counterpropagating in a planar cavity. Contrary to this "conventional" two-mode laser gyroscope, the multioscillator ring laser has four modes in the ring cavity: a pair of right-circularly polarized (RCP) modes and another pair of left-circularly polarized (LCP) modes. Statz *et al.* (1985) presented a review of the multioscillator ring laser and mentioned this scheme is the second generation laser gyroscope, which is under development in Raytheon Company, USA. The multioscillator was conceived as a simple, purely optical means for circumventing the lock-in problem of the conventional two-frequency ring laser gyroscope. The concept is to establish two independent laser gyroscopes operating in a single optical resonator, sharing a common optical path, but statically biased in opposite senses with high apparent rotation rates by common passive optical elements. Unlike the conventional two-mode ring laser, it requires a nonplanar cavity structure for generating four independent lasing modes. When the outputs of these four frequencies are taken differentially, the bias appears as a

common-mode signal and cancels, whereas the rotation-generated signals are of opposite sense and add. The differential operation avoids the usual problems due to drifts in static bias, and results in a sensitivity to rotation that is twice that of conventional two-modes ring laser. Because the bias is not dithered, there are no dither-induced errors to limit instrument performance.

Fig. (5.1) indicates the essential elements of a multioscillator ring laser gyroscope. Fig. (5.2) illustrates the resulting spectrum. In the absence of inertial rotation or of polarization elements in the ring, each longitudinal mode of the resonator would be four-fold degenerate. The CW and CCW propagating modes, each of two possible orthogonal polarizations, would all resonate at the same frequency.

The natural optical activity of certain solid optical materials is one means of realizing reciprocal polarization rotators. An example is crystalline quartz oriented with its optic (c) axis aligned with the laser resonator axis. This reciprocal polarization rotator induces a reciprocal (propagation-direction independent) difference in the optical pathlength, often via a difference in the refractive index seen by orthogonally (e.g. right- and left-circularly) polarized modes. These orthogonal modes experience slightly different frequencies. The polarization rotator forces the resonant modes to be nominally RCP or LCP, since only circular polarization is unchanged in state by propagation through a polarization rotator and can therefore reproduce itself upon each transit of the ring, the condition for resonance. It simultaneously splits the frequencies of the RCP and LCP modes because a polarization rotation θ_{rp} is equivalent to a differential phase shift $2\theta_{rp}$ between the modes. The reciprocal polarization frequency shift, Δf_{rp}, between the orthogonal polarizations of either propagation sense is given by

$$\Delta f_{rp} = (\theta_{rp}/\pi)(c/P), \tag{5.8}$$

where c/P is the free spectral range of the empty cavity. For the case of a 90^0 polarization rotator, the modes are split by one-half the free spectral range and therefore are equally spaced in frequency. This opens the possibility of operating two ring lasers in the same cavity simultaneously, one in RCP, and the other in LCP. However, in the absence of inertial rotation, the counterpropagating modes of each polarization would still resonate at the same frequency and therefore be subject to lock-in and the resulting nonlinear rotation rate readout.

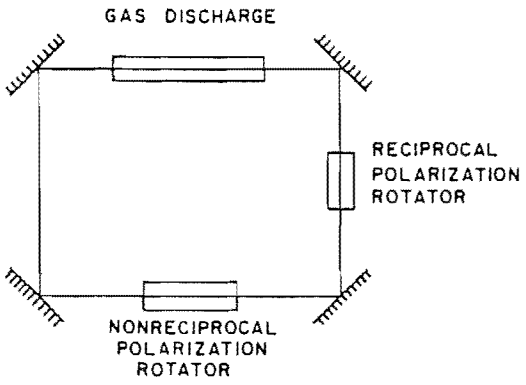

Fig. 5.1. Elements of a multioscillator ring laser gyroscope resonator. The reciprocal polarization rotator may represent a crystalline quartz rotator or the lumped equivalent image rotation of a nonplanar ring. The nonreciprocal polarization rotator may be a distinct element, such as a Faraday rotator, or may be incorporated into one of the other elements, as with a magnetic mirror or a Zeeman-split discharge. From Statz *et al.* (1985).

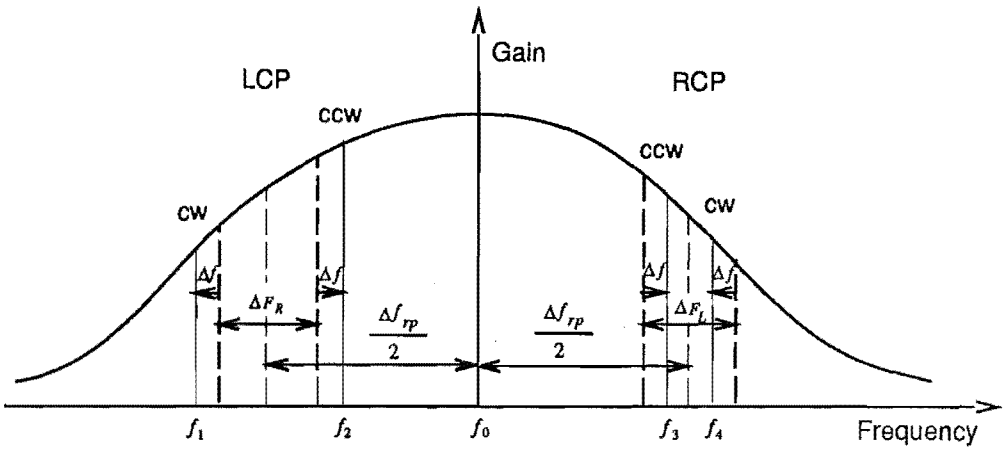

Fig. 5.2. Frequency shifts of the four lasing modes of a multioscillator RLG. The original (fourfold degenerate) longitudinal mode at f_0 is split into LCP and RCP modes (thinner broken lines) by the reciprocal polarization splitting Δf_{rp}. Each polarization is further split by the nonreciprocal (Faraday) biases ΔF_L and ΔF_R, resulting in four distinct lasing frequencies (thicker broken lines). Rotation of the ring shifts each of these four frequencies by Δf, in the senses shown, to yield the four lasing frequencies (solid lines) in the presence of inertial rotation. Splittings are greatly exaggerated. From Statz *et al.* (1985).

The nonreciprocal polarization rotator acts to introduce a nonreciprocal (propagation-direction dependent) differential phase shift between modes of a given polarization propagating in opposite directions. This further splits the resonant frequencies. The nonreciprocal frequency splitting of the modes are

$$\Delta F_L = \theta_F(\lambda_L)/\pi \ (c/P) \tag{5.9a}$$

and

$$\Delta F_R = \theta_F(\lambda_R)/\pi \ (c/P) \tag{5.9b}$$

where θ_F is the nonreciprocal rotation angle. Here λ_L and λ_R are the average wavelengths of the LCP and RCP modes, respectively. This splitting is usually referred to as the Faraday splitting and the rotation θ_F as the Faraday rotation, because the most common realization of the nonreciprocal polarization rotator is the Faraday rotator.

Application of a rotation rate Ω about the ring laser cavity axis further shifts the four frequencies. The magnitude of the rotation-induced frequency shift for each of the four modes is given by

$$\Delta f = 2\vec{A}\cdot\vec{\Omega}/\lambda P \tag{5.10}$$

The results of the various frequency shift on the four resonant modes are given (Statz *et al.* 1985) as follows:

$$f_1 = f_0 - \tfrac{1}{2}\Delta f_{rp} - \tfrac{1}{2}\Delta F_L - \Delta f \tag{5.11a}$$
$$f_2 = f_0 - \tfrac{1}{2}\Delta f_{rp} + \tfrac{1}{2}\Delta F_L + \Delta f \tag{5.11b}$$
$$f_3 = f_0 + \tfrac{1}{2}\Delta f_{rp} - \tfrac{1}{2}\Delta F_L + \Delta f \tag{5.11c}$$
$$f_4 = f_0 + \tfrac{1}{2}\Delta f_{rp} + \tfrac{1}{2}\Delta F_R - \Delta f \tag{5.11d}$$

where f_0 is the frequency of the original (fourfold degenerate) longitudinal mode, f_1, f_2, f_3 and f_4 are the frequencies of the CW LCP, CCW LCP, CCW RCP and CW RCP modes, respectively, as shown in Fig. (5.2). If the differential output, $f_b = (f_4 - f_3) - (f_2 - f_1)$, is taken, the Faraday biases subtract, while the rotation-generated shifts add. Thus, the beat frequency

$$f_b = 8\vec{A}\cdot\vec{\Omega}/\lambda P + (\Delta F_R - \Delta F_L). \tag{5.12}$$

The resulting scale factor for the multioscillator ring laser gyroscope is twice that for the two-frequency gyroscope, giving a rotation sensitivity twice that of a single two-frequency gyroscope.

In principle, the multioscillator ring laser gyroscope needs both the reciprocal and the nonreciprocal polarization rotators in the cavity to get the four modes oscillating in the cavity. However these intracavity parts will cause the backscattering problem as previously mentioned. Two important techniques are under development for removing these optical elements from the cavity. One of them is the use of a nonplanar ring (Chow *et al.* 1985, Statz *et al.* 1985) to achieve the reciprocal polarization splitting, instead of an intracavity element. Nonplanar rings have the inherent property of image rotation which mimics the reciprocal polarization rotation in establishing and splitting the frequencies of RCP and LCP modes. The amount of image rotation imparted to the beam depends on the geometry of the ring.

Another technique is replacing one of the cavity mirrors by a magnetic mirror (Statz *et al.* 1985) for nonreciprocal polarization rotation of the modes. This technique is to combine the magneto-optical material of the Faraday rotator with one of the existing cavity mirrors and use the Kerr rotation resultant upon reflection for bias. This approach offers the prospect of realizing a multioscillator ring laser gyroscope with no extraneous optical elements in the beam path. In the multioscillator ring laser gyroscope, the polar Kerr effect is advantageous for circularly polarized modes. The magnetic field is applied normal to the reflection plane, and the magneto-Kerr effect causes the reflection coefficients for modes of the same handedness but propagating in opposite directions to differ in phase, thereby giving rise to a splitting of the resonance modes exactly as in the case of the intracavity Faraday rotator.

The multioscillator ring laser gyroscope is an attractive approach. The lack of mechanical dither results in an inherently low-noise instrument, as is needed for applications requiring fast response, rapid alignment or calibration, or high resolution. It also enables more than one gyroscope to be mounted in a single instrument and it is not necessary to isolate the individual gyroscopes to avoid cross-coupling. However, performance of the multioscillator ring laser is limited by the characteristic of the magnetic mirrors.

This limit arises from the fact that bare metallic magnetic mirrors are poor reflectors at the He-Ne wavelength. Typical reflectivities lie in the range 0.4 - 0.7 (Krebs *et al.* 1980). These reflectivities are inconsistent with the optical loss requirement of the ring laser gyroscopes. In order to reduce the loss associated

with the magnetic mirrors, one can overcoat the opaque metallic mirror with a multilayer dielectric stack which is tuned to be highly reflecting at the wavelength and angle of incidence used. However, this multilayer coating will reduce the nonreciprocal polarization rotation induced by the magnetic field. Statz *et al.* (1985) give an example of the magnetic mirror. A thin layer of manganese bismuth (MnBi) is deposited onto a mirror substrate and a multilayer dielectric mirror is deposited over the magnetic layer. The dielectric indices used are 2.3 and 1.35, corresponding to high-index layers of zinc sulphide and low-index layers of magnesium fluoride. The trade-off between reflection loss and magneto-optic bias is apparent. With four layer pairs, the nominally 50% loss of the bare MnBi is reduced to about 1%, at the Kerr rotation is simultaneously reduced from about 1.5^0 to about 1.5 min. Different dielectric coatings can be used for other loss level (or Faraday bias levels), but all feasible overcoating are expected to have the same quality factor of about 1.3 min of rotation per % of loss. This corresponds to about 143 kHz bias per % loss for the MnBi mirror and a 25 cm-pathlength ring laser gyroscope. The reflectivity reduction of the magnetic mirror reduces the sensitivity of a ring laser gyroscope as we will discussed later. This inherent problem of the magnetic mirrors has not been solved up to now (Bilger 1992) and no further report about the progress of the multioscillator ring laser gyroscopes is available.

Another means of realizing a nonreciprocal polarization rotation without the addition of optical components to the ring is to use the Faraday rotation of the excited laser gain medium (e.g. Sanders, Anderson, and Scully, 1978). One need simply introduce a magnetic field component along the axis of the gas discharge. External permanent magnets or electromagnets can be used. This field induces a Faraday rotation by means of a splitting of the laser transition known as the Zeeman effect.

Some special problems are encountered with the Zeeman-biased laser (Statz *et al.* 1985). One is that the output bias, as shown in Eq. (5.12), ΔF_R - ΔF_L, depends upon the gyroscope centre frequency, the average frequency of the counterrotating modes, and in particular on the detuning of (or difference between) this average frequency of ring laser with respect to the centre of the gain curve. Statz *et al.* (1985) shows that the bias of the beat frequency of a ring laser is approximately 100 Hz when the averaged frequency of the ring laser has a detuning per MHz with respect to the centre of the gain curve, with a magnetic field of 3.5×10^{-3} T. In general, the higher the magnetic field, the larger this sensitivity on mode frequency becomes. The average mode frequency, which would

change as the ring expands under temperature changes, is normally stabilized using a servo loop and a movable mirror to compensate the pathlength changes. To maintain the output bias stable to within 10^{-2} Hz, about 100 Hz stability of the centre frequency is necessary even with a relatively low Zeeman splitting of 100 kHz while the magnetic field is about 3.5×10^{-3} T. For a ring laser with the cavity length of 25 cm (corresponding to the free spectral range of 1.2 GHz), this requires stabilizing the cavity length to 5×10^{-4} $\mathring{A}$, which may be difficult.

This stabilisation constraint may be seen as follows. To maintain δf = 100 Hz, for the Newport SR-130 supercavity ($\Delta\nu$ = 6 GHz), the cavity length change $\delta l = (\lambda/2)(\delta f/\Delta\nu) = (633 \times 10^{-9}/2)(10^2/6 \times 10^9) = 5.1 \times 10^{-15}$ m. For the 4 m ring ($\Delta\nu$ = 86 MHz), this requires a cavity length change $\delta l = 633 \times 10^{-9}$ $(10^2/ 86 \times 10^6) = 7.3 \times 10^{-13}$ m. Assuming a frequency stability of 1 MHz as the lowest requirement for the beat frequency stabilization, the cavity length change should be less than $\delta l = 7.3 \times 10^{-9}$ m. In an experiment where we locked the NL-1 laser frequency to the resonance of the Newport SR-130 supercavity (with a linewidth of 100 kHz), the requirement for the cavity length is that the change be less than $\delta l = (633 \times 10^{-9}/2)(10^5/6 \times 10^9) = 5.1 \times 10^{-12}$ m. This may explain why the device was then microphonic.

Even if the path length can be maintained, there is still a four-frequency bias contribution for large magnetic fields which itself depends upon temperature because the Doppler linewidth, and hence also the gain and dispersion, are functions of the temperature.

5.8 Self-biased ring laser gyroscope

Self-biasing a ring laser (Scully *et al.* 1978, Anderson *et al.* 1979, 1980) is another approach to overcome the problem of mode locking in conventional ring laser. This theoretical work led to the conclusion that the presence of an additional pair of modes oscillating in the cavity could significantly reduce the lock-in threshold because of nonlinear coupling effects. In this scheme one would have, for example, a pair of TEM_{00n} counterpropagating modes, and then a pair of (in general weaker) TEM_{01n} modes; or the second pair could have a different longitudinal mode number. An internally generated bias was expected to occur when the laser was pumped hard enough that the second pair of modes was brought above threshold. Experiments (Scully *et al.* 1978, Anderson *et al.* 1979) indeed show a

reduction of lock-in in this type of laser. In one particular experiment (Anderson *et al.* 1980) the lock-in region vanished. A self-induced bias was observed that changed sign when the direction of rotation was changed.

The interest of this approach is obvious, because it may lead to the simplest practical laser gyroscope so far, with no moving parts, no intracavity elements, and no applied external magnetic fields or complicated mirror arrangements. The authors did not point out the disadvantage of this scheme in the literature. In our experiments, we find that this self-bias depends on the intensities of the modes, which will be discussed in Chapter 8. Since this bias is induced by the coupling between the four modes, the fluctuation of the intensities of the modes caused by the competition between the modes is a major problem.

5.9 Pulsed ring laser gyroscopes

A pulsed ring laser gyroscope (Buholz and Chodorow 1967, Wax and Chodorow 1972) used another scheme to overcome the lock-in problem caused by the backscattering of the counterpropagating beams on the cavity mirrors. The idea is to isolate the counterpropagating beams by operating the ring laser in many axial modes, and phase locking them using intracavity loss or phase modulation techniques. When phase locked in such a manner, the two beams travel in pulses which are much shorter than the optical path of the cavity; thus the counterpropagating pulses are only coincident when the pulses overlap, and better isolation between them is achieved. Buholz and Chodorow (1967) used an acousto-optic modulator in a ring cavity with the perimeter $P = 411$ cm giving a round trip time $P/c = 1.4 \times 10^{-9}$ sec. The pulse duration was roughly 1/15 (100 ps) of the round trip time of the cavity. The threshold of the lock-in frequency was reduced to 150 Hz, which is two orders of magnitude better than the same system without modulation. Theoretical (Wax 1972) and experimental (Wax and Chodorow 1972) studies of the phase modulation technique in a ring laser showed a similar result, where a 4 m-length ring was used and the limit of rotation sensing was about 15 deg/h.

In general, the lock-in band, the range of rotation rate Ω for which the beat frequency goes to zero, of a pulsed ring laser is given by (Christian and Rosker 1991)

$$\Omega_L \equiv (c\lambda r/8\pi A)\exp[-(\tau'/\tau_D)^2], \tag{5.13}$$

where r is the amplitude reflection coefficient for the scattered light, τ_D is the pulse duration, and $\tau' = s/c$ where s is the separation between the scatterer and the pulse overlap point. From this relation, it is easy to see that the lock-in band is greatly reduced when the pulse duration is a small fraction of the cavity perimeter.

The development of ultrashort pulse lasers made possible a new approach: the ultrashort pulse ring laser gyroscope. Christian and Rosker (1991) demonstrated a 100 picosecond pulsed diode ring laser gyroscope, which is attractive for gyro applications since diode lasers have many desirable properties, such as small size, high efficiency, reliability, low cost, and low power consumption. Within the limits of the system resolution (~ 20 kHz), Christian and Rosker have observed no frequency locking behavior in the device.

Gnass *et al.* (1991) demonstrated the Sagnac effect in a colliding pulse mode-locked (CPM) dye ring laser. The laser was a six-mirror, two-prism CPM dye laser that produces 100 MHz pulse train near 610 nm. The pulses had a bandwidth of 2 nm (1.5 THz), corresponding to 195 fs pulse duration. With a cavity area $A = 0.18$ m^2, the perimeter $P = 3$ m, a sensitivity for the rotation rate of 10^{-3} Hz, corresponding to a rotational sensitivity of 1.3×10^3 deg/h, is achieved.

In principle, the resolution of a pulse ring laser is affected by its spectrum width. For a gaussian pulse $E(t) = \exp(-\alpha t^2)\exp i(\omega_0 t + \beta t^2)$, its time-bandwidth product $\tau_p \Delta f_p = (2\ln 2/\pi)[1 + (\beta/\alpha)^2]^{1/2}$, where τ_p is the pulsewidth defined in usual FWHM fashion and related to the parameter α by $\tau_p = (2\ln 2/\alpha)^{1/2}$, Δf_p is the FWHM spectral width and $\Delta f_p = (2\ln 2)^{1/2}/\pi(\alpha^2 + \beta^2)^{1/2}$ (Siegman 1986). The minimum or unchirped ($\beta = 0$) value of the time-bandwidth product is thus $\tau_p \Delta f_p \simeq 0.44$. For a gaussian pulse with a pulse width of 100 ps, the FWHM of its spectrum $\Delta f_p = 4.4$ GHz, which is about 12 orders in magnitude larger than that of the Canterbury ring laser. Therefore, the resolution of a pulse ring laser is much lower than the continuous wave laser with the same area cavity.

5.10 Argon ion ring laser

An experimental result of an argon ion ring laser with 1.4 m^2 as a gyroscope has been reported by Höling (University of Southern California, Los Angeles, USA), Leuchs (Nanomach AG, Buchs, Switzerland), Ruder (Universität Tübingen, Tübingen, Germany), Schneider (Technische Universitat München, München,

Germany) (1992). One of the purposes of their developing an argon ion ring laser is the potential application in astronomy. Fluctuations of the Earth's rotation which are of the order of 10^{-8} to 10^{-9} Ω_E are measured today by simultaneous data taking runs of several radio telescopes on a long baseline and over periods of hours to days. If ring laser gyroscopes could be improved to a sensitivity of 10^{-9} Ω_E or better, they would provide a much easier method for carrying out these measurements in real time.

Eq. (5.3) shows that the scale factor S is proportional to the area of the cavity. Besides, the fundamental sensitivity limit Δf_{rms} is inversely proportional to the square root of the power of the ring laser. In order to design a ring laser with a higher accuracy, Höling *et al.* (1992) decided to both enlarge the area to above 1 m^2 and to choose as the lasing medium argon ion gas which should provide a circulating power of the order of 100 W inside the cavity, which is larger than that of He-Ne lasers by two orders of magnitude.

Several serious problems have been encountered in their experiments. The first is the beat frequency shift, which they attributed to the flow of the medium inside the plasma tube causing a frequency difference of the counterpropagating waves due to the Fresnel-Fizeau effect (Aronowitz 1971). Four different configurations have been tested. Of these, two setups use two discharge tubes with opposite polarities, in turn, with opposite currents in the two discharge tubes to cancel the bias each other, as used in He-Ne ring lasers (Chow *et al.* 1985). However, it turned out that in none of the four configurations could the expected beat frequency of about 100 Hz due to Earth's rotation be detected. Instead there was a beat frequency from 15 - 45 kHz with a linewidth of 0.5 - 1 kHz.

The gas inside the plasma tube consists mainly of argon atoms at a pressure of 0.25 Torr of which approximately several percent are ionized. Not only ions and electrons are flowing, but also the neutral argon atoms exhibit a drift since they are dragged by the charged particles. The magnitudes of these flows depend critically on parameters such as the geometry of the discharge tube, its bore radius, and the exact percentage of ionized argon atoms. In addition, for a quantitative calculation of the beat frequency shift due to the Fresnel-Fizeau effect, the index of refraction due to argon atoms, ions, and free electrons needs to be determined. In the case of the argon ions with whose lasing transition the light is in resonance, further uncertainties come into play. The total losses of the resonator affect the population inversion and therefore the index of refraction due to the argon ions as can be seen by the Kramers-Kronig relation (Bennett 1977). For all reasons given, the phenomena inside an argon plasma tube are so complex that a quantitative

determination of the contributions caused by argon atoms, ions, and electrons to the beat frequency due to Fresnel-Fizeau effect cannot be given, and a comparison with the experimental results is not possible (Holing *et al.* 1992).

The second major problem is the large frequency lock-in region as two or four Brewster windows for the discharge tubes, and an etalon for selecting the single longitudinal mode have been used in the cavity in their different configurations. The frequency locking thresholds for the four configurations are from 2 - 7 kHz, which is much larger than the nominal beat frequency (~ 100 Hz) of their ring laser frequency expected by the earth rotation.

As a result, the sensitivity of their argon ring laser is about 2-3 Ω_E.

5.11 Comparison of laser gyroscopes

The development of ring laser gyroscopes is an active field. Potential markets for these instruments range from commercial applications in navigation system for marine, land, general and commercial aviation vehicles, to space and military applications (Stowell *et al.* 1978, Martin 1986, Kim and Shaw 1986). With these incentives, the ring laser gyroscope field is quite competitive. There are as many as seven major United States corporations (e.g. Honeywell Inc., Sperry Corp., Litton Industries.) as well as additional European (e.g. Thomson CSF in Orsay, France; Standard Elektril Lorenz in Stuttgart, Germany) and Japanese companies (e.g. Mitsubishi Electric Corp.) which are known to be active in the ring laser field (Statz *et al.* 1985, Martin 1986, Kim and Shaw 1986, Takahashi *et al.* 1990).

Many universities in laser and optics worldwide are also involved in ring laser research, such as the Optical Sciences Center, University of Arizona at Tucson, AZ (e.g. Chow *et al.* 1980, 1985), the Institute for Modern Optics, University of New Mexico at Albuquerque, NM (e.g. Chow *et al.* 1985), the Research Laboratory of Electronics, Massachusetts Institute of Technology, Cambridge, MA (e.g. Sanders *et al.* 1981), University of Rochester, Rochester, NY (e.g. Christian and Mandel, 1988), Stanford University (e.g. Kim and Shaw 1986) etc.

Each of the different types of the laser gyroscopes discussed here has different advantages and problems, induced by different mechanism. The ring laser constructed at Canterbury is for high precision measurement, therefore high sensitivity of the instrument is particularly important for the project. The

sensitivities achieved in the various laser gyroscopes are summarised as shown in the Table 5.1. It should be pointed out that few conferences are dedicated to ring laser gyroscopes because most work and data are regarded as proprietary information by the ring laser manufacturers. All the data presented in this table are from an exhaustive search of the open literature of science and engineering.

Table 5.1 Comparison of laser gyroscope sensitivity

Type	Sensitivity (deg/h)	Reference
Planar active ring laser	10^{-3}	Chow *et al.* 1985
Passive ring cavity	5.6×10^{-3}	Sander *et al.* 1981
Passive fibre resonator	4.8×10^{-3}	Takahashi *et al.*1990
Passive fibre coil	3.2×10^{-4}	Moeller *et al.* 1989
Multioscillator ring laser	2.7×10^{-3}	Statz *et al.* 1985
Pulsed ring laser	1.3×10^{3}	Gnass *et al.* 1991
Argon ion ring laser	30 - 45	Holing *et al.* 1992
Canterbury ring laser	2.4×10^{-6}	Stedman *et al.* 1993

Chapter 6

Ring laser experiments

This chapter is concerned with the major focus of this thesis and of the ring laser research program at the University of Canterbury, conveniently termed the "Canterbury ring laser". Much of my course work for the Ph.D. thesis has been spent in experimental development on this and on related topics. There are several topics to be covered here, which overlap in many ways with each other and with the other chapters of this thesis. Somewhat more rounded if relatively brief overviews of the ring laser program are given in the recent group publications (e.g. Stedman *et al.* 1993 and references therein).

This part of the thesis is a further (and often more specific) announcement of the success of this project than is given in the group's publications. Together with those publications, our account makes an interesting and reassuring contrast with recent negative statements about the usefulness of large ring lasers for precision purposes. For example, a highly respected worker in ring gyroscopes (Rodloff 1989) has stated that useful (precision) rings with a perimeter greater than 60 cm are essentially impossible to achieve: "Aber bereits an dieser Stelle wird deutlich, dass der in der Literatur haufig diskutierte «Superkreisel» mit vielen Metern Umfang ziemlich sinnlos ist. So laesst sich z.B. zeigen, dass der Einfluss des Quantenrauschens bei Resonatoren mit Laengen von mehr als 50-60 cm durch eine weitere Steigerung der Abmessungen kaum noch verbessert werden kann. .. trotz aller Geometrie-Regler so kompakt und solide wie irgend möglich aufgebaut werden muss. Eine Resonatorlaenge von 60 cm bei einer Blockdicke von 44 mm scheint hier ein guter Kompromiss zu sein." Or, roughly translated: "However, already at this level the often-discussed "Supergyro" with a path length of several metres makes no sense ... The influence of quantum noise can hardly be improved by increases in the length of the resonator beyond 50-60 cm ... in spite

of all possible regulation of the geometrical shape .. A resonator of length 60 cm on a 44 mm block is a good compromise." Certainly a simple polygon with an area of the order of square metres will never be a field instrument. However, more than this objection is implied by the above sweeping dismissal of large rings.

In tracing the source of and reasons for Rodloff's arriving at this assertion, Professor Bilger has noted (private communication) that Rodloff's basis for this claim is in part a conference article which he references (Simpson 1988). Simpson makes the above point that an instrument of greater size than say 60 cm is likely to be unwieldy, and that is not disputed. However the statements by Simpson and Rodloff to the effect that for rings with a perimeter greater than 60 cm quantum noise falls off slowly appear to be derived from a curious error of interpretation. Figure 1 of Simpson (1988) plots quantum noise against ring perimeter, and the knee of this curve corresponds to perimeters of a few tens of centimetres. It thus seems that the position of this knee is one origin of the Simpson-Rodloff claim. Indeed Simpson explicitly says: "The quantum limit is found to improve sharply for small cavity lengths and less sharply for lengths over 23 cm." However, the position of this knee is itself purely an artefact of the choice of scale; the curve is a graph of $y = kx^{\frac{1}{2}}$ and by suitable expansion of the scale of the y axis, the knee can be moved to any perimeter. Quantum noise itself does not dictate an intrinsic length scale of this kind.

The successful operation of the Canterbury ring laser shows that it is possible to achieve mechanical stability to a level at which the advantages of the long path length of the previously hypothetical "supergyro" derided by Rodloff in the above words are achieved in practice for quantum noise.

As another, we note again (see chapter 5) the total failure of what in some ways was a very similar project at a prestigious and much better funded laboratory (Höling *et al.* 1992), incidentally for a variety of reasons which were obvious to Professor Bilger from the principles of their design as dooming that laser from the outset. (For example, their use of very high excitation current density of the order of 1000 A/cm^2 for their Ar laser, partly with the aim of reducing quantum [shot] noise, induces a complex flow of the laser medium and enormous dispersion effects which would swamp the desired observations. As another example, one of their ring mirrors is designed to have nearly 0° incidence so as nearly to retroreflect the beam and so to induce a cancellation of drag effects on the beam. This strategy has a catastrophic effect on backscatter and so lockin. This cautionary tale points to the value of the detailed description given in this chapter. The combination of high finesse and high area achieved in the Canterbury ring laser has yielded a working instrument which we believe to be unique at the

present time. This is reflected in the unprecedentedly high capabilities for frequency resolution in this instrument which are reported in this chapter.

In this chapter I describe relevant aspects of the major experimental project itself, in which I shared and of which this thesis forms a part; in particular, the construction, basic operation and initial results of the ring laser. Further results in connection with the parameters of frequency pulling are discussed in chapter 7. The period of my study for the Ph.D. degree overlaps with all the major stages of this project.

In Section 6.1 I describe the components and construction of the ring laser. This is a brief record of some major features not previously documented for archival purposes, regardless of the workers involved. There is special emphasis on those matters in which I participated as one of the team. The operational techniques are discussed, in particular the alignment procedures in whose development I played a major part. Also incorporated here are some general operational notes adapted from those compiled initially by Professor Stedman.

In Section 6.2 I discuss the methods and results of the analysis of the beat frequency data from the Canterbury ring. In particular, I show that not only does the Canterbury ring laser facility have the capability of unprecedentedly high resolution, but our present method of signal analysis has an additional and significant advantage over current practice in ring laser gyroscopes. We record the waveform, as sampled several times in one period, rather than merely count fringes; subsequently we use numerical methods based on the fast Fourier transform (FFT) and the Hilbert transform or analytic signal. I show that as a direct consequence we are able to improve very considerably on the precision of measurement attained in otherwise identical systems where fringe counting methods are employed. In particular, we consistently measure the beat frequency between counterrotating modes in a single run of say 320 s duration at a precision which corresponds to the magnitude of the quantum limit on the beat frequency linewidth; there is no need to average over many such runs. The improvement in measurement resolution attainable by this method as compared to that obtained by counting beats is typically a factor of 30 or greater.

In Section 6.3 I describe some preliminary measurements of ring lasers. A line position in the Fourier spectrum of the ring output gives the value of a beat frequency. This has been measured routinely with an accuracy of better than 1 mHz in runs whose typical duration is 16 s, and in one favourable case an accuracy of 11 μHz in a run lasting 320 s. This last measurement corresponds to a fractional accuracy of 0.16 ppm in the measurement of a beat frequency when expressed as a ratio with the earth-rotation-induced frequency of 68.75 Hz, and

suggests that the system has the potential to be sensitive to changes in rotational frequency at the level of 1.6×10^{-7} of the beat frequency (68.75 Hz) corresponding to the projection of the earth rotational rate Ω_E on the area of the ring. As a fraction of the frequency of the laser radiation itself, this level of precision corresponds to parts in 10^{20}. In practice, however, and for reasons discussed in Chapter 8, the drift in beat frequency between runs is at present very much greater than this figure, and longer-term gyroscope-type measurements are likely to have rather greater errors, approaching the 1 mHz (or 100 ppm) level, with the present system. The cause of this is not an intrinsic limitation (say from mechanical instability, as envisaged by Rodloff) of a ring with such a long perimeter, but the present problems with fully baking out the ring components and so maintaining long-term gas purity. Nevertheless, a figure of 1 ppm for beat frequency precision is a realistic indicator of the capabilities of the Canterbury ring laser system for certain ultra-precise measurements of nonreciprocal optical effects. For example, field-induced effects similar to but much weaker than the effect whose observation is discussed in chapter 5 could be detected by combining the above numerical techniques with phase sensitive detection techniques.

For achieving a stable beat frequency of a ring laser, the single longitudinal mode operation is necessary. This is particularly important for our ring laser as the free spectral range of our ring is very small (only 86 MHz) compared the gain linewidth (~2 GHz for equal isotope mixture of Ne^{20} and Ne^{22}). The mode structure of the Canterbury ring cavity is monitored by using the scanning Fabry-Pérot supercavity (model SR-130 from Newport, Fountain valley, Calif. U S A). The work reported in other chapters of this thesis on the dynamic response of a scanning Fabry-Pérot cavity represents material relevant to this second approach.

6.1 Ring laser facility

6.1.1. Basic construction and equipment of the ring laser itself

The Canterbury ring laser is sited in the Cashmere war bunker, serendipitously revealed on national television in the early stages of this project. As a group, we are most grateful to members of the Cracroft-Wilson family and to the Canterbury Hospital Board for permission to use this facility and for access to electricity, telephone and water.

According to the standard theory of the Sagnac effect (Section 5.2), the beat frequency induced by earth rotation has the form

$$\Delta f = \frac{4\mathbf{A}\cdot\boldsymbol{\Omega}_E}{\lambda P}. \tag{6.1}$$

In this equation the earth rotation rate Ω_E is 7.2722×10^{-5} rad s^{-1}. The (vacuum) wavelength λ is 633.0 nm, corresponding to a frequency of the lasing transition is 473.6 ± 0.1 THz. The area **A** of the ring is defined by the integral $\frac{1}{2}\oint \mathbf{r} \times d\mathbf{l}$ around its contour. In our case it was determined by direct measurement of the lengths of the arms to an accuracy approaching 1 mm, and then adjusting these lengths minimally within the measurement errors so as to conform with the more accurately known perimeter P of 3.47710 ± 0.00010 m, itself determined from the measured beat frequency between adjacent longitudinal modes of 86.218 ± 0.002 MHz. This beat frequency was obtained by using a low (50 Ω) resistor in the final dynode of the PMT detector, whose output was then mixed in a transformer with an oven-controlled 60 MHz signal of ppm accuracy. The beat frequency of 26.218 MHz was detected by a suitable radio receiver. This gave linear dimensions of 900.0 ± 0.2 mm, 838.5 ± 0.2 mm, and an area 0.7547 ± 0.0005 m^2. This in turn has to be projected on the equatorial great circle, which requires a factor $\cos(\Lambda + \frac{1}{2}\pi)$ where Λ is the latitude. The geographic longitude and latitude of this site is estimated (to 5", from Lands and Survey maps with neighbouring grid points at 5′ intervals) to be 172°37″20″ E, 43°34′37″ S. Hence the projected area at this rate of rotation induces a beat frequency of

$$\Delta f = 68.75 \pm 0.06 \text{ Hz}.$$

The error in this value reflects principally the accuracy of adjusting the table to be horizontal, and ignores pulling and dispersion effects (chapters 7, 8).

The Canterbury ring laser is designed to realise the potential of the recent advances in supermirror technology. So that the cavity finesse is maximised, the beam paths are entirely in the helium-neon gas and intersect no interface. Once however one has such high-quality rings, in principle, the Rayleigh scattering of neutral neon gas is a significant and ultimate limiting factor on finesse. We reproduce here some unpublished work of Professor H R Bilger on this matter. It is assumed that dipole scattering off individual atoms dominates; the atomic dimensions are small compared to the wavelength, and the mean free path is large compared to the wavelength at a pressure of a few torr (they become comparable

at ~ 135 torr). The total scattered power off one induced dipole is

$$P_{sc,1} = \frac{4\pi^3}{3}\frac{c}{\varepsilon_0}\frac{W_0^2}{\lambda^4} \tag{6.2}$$

where the dipole moment $W_0 = \alpha E_0 = \alpha\sqrt{2}\, E_{\mathrm{RMS}}$ in an electric field E_0 with a polarisability

$$\alpha = \varepsilon_0(n^2 - 1)/N_\nu \tag{6.3}$$

with $n^2 = \varepsilon$ as the macroscopic relative dielectric constant of the gas, and N_ν is the volume density of scatterers (for an ideal gas $p = N_\nu kT$). Hence the total scattered power on a beam of area A traversing a length L is

$$P_{sc} = P_{sc,1} N_\nu A L \tag{6.4}$$

from which, together with the Lorentz-Lorenz formula $n\text{-}1 \propto N_\nu$, the extinction coefficient can be calculated as

$$\kappa^{-1} = \frac{32\pi^3 T_0 p}{3\lambda^4 N_0 p_0}(n-1)^2\big|_{\lambda p_0 T_0} \tag{6.5}$$

At standard conditions (p_0 = 101 kPa = 1 atm, T_0 = 273 K, p ~ 300 Pa, $n_{air} - 1 = 2.79 \times 10^{-4}$, $n_{\mathrm{He}} - 1 = 0.3500 \times 10^{-4}$, N_0 (Lodschmidt number) = 2.687×10^{25}, this translates into an upper bound for the quality factor Q of order 10^{14}, about two orders of magnitude above the level expected for the present ring with mirrors of the quality supplied.

The limitations are therefore entirely in the mirror quality. Supermirror coatings were generously provided by Tony Louderback of Ojai Research, Ojai, Calif., USA. Zerodur blanks were used which have 0.1 nm rms surface roughness (i.e. smoothness to atomic dimensions), achieved through ion beam milling with argon and nitrogen beams. The ion-beam deposition process coated SiO_2/TiO_2 $\lambda/4$ layers give losses which were measured to be 4 ppm due to scattering (TIS), 4-10 ppm from transmission (as designed, by the choice of the number of layers), and absorption (by difference) of 7 ppm, approaching that currently measured for the bulk materials; however it has recently been argued (Bilger *et al.* 1993, submitted for publication) that the true limits on mirror reflectance in principle are set by other and more fundamental loss mechanisms - the Urbach tails of the ultraviolet absorption dominating - and the thermodynamic limits on density

fluctuations, which together point to a fundamental limit of the order of parts per billion in reflection loss. At the present time, the observed total reduction in reflection is then 15 ppm or less, corresponding to a reflectivity greater than or equal to 99.9985%. After extended use in our environment the total losses increased significantly; mirror cleanliness and the associated problem of laser gas purity have been our most severe problems.

A novel feature of our design, as far as ring laser gyroscopes are concerned, is the use of radio frequency excitation. This is operated by an RF Power Laboratories M150M radio-frequency system incorporating an RS Components LSG-17 signal generator and an rf amplifier. In our application it was tunable over 20 - 50 MHz and with powers of 0 - 50 W. This was fed into a cylindrical drive unit encircling one side of the ring cavity (itself defined by a fused silica tube of inner diameter 4-5 mm, which served also as an aperture to help to isolate longitudinal modes of the ring cavity). The structure of the RF discharge is schematically presented in the upper figure and its matching circuit is shown in the lower figure of Fig. (6.1).

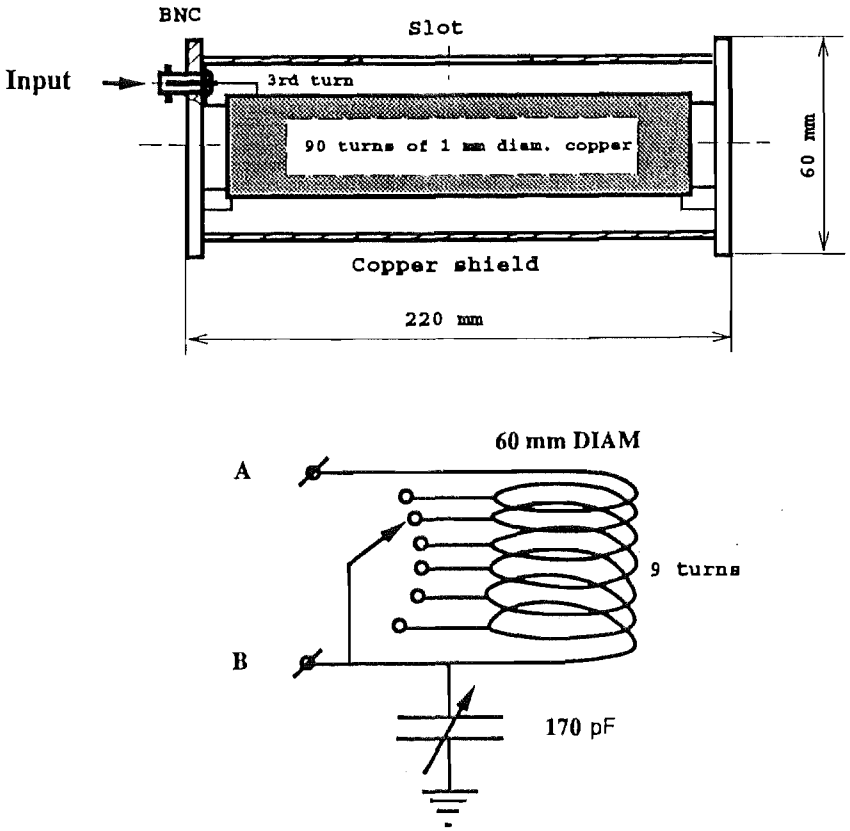

Fig. 6.1. Schematic of the RF discharge device and its matching circuit.

The drive unit consisted of a coil with 90 turns of 1 mm enamelled copper wire on a PTFE former with OD 1.175" and length 8.3". Both ends are earthed on metal cheeks. The input r.f. is supplied through a matching optimiser (LC adjustment, kindly loaned by Dr T J Seed) via a BNC connector to a tap 2 turns from the return lead (at one end). The whole winding is surrounded by a 2" ID copper shield containing some slots for viewing the plasma. This system with the exterior box containing the optimiser for fine tuning the (π) matching proved to have reasonable r.f. resonance properties, with a quality factor greater than 10. This item has now gone through several redesigns, and the latest is yet to be tested. The r.f. frequency was initially taken as 27 MHz, but more recently with the advent of different drive units was raised to approximately 48 MHz. One-way power transmission was measured on an RF Power SWR meter #612-221 (1.80 - 200 MHz). The use of radio frequency avoids the Fresnel-Fizeau effect (Aronowitz 1971, Höling et al. 1992) on the beat frequency which is associated with dc excitation. The laser gas is a 7:1 mixture of He:Ne with a nominal total pressure of 2.3 Torr (300 Pa); however this total pressure can successfully be varied over an order of magnitude, and the proportion of neon also can be varied quite significantly, typically by a factor of 2. This RF discharge system works well and shows no noticeable bias or null shift in the beat frequency in our experiments; the expected beat frequency arising from earth rotation agrees with the upper limiting value of the observed beat frequency, when enriched neon is used to avoid mode pushing, to within 1 Hz.

Our design aimed to achieve single mode operation of the ring by reducing the gain so that all longitudinal modes except one would be starved, and with it the transverse modes. This was amenable to a simple but absolutely vital check of the feasibility of our design, one of the first vital design calculations by Professor Bilger in contemplating the project: would the relatively small spacing of the longitudinal modes, compared to the width of the gain curve of the HeNe plasma, mean that amplification would be reduced to such a level that - given the low transmission of our mirrors - output power would be reduced to a level at which detection became impossible and/or quantum noise dominated? It was shown by Professor Bilger that in fact for a ring of our size this is by no means a danger at least in principle. Starving all modes near the wings of the gain curve should mean that the one remaining mode in the centre would have sufficient net gain, thanks to the curvature in the gain curve, to produce an output beam at each mirror of 30 nW, when conventional detection techniques are perfectly adequate. Nor was quantum noise predicted to inhibit the potential of the ring, so that the strategy of using maximal power to lower quantum noise with all the attendant complexities

resulting from multimode instabilities was unnecessary. We comment in Sec 6. 3 how well this prediction worked out in practice.

For further mechanical and thermal stability the mirrors are mounted in superinvar holders, which rest on a 1 × 1 m^2 Zerodur plate, itself on a granite base. From the Schott Mainz catalogues we glean the properties of Zerodur. In the temperature range 0 - 50 °C the mean linear coefficient of thermal expansion is guaranteed to be less than 15 × 10^{-8} K^{-1} for the third (worst) expansion class. Typically the figure is much lower than this, and a typical plot of longitudinal expansion with temperature is given in Figure (6.2). The differential thermal expansion coefficient plotted in Figure (6.3) reveals a minimum at approximately the temperature of the Cashmere Cavern (13-15 °C) of -5 × 10^{-8}.

The mean specific heat of Zerodur (20 - 100° C) is 0.821 J $g^{-1}K^{-1}$, its thermal conductivity (80-100° C) 1.64 W $m^{-1}K^{-1}$, thermal diffusivity (20°C) 8 × 10^{-7} s^{-1}, and its maximum operating temperature to avoid hysteresis and degradation of the expansion coefficient is recommended as 150°C. These figures were useful to us in indicating the possible limits on bakeout temperature, which ultimately was limited by the stability of the Viton O-rings, and as contributing to the thermal stability of the ring system.

The helium permeability of Zerodur at 20°C of 1.6 × 10^6 atoms per cm s bar was perfectly adequate in our sheet (1.2 m × 1.2 m × 25 mm, from Schott Garscho Pty Ltd, Terrey Hills NSW Australia; of unspecified expansion class) to act as the bottom cover of the corner boxes.

The high dielectric constant of Zerodur (ε_r = 7.4) and loss ($\tan\delta$ = 0.0155 at 1 MHz, 25°C) made it unsuitable in the near vicinity of the radio frequency exciter, which for this and other reasons needed shielding from the base plate.

The density (2.53 × 10^3 kg m^{-3}) and Young's modulus (9.1 × 10^{10} N m^{-2}) of Zerodur with those (estimated) of granite were of interest also in the design of the mounts for these basal plates; they were suspended on four worm-screw-adjustable pantographs, so that the table tilt could be altered with the ring in situ. The aim here was to minimise the droop of the base plates around the localised pressure points of these mounts.

The bending tensile strength of Zerodur, typically of 5 × 10^7 N m^{-3} for a 90% chance of breakage, meant more to us after an attempt to avoid sealing problems with O-rings by using TorrSeal to bond one stainless steel corner box to the Zerodur. The subsequent baking out had the unforeseen effect of shattering a chunk of the Zerodur at that corner on account of the expansion of the stainless steel, with attendant loss of usefulness of this corner area and the enforced

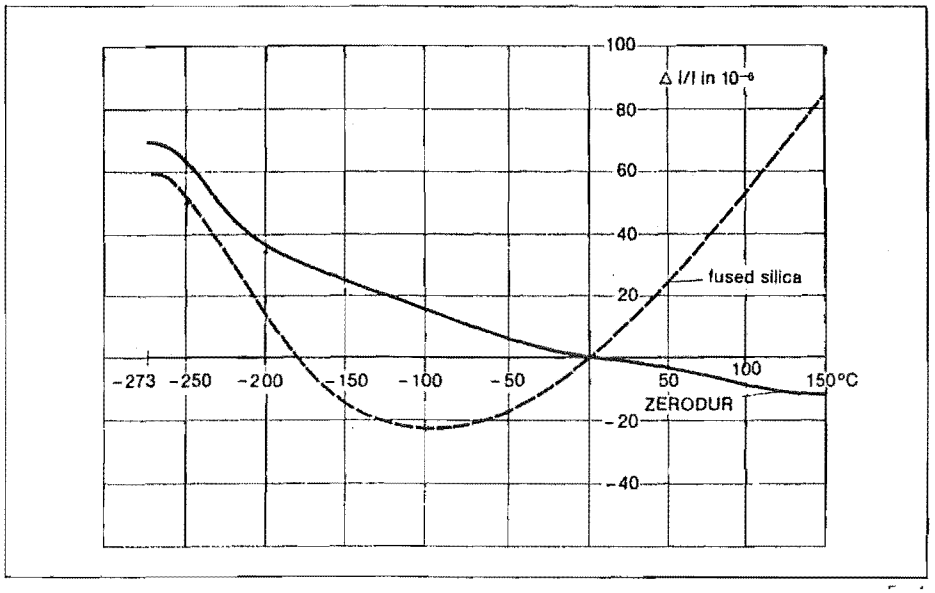

Fig. 6.2. Thermal expansion of Zerodur as a function of temperature in comparison to fused silica. From Schott Garscho Pty Ltd.

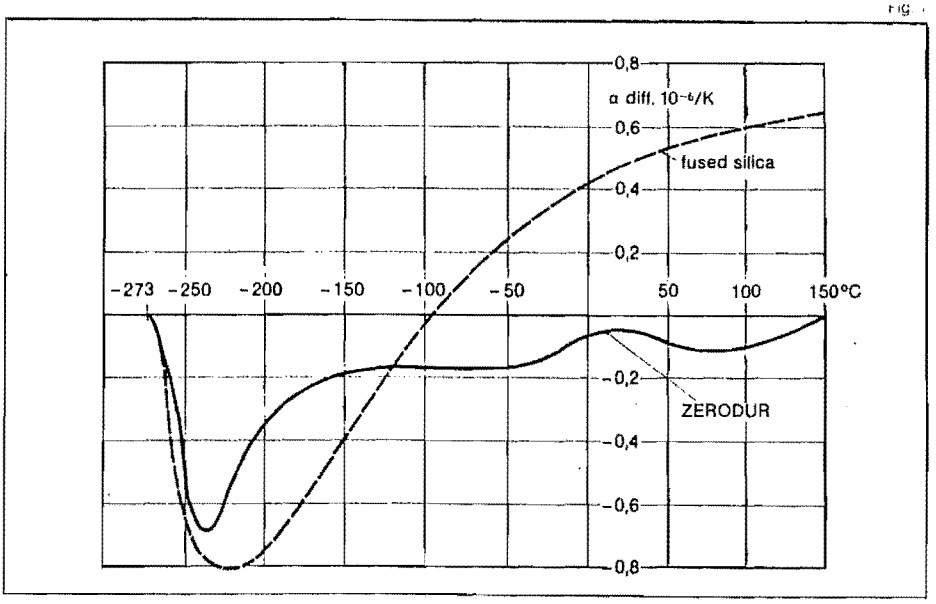

Fig. 6.3. The differential thermal expansion coefficient, which gives information on the longitudinal constancy of Zerodur during temperature changes within the temperature range of -271^0 C to 150^0 C. From Schott Garscho Pty Ltd.

reduction of the dimensions of our laser to those quoted elsewhere in this thesis. Subsequently though belatedly, it was found that similar problems were found at the Mount John telescope facility, where (fortunately small) chunks had been torn out of the rear of the (Zerodur) telescope mirror by thermal expansion of certain mechanical items when so bonded to the mirror.

The index of refraction of Zerodur is inferred to be 1.5398 at 633 nm (more generally, $1.5398 - 5.06 \times 10^{-5}(\lambda(\text{nm}) - 633)$) over the range 540 - 660 nm); this was most useful in determining the refractive transverse displacements on transmission at a mirror when the angle of incidence was 45°. The Rayleigh scatter R_{90} was of the order of 5×10^{-1} m^{-1}, and the intensity transmission of a 5 mm and a 25 mm slab at 633 nm are approximately 88%, 76% respectively; this represents a significant but not serious loss within the output mirror.

From the thermal expansion coefficient of Zerodur (taken now to be a conservative figure of 10^{-7} K^{-1}), we find a change in the optical path length P of the Canterbury ring laser with temperature change of the order of 0.4 μm K^{-1}. Hence a temperature rise of the order of 0.5 K will take the laser through one free spectral range ($\delta P = \lambda/4$), which is a far greater change than is tolerable for stable ring performance, inducing as it would not only major dispersive shifts (Chapter 8) but even the collapse of lasing in the longitudinal mode under study. This points the need for a thermostatically stabilised environment, such as the cave (whose diurnal temperature fluctuations could in principle be reduced to millikelvin). Even this assumes that the Zerodur plate is mechanically isolated from the granite. In fact, no lubricant is applied to the Zerodur-granite interface at this stage; various possibilities have been contemplated (teflon, roller bearings), but the mechanical complications and the effects of fine dust or grease in the environment has inhibited experimentation in view of our mirror contamination problems. To the extent that the Zerodur is mechanically restricted by the granite base, then, this ultimate stability will be degraded in practice; the granite expansion coefficient is estimated to be of the order of 10^{-5} K^{-1}, and if this were unchecked by the Zerodur base, this would give rise to path length variations of 50 μm K^{-1}, or a free spectral range shift corresponding to a 10 mK temperature change. This would have a quite disastrous effect on the stability of our ring output over the period of time in which the temperature changed by this amount. In the Rutherford building this would make the gathering of any significant data impossible, and in the Cashmere cavern under present conditions, where incomplete thermal sealing for the adits etc. is presently achieved, this would limit runs to a few seconds or perhaps minutes at best. Our observations (reported later in this chapter) show that runs of 16 s length achieving 1 mHz precision in the

beat frequency can be achieved in the Rutherford building, and that within the Cashmere cavern the ring laser perimeter changes by the order of a quarter wavelength on the typical time scale of hours. It was observed during alignment phases that once interference fringes were achieved, they were stable in the Rutherford building for seconds at least and under good conditions for minutes, and in the cave for minutes, under good conditions for hours. Either the Zerodur is largely serving its intended purpose, and tends to be mechanically decoupled from the granite, or (since that is unlikely in view of the high coefficient of friction between such rough surfaces, and the relatively thin plate of Zerodur we employ) the thermal conductivity and capacity of the granite-Zerodur system make it respond relatively slowly to changes in ambient temperature.

The superinvar holders were machined from hot rolled slabs of 32.5 Fe-Ni-Co solid solution austenite from Scientific Alloys Inc. Westerly RI USA, and have a thermal expansion coefficient of approximately 2×10^{-7} K^{-1}. Since the mirror holder is mounted directly on the Zerodur plate, and its linear dimensions are of the order of a few centimetres, the effect on the ring laser path length of the extra thermal expansion induced by the relatively poor properties of superinvar is negligible in comparison with that of the Zerodur base. Indeed, we have recently used stainless steel for the mirror holders, as a compromise (on account of its more ready machinability) while fighting the rather more severe problems of gas-handling and vacuum cleanliness. If the cavern were to approach its ultimate thermal stability and if the expansion of the stainless steel holder were measured from a point whose horizontal position was defined (by a suitable weight-bearing pin contacting the Zerodur base) to be less than a millimetre from the pole of the mirror, stainless steel mirror holders could in principle be an adequate permanent solution; but these conditions are not currently achieved, and would in any case have been utterly impossible of fulfilment for the measurements taken in the Rutherford building.

The stainless steel corner boxes avoid mechanical contact with the mirrors; their bottom and top surfaces are open, and are sealed by Viton O-rings against the Zerodur plate below and against plate glass lids above. The Viton A material is quoted by Holland et al. (1974) to have a superior outgassing rate of 2.7×10^{-7} W $s^{-1}m^{-2}$ after a 200°C bakeout. In practice, we were advised and also found in experience that such high baking temperatures were intolerable, at least for some of the supposedly high quality rings we were sold (locally and via colleagues in USA) and in later phases of this project we restricted bakeout temperatures to 80°C. The Viton rings have always been under suspicion as possible contributors to our still-continuing problems with gas purity, though not

as much as formerly. All components of the hardware in contact with the laser gas - the stainless steel corner boxes, the mirror holders, the Viton O-rings, were routinely given a thorough cleaning before assembly, being steamed in hot/boiling water and following that in hot distilled water, each for several hours.

A triangular ring was used in earlier lasers such as that of Bilger and Stowell (1977). We have used a square ring because of its optimal performance in such experiments as we envisage. To be specific, a square ring optimises the parameter $G = A/PN$, where A is the area, P the perimeter of a ring cavity and N the number of mirrors. Given the dependence of the quality factor Q on mirror losses, G is proportional to the signal/noise ratio of the system. Another reason for favouring a square ring over a triangular ring is that since there is an odd number of reflections in the latter case, each of which reverses handiness of the beam, a triangular ring cannot be put in circularly polarised mode. A square ring could be put in circularly polarised mode, should applications require it, for example by introducing nonplanarity (Bilger *et al.* 1990), itself another impossibility with a triangle. Another advantage of a square ring over the triangular ring is the considerable increase in the angle of incidence of the beams at the mirrors. This reduces backscatter, and helps to avoid frequency locking. Such matters are discussed in more detail in Bilger *et al.* (1993).

Partly to preserve the advantages sought from a simple open design with mechanical and thermal isolation for the mirrors, and partly on account of cost, no feedthroughs are installed at this stage in the corner boxes. Hence adequate alignment in angle and position has to be achieved before adding vacuum sealed covers to the corner boxes, pumping down, gas handling and initiating the lasing. The necessary precision has itself been the focus of some contention, with some respected workers (R. Rodloff, communication to the 16 March 1993 Conference on Geodesy at Wettzell, Bavaria, in discussion with H. Bilger) suggesting that arc second accuracy, and with this an extremely high cost (say $500000 per mirror) would be required. In this project we took the requirement to correspond to the tolerances on misalignment needed to provide stability according to the analysis of Bilger and Stedman (1987), which translate in our case (sides of ~ 1 m, curvature radii of ~ 6 m or ∞) to 20 arc sec in angle and 10-20 μm in position. Mirror holders were machined to locate the poles to this precision. External beams from a green and from a red helium-neon laser were overlaid to survey the ring and to assist in mirror alignment. The output interferometer was mounted on top of the glass cover for one corner box. These topics are covered in more detail in Section 6.1.2.

The vacuum and gas handling system of our ring laser is shown in Fig. (6.4).

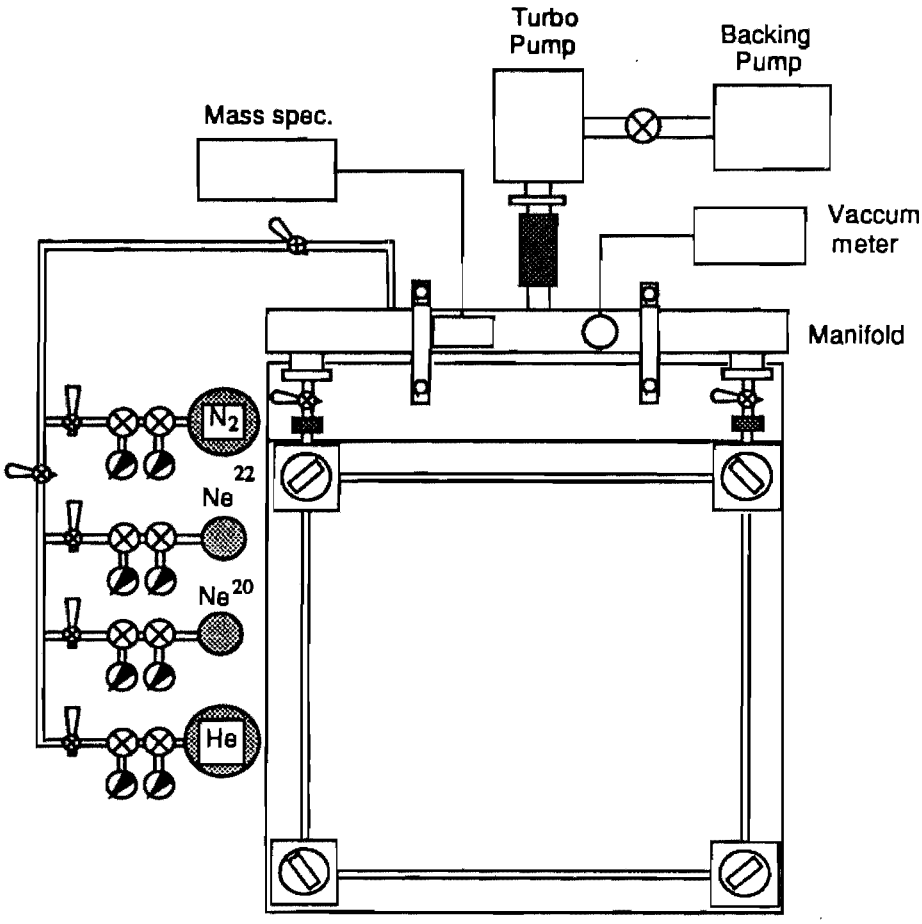

Fig. 6.4. Schematic diagram of the gas handling system and the manifold of the Canterbury ring laser

The helium, natural neon and (from March 1993) isotopically enriched neon gases were housed in separate cylinders. Zero grade helium gas was obtained from NZ Industrial Gases (Christchurch). Zero grade helium is specified as 99.995% pure and with contamination specifications: O: < 5 ppm, N: < 30 ppm, CO, CO_2, hydrocarbons: < 0.5 ppm each, H_2O: < 5 ppm; total: < 50 ppm. A cylinder of similar purity natural neon gas was obtained from the medical physics project at Canterbury. Isotopically enriched neon (70%) was obtained from Cambridge Isotope Laboratories, Woburn Mass. USA in a 1 l cylinder at a pressure of 34 atm. These were dispensed through pressure regulating valves into a system controlled by toggle valves so as to isolate a volume of each of these three gases which was appropriate for the required final partial pressure, ready for injection into a manifold and so the ring itself. The manifold consists of a cylindrical enclosure of

stainless steel, with side arms communicating with two adjacent corner boxes for double pumping action, and with the quadrupole mass spectrometer head, the turbopump system, the Barocel vacuum gauge and of course the gas input system. The manifold functioned as ballast for the ring gas and as attachment for a pressure transducer, vacuum pumps and leak detectors. The pressure transducer was a Barocel transducer (Datametrics, Wilmington Mass USA) Type 600AB, a capacitative pressure gauge set for the range 10^{-3} - 10 torr. Until August 1992 the leak detector comprised a rebuilt Leybold Heraeus AG leak detector Ultratest F incorporating a diffusion pump and a D8A roughing pump, which with much of our vacuum-related equipment was obtained from Duniway Stockroom, Mountain View, Calif., U S A. Oil from the diffusion pump proved to be one major source of contamination, alleviated but not removed by the insertion of cold traps in the connection to the manifold. In the period August-October 1992 this was replaced by a Leybold TMP150 Turbomolecular pump, with a D16 backing mechanical pump from Duniway Stockroom, and a SpectraMass DataQuad 100/DXS microprocessor controlled quadrupole mass spectrometer gas analysis system which also served as a leak detection system (from Christchurch Scientific Instruments Ltd.).

A piezoelectric transducer was obtained from Physics International Co., San Leandro, Calif., U S A, consisting of a stack of 10 prepoled ferroelectric disks, the stack having overall dimensions of diameter 0.75" and length 0.152" (3.86 mm), terminated with low carbon (1018) steel. with a tolerance of up to -200 V at 1 kHz and a resulting movement specified to be 1 μm but in practice rather less and somewhat nonlinear; its vacuum compatibility (chlorine outgassing, corona discharge) was a concern but seems not to be a problem.

The beat signal was monitored by a photomultiplier tube (Thorn EMI type 9214). The system is 7% efficient at 633 nm and has a high bandwidth; this was useful for a variety of reasons. It was possible to beat two adjacent longitudinal modes, thus obtaining the perimeter (3.4771 m) to relatively high accuracy. In normal practice the bandwidth was reduced first to 1 MHz in the final dynode circuitry, and then to the order of 1 kHz before digitisation. The output signal of the PMT was used in several ways (Fig. 6.5). For quick display and monitoring, the signal was displayed as either directly or as a Lissajou pattern (Fig. 6.6) (by beating with a local oscillator) on the Hitachi digital storage oscilloscope (Model V-522/5 from Hitachi Denshi Inc.) used for the work of Chapter 4. This old-fashioned and simple method is apparently novel in this connection. The diagnostic information provided by the Lissajou pattern was quite remarkably prolific, and was a substantial antidote to the unavailability of a state-of-the-art

spectrum analyser.

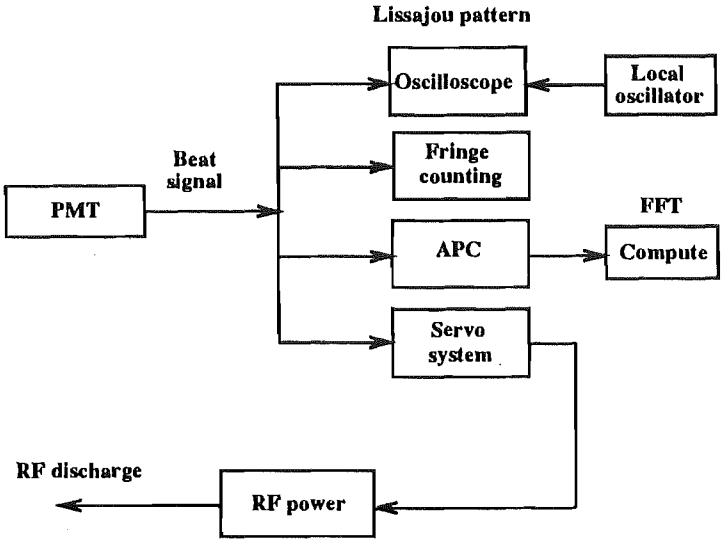

Fig. 6.5. Schematic diagram of the beat signal measurements and the servo system.

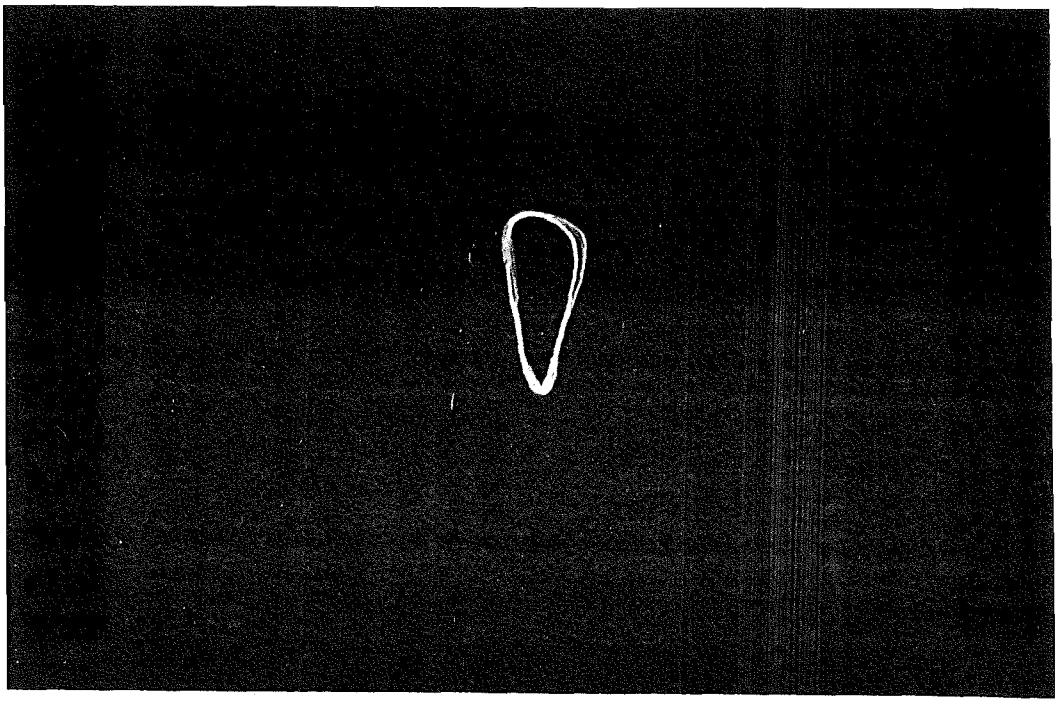

Fig. 6.6. A typical Lissajou pattern of the beat signal of the ring laser by beating with a local sine wave generator. Note that the beat signal is not sine wave owing to the backscattering and in turn the Lissajou pattern is not circle. The variation of the Lissajou pattern reveals the beat frequency change induced by the minute vibration of the ring cavity.

When the laser was operating in multimode state, the effect on the Lissajou pattern was one of extreme complication, and so conspicuous and characteristic. In this manner it was immediately apparent which adjustments of the cavity length (by addition of a piezoelectric transducer, or by adding weights to bend the Zerodur plate) or of the rf power gave combinations and conditions which favoured single mode operation, and at which points instability arose. If the ring were unlocked, very light finger pressure on the table would cause the pattern to rotate; under locking, the display would be insensitive to such mechanical rotation. The shape of the Lissajou pattern gave immediate information on the harmonic content of the signal; as shown in chapter 7, this is of great interest in connection with the frequency pulling. Drift or momentary instabilities in the beat frequency were readily obvious even at the sub-hertz level. And finally quantum (photon shot) noise regimes were also obvious through their effect in giving a jagged and randomly varying form to the Lissajou figure. Jumps of up to 10% (3 mm) in the radius (30 mm) of the Lissajou circle were then conspicuous. Even under apparently stable conditions, the pattern sometimes shows unexpected jumps; possibly due to microseisms, or possibly chaotically unstable behaviour of the laser, a topic which has been studied recently in some depth (McNamara *et al.* 1988, Zeghlache *et al.* 1988, Shelby *et al.* 1988, Chang *et al.* 1991, Merkle *et al.* 1991, Milovsky and Tkachyov 1993).

The signal was also fed to one of several A/D systems for recording and processing. One of these was essentially a frequency counter, geared for very long runs, but results given in this thesis used the Strobes Acquisition-PC system for the measurements of the beat frequency of the ring laser by FFT. This system, also marketed in USA as Rapid Systems #380, is a 14 bit 2-channel A/D converter with a PC package for display, Fourier transforming etc., and samples at 2 ms intervals or more, and for sample sizes of up to 16K (or 8K if FFTs are required). The Nuttall window (with 93 dB attenuation of side lobes) was incorporated in the package for optional use, and was employed in all the results reported here; a description of and compensation for its effects is given in Stedman and Bilger (1992). This performance data was fortuitously and remarkably compatible with our application; Nyquist frequencies of 250 Hz or even 100 Hz were tolerable for production of data whose interest often lay in the 0-75 Hz range, given the high signal/noise ratio of 40 dB or greater. In the higher precision runs, the data collection times for such samples were of the order of 16 s. Often shorter runs were taken, partly to use the system as a real-time poor-man's spectrum analyser (FFT processing was not done in the background but between runs, and on the XT or AT PCs employed took a similar time to the data collection and serial

transfer times) and partly to raise the sampling rate for closer study of the harmonics of the interferometric waveform. A related software package, CHARTPC, also originating from Strobes Engineering, Lower Hutt, New Zealand, uses the same A/D converter and is able to record 64K samples; its availability enabled us to take the longer data runs of 320 s.

A photograph of the ring laser itself is included in Fig. (6.7), at the site (8th floor of the Rutherford building) at which it was first assembled and operated. Further photographs (Figs. 6.8, 6.9) indicate the more recent setup in the Cashmere cavern, differing by the installation of an improved gas-handling and vacuum pumping system and also of external laser alignment systems.

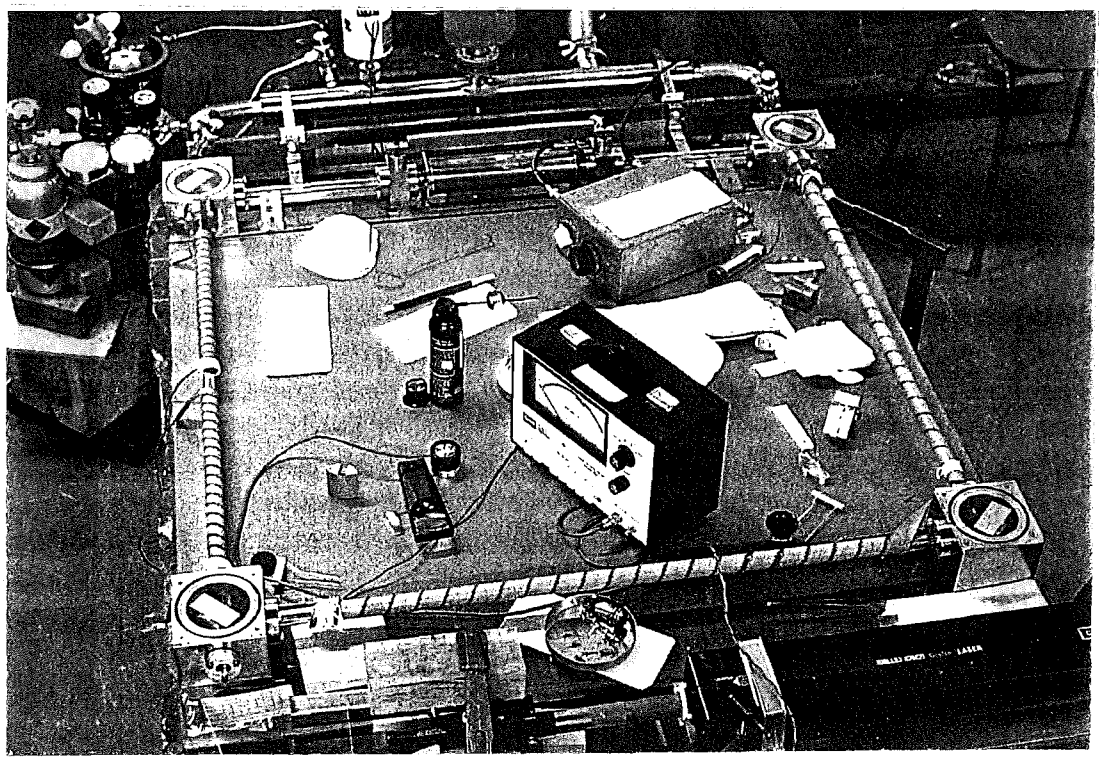

Fig. 6.7. The Canterbury ring laser at the site (8th floor of the Rutherford building). The RF excitation section is in the topmost leg, and the superinvar mirror mounts are visible through the glass lids of the corner boxes.

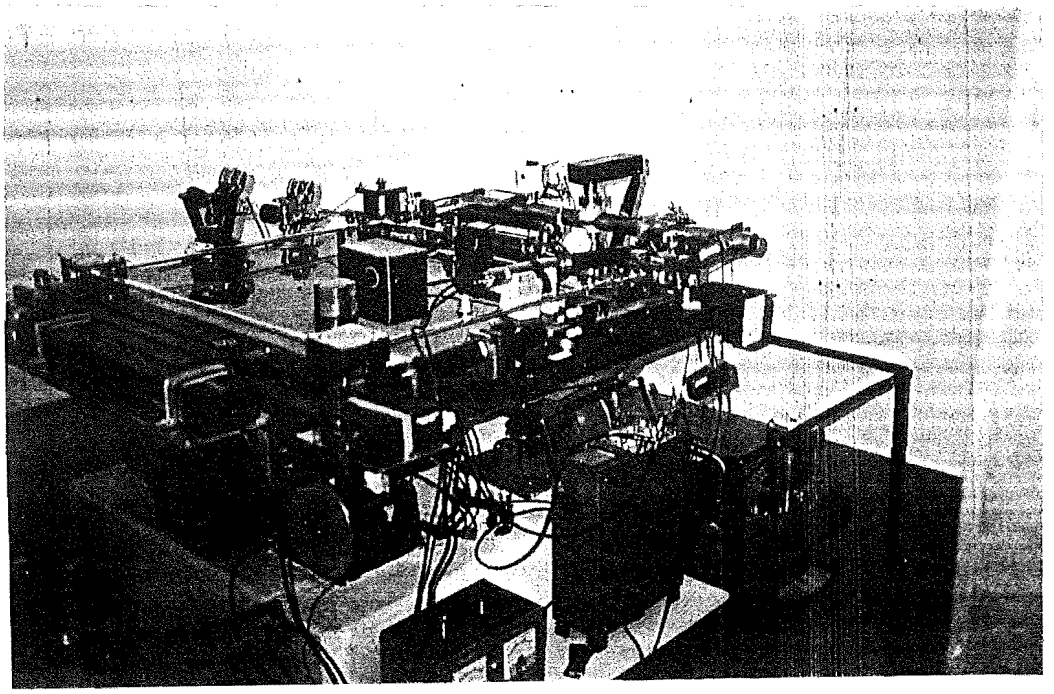

Fig. 6.8. The Canterbury ring laser installed in the Cashmere cavern.

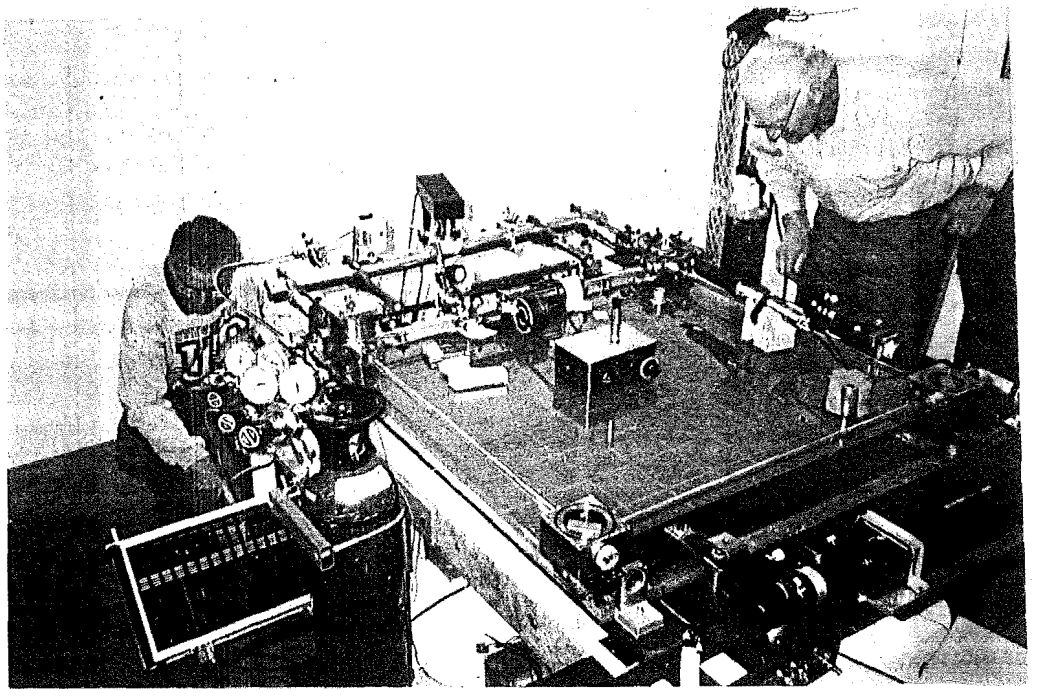

Fig. 6.9. The Canterbury ring laser under test in the cavern by Morrie Poulton (left) and Clive Rowe (right).

6.1.2 Alignment procedures

I mention at this stage several matters which while not on the main interest of this thesis are vital for an understanding of the design and operation of the ring laser and which occupied a considerable amount of time for myself as well as for the team during the preliminary phases of the project. Some of these aspects involve fairly basic and standard mechanical or optical procedures, or methods which have now proved obsolete, although for a novel application. Nevertheless, since this thesis is the first such document from the ring laser project per se, it seems appropriate to give at least a brief summary of a number of such matters. Some of the following material is culled from a variety of internal reports prepared by various members of the group.

On arrival at Canterbury I participated in several minor projects, for example the surface preparation of a 300 kg granite block which was being ground (eventually to an rms deviation of 14 μm). This is the base for the Zerodur plate on which the optical elements and stainless steel corner boxes rest.

At various stages of the project I contributed significantly to the development and implementation of adequate alignment procedures. It was necessary to establish alignment techniques which were sufficiently robust to cope with the required tolerances of 10 μm in position and 20 arc seconds in angle for mirror alignment, taking into account the severe limitations imposed by the lack of maneuverability of the mirrors once under vacuum. Such mirror position and angle adjustments have consistently been done by releasing the vacuum and reexposing the cavity to the ambient, manually adjusting the mirrors with whatever mechanical and optical surveying aids and cavity alignment tests are feasible, resealing the boxes, pumping down, refilling with helium and neon and testing for lasing.

In describing the alignment procedures, we note that the positions of the mirror poles were imposed by careful machining and positioning of the holders to 20 μm, and that the major work was connected with two variables for each mirror: its tilt from the vertical (the corresponding degree of freedom being a rotation about a horizontal axis through the pole) and its azimuthal angle (corresponding to rotation about a vertical axis). The aim was to define position, and then to adjust the tilt and then the azimuthal position of each mirror. As shown by Bilger and Stedman (1987), the first order effects of tilt and azimuthal adjustment are separable; tilt affects only the vertical component of the closure requirement and azimuthal only the horizontal component.

With the superinvar mirror holders used from May 1991 until May 1993, it proved possible (after considerable experience) to adjust the azimuth, or to rotate

a mirror about a vertical axis, using an external magnet to lift most of its weight and provide the necessary torque while gently tapping the Zerodur nearby, all while the system was still under vacuum. In this manner many alignment attempts were salvaged and further mirror surface contamination avoided. This has recently become more difficult with the replacement (for other reasons) of these superinvar holders by stainless steel holders. Since stainless steel is not magnetic, it was necessary first to add a piece of iron at the top of the holder as the magnetic component. While it proved possible to rotate the holder under consideration, it was found difficult to avoid moving the remaining mirror holders disastrously out of alignment at the same time.

The ring was rendered optically stable by choosing two mirrors to be flat, and two to have a curved profile of radius 6 m; this certainly satisfies the stability requirements of Bilger and Stedman (1987). The two flat mirrors are mounted diagonally opposite one another (in the southwest and northeast corners respectively), and one of these (SW) is used for the output mirror, since beam deviations are not a function of position.

First we consider the situation with the original superinvar holders (Fig. 6.10). These had been designed so that the rear, rather than the front, of the mirror was oriented against a reference surface carefully machined in the body of the holder.

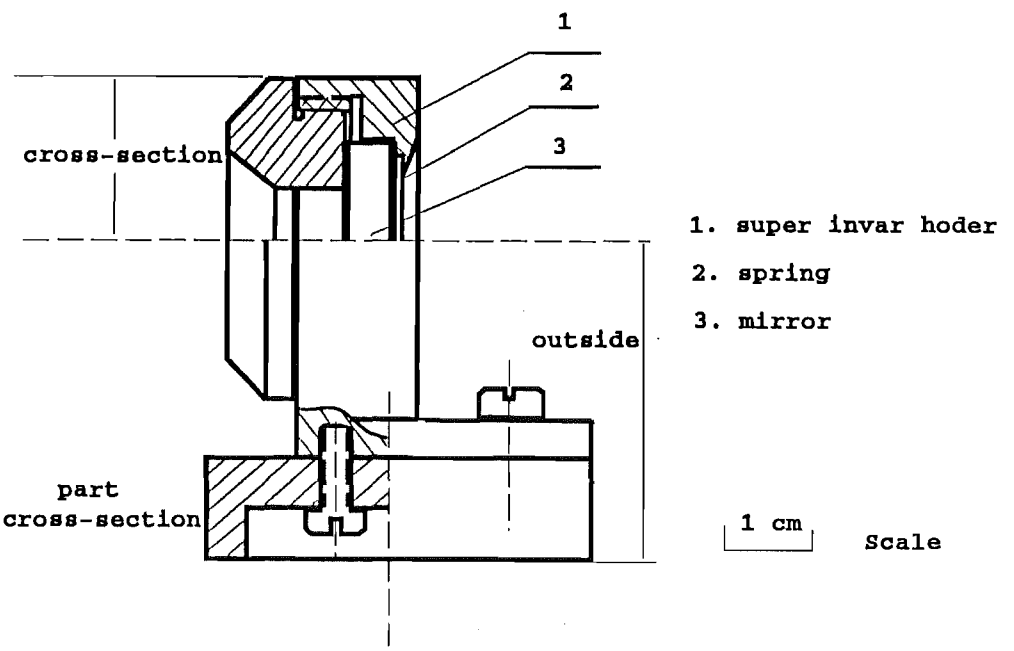

Fig. 6.10. Schematic diagram of the mirror holder for the Canterbury ring laser.

This was to allow a piezoelectric stack to be inserted at a later date between the mirror and the holder, with a spring loading on the edge of the front face of the supermirror allowing bodily movement of the mirror. However since the mirrors obtained were found to have a variable thickness or a wedged cross section, it became necessary to add shims at the back surface to compensate for this wedging. Furthermore, adjustment of the tilt required repositioning the shims. This was an extremely arduous task. We would repeatedly have to insert the mirror and holder in position in the ring, test the tilt of a mirror by checking the round trip closure of an injected survey beam, remove the holder and remove the mirror from the holder, reposition the shims and reassemble. This added hours (initially, days) to the alignment time for a ring, with consequent risk to the mirror surface cleanliness. It is mainly for this reason that these holders were recently replaced. To facilitate the alignment procedures, initially an external 633 nm HeNe (laboratory) laser beam was injected (with suitable beam matching) into the cavity, and fringing was sought for various mirror configurations: the linear laser, the L laser (three mirrors, the end ones being retroreflecting and the middle one having a 45° incidence angle), the U laser (one more intermediate mirror with a 45° incidence), and finally the ring or O laser. Some mirrors designed for 0° incidence were bought for this purpose. However, the red beam was difficult to inject, precisely because the mirrors were of high quality, and it was difficult to use this method alone. The last mirror for insertion would always be the one at the corner where injection was made. Especially in the later stages of this it became essential to use a well-matched beam from the stabilised laser to assist with the surveying, and to utilise the retroreflected beam to ensure alignment of the mirrors by adjusting their holders until the retroreflected beam was overlaid with the input beam in each of this variety of geometries. (After a few months' practice, experience with the intermediate shapes proved unnecessary.) Knife-edges mounted horizontally in machined holders were valuable for accurate (10-20 μm) monitoring of the parallelism of the beam with the Zerodur plate, and were used in all forms of the alignment technique. For both a completed ring and a retroreflecting situation, it proved useful to employ an iris consisting of a small (few mm diameter) hole in a piece of paper; upon repeated circuits of a survey beam, one could check with its aid and with fair accuracy whether the beam path was closed. If an injected red beam induced visible fringing at the mirrors, the ring was certainly sufficiently well aligned to lase. Much of the initial work was performed by and with Professor F.V. Kowalski while on sabbatical leave, especially with regard to his design and manufacture of a simple and effective beam recombiner at the output mirror, with myself and others also

assisting.

Later it became possible to purchase a green (543.5 nm) "GreNe" HeNe laser (from [formerly] Melles-Griot, San Marcus, Calif, U S A) which allowed much improved injection over a 633.0 nm beam for injection at such high-reflectance mirrors. (However, since the loss at each reflection was initially ~ 90%, it was very difficult though not impossible to see multiple circuits of the beam. With the recent change to new mirrors, the reflectance in green light was found to have increased to 25%, and multiple circuits as well as fringing in green light became somewhat easier to recognise.)

This acquisition lead to the development of several different alignment techniques. One is briefly described in Stedman *et al.* (1993) and is shown in Fig. (6.11). In this a green beam and a red beam were each injected but at diagonally opposite corners (NE and SW respectively; the beam recombiner works from the beams transmitted by the SW mirror, and the piezo is installed on the SE mirror).

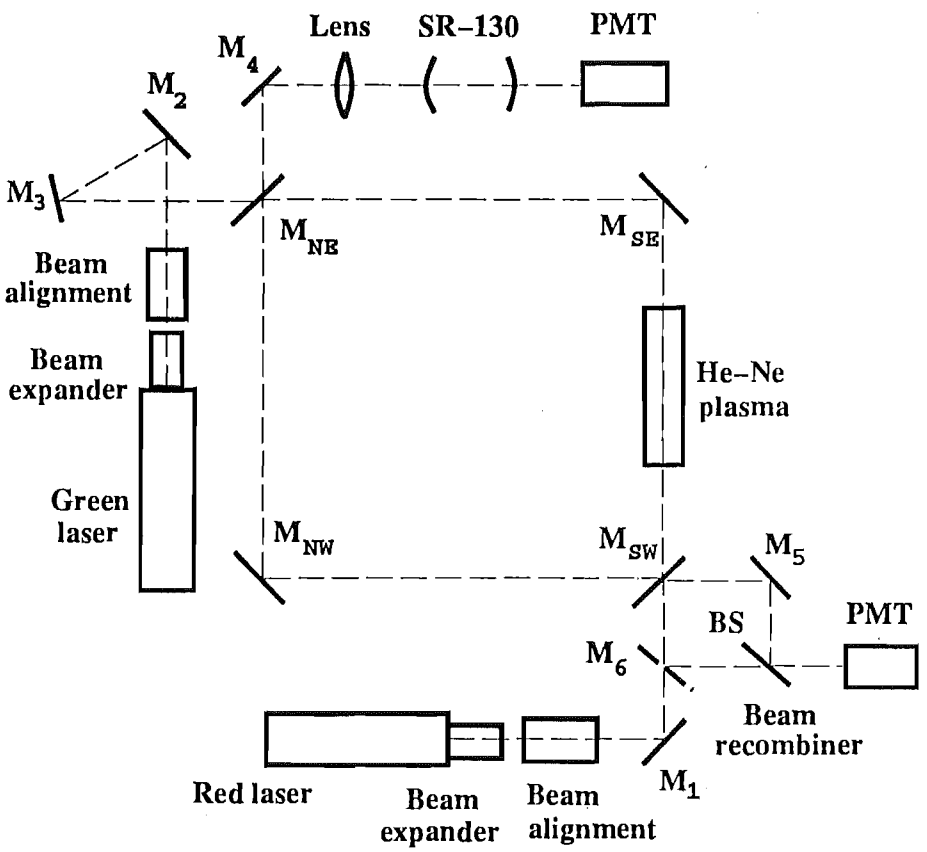

Fig. 6.11. Schematic diagram for the Canterbury ring laser alignment and detection system.

The green beam was injected at the NE (northeast) corner and travelling in the S (South) direction through the appropriate (NE) mirror, which was placed in approximately its final position. This beam was retroreflected off the SE mirror with knife edge tests to check the tilt of the mirror. In later stages this SE mirror was piezo-driven, and the most cumbersome to adjust; hence this test was made at an early stage. The SE mirror was then rotated by approximately 45° till the green beam, travelling W, emerged at the SW corner, where no mirror was placed and also where the red beam was injected in the opposing (E) direction. The red and green beams were independently surveyed with knife-edges to be aligned with the Zerodur on the S leg and by eye to be aligned with each other on the S and E legs. The red beam then was reflected off the NE (initial) mirror and surveyed by knife-edges into alignment on the N leg, so checking the tilt of the NE mirror. The tilt of the NW mirror was then checked by knife-edge and iris studies of a retroreflected beam in the N and E legs. The NW mirror was then rotated azimuthally, and the beam overlaid with the green and red beams at the position of the (still missing) SW mirror, adjusting tilts further as necessary. Finally the SW mirror was inserted (immediately blocking any effective use of the red beam). Its tilt was adjusted, with a check by retroreflection of the green beam and knife-edge tests on the S and E leg, and its azimuth being the final variable to initiate a closed circuit of the green beam around the ring.

At present the technique being followed initially uses a Hilger-Watt autocollimator calibrated by retroreflection off its own calibrated flat mirror lock to check the tilt of the two diagonally opposite flat mirrors (SW, NE), also the tilt of the NW mirror holder (which is sufficiently accessible, as opposed to the piezodriven SE mirror) for insertion of a test flat. (It is impossible to get clear images of the cross hairs and so use the autocollimator effectively on the curved mirrors, even though their radius of curvature - 6 m - is so large.) In the process it is clear that (as expected from a study of the elastic deformation of the Zerodur on the supports) there is a measurable curvature in the Zerodur plate itself, and (which is more significant) a tendency to cylindricality rather than sphericity of the surface with attendant errors of the order of 10 μm, which is tolerable for this purpose. The SW mirror is then inserted at the beginning of the exercise, dispensing with the red alignment laser beam; also the NE mirror, to allow for the refractive lateral displacement of 1.4 mm in the position of the E beam. (For much of the project, this had been "compensated" for by manufacturing spacers of this width for displacement of the knife-edges, but the complications associated with the curved face of the SE mirror have forced the reintroduction of the NE mirror at the start. The tilt and azimuth adjustments are then done by a

modification of the above using only the green beam.

The situation is complicated by the unavailability of antireflection-coated lenses throughout the injection optics, with multiple reflection patterns propagating round the ring, the need to devise strategies to deal with lateral shifts of alignment beams when a mirror was inserted at an intermediate stage, etc.

I also designed the present beam recombiner as shown in Fig. (6.12), an adaptation of the design of Professor Kowalski. The two beams transmitted by one a flat mirror are reflected by small mirrors of flat contour and elliptical shape (Edmonds Scientific) vertically through the plate glass sealing cover of that corner box, and then reflected a further 90^0 so as to combine at a half-silvered mirror. The various adjusters permit the orientation and overlaying of the output beams to the required precision of 0.3 mrad.

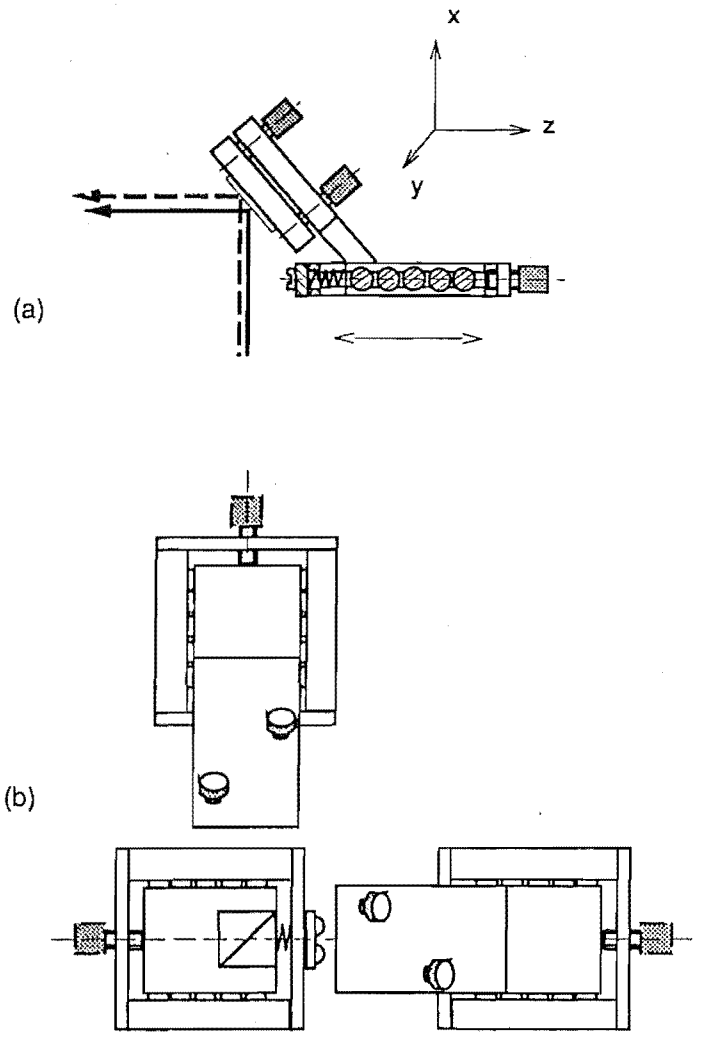

Fig. 6.12. Schematic diagram of the beam recombiner for beat frequency detection. (a) This diagram shows that the displacement in z axis can adjust the height of a reflected beam. (b) The configuration of the beam recombiner.

6.1.3 The advantages of the cavern

The ring laser was induced to operate, although for relatively short periods, in the Physics Department building. It is now installed 30 m underground in a cavern, whose floor has dimensions 23 m × 34 m and whose height is 5 m, under the Cashmere Hill of Christchurch. The concrete socket on which the ring laser is mounted is anchored by stainless steel rods into the volcanic basalt as shown in Fig. (6.13).

This cavern provides our ring laser with two unique advantages for high precision rotational sensing and for other applications. The first is high stability of the temperature for the ring laser long term operation.

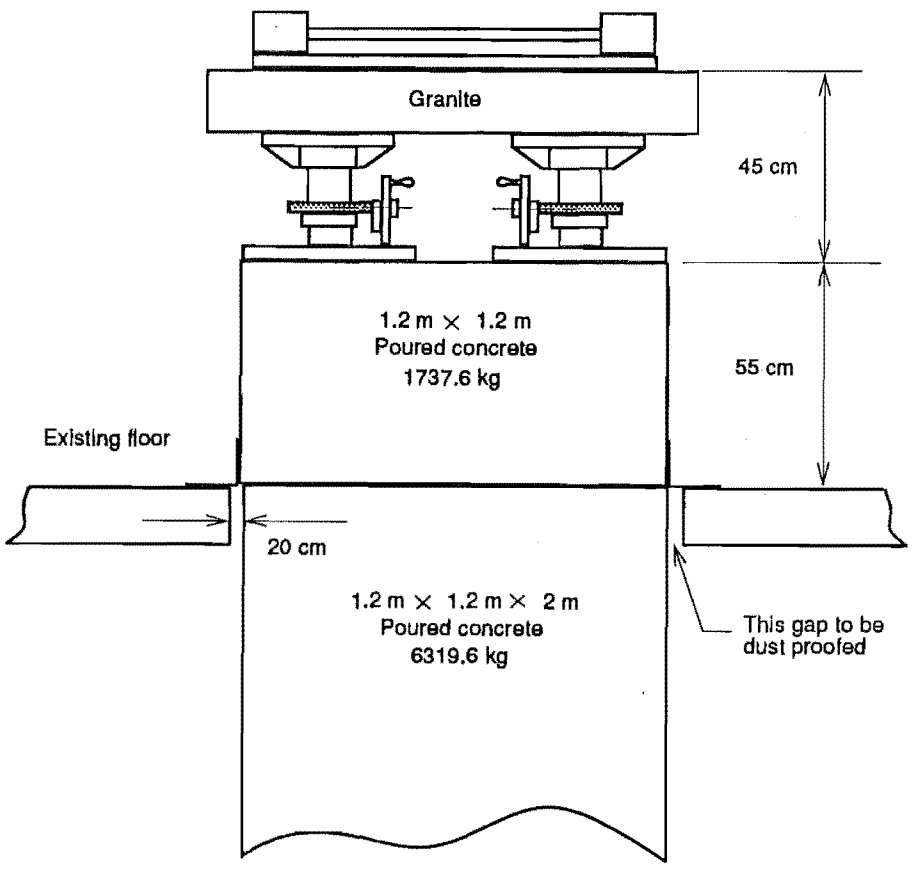

Fig. 6.13. Schematic diagram of the ring laser support installation.

The thermodynamics of the cavern has been investigated by the ring laser group (Rowe and Bilger 1992). By collecting ideas, calculations and measurements since February 1987, the nature and sources of temperature fluctuation have been qualitatively and quantitatively determined. The findings are, in short (Rowe and Bilger 1992):

1. Daily fluctuations are negligible in the cavern, if the leaks to the surface, (shaft, adits) are properly sealed.
2. Under the same conditions, seasonal variations are expected to produce a peak-to-peak temperature variation of about 1 mK.
3. Intracavern heat power sources - lights, dehumidifiers, electronics, humans, determine by and large the temperature fluctuations of the ring base and the cavern at large.
4. Changes of temperature (Fig. 6.14) at any point in the cave, including the ring base, appear on time scales of days and weeks, due to the rather small diffusion constants in the materials (concrete and basalt).

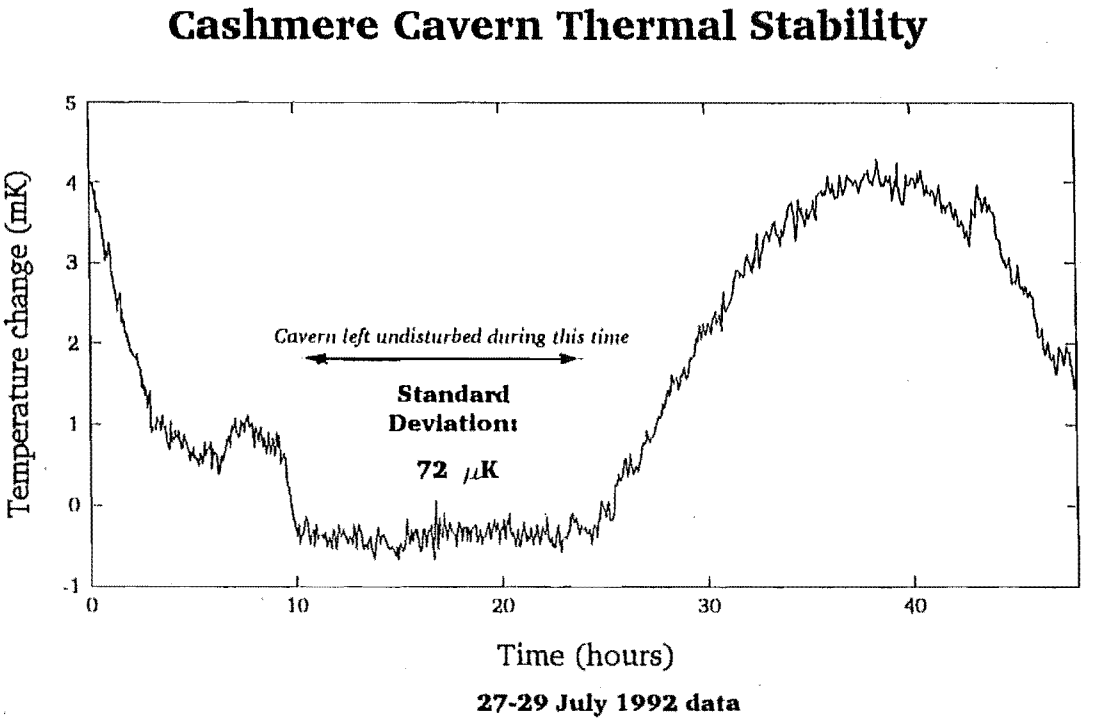

Fig. 6.14. Temperature change in the cavern.

For the Canterbury ring laser, the stability of the temperature in the cavern is very important to achieve a high precision (10 μHz or better) of the beat frequency of the laser for long term measurements. As we will discuss in chapter 8, the beat frequency of the ring laser is a function of the laser frequency detuning subject to the gain curve. For the stabilization of the beat frequency of the ring laser, the cavity length must be stabilized, which is partly achieved by using of Zerodur plate for supporting the mirrors. Given the thermal expansion coefficient of Zerodur as approximately 10^{-8} (see Section 6.1.1), and the cavity length of our ring laser is approximately 3.48 m, for stabilizing the cavity length within the 1/4 wavelength (1.58×10^{-7} m), which corresponds to a laser frequency shift from the centre of the gain curve to a position where the laser mode could be quenched and replaced by another longitudinal mode, the fluctuation of the temperature in the ring laser laboratory should be less than 50 mK.

The second advantage is that of a uniquely stable site for mechanical vibration. The ring laser is very sensitive to any mechanical vibration of the environment which may produce a tiny torsional motion in the ring laser cavity through the coupling of ring laser base. When the ring laser was located in the sixth floor in the Department of Physics, tiny mechanical vibrations, which were caused by the lift motion, walkers or wind, changed the instantaneous frequency randomly, and in turn broadened the spectrum width of the beat frequency of the ring laser. Fig. (6.15) is a typical waveform (the upper figure) of the beat signal with minute vibration of the ring cavity, recorded on the sixth floor of the Physics Department (Rutherford building). The FFT of the beat signal is shown in the lower figure of Fig. (6.15). Its features are fully discussed in Stedman and Bilger (1992). After installing the ring laser in the cavern, the problem of mechanical vibrations is essentially solved. Fig. (6.16) is a typical waveform of the beat signal of the ring laser in the cavern, the noise components can not be seen from this picture, since the ratio of the beat signal to the noise is about 60 dB. The spectral components include a signal at the mains frequency (50 Hz), possibly mechanically transmitted from transformers in the building, and the second harmonic of the beat frequency. This reflects a combination of effects, including frequency pulling, which is caused by the backscattering and will be discussed in Chapter 7.

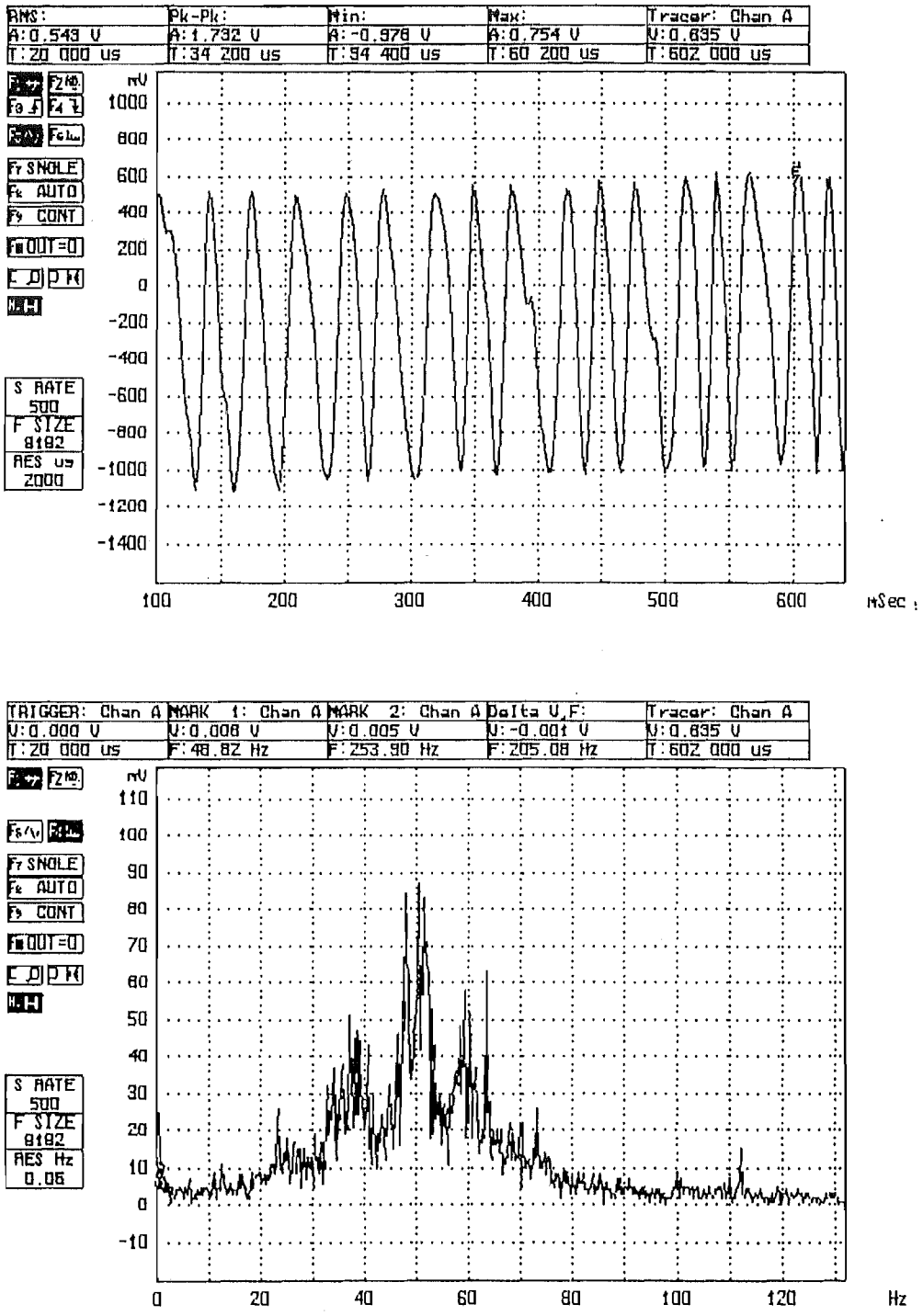

Fig. 6.15. The waveform of the beat signal with minute vibration of the ring laser associated with mechanical noise in the Rutherford building as shown in the upper figure and the corresponding FFT spectrum shown in the lower figure.

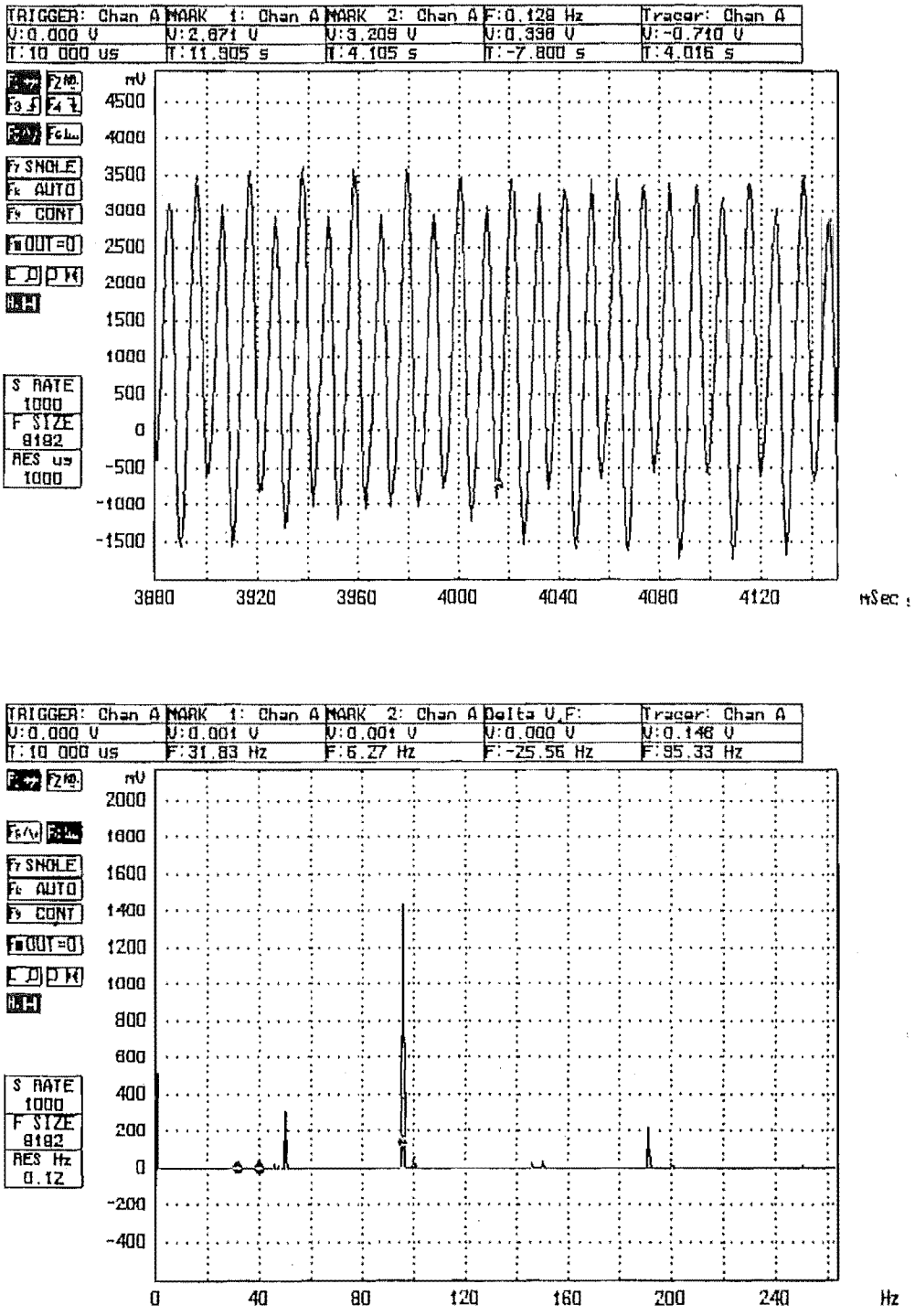

Fig. 6.16. The waveform and FFT spectrum of the beat signal of the ring laser after installing in the cavern.

6.1.4 Operation of the ring laser

The r.f. power is applied at up to approximately 15 W. A servo system is used to adjust the r.f. power in accord with the d.c. level of the PMT signal, lowering the power as the d.c. level is raised. The signal from the anode of the PMT is passed through a 0.22 μF capacitor to the Strobes Acquisition PC system; this capacitance with the input divider resistors gives a high-pass filtering action time constant of approximately 7 s. It is also fed through a 1.5 MΩ resistor to the positive input of an LF356 operational amplifier, this input also being connected to ground through a parallel combination of a 10 μF capacitor and a 1 MΩ resistor. The negative input is connected by a 470 Ω feedback resistor to the output and by another 470 Ω resistor to an adjustable reference voltage. The output is sent to a LED whose optical output is input to an LDR which controls the r.f. amplifier gain. This saves an immense amount of continuous adjustment. When for example room lights are on, adding to the d.c. signal from the PMT, the action is to reduce the r.f. power. As the gas purity degrades, the signal level falls and the r.f. power is automatically adjusted, preserving the stability of the lasing mode.

The backing pump for the turbopump is activated for extraction of the pumped gas. The SpectraMass quadrupole mass spectrometer can be used before or after the run, provided no charge of gas is present in the manifold; typically 4 × 1E-6 torr is achieved for the head pressure, and the major species of atoms/ions present have the following mass numbers A.

A = 1 corresponds to H, visibly dependent on r.f. power and so cracked by the r.f. discharge. A = 2 corresponds to H_2. A = 12 for C, also cracked by the r.f.; and A = 13 to CH. An important signal was A = 14 or N for air contamination, N being a serious inhibitor of lasing. A = 15 for CH_3, A = 16 for O, 17 for OH, 18 for H_2O represent common contaminants. The last three are often dominant; H_2O is adsorbed by our pyrex laser gas tubes connecting the corner boxes in the r.f. section rather than would be the case for quartz, and the use of heating tapes on these tubes has limited effectiveness. A = 20, 22 gives almost (there are other contributors) direct information on the ratio of the Ne isotopes. A = 28, 32 give molecular N_2, O_2, and A = 40 for Ar is a very useful indicator - if sizeable, an indicator of air leaks; if low, a reassurance.

The quadrupole mass spectrometer is totally turned off; without gas, the r.f. should give no more than a very faint blue glow plus glass fluorescence at most in r.f. region. If so, this glow gives sufficient ionisation for the discharge to light up without the use of an ionising gun. The turbopump is also shut off. The main valves on each (He, Ne) cylinder are opened and shut to admit gas to the feed

lines for the gas plumbing system, from which 40 or so fills of the laser are possible using the toggle valves. The He gas is admitted first, and if necessary the pressure (read off the Barocel) being brought to 2.0 torr by use of the turbopump. A recognisable blue-white-orange glow is an indicator of gas purity, and further checks for H_α, water, etc. with a hand spectroscope are useful. With admission of Ne, the plasma contracts and goes bright red-orange. If alignment is correct, the system may well lase directly at this stage. The overall pressure is usually set to 2.3 torr or even less. The PMT voltage should be limited to 900 V, and the coarse range of the PMT is set to 0.500 kV. Room lights generate a d.c. signal in the r.f. servo system and shut the laser down; as the EHT or room lights are increased, laser power decreases.

With the aid of the oscilloscope, the next requirement is that of unlocking the ring. A local oscillator is set to 70 Hz or so, and the beam path adjusted in a search for a suitable point on the mirrors and for the cavity mode in the gain curve, using a heavy (of order a few kilograms) weight or weights on the Zerodur (inducing elastic deformation) as a coarse control and jointly changing the voltage on the piezoelectric transducer as a fine control. With the servo system of the r.f. power, this when successful generates single mode oscillation and so a Lissajou pattern on the oscilloscope, whose diagnostic value has already been discussed. At the same time the loudspeaker should signal the earth's vitality. Further adjustment is made to maximise the fringe amplitude.

If the ring is unlocked, light finger pressure on the side of the table will immediately rotate the Lissajou pattern. Another black art is that of placing the tip of a screwdriver on the table and tapping it, often shocking the mirror alignment/plasma/laser system into a new mode; the Lissajou pattern may well collapse completely on trying this. All variables need tinkering to find a suitable region of stability.

On efficient lasing, the r.f. power should have fallen to a few watts, and from this point should look after itself via the servo system. If long-term pumping has been applied (of the order of months) since the last major disassembly of the ring, the laser can run for several hours without refill starting at 2.5 - 3 W, and finishing at 5-7 W. An annular magnet adjacent to the r.f. section helps in stabilising the discharge for the case of natural neon. The output power through the spare port for high-precision single mode behaviour is typically 23 nW, which can be increased to 200 nW if the EHT fine control was taken to its upper limit. Optical beam powers are measured via a Newport 820-SL-01 power meter whose lowest range has a scale 0-100 nW, using a 633 nm interference filter with a transmission factor of 2.5 (i.e. the 23 nW signal would be 91 nW without the

filter). If we take the mirror transmission to be T = 4 ppm and allow for the 8 ports at which this transmission takes place, the circulating power would then be 0.02 - 0.2 W.

As mentioned, the shape of the Lissajou pattern is a powerful diagnostic tool. Its rotation rate directly measures instantaneous frequency. With a 1:1 frequency ratio it can have a classical near-elliptic shape. Buckling around the pattern denotes harmonic structure. Sometimes the Lissajou pattern is obtained only when the system was on the point of breaking into multimode oscillation (a sudden complication as the frequency jumped by factors ~ 2-3, verified by changing the local oscillator frequency) and this was precursored by increasing harmonic structure over a fraction of a second.

In collecting data, it was usual to set the sample rate at 200, 500 and 1000 for a Nyquist frequency of 100, 250 and 500 Hz respectively. For an 8K (8192) sample size - the largest that will FFT within the Strobes APC package - the collection time T is 40.96, 16.384 or 8.192 s, respectively, and the corresponding bin resolution is 0.024414, 0.061035 and 0.12207 Hz respectively; so slower sample rates allow better frequency resolution. Faster sampling rates are less affected by drift, clear the alias problem and get more detail for the instantaneous frequency, e.g. for the effects of pulling. A sample size of 16384 is possible on time mode only. With one channel collection and 8K sample size we get an uncompressible binary DOS file *.SDT of about 17 Kb (two 8-bit bytes covering the 14 bits for each data point). The Chart program appears to store the corresponding data less efficiently (4 bytes per data point) taking 264Kb per 64K sample. In using the APC package, the choice of SAVE OPTIONS and FAST (or possibly AUTO with the number > 100), is recommended, followed by going to SAVE AS and give a header of up to 4 characters for the file series. Arming the system then enables the taking of data, which can be interrupted before but not during the transfer stage.

The Fourier transform is based on the integrals

$$\mathcal{V}(f) = \mathcal{F}[V(t)] = \int_{-\infty}^{\infty} V(t)\, e^{-2\pi i f t}\, dt \qquad (6.6a)$$

$$V(t) = \mathcal{F}^{-1}[\mathcal{V}(f)] = \int_{-\infty}^{\infty} \mathcal{V}(f) e^{2\pi i f t}\, df \qquad (6.6b)$$

The discrete transform used in the FFT (fast Fourier transform) takes a signal sampled at a rate of R_s samples/sec. For N points labelled by n, corresponding to a total sample time of $T_s = N/R_s$: $V_n = V(n/R_s)$ and has the form

$$\mathcal{V}_k = \sum_{n=0}^{N-1} V_n \, e^{-2\pi i n k/N} \tag{6.7}$$

Hence (comparing the exponentials) the bin index k of the FFT corresponds to a frequency f of the continuous transform given by $f = kR_s/N = k/T_s$; $k = T_s f$.

The Nyquist frequency Y (the maximum frequency f of the Fourier component in the discrete FFT transform) is $Y = R_s/2$ Hz; one can detect frequencies f without aliasing only when $f < R_s/2$, that is then they are sampled twice per cycle. We get a spectrum V_k ranging from 0 to the Nyquist frequency Y (that is, the bin range $k = 0$ to $N/2$). For a real signal the negative frequencies in the continuous spectrum give no new information ($\mathcal{V}(-f) = \mathcal{V}^*(f)$), and corresponding to this the above FFT algorithm throws up an exact reflection of this about the frequency Y in the range of Fourier frequencies from $R_s/2 = Y$ to R_s; this is suppressed in the Strobes and MATLAB displays and in the MATLAB FFT routines as written by Prof. Stedman. In addition the Strobes (and MATLAB, in general) screen displays show (and the Strobes FFT numbers give) only the absolute or power spectrum: the (real, positive) square modulus or absolute value of the Fourier coefficient V_k. Since the Strobes system input voltage is related to the intensity of the interferometer signal, the conversion to decibels should be using $5 \log_{10}(X)$ where X is the square modulus of the Fourier coefficient.

Aliasing is of special importance in determining the harmonic content of a signal, and (because of the expected harmonic performance) in obtaining confirmatory evidence for a signal and indeed increased accuracy in the measurement of its centroid frequency. If any frequency f is greater than Y, it will be aliased, i.e. replaced by a frequency in the Nyquist range 0 - Y Hz. The replacement amounts to alternate reflections in the upper (Y) and lower (0) ends of the range as many times as are necessary. If the signal is $\cos 2\pi fn/R$, and if $f = R - f'$ where $f' < Y$, then the signal is effectively replaced by one at the 'reflected' frequency $f' = R - f$ which is then the natural interpretation of the sampled signal. If $R < f < 3R/2$ we write $f = f'' + R$, giving f'' as the aliased frequency. In general when $f = (n + p)Y$, n is an integer and when $0 \leqslant p \leqslant 1$, for the cases where n is odd/even, the aliased frequency is

$$f_o = (n + 1)Y - f, \; n \text{ odd}; \quad f_e = f - nY, \quad n \text{ even} \tag{6.8}.$$

The odd and even aliases involve alternate reflection and translation; this is reflected in the sideband disposition. The FFT resolution r (bin spacing) is then

determined by having $\frac{1}{2}N$ points in $\frac{1}{2}R$ Hz, and so is given by $r = R/N$ Hz - the sampling rate divided by the number of samples. An alias-frequency computing routine is incorporated in our processing software, which has the capability of searching a plain text file of Fourier frequency coefficients for peaks and determining their properties. The present peak decision algorithm is to keep a running mean over the order of 1 Hz, look for a peak within an adjustable bin range, fit the peaks to a Gaussian and order and check for aliases of the strongest, also fitting the harmonics so detected to a geometric progression.

6.1.5 Noise limits on the ring laser

The fundamental limits of the resolution attainable with a ring laser are determined by quantum noise (Dorschner *et al.* 1980, Statz *et al.* 1985) and $1/f$ noise. The transition between these two noise sources is clearly evident in the earlier work of Bilger and Sayeh (1986), and when $1/f$ noise takes over, further time averaging does not improve the data. However, both of these are reduced by a factor of order $1/P^n$, where P is the perimeter and $n \sim$ 2-3 (Stedman *et al.* 1993), by using larger rings through the increasing finesse and decreasing solid angle in backscatter of the laser beams. When this is done, as in our present ring, $1/f$ noise is essentially eliminated in that the ultimate resolution is restricted by other considerations such as quantum noise or the drift in the beat frequency induced by variation of the operational characteristics of the laser plasma and/or beam geometry.

If we assume that such presently experienced beat frequency drifts can be solved by the thermal stabilization and servo systems of the cavity length, the resolution of the ring laser will be essentially limited by quantum noise. Even with drifts of the order of 0.3 Hz over the duration of a run (300 s say), it is possible to find relatively narrow lines in the Fourier spectrum of the beat frequency, corresponding to regions of relative stability within the drift, and to measure the widths of these lines to precisions of a few tens of microhertz. In this case also, it makes sense to study the fundamental limitations imposed on our resolving power by quantum noise as a very practical limit.

As already discussed in Section 2.1, with a measurement time of T, the contribution of quantum noise to the rms frequency fluctuation of the beat frequency is given by

$$\Delta f_{rms} = (1/\pi t_c)(h\nu/2P_{loss}T)^{1/2}, \tag{6.9}$$

where t_c is the ring cavity intensity decay time, h is Planck's constant and P_{loss} is the power loss of each laser mode. Eq. (6.9) shows that Δf_{rms} is inversely proportional to the cavity decay time t_c, which is proportional to the quality factor $Q = \omega t_c$, the finesse $F = (\Delta\nu_{FSR}/\nu)Q = 2\pi\Delta\nu_{FSR}t_c$ and inversely to the round trip losses $\Gamma = \tau/t_c = 1/(\Delta\nu_{FSR}t_c)$, where $\Delta\nu_{FSR}$ is the free spectral range and τ is the round trip time of the ring cavity.

Another important factor to be considered in the design is frequency pulling by backscattering, which we will discuss in chapter 8. The backscatter in the ring laser mainly is caused by the imperfection on the coatings of the mirror or on any intracavity surfaces.

6.1.6 Resolution of beat frequency measurement by FFT

The beat frequency of a ring laser is normally measured by counting the beat notes (Aronowitz 1971, Chow *et al.* 1985). As we mentioned, the fundamental limits on the resolution of the beat frequency measurement are determined by quantum noise. The fundamental limit imposed by quantum noise on the rms fluctuation of the count rate for the beat frequency signal is given by Eq. (6.9). For the case of the Canterbury ring laser with new mirrors (whose scattering etc. is that of their manufacture and not subsequent contamination), with the round trip losses of the cavity Γ = 60 ppm (total losses of the four mirrors), the power loss P_{loss} = 0.5 μW and t = 1 h, a frequency fluctuation of 15 μHz can be achieved. Other noise sources, principally $1/f$ noise, will be important at low frequencies. For the case just defined, $1/f$ noise will be negligible in the Canterbury ring laser. Indeed the noise apparent in the Strobes APC spectra obtained from the ring directly reflect all sources of noise, and in particular demonstrate the dominance of white noise in the spectrum as well as a reasonably conspicuous $1/f$ component under certain conditions.

Determining the expected level of quantum noise demands from Eq. (6.9) a knowledge of the cavity decay time t_c and the power loss P_{loss} in the ring. In order to determine these parameters several measurements are available to us. First, we have the possibility of measuring the cavity decay time directly by turning off the r.f. power and monitoring the output beam intensity. This yields figures of 15 μs upwards (Stedman *et al.* 1993). For new mirrors at their design specification, the power loss can be assumed in view of the relative unimportance of scattering at the mirror and in the gas to be determined by the transmitted power, which is also

measureable.

In a single run of length T, there is the possibility of additional noise arising from the finiteness of the sampling time. I note here that this has fundamentally different effects, depending on the method of data collection and analysis. If beat fringes are merely counted, as is standard practice in all commercial gyroscopes, there is a truncation error in determining the nearest integer N as a fringe count for the given observation time T. In sampling the waveform more often in the same time interval T and Fourier transforming, one may fit a Gaussian line to any spectral feature and determine its centroid more accurately; truncation error in the counting method translates into one frequency bin in the Fourier domain. While this error is not as fundamental as quantum noise etc. - it is readily overcome by taking more counts - and while beat counting methods have the same potential to measure quantum noise limits, it is worth mentioning that higher precision in the determination of a beat frequency is possible using the Fourier transform of a waveform than by fringe counting in a given time interval T. In this sense our (in this context) novel method of data analysis has a natural advantage. For simplicity of discussion, we assume that the Fourier transform $\mathcal{V}(f)$ of the beat signal $V(t)$ has a lineshape with Gaussian distribution

$$\mathcal{V}(f) = \frac{1}{(2\pi)^{1/2}\sigma} \exp\,[-(f-f_b)^2/2\sigma^2]. \tag{6.10}$$

We obtain the mean of this spectral distribution to be f_b and its rms fluctuation $\Delta f_{rms} = \sigma$. The FWHM of the spectrum, $f_{\frac{1}{2}}$, is then given by

$$f_{\frac{1}{2}} = 2(2\ln 2)^{\frac{1}{2}}\,\Delta f_{rms}. \tag{6.11}$$

6.2 Fourier analysis of the beat signal

6.2.1 An example

Fig. 6.17(a) shows a typical FFT spectrum of the beat signal with sample rate of 500/s and the Nyquist frequency of 250 Hz. The beat frequency is 72.99 Hz. Its second and third harmonics are at 146.0 and 219.0 Hz, respectively. We will explain the origin of these harmonics in Chapter 7. These frequency components are less than the Nyquist frequency and are not aliased. Fig. 6.17(b) shows the FFT spectrum with the aliasing. The sample rate is 200/s and Nyquist frequency is

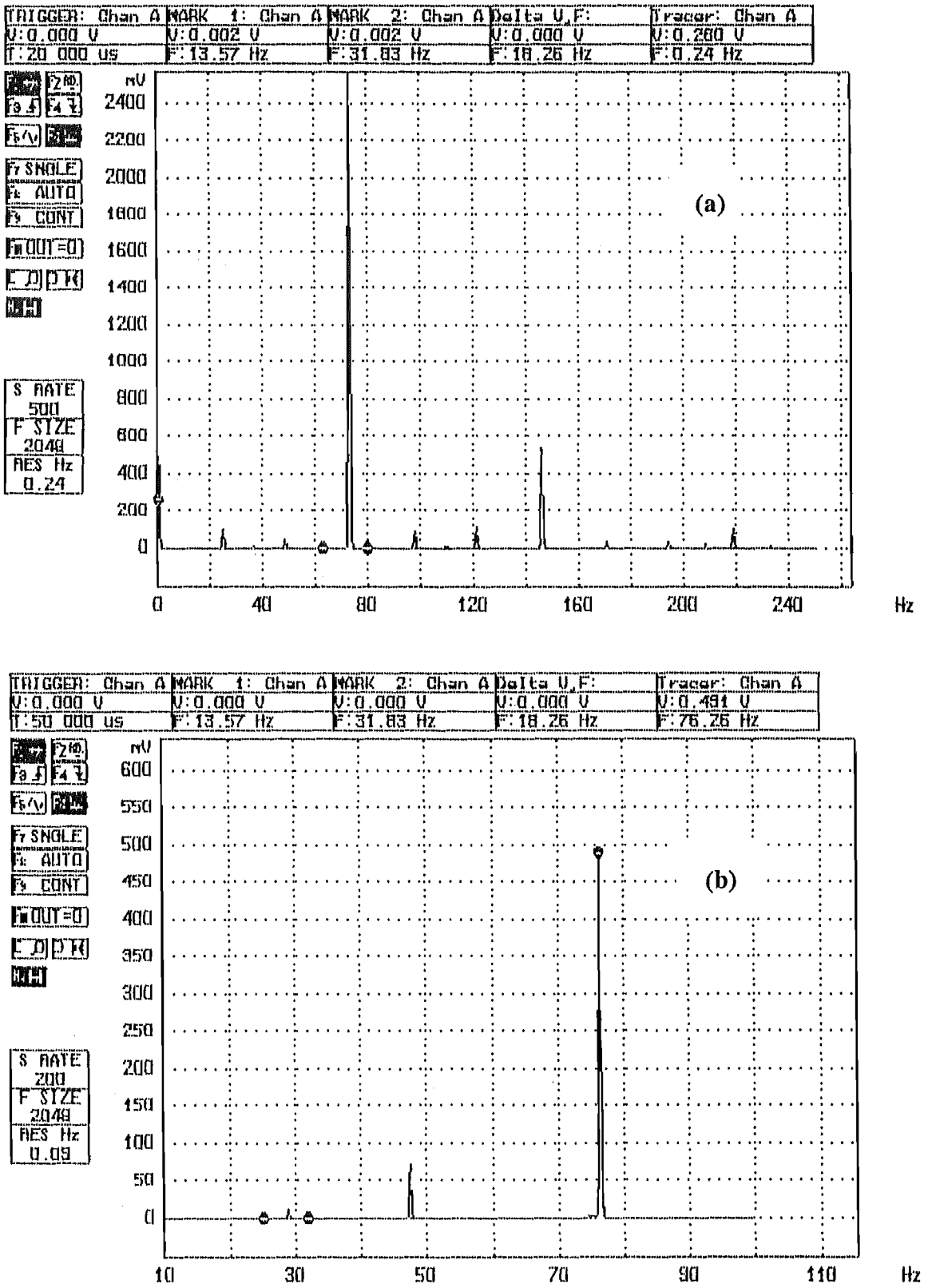

Fig. 6.17. (a) The FFT spectrum of the beat signal without aliasing. (b) The FFT spectrum of the beat signal, whose harmonics have been aliased.

then 100 Hz. The beat frequency is 76.26 Hz and its second and third harmonics should be 152.5 and 288.8 Hz, respectively if not aliased. Since the harmonic frequencies are larger then the Nyquist frequency, the aliased frequency for the second harmonic is 47.48 Hz. and the third aliased harmonic frequency is 28.78 Hz given by Eq. (6.8).

It is clear that the observed frequency is indeed principally the bias induced by earth rotation; as mentioned in Section 6.1, additional table motion by finger pressure is conspicuous in its effects and gives a direct confirmation of the sign of the signal as being appropriate for the Southern Hemisphere (a clockwise rotation increasing the beat frequency). However the departure of the observed magnitude of the signal frequency is many standard deviations removed from the naive estimate based on the Sagnac formula. Several factors are responsible for making the FFT spectrum complicated. The major factors are the frequency pulling induced by backscattering in the cavity, the frequency modulation of the beat frequency caused by the dithering of the ring and the bias and scale factor changes induced by the dispersion and saturation of the laser medium. We will deal with the frequency pulling problem in chapter 7 and the dispersion effects on the beat frequency in chapter 8, respectively, since they are very important for the precision measurements of the ring laser. Here we only introduce as much discussion of these topics as will permit an appreciation of the resolving power of the ring laser.

6.2.2 Sinusoidally dithered ring signal

In our experiment, the slightest mechanical vibration could produce a torsional motion to the ring cavity; it will be transmitted most readily at the resonant frequency ω_d of the granite table. This torsional motion is sometimes deliberately introduced to change the locking range, and in particular lower the lockin threshold, and is then called dithering. We use the term for brevity for any periodic modulation of the rotation rate.

Let us consider the beat frequency of the ring laser at the earth rotational rate Ω_E to be modulated at a frequency ω_d. The phase difference between the cw and ccw beams may be written as

$$\psi_{FM} = S\Omega_E t + (\alpha_d/\omega_d)\sin(\omega_d t) \tag{6.12}$$

where $S/2\pi$ is the scale factor (Section 5.2), and α_d, ω_d are the magnitude and angular frequency of the frequency modulation. The beat signal $V(t)$ is then

$$V(t) = \cos[S\Omega_E t + (\alpha_d/\omega_d)\sin(\omega_d t)]\} = R\{\ \mathrm{expi}[\Omega_E t + \alpha_d \sin(\omega_d t)]$$

$$= R\{\ \exp(\mathrm{i}S\Omega_E t) \sum_{m=-\infty}^{\infty} J_m(\alpha_d/\omega_d)\ \exp(m\mathrm{i}\omega_d t) \qquad (6.13)$$

On Fourier transforming,

$$\mathscr{V}(\omega) = \sum_{m=-\infty}^{\infty} J_m(\alpha_d/\omega_d) \int_{-\infty}^{\infty} \exp[\mathrm{i}(S\Omega_E + m\omega_d - \omega)t]\ \mathrm{d}t$$

$$= 2\pi \sum_{m=-\infty}^{\infty} J_m(\alpha_d/\omega_d)\ \delta(2\pi f + m\omega_d) \qquad (6.14)$$

where $f = S\Omega_E/2\pi$. This results tell us that with single frequency dithering there will be an infinite series of satellites above and below the earth line, separated precisely by $m\omega_d$, and with amplitudes controlled by the Bessel function.

Fig. (6.18) is a typical FFT spectrum of the beat signal with the ring cavity under dither. The beat frequency is 136.35 Hz and the dithering frequency is 10.9 Hz.

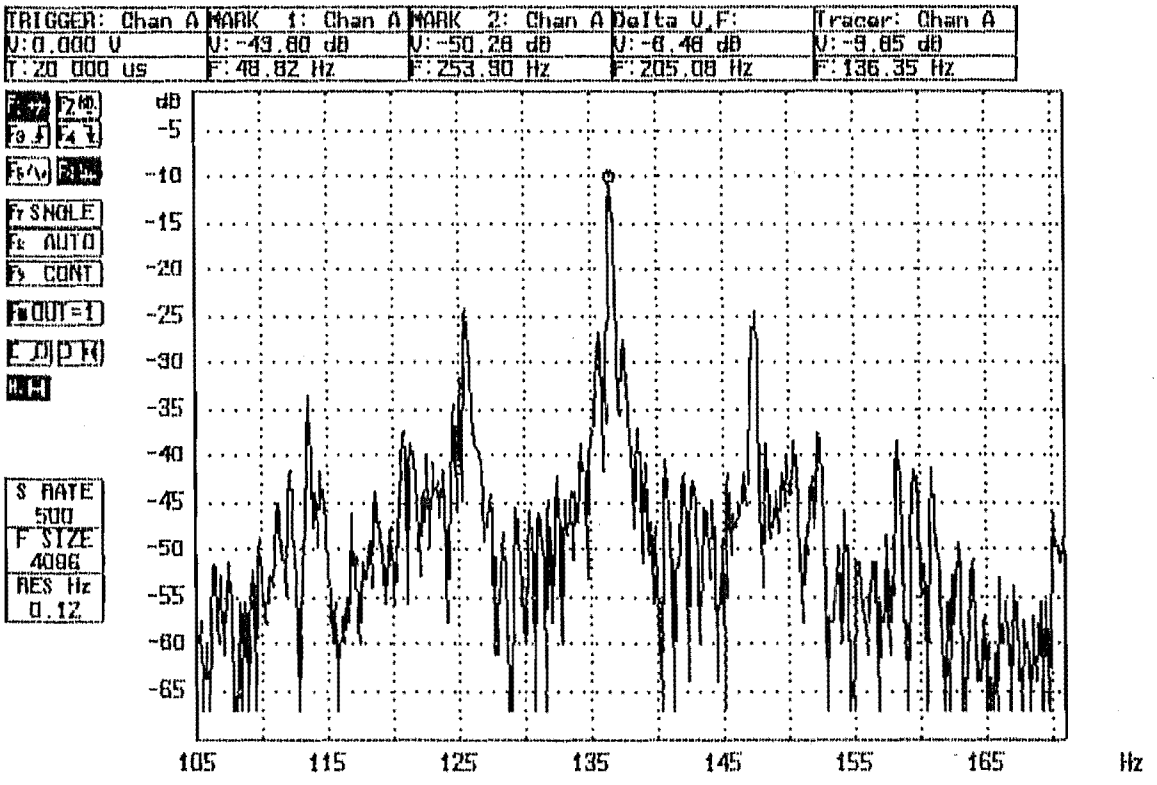

Fig. 6.18. The FFT spectrum of the beat signal with dithering of the ring cavity.

6.3 Experimental results

6.3.1 Mode structure of the ring laser

Since the gain curve for natural neon and enriched isotope neon mixtures are about 1.5 and 2 GHz respectively, several longitudinal modes could readily be excited, and of course the intermediate transverse modes. Following the strategy described in Section 6.1, it was attempted to starve out all modes but one by gain reduction. In practice, we were pleasantly surprised at the ease at which such gain control achieved single mode excitation of the ring. Typical RF powers for single mode excitation were 5-7 W, and output beam powers were then indeed of the order of 30 nW. For higher excitation power, say 30 W, output beam powers reached 2 μW, which corresponds (since the mirror transmission is 4 ppm) to a circulating power of 0.5 W. Although high circulating powers reduce quantum shot noise, the multimode rings give new branches in the beat-frequency-rotation-rate plot (Chow *et al.* 1985), which will be discussed in chapter 8. Mode structure was monitored with a Newport SR-130 Scanning Fabry-Perot.

6.3.2 Resolution limits on the beat frequency

The ring cavity decay time has been measured to be approximately t_c = 15 μs by monitoring lasing output as the radio frequency pumping is turned off, using a digital storage oscilloscope; this aspect of my work was reported in Stedman *et al.* (1993). The result translates into a quality factor $Q = \omega t_c = 4.5 \times 10^{10}$. The fractional power loss of one beam on one circuit of the ring cavity $\Gamma = 1/(\Delta\nu_{FSR}t_c)$; $1/\Delta\nu_{FSR} = P/c$ and is the time for one round trip and t_c is the power decay time ($\delta I/I\delta t = 1/t_c$, see Chapter 3). From these figures, Γ = 770 ppm, noticeably below the ideal value of 60 ppm or $4(1 - R)$ where R is the power reflectance at any mirror; the 4 arises because of the 4 mirrors in a round trip. The causes of this long-term contamination of mirror coatings are being identified, and within our limited budget we are working towards their elimination. initially the oil from the Leybold Hereaus leak detector diffusion pump and the performance of the Viton O-rings were serious suspects, and justifiably so; however the advent of a turbopump all but eliminates oil as a possible contaminant, and it is clear from the output of the quadrupole mass spectrometer

that impurities of all mass numbers are outgassing seriously the moment the ring cavity is sealed off. It appears that much more refined bakeout systems and clean-room mirror installation procedures are vital for further progress. A vacuum bakeout facility and a mini-clean room are being built at the present time.

Nevertheless the above results permit a very significant advance in the resolution of ring laser systems. In the above case we can calculate the rms frequency fluctuation Δf_{rms} of the beat signal by using Eq. (6.9). The power loss P_{loss} can be obtained by $P_{loss} = (\Gamma/T)P_{out}$, where T is the transmission of one mirror and P_{out} is the output power at that mirror. For our ring laser, with T = 4 ppm and P_{out} = 30 nW, we obtain P_{loss} = 5.8 μW, $\Delta f_{rms} = 3.48 \times 10^{-3}\ t^{-\frac{1}{2}}$ Hz and the FWHM of the beat frequency $f_{\frac{1}{2}} = 5.81 \times 10^{-3}\ t^{-\frac{1}{2}}$, where t is the measurement time. With a measurement time of 16.384 sec., we obtain an expected rms fluctuation of the beat frequency (Eq. 6.9) of Δf_{rms} = 0.860 mHz and the corresponding FWHM of a peak in the Fourier spectrum (Eq. 6.3) of $f_{\frac{1}{2}}$ = 1.43 mHz.

We have already reported some relevant experimental results (Bilger *et al.* 1993. Stedman *et al.* 1993 as Appendix 2 and 3 in this thesis). In summary, it was found that the FWHM of the beat frequency was 32.7 ± 1.7 mHz for the runs of 16.384 s duration. The line profile was fitted to a Gaussian and the position of the centre of the line obtained to a precision of 1.0 mHz; some complications in this analysis are described in the cited references, and it was valuable to include the corresponding determinations from higher harmonics to reduce the errors. Although the linewidth of the beat frequency in our preliminary experiment is about 30 times larger than the Δf_{rms}, the resolution of our measurement of line position is of the same order of magnitude as the quantum limit expect for the linewidth. In this sense, even these preliminary measurements show that frequency resolution at the quantum limit are possible.

The broadening of the beat frequency spectrum in our preliminary experiment is due to beat frequency drift during the measurement duration. The mechanism for this drift will be discussed in Chapters 7 and 8.

In more recent and unpublished experiments of December 1992-March 1993, the system is in the Cashmere cave and so more stable thermally. Data was taken for longer periods using the newly-acquired CHART-PC system. The Lissajou pattern was even used to monitor the instantaneous beat frequency and as a signal to the operator to compensate manually for drifts in the beat frequency by controlling the EHT voltage. With a measurement time of 320 s, in one run a Fourier spectrum was obtained (Fig. 6.19) in which a line position could be resolved to a precision of 11 μHz. In this case, using the same decay and loss

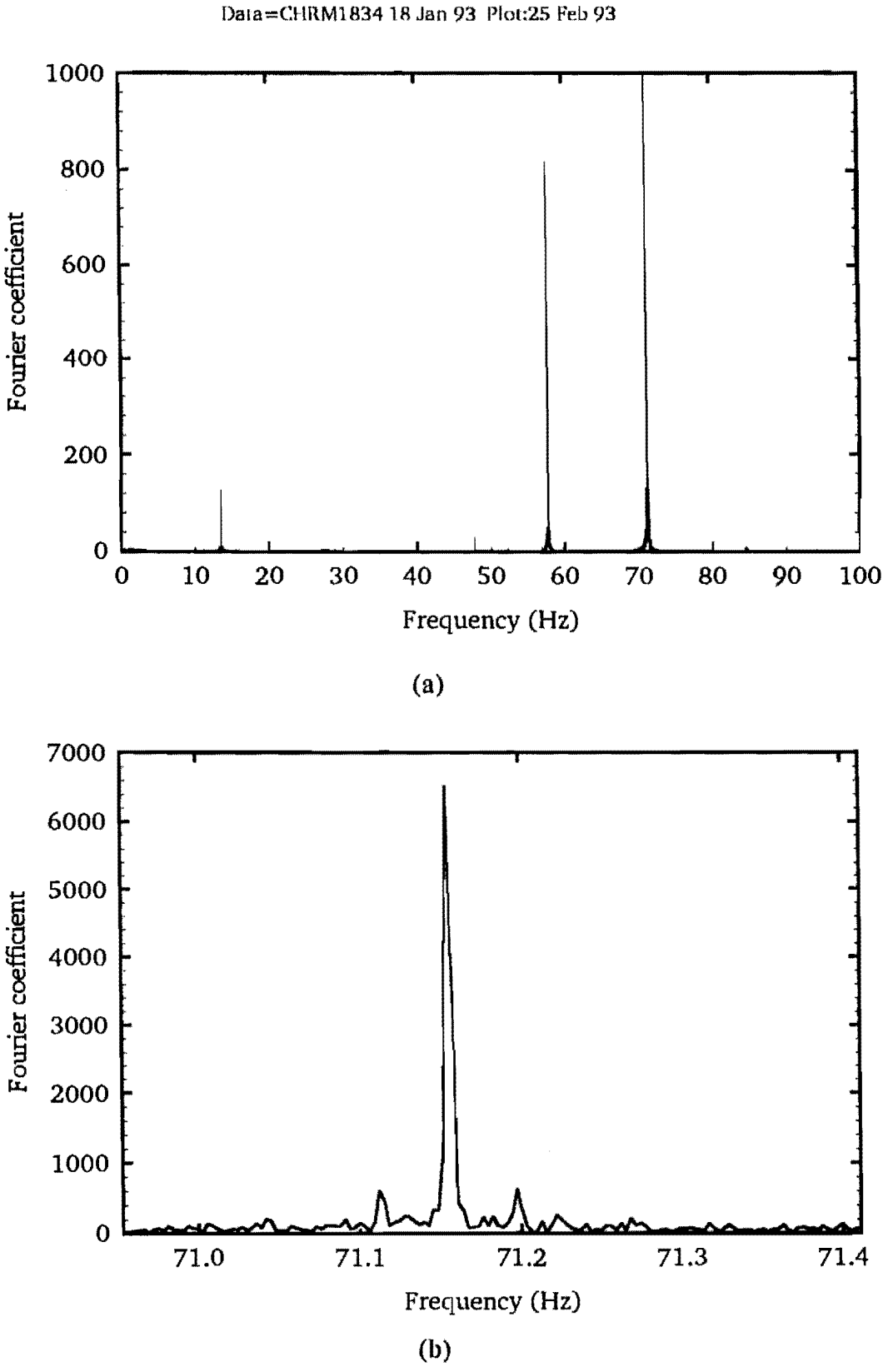

Fig. 6.19. (a) The FFT spectrum of the beat signal with a measurement time of 320 s. (b) An expanded view of the lineshape of the beat frequency signal.

parameters as before, the expected quantum limit on the line width from Eqs. (6.9) and (6.11) give Δf_{rms} = 200 μHz and $f_{\frac{1}{2}}$ = 330 μHz. This suggests that even the linewidth is much closer to the quantum limit for this situation. This is further experimental evidence that the Canterbury ring laser is operating at the quantum limit given by Eq. (6.9), and that only drifts of the beat frequency, principally those associated with outgassing and laser gas degradation, prevent our finding linewidths of this magnitude routinely.

The method we used for evaluation of the FFT line locations and width of a beat signal of a ring laser is presented by Stedman and Bilger (1992). In processing the FFT of a beat signal a Nuttall filter is used with an excellent sidelobe rejection (93 dB min.) and we assume the line shape of the beat frequency to be a Gaussian (Stedman and Bilger 1992). Therefore the line shape of FFT spectrum of the beat signal is the convolution of the Gaussian and the Nuttall window, whose Fourier transform is given by (Stedman and Bilger 1992)

$$W(x) = a\ \mathrm{sinc}(x)\left(1 + b\frac{x^2}{1 - x^2} + c\frac{x^2}{4 - x^2} + d\frac{x^2}{9 - x^2}\right), \tag{6.15}$$

where $x = fT$, a = 0.355768, b = 1.369983, c = -0.405410 and d = 0.0354276. By numerical calculation of the deconvolution, we obtain that the linewidth of the beat frequency (Fig. 6.16) is 1.087 mHz, which is about 3 times bigger than the quantum limit ($f_{\frac{1}{2}}$ = 330 μHz) at present status of the Canterbury ring laser.

Chapter 7

Frequency Pulling in Ring Lasers

In 1865 Christiaan Huygens, while confined to bed with an illness, noticed that the pendula of two clocks in his room invariably locked into synchronism if the clocks were hung close to each other, but became free-running when hung further apart. He eventually traced the coupling mechanism to mechanical vibrations transmitted through the wall, thus providing one of the first observations of the coupling of two oscillators by injection locking. Injecting a weak signal into a more powerful free-running oscillator can produce an interesting and useful set of injection locking effects, not only in clocks, but also in lasers and almost any other kind of self-sustained periodic oscillator. These injection-locking effects, besides having important practical applications, provide an excellent illustration both of laser theory and of the fundamental principles of oscillator dynamics. The frequency locking or pulling caused by the backscattering of the mirror imperfections in the ring laser is a most important problem that has to be overcome in order to have a high precision rotation sensor.

We will briefly introduce the effects of the backscattering in ring lasers in Sec. 7.1. A theoretical analysis of the frequency locking or pulling in the ring laser is presented in Sec. 7.2. Methods of avoiding the frequency locking problem in a planar ring laser are described in Sec. 7.3. Finally, we present a novel method of determining the frequency pulling in the ring laser in Sec. 7.4.

7.1 Effects of backscattering

The effects of backscattering in ring lasers have attracted a great deal of interest

during the past two decades and still are under active study. Backscattering in the ring laser means that, due to imperfections in the optical path, a small fraction of the wave is scattered back in the direction of the oppositely travelling wave. A scattering event itself might be expected to be more or less uniform in a solid angle of about 4π steradians; more accurately, one might expect a Lambert's law dependence, which incidentally cancels right angle scattering and so favours a square rather than a triangular ring laser. In any case, only the light which falls into the solid angle of the counter-rotating beam contributes to coupling the two waves. The resulting coupling coefficient is usually very small, yet it becomes a dominant effect on the ring laser at low rotation rates.

Generally, backscattering can give rise to frequency locking or pulling phenomena in ring lasers (Aronowitz and Collins 1966, 1970, Aronowitz 1971, Aronowitz and Lim 1977). Backscattering can also modify the intensity correlations of the counterpropagating beams (Christian and Mandel 1986, 1988; Pesquera 1989) and can cause in particular oscillatory instabilities or intensity oscillations (Aronowitz 1972, Kuhlke 1982, Christian *et al.* 1988, Chyba 1989).

The first observation of frequency locking in ring lasers is given by Macek *et al.* in 1963 (Aronowitz 1966). When the rotation rate of a ring laser cavity is reduced below some critical value (so-called frequency locking threshold), the frequency difference between the oppositely directed travelling waves vanishes. Thus, for rotation rates below the lock-in threshold, the laser is not responsive to rotations.

Aronowitz (1966) first presented a model for analyzing the frequency locking in ring lasers. He assumed that the frequency locking in a ring laser is caused by the scattering of laser beams from one mode into the other. This mechanism reminds one of locking of an oscillator on to an externally injected signal which has been described in an important paper by Adler (1946). Unfortunately, the Adler formalism does not straightforwardly apply to the locking of two interacting oscillators. In the Adler formalism, the phase of the injected signal is prespecified and it determines the phase of the locked oscillator. The frequency locking of two free-running oscillators to each other is more complicated. Neither of the two phases is prespecified. The final phase relationship between the two oscillators is established self-consistently from the equations describing the mutual phase pulling.

Backscattering in a ring laser is predominantly caused by imperfections of the dielectric mirrors (Thomas 1978); in our application (Chapter 6, 7) contamination of the surface is an important contribution. Haus *et al.* (1985) further defines two kinds of mode-to-mode scattering: conservative and

nonconconservative. Their choice of the word "conservative" is to be understood rather narrowly. If the amount of energy added per unit time to oscillator 1 is equal in magnitude, but opposite in sign, to the energy given to oscillator 2, then this coupling energy is called conservative. Conservative scattering of the mirrors leads to no locking, to a high degree of approximation. Examples of conservative scatterers are nonabsorbent particles, small compared to a wavelength, and loss-free objects of larger size that represent only a weak perturbation of the dielectric constant in the cavity. The presence of two types of scattering makes it impossible, in general, to calculate the frequency locking threshold of a ring laser from measured scattering intensities from optical components such as mirrors.

A similar conclusion is also given by Christian and Mandel (1986). They have studied the coupled third equations of motion of the ring laser with spontaneous emission noise in the presence of detuning and backscattering. The steady-state solution is shown to depend on scattering only through the sum $R_1+R_2^*$, where R_1, R_2 are complex backscattering coefficients and R_2^* is the conjugate of R_2. The important conclusion they obtained is that when the sum $R_1 + R_2^* = 0$, then the steady-state time-independent solution of the laser-field equation is the same as if backscattering were completely absent. Christian and Mandel (1988) have measured the intensity fluctuations and the intensity cross correlation between the two counterpropagating modes as the pump parameter and the phase of the backscattering are varied. The experimental results confirmed their prediction above.

Christian *et al.* (1988) observed random phase jumps of $\pm\pi$ in the phase difference between the two counterpropagating modes of a ring laser whenever the complex backscattering coefficients R_1 and R_2 satisfy the condition $R_1 + R_2^* = 0$. Similar discussions about the phase and frequency jumps and intensity instabilities in ring lasers were also given by Hoffer *et al.* (1988), Pesquera and Blanco (1989), Abraham and Weiss (1988), Pesqera et al (1989), Chyba (1990) and Cheng (1991).

The ring laser facility at University of Canterbury is designed to extend the horizons of experimental and theoretical work on ring lasers for a variety of fundamental measurements in relativity and in quantum mechanics. The resolution of our ring laser has reached 11 μHz. In order to achieve a precision of the beat frequency at the same order in magnitude, the frequency pulling effects on the beat frequency, caused by the backscattering in a ring laser, is clearly a very important problem that has to be overcome.

7.2 Initial theoretical analysis

The problem of frequency locking caused by backscattering in ring lasers has been theoretically studied by a number of authors. Before the discovery of the frequency locking in the ring laser, Aronowitz (1963) presented a formal treatment of a ring laser, by applying Lamb's theory to the ring laser, in which an assumed electromagnetic field in a rotating cavity, obeying Maxwell's equations, nonlinearly polarizes the moving gaseous atoms. The interaction is treated quantum mechanically in the frame of the moving atom. The resultant polarization, statistically summed over all velocity ensembles, is used as a source term in Maxwell's equations to calculate a reaction field. Self-consistency gives a set of equations which determine the amplitudes of oscillation of the modes of the independent oppositely directed travelling waves in term of parameters of the system. This theory did not predict the experimentally observed frequency locking in the ring laser.

Aronowitz (1966) extended the model of the ring laser to include a coupling between CW and CCW waves in the form of a mutual backscattering of energy from each beam into the direction of the other. Self-consistent equations are obtained by introducing a fictitious backscattering conductivity and treating the effects of backscattering as a source term in Maxwell's equations. These equations and their alternative forms have been used in most later literature about ring lasers (Aronowitz 1971, 1972a, 1972b, 1974; Christian and Mandel 1986, 1988; Christian *et al.* 1988, Abraham and Weiss 1988, Pesquera and Blanco 1989, Pesqera *et al.* 1989, Chyba 1990, Cheng 1991).

On the other hand, Siegman (1986) presented a phasor analysis for the injection locking of a laser oscillator, where a very weak or low-power external signal is injected into this laser oscillator via some suitable coupling method, at a frequency which is close to but not exactly coincident with the free-running oscillation frequency of the laser. The advantage of this model is that the injection-locking behavior of a laser cavity with an external signal can perhaps best be understood from this simple phasor analysis.

In Siegman's formalism, the phase of the injected signal is prespecified and it determines the phase of the locked oscillator. However, the locking of two free-running oscillators to each other is more complicated. Neither of the two oscillators is established self-consistently from the equations describing the mutual phase pulling. Therefore Siegman's formalism does not straightforwardly apply to locking of two interacting oscillators.

In the following analysis, we intend to give a clear physical interpretation of the frequency locking and pulling in a ring laser when there is a backscattering in the cavity, by applying the phasor model to ring lasers. In this Section, we give the

general equations for the laser system and then confine attention to a particular and often-used set of approximations which justify a complete analogy with Adler pulling. This shows all the results at least qualitatively. Its inadequacies will be discussed in Section 7.4, and then to some extent remedied.

7.2.1 Fundamental Equations

We assume that the laser field amplitude will be quasi-sinusoidal quantity, with slowly varying amplitude and phase referenced to some carrier frequency ω, which can be writen in the form $E(t) = \frac{1}{2}[\tilde{E}(t)e^{j\omega t} + c.c]$. The frequency-locking behaviour of a ring laser with backscattering can be understood from a simple phasor picture such as that shown in Fig. (7.1). As shown in this model, let $\tilde{E}_1(t)$ and $\tilde{E}_2(t)$ be the complex phasor amplitudes of the CW and CCW waves travelling around the cavity, respectively. For each of them the real field $\mathscr{E}_i$ = Re$[E_i(t)\exp(i\omega_i t)]$, where i = 1, 2. Let $\tilde{E}_{12}$ be the phasor amplitudes of a backscattering coupling from $\tilde{E}_1$ into $\tilde{E}_2$, and $\tilde{E}_{21}$ be the amplitude of the backscattering coupling from $\tilde{E}_2$ into $\tilde{E}_1$.

These waves must satisfy two separate physical conditions. First, at every instant of time these complex phasor amplitudes must by definition satisfy the condition that $\tilde{E}_i(t) \equiv \tilde{E}_{ri}(t) + \tilde{E}_{ji}$, where j = 1, 2. The second is that the reflected phasor amplitude $\tilde{E}_{ri}(t)$ at any time t is derived from the total

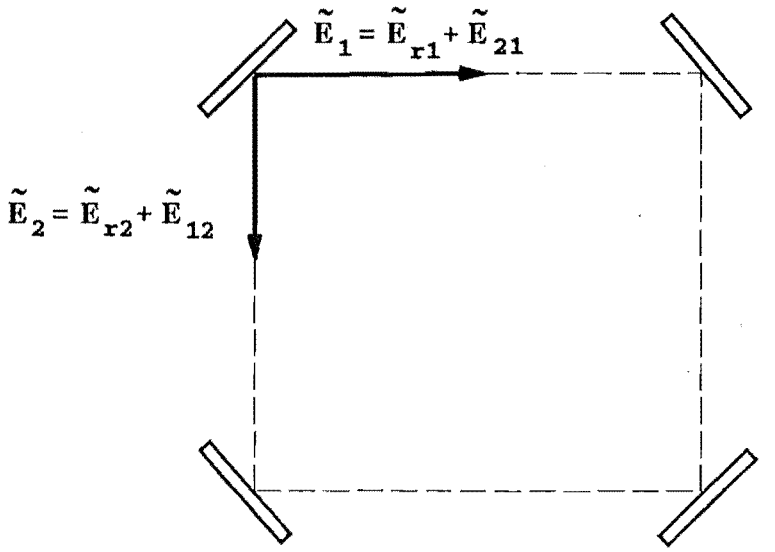

Fig. 7.1. Analytical model for frequency pulling of ring laser.

circulating field $\tilde{E}_i(t-\tau)$ which left that same plane one transit time τ earlier multiplied by the net gain, loss and phase shift for one round trip inside the ring cavity. In detail, we assume that $\tilde{E}_{ri}(t) = \tilde{E}_i(t-\tau)\exp[\delta_{mi}-\delta_{ci}-i\tau(\omega_i-\omega_0)]$. Therefore, at every instant of time t these complex phasor amplitudes should satisfy the condition that

$$\tilde{E}_1(t) = \tilde{E}_1(t-\tau)\exp(\delta_{m1}-\delta_{c1}+i\tau\Delta\omega_1)+\tilde{E}_{21} \tag{7.1a}$$

$$\tilde{E}_2(t) = \tilde{E}_2(t-\tau)\exp(\delta_{m1}-\delta_{c1}+i\tau\Delta\omega_2)+\tilde{E}_{12} \tag{7.1b}$$

where δ_m and δ_c are the round trip gain and losses in the ring lasers, respectively, τ is the round trip time, $\Delta\omega_1 = \omega_1 - \omega_0$ and $\Delta\omega_2 = \omega_2 - \omega_0$. Equation (7.1) is strictly true only if the gain and loss factors δ_m and δ_c do not change during one round-trip time τ. However even in a rapidly changing situation Equations (7.1) will be approximately valid if average values of δ_m and δ_c are used.

The phasor model given by Eqs. (7.1) can be readily converted into an approximate but generally adequate set of differential equations. In this section we ignore saturation effects and suppose that the net round-trip gain is very small: $|\delta_m - \delta_c + i\tau\Delta\omega| \ll 1$ (this restriction will be removed in Section 7.4.4). This allows an approximation (Siegman 1986): $\tilde{E}_1(t) \simeq (1+\delta_{m1}-\delta_{c1}+i\tau\Delta\omega_1)\tilde{E}_1(t) - \tau d\tilde{E}_1(t)/dt + \tilde{E}_{21}$ and $\tilde{E}_2(t) \simeq (1+\delta_{m2}-\delta_{c2}+i\tau\Delta\omega_2)\tilde{E}_2(t) - \tau d\tilde{E}_2(t)/dt + \tilde{E}_{12}$. Then Eqs. (7.1) converts to

$$d\tilde{E}_1(t)/dt + [(\delta_{c1}-\delta_{m1})/\tau - i\Delta\omega_1]\,\tilde{E}_1(t) = \tilde{E}_{21}/\tau, \tag{7.2a}$$

$$d\tilde{E}_2(t)/dt + [(\delta_{c2}-\delta_{m2})/\tau - i\Delta\omega_2]\,\tilde{E}_2(t) = \tilde{E}_{12}/\tau. \tag{7.2b}$$

These two equations are essentially the phasor amplitude equations for a ring laser with backscattering. It is useful in our discussions to break these phasor equations into separate equations for the amplitudes and the phases of the phasors. In this modification the complex signal phasors in the equations are unravelled into their magnitudes and phases by the replacements $\tilde{E}_1(t) \equiv E_1(t)\exp i\phi_1(t)$, $\tilde{E}_2(t) \equiv E_2(t)\exp i\phi_2(t)$, $\tilde{E}_{12} \equiv E_{12}\exp i[\phi_1(t)+\varepsilon_1]$ and $\tilde{E}_{21} \equiv E_{21}\exp i[\phi_2(t)+\varepsilon_2]$, where ε_1 and ε_2 are respectively the phases of the backscattering of the two beams.

By substituting these expressions into Equations (7.2) and separating the real and the imaginary parts of the equations, we get four coupled purely real equations which consist of equations describing the dynamics of the phase and

amplitude of the electric field phasors, namely:

$$dE_1(t)/dt + (\delta_{c1} - \delta_{m1})E_1(t)/\tau = (E_{21}/\tau)\cos[\varepsilon_2 + \psi(t)], \quad (7.3a)$$
$$dE_2(t)/dt + (\delta_{c2} - \delta_{m2})E_2(t)/\tau = (E_{12}/\tau)\cos[\varepsilon_1 - \psi(t)], \quad (7.3b)$$
$$d\phi_1(t)/dt - \Delta\omega_1 = [E_{21}/\tau E_1(t)]\sin[\varepsilon_2 + \psi(t)], \quad (7.3c)$$
$$d\phi_2(t)/dt - \Delta\omega_2 = [E_{12}/\tau E_2(t)]\sin[\varepsilon_1 - \psi(t)], \quad (7.3d)$$

where $\psi(t) = \phi_2(t) - \phi_1(t)$ and corresponds to the phase difference between the CW and CCW waves. Then we can get the expression for the beat frequency of the ring laser in the forms

$$\psi'(t) = \omega_2-\omega_1+(E_{12}/\tau E_2)\sin[\varepsilon_1-\psi(t)]-(E_{21}/\tau E_1)\sin[\varepsilon_2+\psi(t)]. \quad (7.4)$$

In this equation, the term $\omega_2 - \omega_1$ represents the angular frequency difference of CW and CCW beams in the ring laser induced by the laser ring cavity rotation. The last two terms on the right side of the equation describe the frequency-locking or pulling caused by backscattering.

For the general case, $E_{12}/E_2 \neq E_{21}/E_2$, Aronowitz and Collins (1970) presented numerical results for some particular values of the amplitudes and phases of the backscattering. A special case where the backscattering coupling from each beam into another is the same, eg. $E_{12}/E_2 = E_{21}/E_1$, has been discussed by Haus *et al.* (1985), where an expression for the connection between the frequency-locking range and the relative phases is given for this special case.

For convenience of discussion in the general case, we rewrite Eq. (7.4) in an explicit form as

$$\psi'(t)/2\pi = f + f_l\sin[\varepsilon_0 - \psi(t)] \quad (7.5)$$

where

$$f_l = [a^2 + b^2 + 2ab\cos(\varepsilon_1+\varepsilon_2)]^{1/2}/2\pi, \quad (7.6a)$$
$$\varepsilon_0 = \tan^{-1}(a\sin\varepsilon_1 - b\sin\varepsilon_2)/(a\cos\varepsilon_1 + b\cos\varepsilon_2) \quad (7.6b)$$

and $f = (\omega_2 - \omega_1)/2\pi$, $a = E_{12}/\tau E_2$ and $b = E_{21}/\tau E_1$. We take a, b to be constants, and in Section 7.2-7.4.3 assume that the PMT signal from the interferometer essentially measures the relative phase ψ, and that the intensities of each countercirculating beam is a constant. These assumptions will be avoided in Section 7.4.4.

From Eqs. (7.5) and (7.6), one can estimate the frequency-locking range and study the frequency-locking behaviour in the general case. Eq. (7.5) is the same as

Adler's (1964) pulling equation, except for the expressions defining f_l and ε_0. This will allow us to study the frequency-locking behaviour of the two self-sustained oscillations in a ring laser in the same way, as that of solving the other injection locking problems where one self-sustained oscillation controlled by an injected weak signal, with some interesting but different results.

7.2.2 Steady-state solution

a) Limiting cases for the beat frequency

The primary equation that describes the frequency-locking behaviour is the phase difference Eq. (7.5). The requirement for a steady-state frequency-locked ring laser where the frequencies of two beams lock up together, or $\psi'(t) = 0$, is equivalent to the condition that

$$f + f_l \sin[\varepsilon_0 - \psi] = 0. \tag{7.7}$$

Since $|\sin[\varepsilon_0 - \psi] \equiv f/f_l| \leqslant 1$, this condition can be satisfied if the beat frequency, $f = f_2 - f_1$, remains within the range

$$|f_2 - f_1| \leqslant f_l. \tag{7.8}$$

f_l represents the frequency locking threshold of a ring laser at a low rotation rate. f_l can be calculated by Eq. (7.6a), where f_l is related to the backscattering phases and is then different from the Adler equations (Adler 1946). In Adler's expression, $f_l \equiv (\nu_0/Q)(E_1/E_0)$, Q is the quality factor of the oscillator, ν_0 and E_0 are the frequency and amplitude of the oscillator respectively, and E_1 is the amplitude of the injected external field (Siegman 1985). That is, in Adler's analysis, f_l is independent of the phase of the injected signal. From Eq. (7.6a), the maximum and minimum of f_l are obtained

$$f_{lMAX} = (a + b)/2\pi \qquad \text{when } \varepsilon_1 + \varepsilon_2 = 2n\pi \tag{7.9a}$$

$$f_{lMIN} = |a - b|/2\pi \qquad \text{when } \varepsilon_1 + \varepsilon_2 = (2n\text{-}1)\pi \tag{7.9b}$$

where n is an integer, and parameters a and b are defined in Eq. (7.6b). In the simplest case where the backscattering coupling from each beam into another is the same, $a = b$. Eq. (7.6a) then becomes to $\omega_L = 2a\cos[(\varepsilon_1 + \varepsilon_2)/2]$, which is

the same result given by Haus (1985).

Figs. (7.2) and (7.3) are illustrations of phase diagrams for CW and CCW beam and their backscattering. Fig. (7.2) shows two typical cases where the backscattering phase sum $\varepsilon_1 + \varepsilon_2$ is equal to π and to $-\pi$, respectively, in (a) and (b). In both situations, the backscattering of the two beams changes the phases of the beams with respect to each other, but in the same direction. In this case the phase difference between the CW and CCW beams is minimally affected by backscattering.

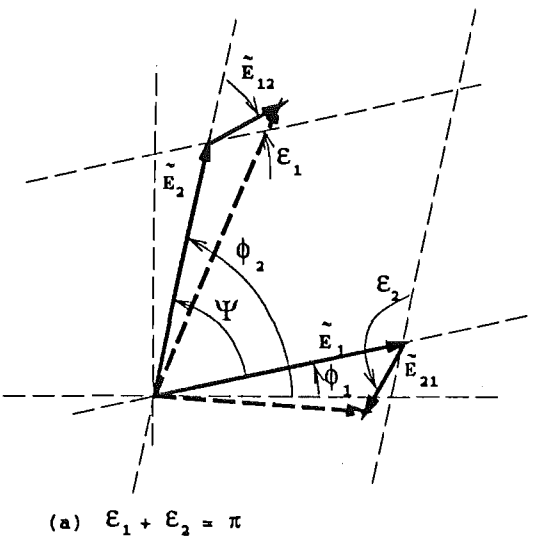

(a) $\varepsilon_1 + \varepsilon_2 = \pi$

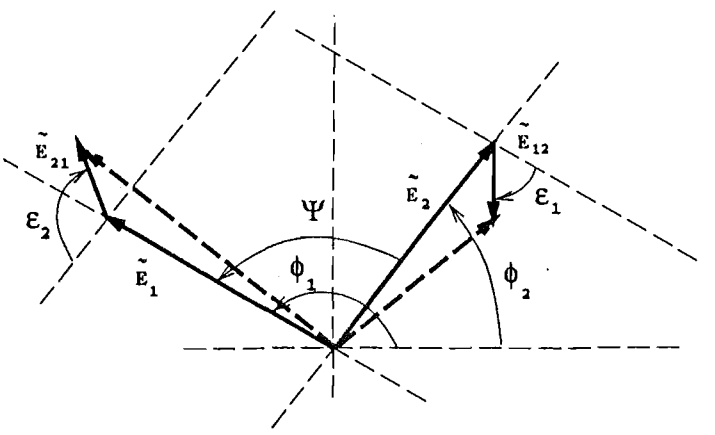

(b) $\varepsilon_1 + \varepsilon_2 = -\pi$

Fig. 7.2. Phase diagram for CW and CCW beams and their backscattering when the backscattering phase sum is equal to $(2n + 1)\pi$ where n is an integer.

Fig. (7.3) shows two opposite cases where the backscattering phases $\varepsilon_1 = \varepsilon_2 = 0$ in (a) and $\varepsilon_1 + \varepsilon_2 = 2\pi$ in (b). In both situations, the backscattering of the two beams will shift the phasor of each beam closer to the other, changing the phase difference ψ. In these cases, the beat frequency of the ring laser will be maximally changed by the backscattering.

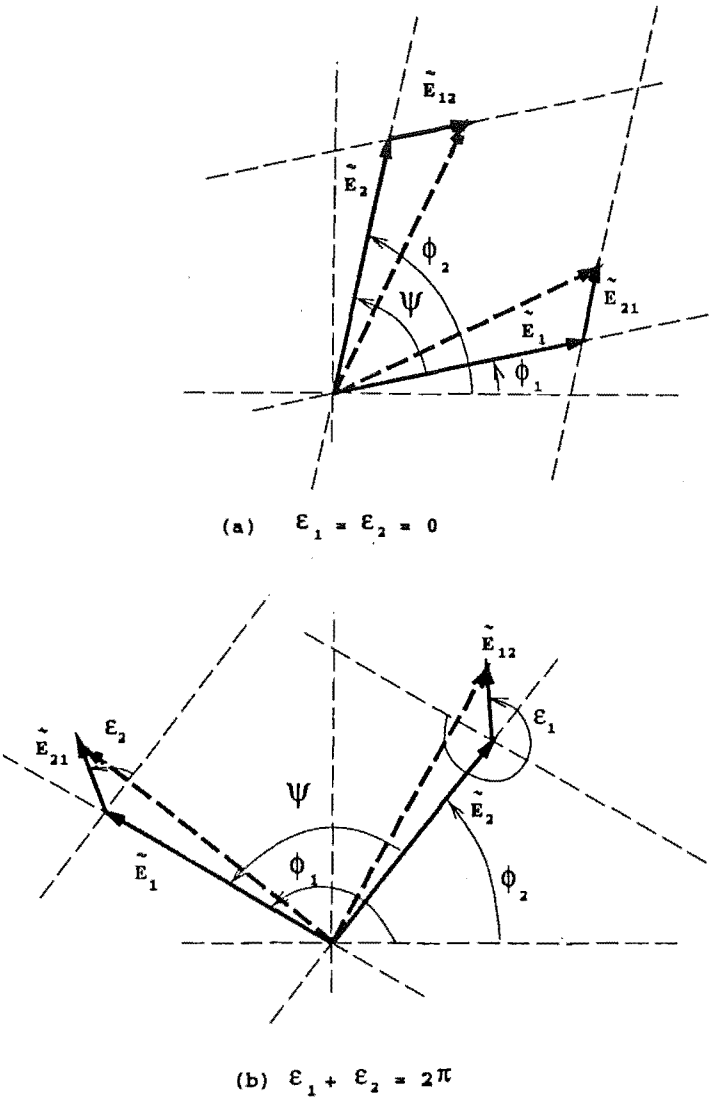

Fig. 7.3. Phase diagram for CW and CCW beams and their backscattering when the backscattering phase sum is equal to $2n\pi$ where n is an integer.

b) Phase difference of ring laser beams in lock-in range

In the Adler formalism, the phase angle $\psi(\omega_1)$ of the output signal E_0 with respect to the injected signal E_1 will shift through π as the injected signal is tuned across the locking range, as given by the formula $\psi(\omega_1) = \sin^{-1}[(\omega_0 - \omega_1)/\omega_L]$ (Siegman 1986), where ω_0 is the angular frequency of a free-running oscillator, ω_1 is the angular frequency of the injected signal and $\omega_L = 2\pi f_l$. The phase difference between the output of the oscillator and the injected signal depends only on the frequency difference between the injected signal and the oscillator in the free-running case. This dependence of phase shift on frequency can have useful applications in the use of locked oscillators or phase-locked loops as frequency demodulators and in other situations (Siegman 1985).

For a ring laser operating in the locking range, however, the phase difference between the two beams will depend on the backscattering phase. From Eq. (7.7), we get the phase difference

$$\psi = \varepsilon_0 - \sin^{-1}(f/f_l). \tag{7.10}$$

This shows that the phase difference of the CW and CCW beams will depend not only on f, the beat frequency of the ring laser, but also on the resultant backscattering phase ε_0 which is defined by Eq. (7.6b).

c) Frequency of ring laser in lock-in regime

For a single oscillator in the locking range, the frequency of the oscillation will be locked onto the frequency of the injected signal (Siegman 1986). In the ring laser case, the frequencies of the counterpropagating waves are synchronized, as expressed in Eqs. (7.3c) and (7.3d), $d\phi_1(t)/dt = d\phi_2(t)/dt = \omega_s - \omega_0$. In this case, the synchronized frequency of the ring laser can be determined either by Eq. (7.3c) or Eq. (7.3d), but where the phase difference ψ is given by Eq. (7.10) and no longer varies with time.

An interesting finding is that the synchronized frequency ω_s does not always fall within the range $\omega_1 < \omega_s < \omega_2$ when $\omega_1 < \omega_2$, or $\omega_1 > \omega_s > \omega_2$ when $\omega_1 > \omega_2$. This synchronized frequency may in some conditions be located outside the range defined by the two free-running frequencies.

Let us discuss the frequency of the ring laser in the locking range. From Eqs. (7.3c) and (7.3b), we get the equations, $\omega_1 + b\sin(\varepsilon_2+\psi) = \omega_s$ and

$\omega_2 + a\sin(\varepsilon_1-\psi) = \omega_s$. By eliminating ψ between these two equations, we get the equation

$$\varepsilon_1 + \varepsilon_2 = \sin^{-1}[(\omega_s-\omega_2)/a] + \sin^{-1}[(\omega_s-\omega_1)/b]. \quad (7.11)$$

From Eq. (7.11), we get the conditions for the synchronized frequency ω_s to coincide with either ω_1 or ω_2: $\varepsilon_1 + \varepsilon_2 = \sin^{-1}[(\omega_1 - \omega_2)/a]$ (note that this quantity then < 0) when $\omega_s = \omega_1$, and $\varepsilon_1 + \varepsilon_2 = \sin[(\omega_2 - \omega_1)/b]$ (> 0) when $\omega_s = \omega_2$. For the frequency ω_s to fall into the range $\omega_1 < \omega_s < \omega_2$, the backscatter phase sum should satisfy the condition

$$\sin^{-1}[(\omega_1 - \omega_2)/a)] < \varepsilon_1 + \varepsilon_2 < \sin[(\omega_2 - \omega_1)/b] \quad (7.12)$$

where $(\omega_s-\omega_2)/a > -1$ and $(\omega_s-\omega_1)/b < 1$. (In the above, relatively small pulling is assumed so that the trigonometric functions are all of acute angles, making the sine monotonic.) Now let us discuss the case $\omega_s > \omega_2$. From Eq. 7.12, the maximum of ω_s is found to be $\omega_2 + a$. Then we find that the condition for $\omega_2 + a > \omega_s > \omega_2$ is given by

$$\sin^{-1}[(\omega_2-\omega_1)/a] < \varepsilon_1+\varepsilon_2 < \pi/2+\sin^{-1}[(\omega_2-\omega_1+a)/b] \quad (7.13)$$

Similarly we get that the minimum value of ω_s is $\omega_1 - b$ and that the condition on the backscatter phase sum for $\omega_1-b < \omega_s < \omega_1$ is

$$-\pi/2+\sin^{-1}[(\omega_1-\omega_2-b)/a < \varepsilon_1+\varepsilon_2 < \sin^{-1}[(\omega_1-\omega_2)/a)] \quad (7.14)$$

7.2.3 Solution outside frequency-locking range

For a working ring laser, some particularly complex and interesting phenomena occur in this range, $|f_2-f_1| > f_l$. For example, the frequency pulling of the ring laser operating in this range will affect the accuracy of the beat frequency of the ring laser.

Eq. (7.5) is a standard differential equation and its solution outside the frequency-locking range is given, on changing to the variable $\Psi = \psi - \varepsilon_0$, by

$$\Psi(t) = 2\tan^{-1}\{[f_l + f_b\tan(\pi f_b t)]/f\} \quad (7.15).$$

where

$$f_b \equiv [f^2 - f_l^2]^{\frac{1}{2}} \tag{7.16}.$$

Eq. (7.16) shows that the phase difference between the CW and CCW beams is no longer a linear function of time. This in turn predicts that the instantaneous beat frequency f_l should itself vary in time. It is obtained by calculating the derivate of $\Psi(t)$, namely

$$f_l = \frac{f^2 - f_l^2}{f + f_l \sin(2\pi f_b t + \epsilon)} \tag{7.17}$$

where $\epsilon = \tan^{-1}(f_l/f_b)$. (Note that the numerator is f_b^2.) Eq. (7.17) shows that the instantaneous beat frequency of a ring laser with backscattering is a periodic function of time. Its maximum and minimum values are respectively given by $f_{lmax} = f + f_l$ and $f_{lmin} = f - f_l$. From these relations, we obtain the nominal beat frequency f and the frequency locking threshold f_l in the forms

$$f = (f_{lmax} + f_{lmin})/2 \tag{7.18a}$$
$$f_l = (f_{lmax} - f_{lmin})/2 \tag{7.18b}$$

We define the average period T_b of the beat signal as $T_b = 1/f_b$. By substituting Eqs. (7.18) in Eq. (7.16), we can obtain the average period of the beat signal as

$$T_b = 1/f_b = (f_{lmax} f_{lmin})^{-\frac{1}{2}}. \tag{7.19}$$

Substituting Eqs. (7.18) and (7.19) in Eq. (7.17), we can rewrite this equation as

$$f_l = [c_1 + c_2 \sin(\omega_b t + \epsilon)]^{-1} \tag{7.20}$$

where $c_1 = (f_{lmax} + f_{lmin})/(2f_{lmax} f_{lmin})$, $c_2 = (f_{lmax} - f_{lmin})/(2f_{lmax} f_{lmin})$ and $\omega_b = 2\pi f_b = 2\pi(f_{lmax} f_{lmin})^{\frac{1}{2}}$. Eqs. (7.18)-(7.20) show an important fact that the nominal beat frequency f and the frequency locking threshold f_l, in turn the instantaneous beat frequency function, can be determined by the extremes of the instantaneous beat frequency. This is one of the basic ideas which we use for determining the frequency pulling. We will further discuss this method and give our experimental results in Sec. (7.4).

The average beat frequency is that determined from gyroscope output counts or by the frequency of the fundamental in the Fourier spectrum, the pulled frequency $\overline{f_l}$:

$$\overline{f_l} = \frac{f^2 - f_l^2}{2\pi}\int_0^{2\pi} \frac{d\phi^2}{f + f_l \sin\phi} = f_b \tag{7.21}$$

where we have changed variable to $\phi = 2\pi f_b t + \epsilon$ and used the integral $\int_0^{2\pi} (f + f_l \sin\phi)^{-1} d\phi = 2\pi/(f^2 - f_l^2)^{\frac{1}{2}}$ (Chow *et al.* 1985), where the average beat frequency f_b is defined by Eq. (7.16) and f_b is always less than f. This shows that the fringe counts of the ring laser output or the average beat frequency f_b is pulled down by the backscattering in the ring cavity. Fig. (7.4) shows the variation of the average beat frequency f_b versus input rotation rate Ω. For precision measurements of a ring laser, this beat frequency locking problem and the beat frequency pulling error must be solved by different means for different ring laser designs.

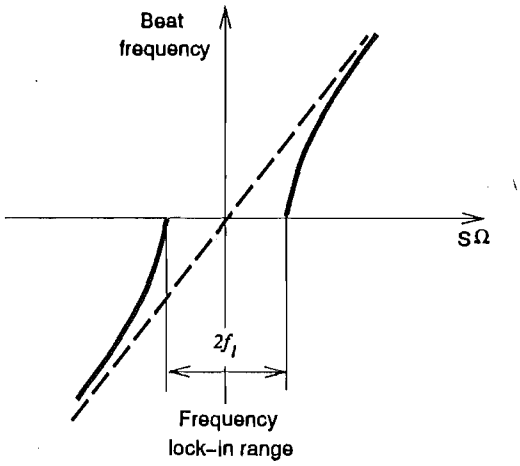

Fig. 7.4. Variation of the average beat frequency f_b (solid line) versus input rotation rate Ω. The broken line is nominal frequency f (in the case of absence of the backscattering).

Fig. (7.5) shows the variations of the instantaneous beat frequency predicted by Eq. (7.17) versus time t at different frequency locking thresholds. In these diagrams, the frequency locking threshold f_l = 10, 30, 50 and 65 Hz in (a)-(d), respectively, with the nominal beat frequency f = 70 Hz. Fig. (7.5) shows that with an increase of the frequency pulling, the difference between the extremes of the instantaneous beat frequency will increase and the average beat frequency f_b will decrease.

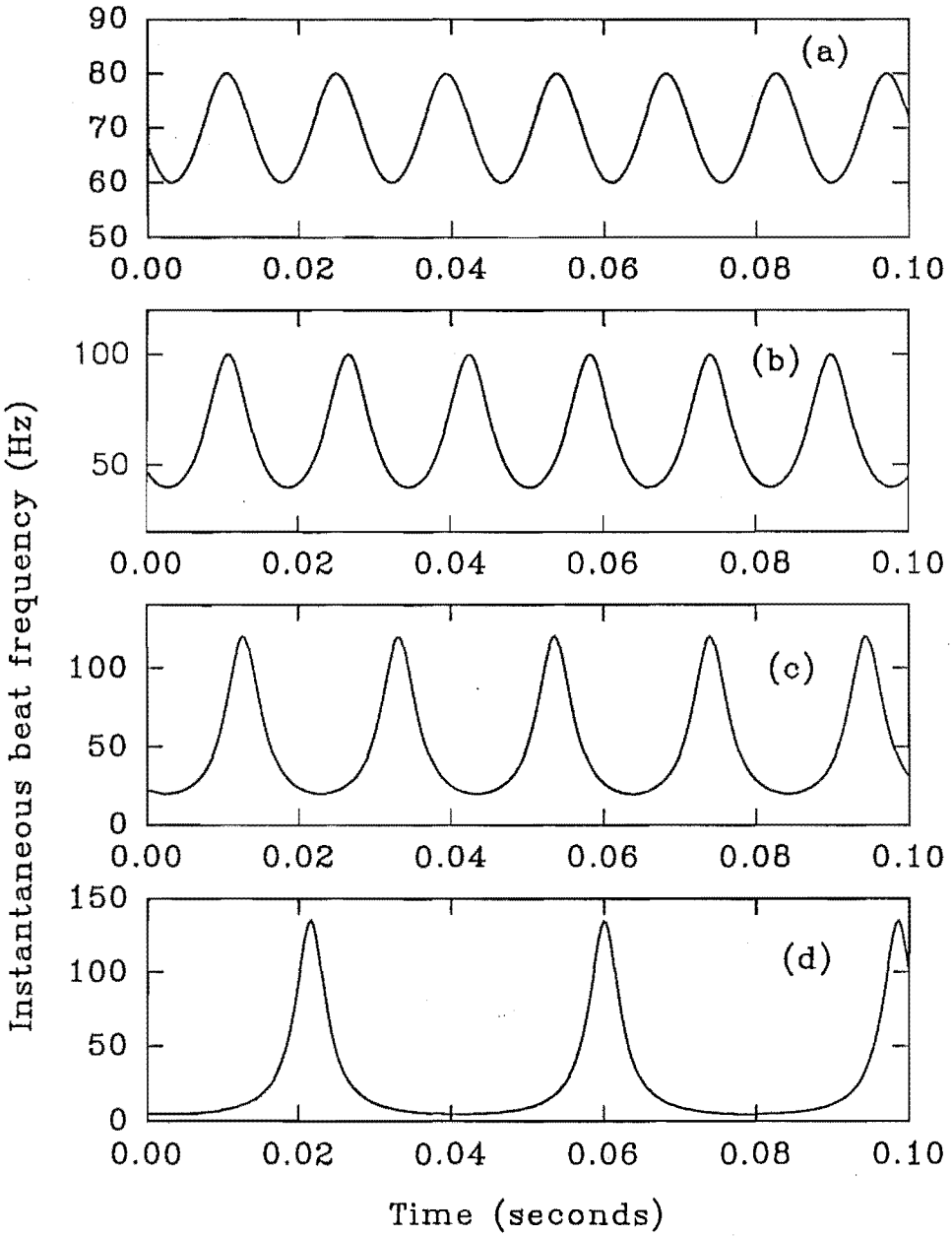

Fig. 7.5. Variation of the instantaneous beat frequency versus time at different frequency locking thresholds: (a) f_l = 10 Hz, (b) f_l = 30 Hz, (c) f_l = 50 Hz and (d) f_l = 65 Hz.

7.2.4 Evaluation of backscattering

From Eqs. (7.6a) and (7.6b), we can estimate the frequency locking threshold f_l, which is a function of the fractional amplitude scattering coefficients, $a = E_{12}/E_2\tau$, $b = E_{21}/E_1\tau$, and the backscattering phases, ε_1 and ε_2. In current ring laser designs, the dominant source of the lock-in threshold is the multilayer dielectric mirror coatings. Eq. (7.6a) gives the maximum value $f_{lmax} = (a+b)/2\pi$ when $\varepsilon_1 + \varepsilon_2 = 2n\pi$.

An estimate of the fractional amplitude scattering coefficient a or b can be made with the following assumptions (Aronowitz 1971). Let us for this purpose avoid any particular model of backscattering such as Lambert scattering and assume that a percentage r_s^2 of the light from one of the beams, when it strikes a mirror, is uniformly scattered into 4π radians. Only the part of the light which is scattered in the solid angle of the oppositely directed beam is effective in the coupling. Thus $(E_{ij}/r_sE_i)^2 = d\Omega/4\pi$ where subscripts i, j represent 1, 2. The solid angle determined by the diffraction angle of the beam is $d\Omega = \pi\theta^2$ where θ is the diffraction angle of laser beam. For a ring laser, the TEM_{00} mode is required and its diffraction angle in far field is given by (Siegman 1986) $\theta = \lambda/\pi\sigma_0$, where λ is the wavelength and σ_0 is the spot size at the beam waist. Then we get $E_{ij} = r_sE_i\lambda/\pi d_0$ where $d_0 = 2\sigma_0$, is the diameter of the beam at the waist. Substituting E_{ij} in the expressions of the fractional backscattering coefficients, we get

$$a = (E_1/E_2)(r_{s1}\lambda/\pi d_0)(c/P), \tag{7.22a}$$

$$b = (E_2/E_1)(r_{s2}\lambda/\pi d_0)(c/P), \tag{7.22b}$$

where $c/P = \tau$, c is the speed of light and P is the perimeter of the ring cavity.

Eqs. (7.22a) and (7.22b) show that the fractional backscattering coefficients are proportional to $1/P$. Therefore, the larger the perimeter of a ring cavity, the less the latter is affected by backscattering for given quality of the mirrors. This is one of the reasons for our interest in a ring laser with an area of order 1 m^2. The perimeter of our ring cavity is about 10 times bigger than those of commercial laser gyroscopes, so that the lockin band of our ring laser will be one order less than that of commercial rings for equivalent mirror quality.

For our 0.633 μm He-Ne ring laser with a average beam diameter d_0 of 1.31 mm ($d_0 = (d_x + d_y)/2$ since the beam spot is elliptical in our cavity) at the beam waist, and with a perimeter of 3.47 m, we obtain the backscattering coefficients $a = b = 1.3 \times 10^{-4}\, r_s$ where we assume $E_1 = E_2$ and $r_{s1} = r_{s2} = r_s$. For a total round-trip mirror scattering of the order of 16 ppm (there are four

mirrors in our cavity, and each one has a minimum scattering ~ 4 ppm), corresponding to $r_s = 4 \times 10^{-3}$, we get $a = b = 54$ radian/sec, which is equivalent to a frequency locking threshold $f_l = 17$ Hz where we assume $\varepsilon_1 + \varepsilon_2 = 0$. In this case, we obtain an average (pulled) beat frequency $f_b = 65.8$ Hz, whose fractional shift relative to the nominal beat frequency f (the beat frequency without backscattering) is $\delta f/f = 3.2\%$.

In our experiments, scattering at a mirror can reach 100 ppm, and in extreme cases of contamination 1000 ppm. in such situations, f_l will increase to 132 Hz under the same phase condition. In this case, the frequency locking threshold f_l is larger than the nominal frequency f, the frequencies of the CW and CCW beams are locked together, and the interference pattern is frozen. This is readily visible in practice by searching for a fringe pattern in the overlaid beams.

The advantage of a long perimeter is pointed by the feasibility of using earth rotation to bias a fibre-optic gyroscope in an analysis of circular dichroism in high-temperature superconductors by Spielman *et al.* (1990), the only other case known to us of this technique. However, their precision for measuring the earth rotation rate is of the order of a few percent at best, and the phase resolution of their interferometer is many orders of magnitude less precise than that of our ring.

On the other hand, a commercial ring laser operating under the earth's rotation, even with minimal backscattering of 60 ppm, would suffer frequency lock-in at the threshold of ~300 Hz (Aronowitz 1971), since those ring lasers have much smaller areas than our ring laser. Therefore different techniques are needed to overcome the frequency locking problem.

7.3 Methods for the avoidance of lock-in

7.3.1 Constant bias

The most straightforward technique to avoid lock-in and the "dead band" about zero rotation rate is to introduce a constant, externally controlled null shift or "bias," large enough so that the laser is always in the unlocked region. The frequency difference will then be given

$$\psi'(t)/2\pi = S\Omega + a_b \tag{7.23}$$

where α_b represents the bias, from which one can recover $S\Omega$ by subtracting the known constant bias. A difficulty is immediately apparent here: the bias to be a large number to avoid lock-in, and yet known with very high accuracy, so that no significant errors are introduced when subtracting it from the measured frequency difference. For example, to get Ω with an accuracy of 10^{-3} deg/h, with a bias of 10^4 deg/h, the latter has to be known, and kept constant, to within one part in 10^7. Note that a very large bias is required, not only to overcome locking, but also to be allowed to treat the scale factor as a constant, that is, to linearize Eq. (7.23) to a sufficient accuracy, namely

$$\begin{aligned}\langle d\psi(t)/dt\rangle/2\pi &= [(S\Omega+\alpha_b)^2-f_l^2]^{1/2} \\ &\simeq (s\Omega+\alpha_b)\{1-\tfrac{1}{2}[f_l/(S\Omega+\alpha)]^2\}. \end{aligned} \tag{7.24}$$

This means that a bias of the order of 10^2-10^3 times the frequency locking threshold is needed to get scale factor to an accuracy of 10^{-5}.

Many methods have been suggested to provide a constant null shift. Macek *et al.* (1964) suggested a fixed offset of the beat frequency in a ring laser using Fresnel drag introduced by a spinning glass disc, flowing liquids, and flowing gases. Langmuir flow and cataphoresis effects were suggested by Dessus, Catherin, and Migne in 1966, Batifol and Pecile in 1966 (Heer 1984), and investigated in some detail by Podgorski and Aronowitz (1968) for their use in ring lasers. Thomson and King (1966) used a constant rotation rate to keep the beat frequency away from small values. In practice all of these methods suffer from the same problem: the accuracy with which they have to be known and kept stable is simply too high either to attain or to be economically practicable.

Another scheme providing a constant beat note offset uses the Faraday effect (Lee and Atwood 1966, Chow *et al.* 1980, 1985; Statz *et al.* 1985). The application of an axial magnetic field to an amorphous, isotropic material placed in the ring cavity splits the cavity frequencies of the two counterrotating laser modes. The beat note is proportional to the product of the magnetic field and the material length. The constant of proportionality is the Verdet constant of the material. Using this technique, a bias on the order of 10^5-10^6 deg/h can be obtained. To keep it as stable as possible, it has been found convenient to use ferromagnetic or ferromagnetic materials, with a low saturation magnetization. An external magnetic field is used to saturate the material, thus making sure the bias is not affected by stray magnetic fields (including the earth's own). There still remains the problem of measuring it with enough accuracy to compensate for it in the output.

7.3.2 Alternating bias

In this scheme, the bias is operated in both the positive and negative rotation rate direction. Over each of these cycles, the net bias averages to zero, so that the output of the ring laser, being intrinsically an integrated magnitude, would only reflect the net rotation rate. The most successful alternating technique to date is the mechanical one (Aronowitz 1971, Chow *et al.* 1985), in which the laser gyroscope is rotated alternately in one direction and the opposite. This process has come to be known as "dithering." It is usually done by mounting the laser on a rotational spring system which is oscillated by means of a piezoelectric transducer.

The effect of an alternating bias that changes sinusoidally in time may be described by the modified phase equation (Aronowitz 1972, Chow *et al.* 1980, 1985)

$$\psi'(t)/2\pi = f + f_I\sin(\psi) + \alpha_D\cos(\omega_D t) \tag{7.24}$$

where α_D and ω_D are the amplitude and angular frequency, respectively, of the oscillating bias. The bias amplitude α_D is made large so that the ring laser is unlocked most of the time. Assuming $\psi(t)/2\pi \simeq ft + \alpha_D/\omega_D \sin(\omega_D t)$ and substituting in Eq. (7.24) we find

$$\psi'(t)/2\pi = f + f_I\sin[2\pi(ft + (\alpha_D/\omega_D)\sin\omega_D t)] + \alpha_D\cos\omega_D t \tag{7.25}$$

Using

$$\cos[(\alpha_D/f_D)\sin\omega_D t] = J_0(\alpha_D/f_D) + 2\sum_{n=1}^{\infty} J_{2n}(\alpha_D/f_D)\cos(2n\omega_D t)$$

and

$$\sin[(\alpha_D/f_D)\sin\omega_D t] = 2\sum_{n=1}^{\infty} J_{2n-1}(\alpha_D/f_D)\sin[(2n-1)\omega_D t]$$

where J_n denotes the nth Bessel function and $f_D = \omega_D/2\pi$, we rewrite Eq. (7.25) as

$$\begin{aligned}\psi'(t)/2\pi &= f + f_I \sin 2\pi ft\{J_0(\alpha_D/f_D) + 2\sum_{n=1}^{\infty} J_{2n}(\alpha_D/f_D)\cos(2n\omega_D t)\} \\ &+ f_I \cos 2\pi ft\{2\sum_{n=1}^{\infty} J_{2n-1}(a_D/f_D)\sin[(2n-1)\omega_D t]\} + \alpha_D \cos\omega_D t\end{aligned} \tag{7.26}$$

Since the beat note measurement time is greater than a dither period Eq. (7.26) reduces to

$$\psi'(t)/2\pi = f + f_I J_0(\alpha_D/f_D)\sin(2\pi ft) \tag{7.27}$$

Therefore, whereas without dither, locking occurs when $f \leqslant f_l$, with dither locking occurs only when $f \leqslant f_l J_0(\alpha_D/f_D)$. Furthermore, if α_D/f_D is a root of J_0 (i.e. α_D/f_D = 2.405, 5.520, ...), we have $\psi'(t)/2\pi = f$, i.e. lock-in vanishes. In practice this is usually not accomplished because the dither may be constrained to a ring laser at only certain resonant frequencies and amplitudes. What can be done is to choose α_D/f_D as large as possible, since for large arguments α_D/f_D the Bessel function $J_0(a_D/f_D)$ can be written as (Chow *et al.* 1985)

$$J_0(\alpha_D/f_D) = (2f_D/\pi\alpha_D)^{1/2} \cos(\alpha_D/f_D - \pi/4) \tag{7.28}$$

and therefore the width of locking band goes to zero. In commercial ring laser with mechanical dither, one my have α_D = 190 kHz and f_D = 200 Hz give α_D/f_D = 950 and $J_0(\alpha_D/f_D) \leqslant 0.02$.

The Faraday effect can also be used to induce an alternating bias, by periodically reversing the magnetic field applied to the Faraday cell (Chow *et al.* 1985). In addition to the characteristic already mentioned, of having a low saturation magnetization, it is desirable for the magneto-optic material used to have short switching times, again so that the laser spends as little time as possible in the locking region. Most importantly, the inclusion of any external element in the cavity (such as, in this case, the Faraday cell and optionally the quarter-wave plates) may increase the losses and especially the backscattering problem.

As an alternative to the Faraday effect, the so-called transverse magneto-optical Kerr effect has been suggested as a means to achieve the alternating bias in the ring lasers (Krebs *et al.* 1980). In this case the magnetic field is perpendicular to the direction of propagation of the waves, rather than parallel (or antiparallel) to it, as was the case for the Faraday effect. The related technique is that of so-called "magnetic mirrors" (Statz *et al.* 1985), in which the magneto-optic layer is incorporated into one of the mirrors in the cavity. The magnetic field is therefore applied in the plane of the mirror, and perpendicular to the plane of the cavity. The phase shift for the reflected p fields of the counterpropagating waves on the magnetic mirror of is proportional to the vector of the magnetic field (Freiser 1968). The magnetic field is switched periodically to effect a magnetic-optical dither. This results in a nonreciprocal phase shift and leads an alternating bias in output of a ring laser.

To be a useful bias element for the ring lasers, a magnetic mirror must satisfy a number of special and stringent requirements. In brief, the magnetic mirror must be a low-loss device, because the losses of a ring laser are a determining factor for the noise level of the instrument. Higher losses give rise to

increased quantum noise, the dominant source of noise for the limitation measurement of a ring laser. The bare metallic magnetic mirrors are poor reflectors at the He-Ne wavelength. Typical reflectivities lie in the range 0.4 - 0.7 (Krebs *et al.* 1980). In order to reduce the loss associated with the magnetic mirror one can overcoat the opaque metallic mirror with a multilayer dielectric stack which is tuned to be highly reflecting at the wavelength and angle of the incidence used. However, this multilayer dielectric coating will reduce the effect of the magnetic field on phase shift of the reflected fields (Statz *et al.* 1985). Therefore, one has to balance the development of a sufficiently large phase shift and the concomitant reflection losses at the magnetic mirror.

7.4 Measurement of frequency pulling

7.4.1 Importance of the frequency pulling measurements

As discussed in Sec. (7.2) on the frequency-locking theory in the ring laser, the frequency pulling phenomenon is always to be expected, since it is not possible to completely remove all sources of coupling between the two beams. This frequency pulling will affect the precision of the measurements of rotation rate or nonreciprocal effects in ring laser, particularly when the ring laser is operated at a low rotation rate. Even for the state-of-the-art supermirrors, which have a few ppm backscattering for each coating, they still cause a significant error on the beat frequency. As we mentioned previously, with the backscattering of 4 ppm for each mirror, the frequency locking threshold f_l = 17 Hz and the fractional error of the beat frequency $\delta f/f$ =3.2% for our ring laser cavity with the earth rotation.

In practice, the mirror backscattering will be larger than this ideal case as any dust and contamination on the mirror coatings during alignment and use will increase the amount of backscattering. In the present status of our experiment, the estimated total backscattering of our four mirrors is from one to several hundred ppm. In this case, this backscattering at the mirrors provides the largest error source on the beat frequency accuracy. For instance, with a total backscattering of 200 ppm in our ring cavity, the frequency locking threshold f_l = 60.3 Hz; this in turn predicts an average beat frequency f_b = 33.1 Hz given by Eq. (7.16) and a fractional error $\delta f/f$ on the nominal beat frequency f (68.8 Hz for the earth rotation), $\delta f/f$ = 48%.

The determination of frequency pulling is not simple. Although the

scattering of mirrors can be measured by a scatterometer (Thomas 1978), it is impossible, in general, to calculate the frequency pulling from measured scattering intensities from mirrors. We base this on the following facts.

In principle, the fractional backscattering coefficients and the backscattering phases in above analysis are uncontrolled. In our case the ring cavity consists of four mirrors. Let us label the scattering sites on these four mirrors by $n = 1,...,N$. The individual backscattering fields provided by these scatterers may interfere; the total backscattering coefficient should be the sum of the individual backscattering amplitudes, i.e. $S_{ij} = \Sigma_{n=1}^{N} s_{ij,n} \exp(-ikz_n)$, where z_n is the distance as measured around the perimeter. Therefore the phase and amplitude of the total backscattering will depend on these positions z_n of the backscattering events. Movement of a scattering centre will then lead to changes both in the amplitude and the phase of total backscattering, which in turn will change the frequency locking threshold of a ring laser.

An obvious and important cause of such movement of the scatterers in a ring laser is thermal expansion of the ring. In general, a change in frequency pulling is produced even if the overall path length of the ring is maintained constant by path length control: the distance between any two scattering mirrors may change even if the total round trip path length remains constant. In our experiments, a very gentle vertical tap on the Zerodur plate with a screwdriver can significantly change the response of the ring, and in particular can switch it from locking to unlocking or vice versa. This may be due to the marginal stability of the lasing mode-plasma system in such a case, but changes in the form of the optical beam do not always accompany the locking switch, and the event is very possibly and simply the result of altering the phase of the backscattering.

This important fact, that the frequency locking threshold f_l and in turn the average beat frequency f_b will depend on the phase of the backscattering of the CW and CCW beams, forces us to determine f_l from precision measurements in our ring laser other than the simple index of mirror reflectance.

From Eq. (7.16) we note that the average beat frequency $f_b \equiv [f^2 - f_l^2]^{1/2}$ where in the absence of dispersion effects $f = S\Omega$, Ω is the rotation rate and S is the scale factor. One can determine the locking threshold f_l by repeating the measurements of the average beat frequency f_b at different rotation rates. This produces different f_b values and allows a fit to the above formula. This is already done for the commercial ring laser gyroscopes (Aronowitz 1971, Chow *et al.* 1985). However, this method is not suitable for the case of our ring laser, since at this stage there is no provision for adding controlled and calibrated dither to our ring laser cavity, which rather has a constant earth rotation rate. Determining the

average beat frequency f_b (say by counting) from the ring laser output is itself inadequate to determine the two parameters, f and f_l, given that the former is affected not only by the (known) rotation rate, but is also affected by the nonlinear dispersion of the active medium (as discussed in Chapter 8).

We present a novel method to determine the beat frequency pulling and other parameters of a ring laser. Instead of merely counting the crests of the interferomgram and deducing only an average beat frequency (as in Aronowitz 1971, Chow *et al.* 1985), we show the feasibility of extracting frequency pulling and other information concerning the ring laser from an analysis of the waveform and harmonic content of the interference pattern, or time-dependent output. A direct way of achieving this is to process the output signal using the techniques of the analytic signal, or Hilbert transform, so as to derive the instantaneous beat frequency (basically the temporal derivative of the interference phase). The extreme values of this beat frequency suffice in principle within the above simple model of pulling and locking to derive the locking threshold and the unpulled frequency. In practice this gives quite sensible results. A more general analysis of the Fourier transform of both the input waveform and the instantaneous beat frequency in principle gives even more information, such as the gain of the laser tube. A preliminary analysis in this direction is presented.

7.4.2 Determination of instantaneous beat frequency

Our aim here is to extract the instantaneous beat frequency from the interference or beating signal delivered by a ring laser using the model of Section 7.2. When dealing with a frequency modulated signal, it is often convenient to define a quantity called the *analytic signal*, which is defined so as to make deriving the phase of a narrow-band signal easier. We define the analytic signal:

$$V(t) = V^{(r)}(t) + iV^{(i)}(t) = |V(t)|e^{i\Psi t} \tag{7.29}$$

where the imaginary part $V^{(i)}(t)$ is related to the real part, the actual (real) input voltage $V^{(r)}(t)$, by the Hilbert transform (Born and Wolf 1980)

$$V^{(i)}(t) = \frac{1}{\pi}\int_{-\infty}^{\infty} \frac{V^{(r)}(t')}{t'-t}\,dt' \tag{7.30a}$$

and

$$V^{(r)}(t) = -\frac{1}{\pi}\int_{-\infty}^{\infty} \frac{V^{(i)}(t')}{t'-t}\,dt'. \tag{7.30b}$$

In all cases the principal value of the integral is taken. The argument $\psi(t)$ of the analytic function $V(t)$ is then related to the phase of the interference pattern.

McGregor (1992) and Stedman (unpublished) have developed various MATLAB programs to perform this signal processing in a manner suitable for the ring laser: constructing the analytic signal $V(t)$, deriving $\psi(t)$, and finally differentiating to obtain the instantaneous beat frequency $f_i(t) = \psi'(t)/2\pi$.

A preliminary experimental result is shown in Fig. (7.6), where a waveform of the beat signal with backscattering is shown in the lower figure. Its instantaneous beat frequency $f_i(t)$ derived from this beat signal is shown in the upper graph. In this picture, the sample rate from the beat signal of our ring laser is 100 kHz. Fig. (7.6) gives much fuller information on the beat signal and its instantaneous frequency. The waveform of this beat signal is no longer sinusoidal and will be discussed in Sec. 7.4.4. The instantaneous beat frequency is that of Eq. (7.17); as explained in the context of that equation, it is not symmetric about its mean, owing to the effects of backscattering.

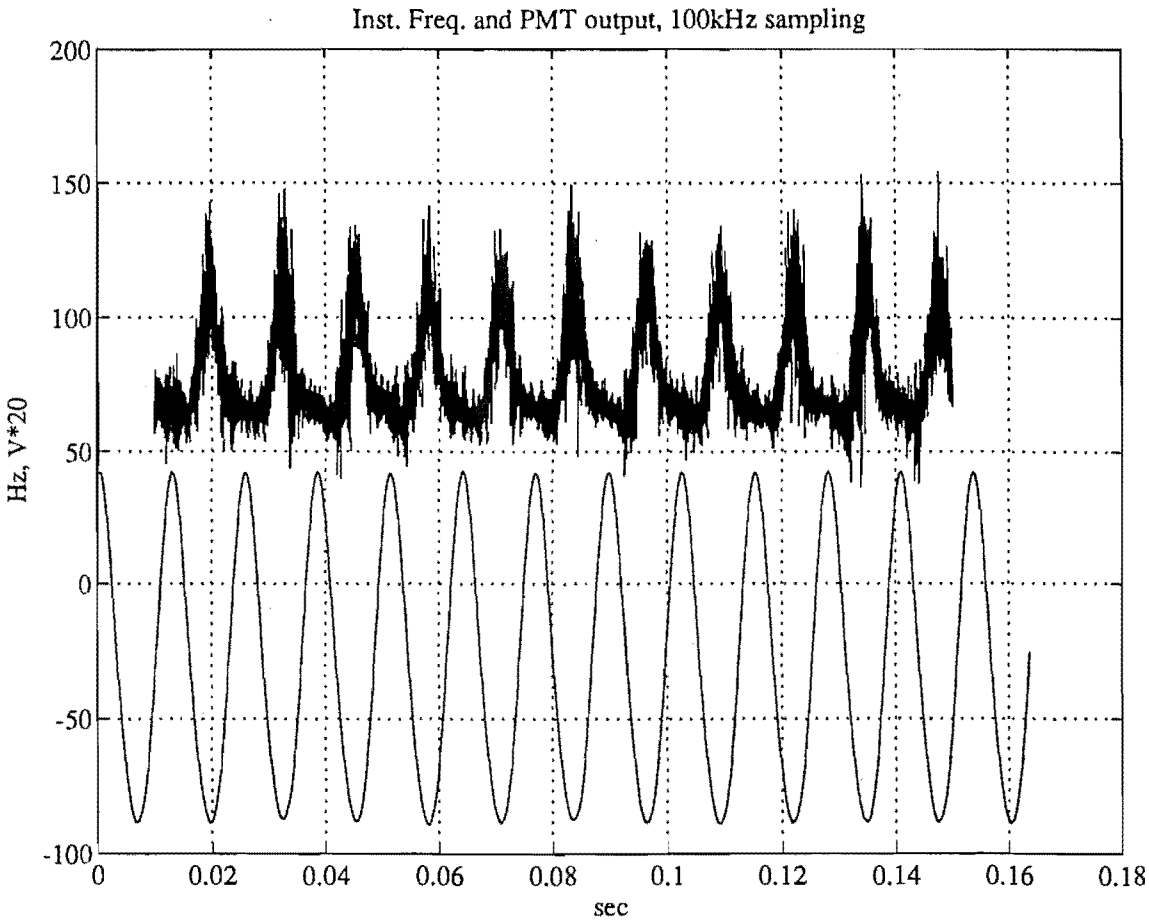

Fig. 7.6. A typical waveform (lower figure) of the beat signal and its instantaneous beat frequency (upper figure) with backscattering.

The noise on the instantaneous beat frequency is caused by numerical errors in the various transformations and in particular the digitizing error in the sampling and A/D conversion. By high-pass filtering out of this noise in MATLAB, the smoothed instantaneous beat frequency shown in Fig. (7.7) is obtained.

In this particular run, the maximum and minimum values of the instantaneous beat frequency are 112 Hz and 63.0 Hz on average. From these extreme values, we obtain the nominal beat frequency $f = (f_{imax} + f_{imin})/2 = 87.5$ Hz and the frequency locking threshold $f_l = ((f_{imax} - f_{imin})/2 = 24.5$ Hz. The average beat frequency calculated from Eq. (7.6), $f_b = (f_{imax} f_{imin}) = 84.0$ Hz, while the measured average beat frequency from Fig. (7.7) is 78.1 Hz. Fig. (7.7) reveals that the experimental results for the instantaneous beat frequency depart for lower frequencies from the prediction of Eq. (7.17); this could well reflect truncation error, in that the signal level may in these excursions exceed the -8V limit acceptable to the Strobes A/D system.

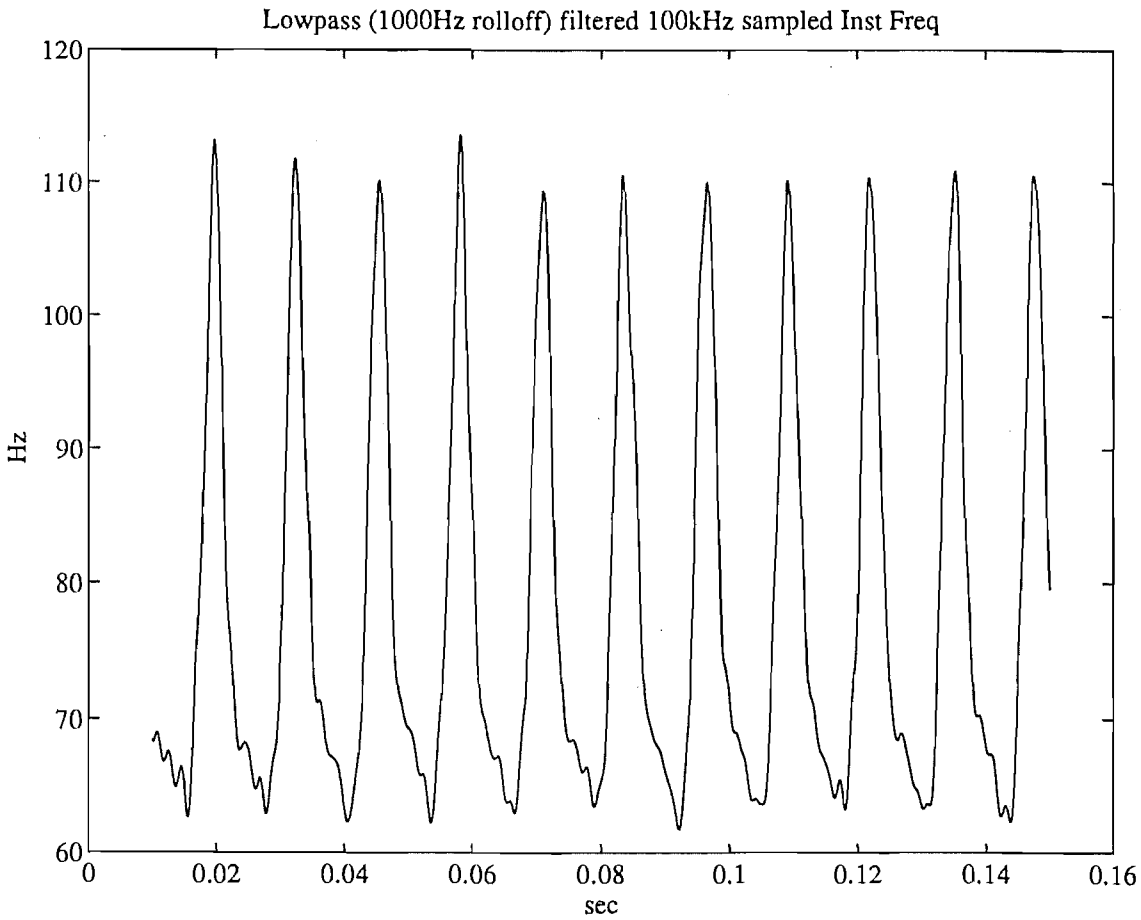

Fig. The instantaneous beat frequency of a beat signal.

7.4.3 Simple Fourier analysis of the instantaneous beat frequency, and its experimental inadequacies

A fuller analysis of frequency pulling information may be obtained from the Fourier analysis of the instantaneous beat frequency $f_i(t)$ given by Eq. (7.17). In principle, this allows the use of all data points and not merely the extreme values.

We now Fourier analyse Eq. (7.17). It is convenient to choose an origin of time such that the waveform is even. We then obtain the spectral components:

$$F_n = \frac{2}{T}\int_0^T dt \cos\left[\frac{2\pi n t}{T}\right] \frac{f_b^2}{f - f_i \cos 2\pi f_b t}$$
$$= \frac{2f}{\pi}\int_0^{\pi} \frac{\cos(n\phi)\, d\phi}{1 - (f_i/f)\cos\phi} \qquad (7.31)$$

using $\phi = 2\pi t/T$. This integral is tractable, as can be seen by using the further substitution $z = \exp(i\phi)$, and integrating over the unit circle with the aid of Cauchy's residue theorem. This gives

$$F_n = 2f_b\left[\frac{f - f_b}{f_i}\right]^n. \qquad (7.31a)$$

Hence the Fourier amplitudes are in geometric progression. On a logarithmic plot, which is customary to cover the great dynamic range of our device and which is permitted by most computer packages including the Strobes APC package, these amplitude values should lie on a straight line. This immediately suggests an alternative and possibly a better way than taking extreme values of the instantaneous frequency in time is to average across all visible harmonics to gain an estimate of the ratio

$$r = (f - f_b)/f_i \qquad (7.31b)$$

of this geometric progression, and from that ratio and the observed pulled frequency f_b (the harmonic interval) to deduce the unpulled frequency f and the lockin threshold f_i.

While indeed geometric progressions of harmonics were readily found, the initial quantitative estimates of the unpulled frequency and lockin threshold were remarkably disappointing. Often values were obtained which were quite at variance with those obtained from the temporal extremes of the beat frequency, and with reasonable expectations. Often the ratio was remarkably close to unity, giving

unconvincing values of lockin thresholds well above the pulled frequency and correspondingly close to the unpulled frequency, which was thus unreasonably well removed from the Sagnac frequency. Clearly the model used in Section 7.1 and enshrined in Eq. (7.17) was inadequate. The ratio measurement was particularly sensitive to its inadequacies. Nor could the method of temporal extremes of the instantaneous beat frequency be trusted.

There are several possible - and probably important - reasons for this, and accordingly several solutions, not all of which are worked out in this thesis. First, the effects of plasma gain and saturation on the interferometer waveform have not been included in Eq. (7.17). This is investigated in the next section. Second, numerical tests with a synthesised signal of the form of Eq. (7.17) when passed through the mathematical analysis (including sampling, FFT, analytic signal, numerical differentiation etc.) yielded a spectrum whose harmonic ratio r disagreed somewhat with that of Eq. (7.17). This inconsistency has yet to be understood, and requires some delving into the bowels of the algorithms used by MATLAB. Third, it was only recently realised that one factor is the phase window accepted by the photomultiplier. Since the photomultiplier accepts a significant fraction of a period of the interferometric waveform, and since this fraction varies with the essentially undocumented adjustment of the beam splitter feed mirrors, the degree of alignment of the output beams etc., the interferometer waveform is effectively convolved with a square window of unknown but significant size. This will have the effect of decreasing the amplitudes of higher harmonics relative to the fundamental, and giving a departure from a geometric progression. We shall assume that observation of a geometric progression in data already recorded is evidence that this effect may be ignored. Its effects cannot be to make the geometric ratio inferred from fitting to observations of Fourier amplitudes higher than the true value; however the first and second problem will have this effect, and so deserve the initial scrutiny.

Another experimental observation which is not accommodated so far is that we sometimes find that the intensity of each beam in the ring laser to be modulated with the average beat frequency. This also makes analysis of the intensity of the beat signal more complicated than that of Section 7.2.4. We turn to a fuller analysis.

7.4.4 Refined analysis of the temporal waveform of the beat signal

We revert to the general development of Section 7.2.1, and avoid in particular the

assumption of fixed and equal intensities of the counterrotating beams. We show that the temporal waveform of the beat signal and its Fourier analysis together with the Fourier analysis of the instantaneous beat frequency can together reveal not only the frequency pulling parameters but other information, such as the laser gain and saturation effect. The interferometer signal obviously depends not only on the relative phase of the travelling waves, but on the amplitudes of each beam. These amplitudes are themselves time-dependent, from Eqs. (7.3a,b). The importance of this time dependence itself depends on the gain of the plasma; at low gains, the oscillation system can respond only slowly to changes, and little temporal effect is seen in the intensities of the beams, the harmonics are relatively small and (as we in fact observe) the Lissajou figure is a more pure ellipse. As the gain is increased, the intensity can be changed more rapidly, the waveform is more complicated, the harmonic ratio r increases, and the Lissajou figure on the oscilloscope becomes appropriately distorted. We verify these observations and empirical interpretations in the following analysis. In the process of verifying this, we explain also the observations that analysis of the intensity of a single beam *may* (if the gain is high) show beats between the beam, and that the ratio r found in the geometric progression of harmonics can be significantly different from that of Eq. (7.31a).

Adding Eqs. (7.3a) and (7.3b) we obtain a differential equation involving the amplitudes of the beat signal, namely

$$\frac{dE_1}{E_1\,dt} + \frac{dE_2}{E_2\,dt} = \frac{(\delta_{m1}-\delta_{c1})+(\delta_{m2}-\delta_{c2})}{\tau} + a\cos(\epsilon_1-\psi) + b\cos(\epsilon_2+\psi) \tag{7.32}$$

where $a = E_{12}/\tau E_2$ and $b = E_{21}/\tau E_1$, as defined previously. In the following discussion of the temporal waveform of beat signals, we include the saturation effect, which is qualitatively related to the intensity of the laser beam. For simplicity, we assume $E_1 = E_2 = E$ and define $a_g = 2\pi[(\delta_{m1}-\delta_{c1}) + (\delta_{m2}-\delta_{c2})]/\tau$. We obtain the differential equation of the intensity of the beam:

$$\frac{dI/dt}{2\pi I} = a_g - b_g I + f_i\cos(\Psi) \tag{7.33}$$

where b_g is the saturation coefficient and $\Psi = \psi - \epsilon_0$, ϵ_0 is defined by Eq. (7.6b). From Eq. (7.15) we obtain $\tan(\Psi/2) = [f_i + f_b\tan(\pi f_b t)]/f$, and then

$$\cos(\Psi) = \frac{f_b\cos(2\pi f_b t + \epsilon)}{f + f_i\sin(2\pi f_b t + \epsilon)} \tag{7.34}$$

whre $\in = \tan^{-1}(f_l/f_b)$. The fact that Eq. (7.33) is amenable, like Eq. (7), to an analytic solution was pointed out recently by Etrich *et al.* (1992). Following these authors, we substitute into Eq. (7.33)

$$I = \frac{a_g}{b_g + J(t)\exp(-2\pi a_g t)} \tag{7.35}$$

which gives the linear differential equation

$$\frac{dJ}{dt} + 2\pi f_l J\cos\Psi = -2\pi b_g f_l \exp(2\pi a_g t)\cos\Psi \tag{7.36}$$

Substituting Eq. (7.34) in Eq. (7.36), we find the solution given by

$$J = -b_g f_l f_b \exp(2\pi a_g t)\frac{-2(a_g f_l - f_b^2)\tan\pi f_b t + f_b(f_l + a_g)(1-\tan^2\pi f_b t)}{(a_g^2 + f_b^2)[f^2 + (f_l + f_b \tan\pi f_b t)^2]} \tag{7.37}$$

Substituting in Eq. (7.35), we obtain an expression for the time-dependent beam intensity:

$$I = \frac{a_g(a_g^2 + f_b^2)^{1/2}}{b_g}\frac{f + f_l\sin(2\pi f_b t + \in)}{a_g f_l \sin(2\pi f_b t + \xi) + f(a_g^2 + f_b^2)^{1/2}} \tag{7.38}$$

where $\xi = \tan^{-1}\{f_l(a_g f_l - f_b^2)/[f f_b(f_b^2 + a_g^2)^{1/2}]\}$. The observed signal is the result of beating together the two individual beams, we assume in equal proportions: the intensities are the same (time-dependent) value I and the phases differ by Ψ. This gives an intensity for the interferometric pattern proportional to $X = I(t)[1 + \cos(\Psi + \theta_0)]$. θ_0 is introduced as the extra phase difference induced by the external interferometer (or beam combiner), where the two beams are combined for measuring the beat frequency. The optical paths of the two beams travelling through this interferometer may be different, and it has been found that when the the glass plate on which the beam combiner is mounted is touched very gently, the waveform of the beat signal is significantly changed because of a variation in θ_0. As a result the full interferometer signal - incorporating both the intensity and phase time dependence of the laser beams - has a form in which two major time-dependent terms, one in the intensity factor $I = [f + f_l\sin(2\pi f_b t + \in)]/c_1$ where $c_1 = [a_g f_l \sin(2\pi f_b t + \xi) + f(a_g^2 + f_b^2)^{1/2}]$ and one in the phase factor $\cos(\Psi + \theta_0) = c_2/[f + f_l\sin(2\pi f_b t + \in)]$ where $c_2 = [f_b\cos\theta_0\cos(2\pi f_b t + \in) - f_l\sin\theta_0 - f\sin\theta_0\sin(2\pi f_b t + \in)]$, have cancelled. We finally obtain a waveform which has a time dependence similar to that in each of the phase and the intensity:

$$X = \frac{a_g(a_g^2+f_b^2)^{1/2}}{b_g} \frac{(f-f_L\sin\theta_0) - [1 + \cos(2\pi f_b t + \epsilon - \theta_b)]}{a_g f_l \sin(2\pi f_b t + \xi) + fg} \qquad (7.39)$$

where $g = (a_g^2 + f_b^2)^{\frac{1}{2}}$ and $\theta_0 = \tan^{-1}[(f_l - f\sin\theta_0)/f_b\cos\theta_0]$.

Eq. (7.39) is a more accurate analysis of the waveform of the ring laser interferometer signal, and it should be this waveform that is Fourier analysed in considering the FFT of the signal naturally displayed by the Strobes APC package, for example. Its dependence on laser gain a_g helps to explain why the relative strengths of harmonics alter with plasma conditions within a set of runs. Indeed we find two limiting cases when there should be no harmonics present: either with no laser gain even when frequency pulling is present, or with no pulling even when laser gain is present; in each case the term $a_g f_l \sin(2\pi f_b t + \xi)$ in the denominator vanishes.

The form of Eq. (7.39) is that of a product of a purely sinusoidal function with a denominator of the form of Eq. (7.17), but with different constants. In the Fourier domain, the spectrum will therefore be a convolution of the Fourier transforms of the numerator and the denominator. Since the numerator is a pure sinusoidal function with a single harmonic, its convolution will merely give an overall scaling of the Fourier components of the denominator, whose relative amplitudes are therefore preserved under the convolution. Once again, then, we have a geometric progression of harmonics in accordance with our observations, and the ratio of this geometric progression is defined (just as Eq. (7.31b) is defined by Eq. (7.17)) by the ratio of the constants in the denominator. This gives the gain-modified ratio

$$r' = \left[\frac{fg - a_g f_L}{h}\right] \qquad (7.40)$$

where $h = (f^2g^2 - a_g^2 f_l^2)^{\frac{1}{2}} = (f^4 - a_g^2 f_b^2)^{\frac{1}{2}}$. Clearly the presence of significant gain can introduce time-dependence into the beam intensities in such a manner as to mask the effects of pulling alone; as a_g increases, $g \to a_g$. If we consider the second term in h^2 to be significant, we might expect that as the gain increases $h \to 0$ and the ratio increases. This accords with the effect noted in Section 7.4.4; in this case gain should further distort the waveform. The ratios of Eqs. (7.40) and (7.31b) are related in the limit $g \to a_g$ by

$$r'/r = ((f^2 - f_l^2)/(f^4/a_g^2 - f^2 + f_l^2))^{1/4}.$$

Fig. (7.8) shows the variations of waveform of beat signal with the frequency threshold f_l, where f_l = 10, 20, 50 and 65 Hz in (a)-(d) respectively, and we assume f = 68.8 Hz, a_g = 60/s, b_g = 30/s and θ_0 = 0. In this case, both the average beat frequency and waveform change with the frequency locking threshold f_l.

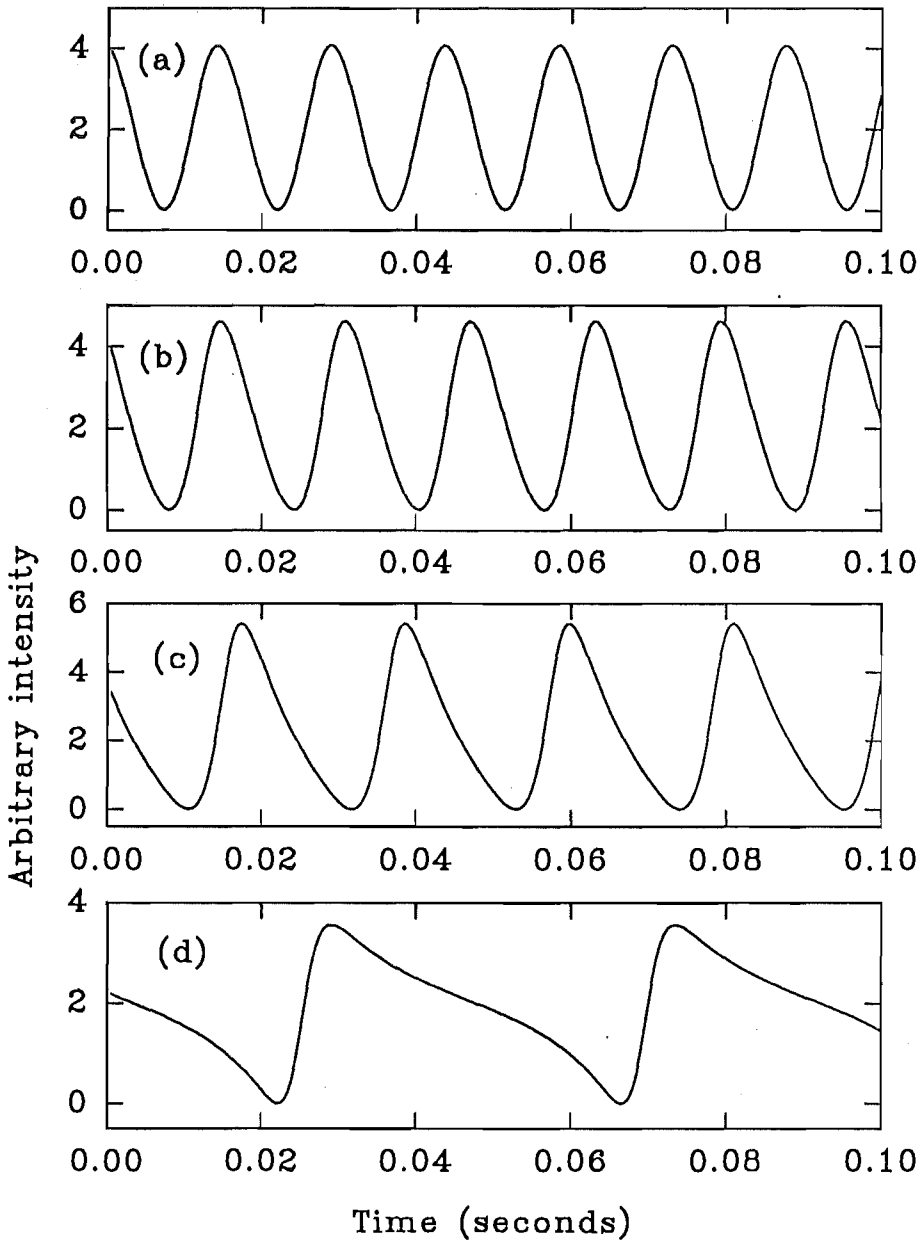

Fig. 7.8. Variation of the waveform of the beat signal with the frequency threshold f_l: (a) f_l = 10 Hz, (b) f_l = 20 Hz, (c) f_l = 50 Hz and (d) f_l = 65 Hz.

Fig. (7.9) shows the variation of the waveform with the laser net gain rate a_g, where a_g = 1, 10, 40 and 100 per second in (a)-(d) respectively, and we suppose f = 68.8 Hz, f_l = 65 Hz, $b_g = a_g/2$. Fig. (7.8) shows that the variation of the laser gain will change the waveform of the beat signal, but does not affect the average beat frequency.

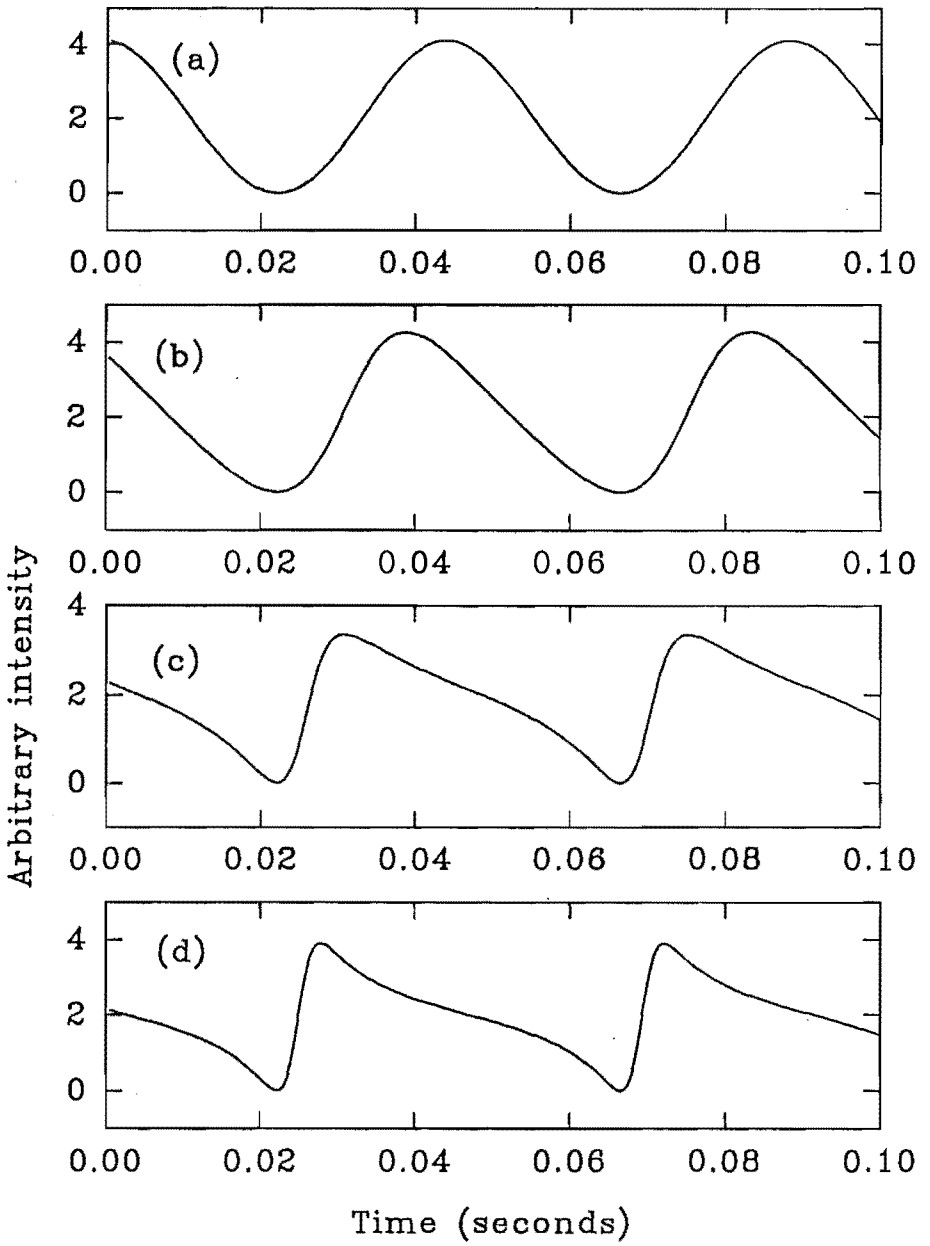

Fig. 7.9. The variation of the waveform of the beat signal with the laser net gain rate a_g: (a) a_g = 1/s, (b) a_g = 10/s, (c) a_g = 40/s and (d) a_g = 100/s.

Figs. (7.9) shows the waveform variation with the external phase difference θ_0. In this diagram, $\theta_0 = \pi/4$, $3\pi/8$, $\pi/2$, $5\pi/8$, $3\pi/4$, π, $5\pi/4$, $3\pi/2$ and $7\pi/4$ in (a)-(j), respectively. Here f = 68.8 Hz, f_l = 50 Hz, a_g = 60/s and b_g = 30/s. This shows that the waveform also varies with the external phase shift, which may induce by the difference of the external interferometer. This variation of the waveform in turn will be shown in the FFT spectrum of the beat signal.

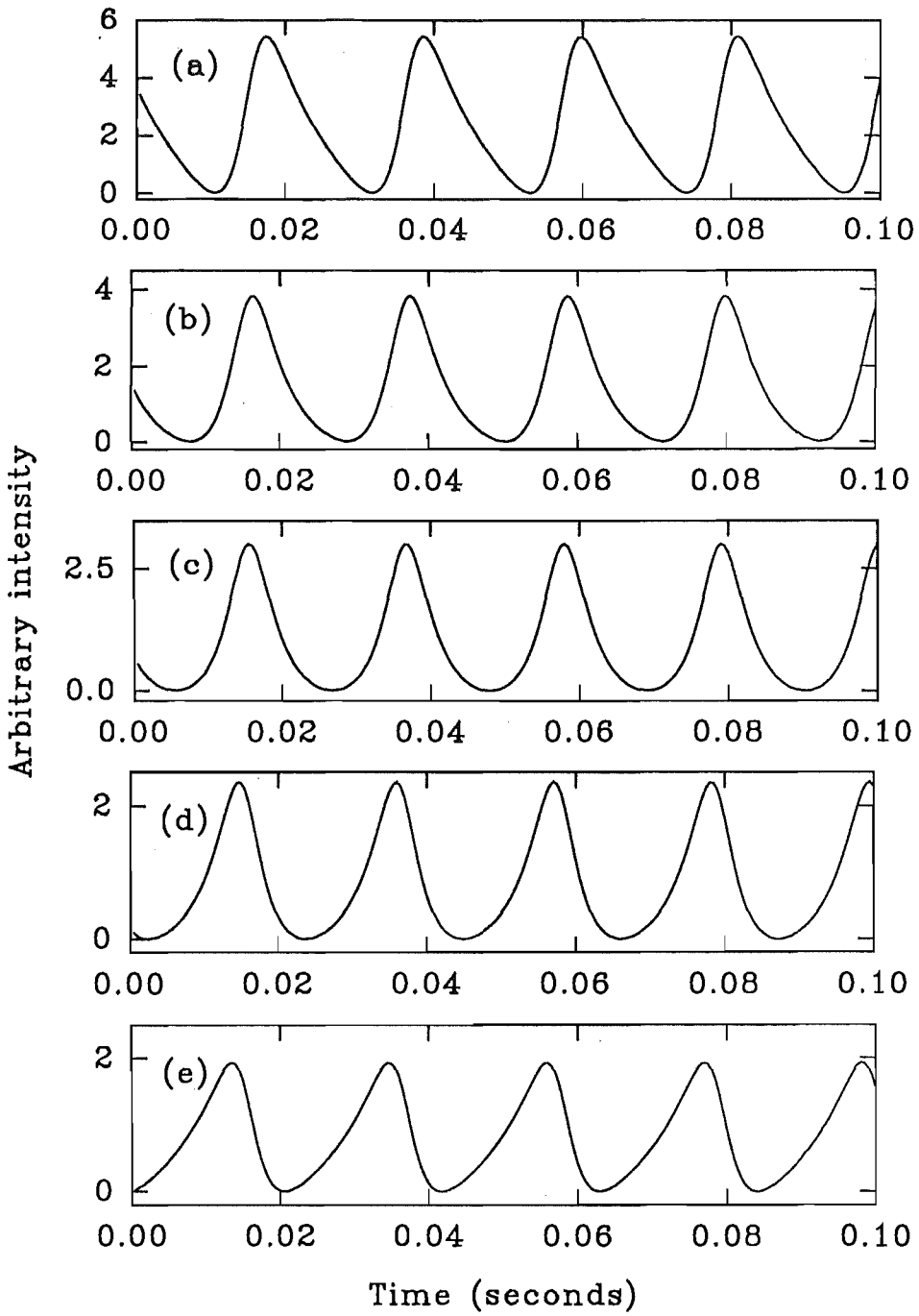

Fig. 7.10a. Variation of the waveform of the beat signal with the external phase difference θ_0: (a) $\theta_0 = 0$, (b) $\theta_0 = \pi/4$, (c) $\theta_0 = 3\pi/8$, (d) $\theta_0 = \pi/2$ and (e) $\theta_0 = 5\pi/8$.

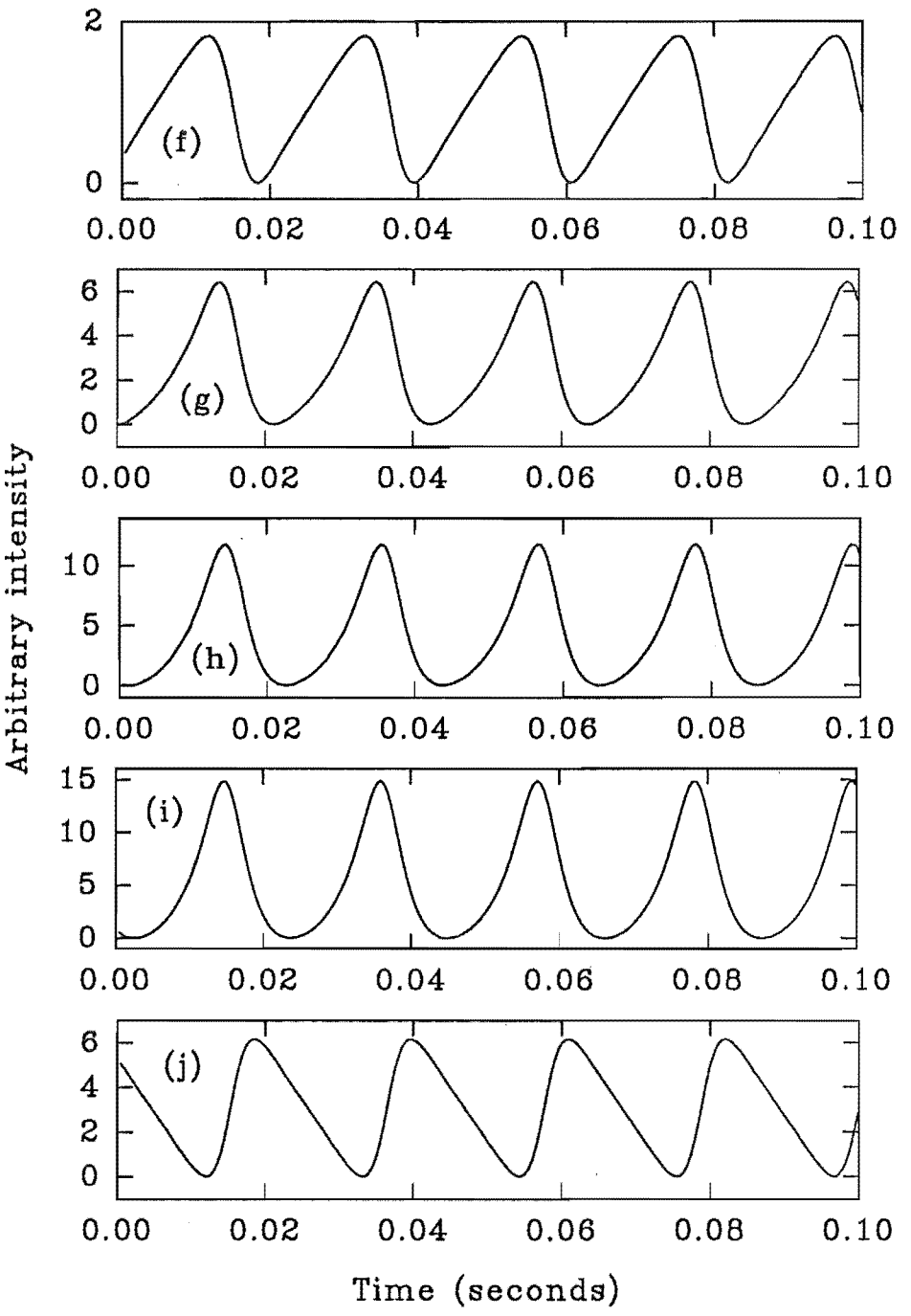

Fig. 7.10b. Variation of the waveform of the beat signal with the external phase difference θ_0: (f) $\theta_0 = 3\pi/4$, (g) $\theta_0 = \pi$, (h) $\theta_0 = 5\pi/4$, (i) $\theta_0 = 3\pi/2$ and (j) $\theta_0 = 7\pi/4$.

Figs. (7.11) and (7.12) give two typical experimental waveforms of the beat signals and their FFT spectra. Fig. (7.11) shows the situation where the oscillating frequencies of CW and CCW modes are highly affected by the backscattering. Its FFT spectrum is shown in the lower diagram; the average beat frequency f_b is 61.03 Hz (the first peak in the spectrum) with its harmonics caused by the backscattering.

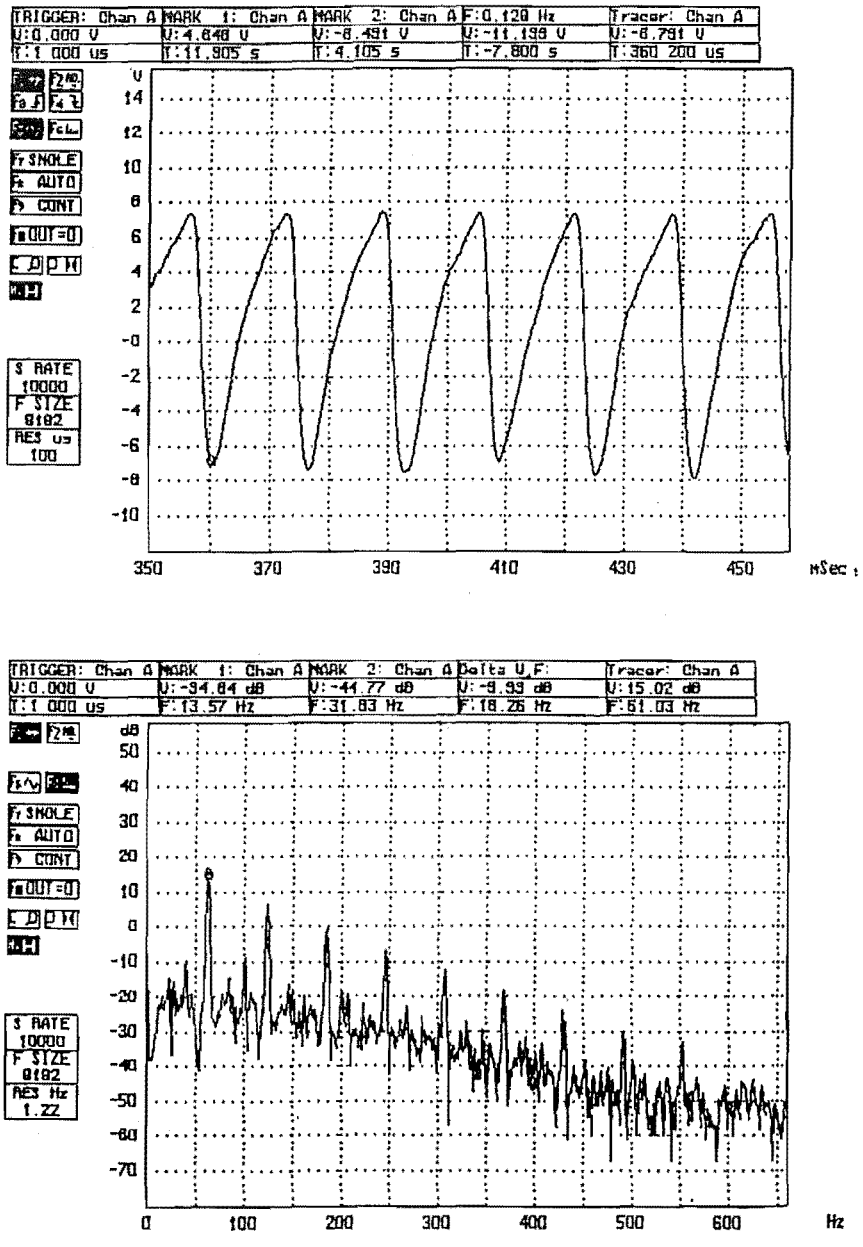

Fig. 7.11. The typical waveform of a beat signal and its FFT spectrum with strong backscattering effect on the beat frequency.

Fig. (7.12) shows the situation where the backscattering effect on the beat frequency is weaker than the above case. The average beat frequency in FIg. (7.12) is 69.58 Hz. In all cases, the magnitudes of the harmonics of beat frequency in the Fourier spectrum are approximately related by a geometrical progression.

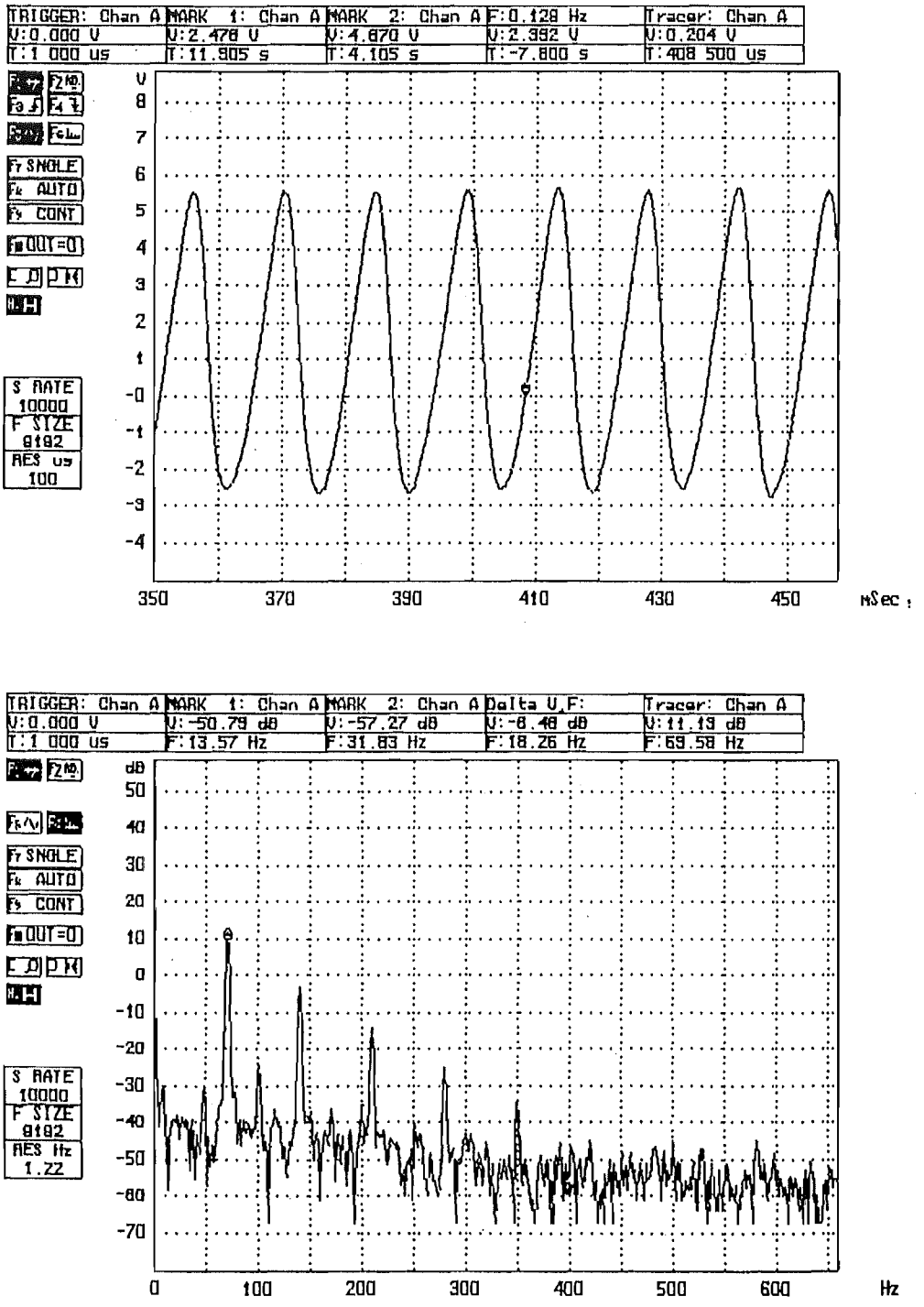

Fig. 7.12. The waveform of a beat signal and its FFT spectrum, but with a less backscattering effect on the beat frequency than the case shown in Fig. 7.11.

Another way of extracting information from the data is to Fourier analyse the instantaneous beat frequency itself, as determined from the MATLAB analytic signal analysis. One's first assumption is that this numerical method is designed precisely to obtain the result of Eq. (7.17), and that its Fourier components at least, if not those of Eq. (7.39), will be in the ratio r of Eq. (7.31a). Therefore even if the raw signal waveform is approximately sinusoidal because of low plasma gain, the instantaneous beat frequency may be expected to show substantial harmonic structure provided only that pulling is important. However as mentioned previously the experimental ratios tend to be much higher than expected, nor does the equivalent numerical processing of a synthesised signal yield the expected answer. These problems have not yet been solved, but are under investigation. In addition, future experimental work will need to check that beam divergences are kept small and so only a small window of the waveform is accepted by the PMT (see Section 7.4.4.).

While this analysis has therefore so far failed to achieve one objective - that that of confirming numerical values for the ratio of the geometric progression of Fourier harmonics in a pulled waveform - on the other hand it has introduced a totally new idea into ring laser data analysis; it has pointed a clear route to this goal; it has answered several previously open questions, and has greatly increased the scope for understanding in much greater depth than previously the physical content of the signal which is obtained from a ring laser. It shows that an analysis of the sampled waveform has far more potential than an analysis of counts of beat notes for determining several key parameters of the ring laser, and gives considerable incentive to a new round of experimental work which will implement these procedures and test the adequacy of the related theory.

It may be remarked here that until the above analyses were worked through, we had no certain knowledge even of the true origin of harmonic terms in the ring laser signal. One suggestion had been that pulling was the principal factor; another, that nonlinearity in the gain of any oscillator would induce harmonics. The above solution of Eq. (7.39) is a curiously satisfying amalgam of these two previous thoughts on the occurrence of harmonics in the signal: both are necessary. Many important points may be noted as corollaries of this analysis. First, the harmonics are not partials; their frequencies are exact multiples of the fundamental. Second, any noise contribution to f, viewed as a temporary variation, will affect the nth harmonic frequency by a factor which is proportional to n. These conclusions were expected, and indeed were employed albeit without such thorough justification in the analysis of Stedman and Bilger (1992).

In short, this analysis is obviously fruitful and is quite novel as far as we are aware, and is being prepared for publication.

Chapter 8

Dispersion of the Laser Medium

The presence of the gain medium (the excited He-Ne gas mixture) and in particular the dispersion associated with it, including the effects of its excited character, induce certain nonlinear shifts in the frequencies of the cavity modes, both excited and unexcited. Both these effects have non-negligible effects on the beat frequency of a ring laser, inducing a bias in its value (Aronowitz 1974). With the presence of gain, which is frequency-dependent, a medium will have enhanced frequency-dependent dispersion. The relation between gain and dispersion can be obtained from the Kramers-Kronig relations (Bennett 1977). Such dispersive effects of the laser medium on the splitting of the counterrotating ring laser modes has been discussed by for example Aronowitz (1971).

The model introduced by Lamb (1964) has met with much success in explaining experimental results for linear He-Ne lasers, such as mode pulling and mode pushing phenomena (Bennett 1962). In Lamb's semiclassical self-consistent approach, an electromagnetic field is assumed to exist in the cavity. The electromagnetic field polarizes the moving atoms. A macroscopic polarization results, which is then used as a source term in Maxwell's equations to calculate a reaction field. Self-consistency gives a set of equations which describes the amplitude and frequencies of the oscillating modes.

Aronowitz (1965) modified Lamb's linear laser theory to account for the behaviour of ring lasers as opposed to linear lasers. The basic distinction between ring laser theory and linear laser theory is that in the ring laser the number of degrees of freedom of the system are doubled. This is due to the independence of the oppositely directed travelling waves. This leads to twice as many equations and added complexity in the analysis. The second major distinction is the nature of

mode coupling. Coupling between the oppositely directed beams can occur through their mutual interaction with the gain medium. Aronowitz (1972a) demonstrated mode competition in a He-Ne ring laser with a natural distribution of neon isotopes (hereafter referred to for simplicity as the "single isotope case, since Ne^{20} then dominates). One of the travelling waves could be appreciably reduced in amplitude and even quenched. Oscillation of each mode results in a measure of gain saturation. The saturation extends over a large range of the atomic transition. Saturation due to the stronger mode can reduce the gain of the weaker below threshold such that it will not oscillate.

Let us summarise here the manner in which such dispersive shifts of a beat frequency are induced. Even when the laser medium is neutral and unexcited, the neon absorption lines will induce in principle some dispersion and so will have an effect on the frequency of the (unexcited) ring laser cavity modes. This effect will be to split the counterrotating further apart, provided they lie well within the line profile. This and the following cases will be discussed in more detail later; the present case is the inverse of that for gain-induced dispersive effects.

In an active ring laser with both (counterpropagating) modes in existence, gain saturation effects associated with mode coupling will act similarly on the beat frequency (although more strongly), since these reduce the effect of gain and so mimic a component of absorption: saturation pushes the resonant frequencies of the oscillating modes away from the centre of the gain curve. Since the furtherest frequency is pushed most, the two frequencies become more widely separated, and so are effectively pushed apart from each other (Aronowitz 1971). This effect of gain saturation on mode frequency is termed mode pushing.

It has been found useful as an experimental way of reducing intermode coupling and so of reducing this pushing effect to replace natural neon, with its 9.1:1 mixture of the Ne^{20} - Ne^{22} isotopes, by an isotopically enriched mixture with approximately 1:1 Ne^{20} - Ne^{22} isotopic ratio. This significantly reduces mode competition in ring lasers (Aronowitz 1971, Chow *et al.* 1980, Statz *et al.* 1986). In this case, the oppositely travelling modes oscillate near the centre of the combined gain curve of the two isotopes, rather than near the peak of either, and so tend to interact with different velocity groups of neon atoms. The system approaches a limit in which the amplifiers for the cw and ccw waves are separate. A detailed discussion of these and other such points is given in later sections.

Although the mode pushing problem can be largely overcome in this manner by using isotopically enriched neon mixtures, the beat frequency of a ring laser still varies with the detuning of the oscillating frequencies of the oppositely travelling modes from the gain centre and with the variation of the gain level of the laser

(Aronowitz 1974). This is because the nonlinear dispersion associated with and dependent on the gain will pull the frequencies of the ring laser cavity modes towards the centre of the gain profile, so decreasing their beat frequency. This effect is called mode pulling. It can be reduced by lowering the gain to its minimal level, and this (with the effort to achieve high frequency resolution and single mode operation) is another strong reason for using high-quality mirrors and minimal plasma excitation in such a device as the Canterbury ring laser.

In our ring laser experiments, both the natural and various enriched Ne^{20} - Ne^{22} isotope mixtures have been used. We indeed confirm that Ne^{20} - Ne^{22} isotope mixture is helpful for improving the stability of the frequency splitting (or beat frequency) of our ring laser, and in particular prevents mode pushing in the earth rotation induced beat frequency at the hertz level. Another and (as far as we know) a completely novel finding in our experiments is that a transverse magnetic field applied to the laser plasma also helps to stabilize the beat frequency against the effects of gain fluctuations, although it introduces a relatively substantial bias, a simple permanent magnet being adequate to push the beat frequency from the nominal 68.68 Hz to well over 100 Hz. While Aronowitz (1971) has discussed qualitatively the effects of longitudinal magnetic fields, the mechanism of this new phenomenon using a transverse magnetic field is not clear and has not been discussed in the literature.

The basic ring laser equations which are derived by Aronowitz (1971) and various equivalent forms have been widely used in the literature (Aronowitz *et al.* 1974, M-Tehrani and Mandel 1978a, 1978b, Christian and Mandel 1986, 1988, Christian *et al.* 1988, Pesquera and Blanco 1989, Pesquera *et al.* 1989, Blanco, and Spreeuw *et al.* 1990, Chyba 1990, Etrich *et al.* 1992). However, if one requires an analysis of dispersion from the basic mechanisms of laser operation, the interpretation and analysis of these equations is difficult.

Statz *et al.* (1985) presented an explicit analysis for the effects of dispersion in a multioscillator ring laser where four modes are operating in a nonplanar cavity. In the following analysis, we adopt the method of analysis presented by Statz *et al.* (1985). In Sec. 8.1, we give an analysis to explain the mode pulling effect on the beat frequency of the ring laser, following the calculations particularly for the case of our ring laser. In Sec. 8.2, we will discuss the mode pushing effect caused by the saturation of the gain medium in a ring laser. We use the Yntema diagram (Chow *et al.* 1980) to explain the mode pushing effect induced by the gain saturation. We will explain why an enriched neon Ne^{20} - Ne^{22} mixture can avoid the mode coupling problem in Sec. 8.4. Finally, we will present in Sec. 8.5 our experimental results and a preliminary analysis of the effect of a

transverse magnetic field effect in biasing and stabilizing the beat frequency of the ring laser.

8.1 Dispersion of unsaturated gain medium

In a ring laser system, the effects on the beat frequency of dispersion in the unsaturated and in the saturated gain medium are totally different. In this chapter, we will first discuss the case of unsaturated dispersion of the laser medium.

8.1.1 Equations for dispersion

We assume in the following analysis that each neon atom, when probed by a laser beam, exhibits a Lorentzian power gain shape of the form (Statz *et al.* 1985)

$$g(\nu, \nu_0) = g_0\{1 + [(\nu - \nu_0)/\Delta\nu_L]^2\}^{-1} \tag{8.1}$$

where g_0 is the gain at line centre for unit density of active atoms and unit length of gain section, ν_0 is the line centre, and $\Delta\nu_L$ is the halfwidth of the line at half maximum. This Lorentzian gain shape is produced by the homogeneous broadening mechanism. Homogeneous broadening in He-Ne lasers is dependent on spontaneous emission of the radiating atoms and on their dephasing collisions with various collision partners (Siegman 1986). In a typical gas mixture atoms may collide with other atoms of the same kind (called "self-broadening"); with atoms of different kinds (called "foreign-gas broadening"); or with the tube walls (generally not of importance at optical frequencies). The total collision-broadening contribution to the homogeneous linewidth of a given atomic transition will then be directly proportional to the density, or to the partial pressure, of each species that is present. According to Statz *et al.* (1985), $\Delta\nu_L$ will increase linearly with total gas pressure in the form

$$\Delta\nu_L = (15 + 57p[\text{Torr}]) \times 10^6 \tag{8.2}$$

where p[Torr] is the total gas pressure in Torr. A 7:1 ratio of He:Ne partial pressure is assumed in this result.

The optical phase shift associated with the power gain in Eq. (8.1) is given by utilizing the Kramers-Kronig relation (Bennett 1977) as

$$\phi_d(\nu, \nu_0) = g(\nu, \nu_0)(\nu - \nu_0)/2\Delta\nu_L$$
$$= g_0\{1 + [(\nu - \nu_0)/\Delta\nu_L]^2\}^{-1}(\nu - \nu_0)/2\Delta\nu_L \quad (8.3)$$

For a He-Ne laser system, the line frequencies ν_0 as seen by the laser beam are spread out because of the Maxwellian velocity distribution (itself of Gaussian functional form) of the neon atoms, thus causing a spread of Doppler shifts. Therefore, the actual frequency distribution of the He-Ne laser line is a Gaussian distribution of Lorenzians. For a ring laser, Ne^{20}-Ne^{22} isotope mixture are used for reducing the saturation effects on the laser oscillating frequencies. Therefore, there are two Doppler-broadened lines, one for each isotope. The gain function and phase shift equtions (8.1) and (8.3) thus have to be multiplied by a weighting function $W(\nu_0)$ which describes the relative density of atoms which have their resonant frequencies, as seen by the laser beam, at ν_0.

The total gain $G(\nu)$ in the laser transition line may be thus be written (Statz *et al.* 1985)

$$G(\nu) = \int_{-\infty}^{+\infty} g(\nu, \nu_0)W(\nu_0)\, d\nu_0 \quad (8.4)$$

and the total phase shift $\Phi_d(\nu)$ of the complete line is similarly

$$\Phi_d(\nu) = \int_{-\infty}^{+\infty} \phi_d(\nu, \nu_0)W(\nu_0)\, d\nu_0. \quad (8.5)$$

The weighting function used in Eqs. (8.4) and (8.5) is

$$W(\nu_0) = N\{(F_{20}/\Delta\nu_{20})\exp-[(\nu_0-\nu_{00}+\nu_{sh}/2)/\Delta\nu_{20}]^2$$
$$+ (F_{22}/\Delta\nu_{22})\exp-[(\nu_0-\nu_{00}-\nu_{sh}/2)/\Delta\nu_{22}]^2\} \quad (8.6)$$

where N is a normalizing factor proportional to the density of Ne atoms in the upper state minus the number in the lower state times the length of the gain medium. F_{20} and F_{22} are the fractions of the Ne^{20} and Ne^{22} isotopes in the laser medium; $\Delta\nu_{20}$ and $\Delta\nu_{22}$ represent the 1/e halfwidths of the Ne^{20} and Ne^{22} lines due to Doppler broadening; ν_{00} is the average frequency of the Ne isotope transition; ν_{sh} is the isotope splitting, which is 900 MHz (Statz *et al.* 1985). Furthermore

$$\Delta\nu_{20} = \nu_{00}(2kT/M_{20}c^2)^{1/2} \tag{8.7a}$$
$$\Delta\nu_{22} = \nu_{00}(2kT/M_{22}c^2)^{1/2} \tag{8.7b}$$

where k is Boltzmann's constant, T is the absolute temperature, and M_{20} and M_{22} are the atomic masses of the Ne^{20} and Ne^{22} isotopes.

The phase shift in Eq. (8.5) can readily be converted into a frequency shift $\Delta\nu$ by

$$\Delta\nu = -c\Phi_d(\nu)/2\pi P \tag{8.8}$$

By using Eqs. (8.1)-(8.8), we can calculate the dispersion effects on the frequency shifts of the oppositely travelling modes in a ring laser. We assume that the frequency splitting of a ring laser $\eta = \nu_2 - \nu_1$, caused by the ring rotation. For the convenience of calculation, we change variables to $x = \nu_0 - \nu_{00}$ and $\zeta = [(\nu_2 + \nu_1)/2] - \nu_{00}$, we can rewrite Eq. (8.1) for two oppositely traveling modes as $g_1 = g_0\{1 + [(\zeta + \eta/2 - x)/\Delta\nu_L]^2\}^{-1}$ and $g_2 = g_0\{1 + [(\zeta - \eta/2 - x)/\Delta\nu_L]^2\}^{-1}$. Then Eq. (8.3) for the phase shifts of the two oppositely travelling modes can be written as

$$\phi_{d1} = g_1(\zeta + \eta/2 - x)/2\Delta\nu_L \tag{8.9a}$$
$$\phi_{d2} = g_2(\zeta - \eta/2 - x)/2\Delta\nu_L \tag{8.9b}$$

where the parameter ζ describes the detuning of the average frequency of the laser modes from the average frequency of the Ne isotopes. The total gain and phase shift for the each mode in the ring laser can be rewritten as

$$G_i(\zeta, \eta) = \int_{-\infty}^{+\infty} g_i(\zeta, \eta, x)W(x)\,dx \tag{8.10}$$
$$\Phi_{di}(\zeta, \eta) = \int_{-\infty}^{+\infty} \phi_{di}(\zeta, \eta, x)W(x)\,dx \tag{8.11}$$

where i represents 1 and 2, and the weighting function

$$W(x) = N\{(F_{20}/\Delta\nu_{20})\exp-[(x + \nu_{sh}/2)/\Delta\nu_{20}]^2 + (F_{22}/\Delta\nu_{22})\exp-[(x - \nu_{sh}/2)/\Delta\nu_{22}]^2\} \tag{8.12}$$

8.1.2 Numerical calculations for the gain dispersion

We assume the neon isotopes have the equal proportion in the gas mixtures. The neon isotope splitting are near 900 MHz (Statz *et al.* 1985). Fig. 8.1(a) shows a series of gain curves calculated from Eq. (8.10), with the peak gain of 0.05%, 0.1%, 0.2% and 0.5% respectively. When we neglect saturation effects, then the peak gain of the medium is equal to the cavity loss for steady-state operation. Fig. 8.1(b) represents the phase shifts related with the different gain curves.

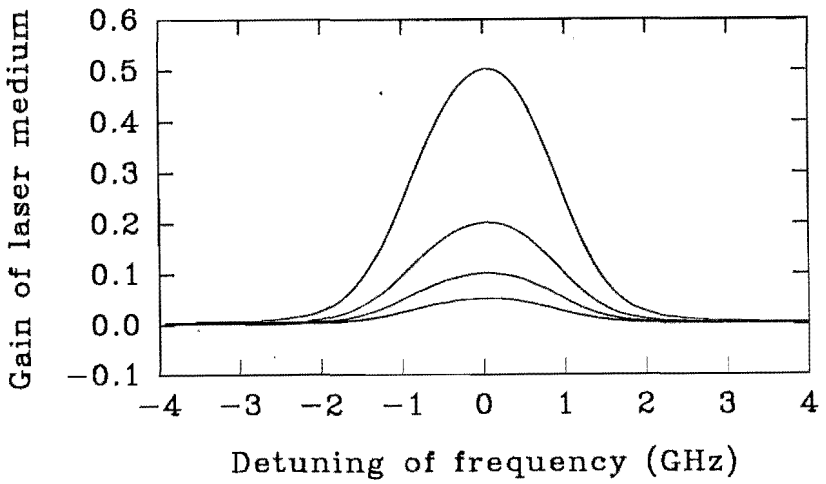

(a)

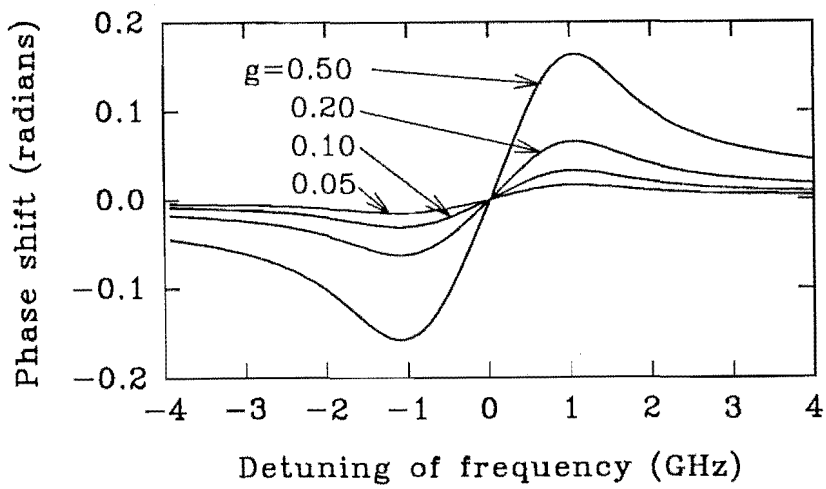

(b)

Fig. 8.1. Gain (a) and dispersion (b) curves versus frequency for a He-Ne with an equal isotope mixture of Ne^{20} and Ne^{22}. Peak gain is 0.05, 0.10, 0.20 and 0.5, respectively as in all following curves.

The frequency shifts of a laser mode in the cavity with the different gain values are plotted in Fig. 8.2(a). By using this diagram, the frequency pulling effect of the dispersion may be more easily interpreted. When the laser frequency ν is less than the central frequency ν_{00} of the gain curve, the frequency shift caused by the dispersion of the gain medium is positive, so that the laser frequency is always pulling towards the centre of the gain medium. On the other hand, when the laser frequency is larger than ν_{00}, the frequency shift of the laser mode is negative, the laser frequency is then also pulling towards the centre of the gain medium.

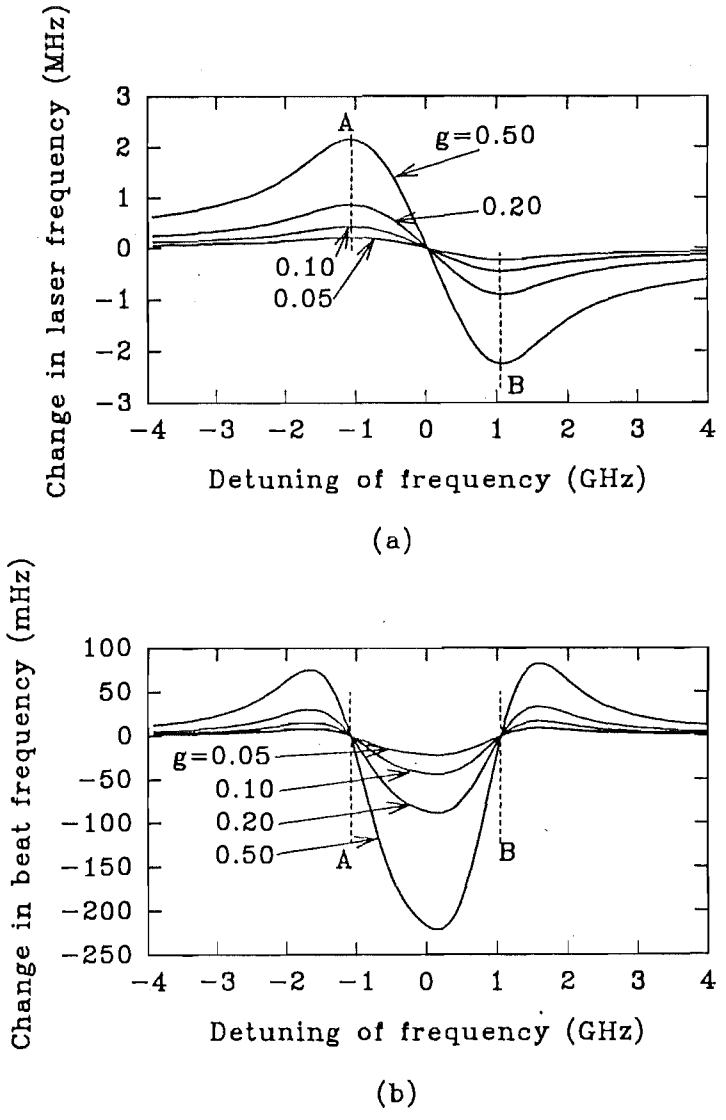

Fig. 8.2. The laser frequency shifts induced by the dispersion of the laser medium with the different gain levels are shown in (a). The beat frequency (or differential laser frequency shift) shifts are plotted in (b).

For a ring laser, what is of interest is not so much the pulling of both the oppositely traveling modes, as the difference in this pulling. We now examine the beat frequency shifts (or differential pulling) induced by the dispersion of the gain medium; these are presented in Fig. 8.2(b). We find that the beat frequency shifts will decrease in the range between the points A and B, but will increase out of this range. The explanation can be given by means of Fig. 8.2(a). We assume the frequency difference f_R of the two oppositely travelling modes, induced by the rotation of the cavity, is sufficiently small (about 70 Hz for our ring laser, as compared to the neon isotopic linewidths of 800 MHz), that the beat frequency shift Δf can be expressed as $\Delta f = f_R \, d\nu/dx$, where ν is the averaged laser frequency of the two modes and $x = \nu - \nu_{00}$, is the dutuning of the laser frequency. Then the beat frequency depends on the derivative of the laser averaged frequency. Therefore, for the range between points A and B, $d\nu/dx < 0$ and the beat frequency will decrease. If the laser frequencies of the two modes are out of this range, $d\nu/dx$ becomes positive and the beat frequency will increase.

Close inspection of the gain, phase shift, laser frequency shift and, in particular, of Fig. 8.2(b) reveals small asymmetries for equal mixtures of the isotopes. This is because the atomic Doppler line width for a gas of Ne^{20} at a given temperature is greater than that for Ne^{22}. The linewidth ratio of Ne^{20} to Ne^{22} is $(M_{22}/M_{20})^{1/2}$, a result given by Eqs. (8.7a) and (8.7b).

Fig. (8.3) shows the deviation of the gain peak of the isotope mixture with the proportion of Ne^{20}. For a ring laser, as we shall show, it is preferable for the

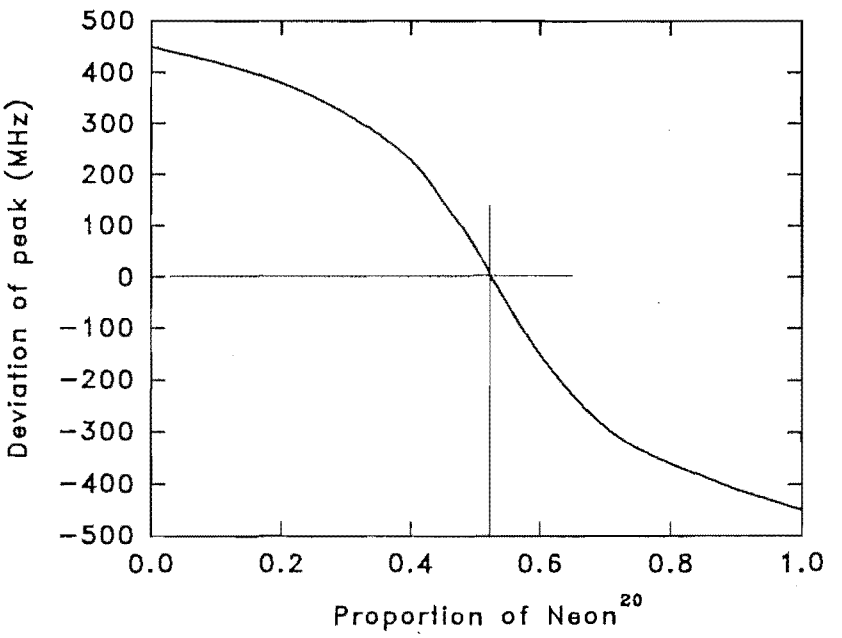

Fig. 8.3. The deviation of the gain peak of the isotope mixture with the proportion of Ne^{20}.

laser mode frequency to be the average of the frequencies for the peaks of the Ne^{20} and Ne^{22} transitions, so as to reduce the mode competition effects on the beat frequency. To this end we make the overall gain curve itself peak at this average frequency of the two neon isotope transitions. Because of the slight difference in the Doppler widths, this in turn requires a choice of the abundance ratio for Ne^{20}:Ne^{22} which is slightly greater than 50%, while still much less than the abundance ratio for naturally occurring neon. Fig. (8.3) shows that the mixture with 53% Ne^{20} and 57% Ne^{22} has its gain peak at the appropriate average frequency.

8.2 Hole-burning in gain curve

The gain coefficients in laser materials are directly proportional to the population difference in the states involved in the laser transition. In a great many atomic systems the population difference in the atomic transition will very often saturate with increasing signal strength. This saturation of the gain medium changes the dispersion of the gain medium and so affects the beat frequency of a ring laser. The hole-burning phenomenon is the consequence of the gain saturation in the inhomogeneous broadening line shape (Bennett 1962).

We have seen that the line shape of the inhomogeneous broadening gain medium is a Gaussian distribution of Lorenzians. All the atoms in each Lorentzian profile (or spectral packet) have essentially the same (homogeneous) response to the laser beam in the laser. The total response of an inhomogeneously broadened line is then the sum of the individual responses of all the spectral packets, each at a different resonance frequency.

When a laser wave at frequency ν_1 exists in a ring cavity, this laser signal will saturate the population difference only for those spectral packets, whose resonance frequencies are in resonance or nearly in resonance with the laser frequency ν_1. These are the only atoms with which the laser signal strongly interacts. As the laser wave increases in strength, only those spectral packets coincident with or immediately adjacent to the laser frequency will be saturated. The spectral packets at more distant frequencies will be essentially unchanged. As a result, with increasing laser power the strong saturating signal will burn a hole in the atomic gain curve.

Now, a spectral packet at frequency ν_0, in the presence of the laser wave within the inhomogeneous linewidth of a He-Ne laser, will have its effective population reduced by a saturation factor which we will write in general as $S(\nu_0)$.

For the particular situation of a single laser signal with the intensity I_1 at frequency ν_1, this saturating factor for the packet at ν_0 will be given by (Siegman 1986)

$$S(\nu_0) = [1 + F(\nu_0, \nu_1, I_1, I_{sat})]^{-1} \tag{8.13}$$

where the factor F is given by

$$F(\nu_0, \nu_1, I_1, I_{sat}) = (I_1/I_{sat})\{1 + [(\nu_1 - \nu_0)/\Delta\nu_L]^2\}^{-1}, \tag{8.14}$$

and I_{sat} is the saturation intensity, or the value of laser signal intensity passing through the gain medium whose saturation effect reduces the gain coefficient to one half of its unsaturated value.

8.3 Mode-pushing effect on beat frequency

8.3.1. Laser frequency far away from gain centre

For a He-Ne laser, the atoms in the atomic gas will have thermal or kinetic motion with a Maxwellian or Gaussian distribution of kinetic velocities, given by (e.g. Siegman 1986)

$$g(v_z) = (1/2\pi\sigma_v^2)^{1/2} \exp(-v_z^2/2\sigma_v^2) \tag{8.15}$$

The rms spread is given by $\sigma_v^2 = kT/M$. For a ring laser in a nonrotating state, the two oppositely travelling modes oscillate at the same frequency ν. Let us assume that the clockwise (cw) wave moves parallel to the local z axis used to describe the velocity of the gas/plasma particles, and that the laser cavity mode frequency ν is detuned from the central frequency, ν_0, of the gain curve of the plasma. In this case, as shown in Fig. 8.4(a), the cw mode will interact with, and will tend to saturate, those atoms whose axial velocity v_+ is given by

$$v_+ = v_z = (\nu_0 - \nu)c/\nu_0 \tag{8.16a}$$

where c is the speed of light. Now the counterclockwise (ccw) beam oscillating at the same frequency will interact with an oppositely moving group of atoms whose

velocity v_- is given by

$$v_- = - v_z = - (\nu_0 - \nu)c/\nu_0. \tag{8.16b}$$

Therefore, for the inhomogeneous-broadened line shape, the saturation caused by the laser waves, even through they have the same frequency, will burn two holes which are symmetrically on opposite sides of the excited-atomic distribution of the kinetic velocities, as shown in Fig. (8.4b). Here we use the Yntema diagram (Chow *et al.* 1980) to translate between mode frequency and the atomic axial velocities.

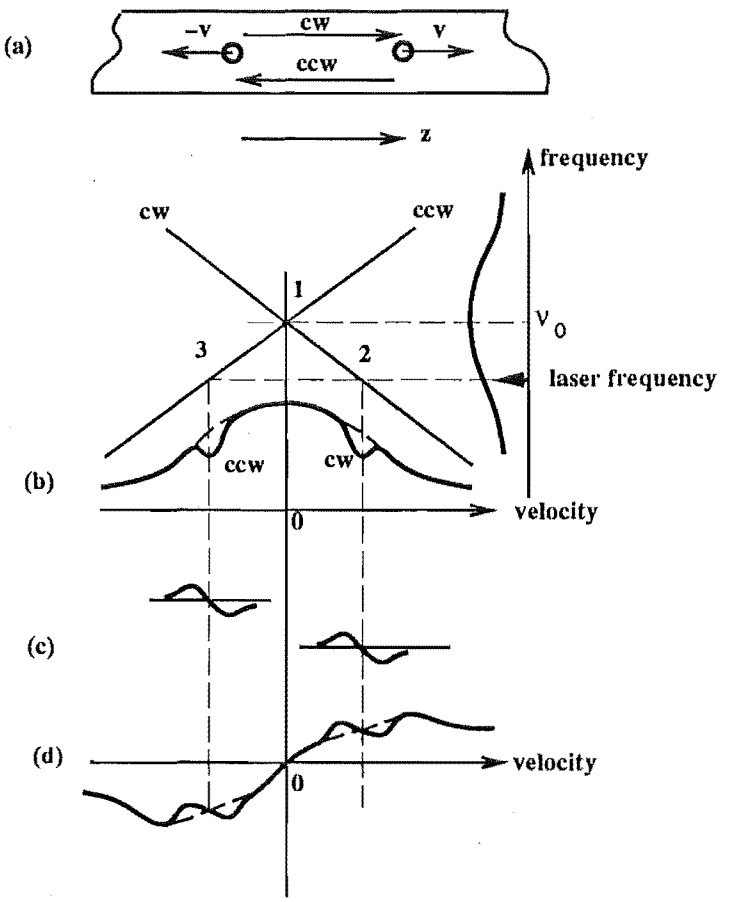

Fig. 8.4. (a) A model for analysis of He-Ne laser interaction with the excited atoms. (b) Yntema diagram for determine the location of the hole burning. (c) The dispersion changes induced by the individual hole burning. (d) This diagram shows that the CW and CCW modes do not interfere with each other when the separation of the two holes on the gain distribution is far larger than the hole width.

The Yntema diagram method is very useful for illustrating the mode interactions which will be the subject of the following discussions. In Fig. 8.4(b), the abscissa represents the atomic axial velocity with positive values taken clockwise. A Gaussian curve representing the unsaturated population inversion (broken line) is plotted on the abscissa. The ordinate on the right represents the optical mode frequencies and has the unsaturated gain plotted on it. With no detuning, a stationary atom ($v_z = 0$) interacts with the natural atomic frequency ν_0. Hence, to translate between ν_0 and $v_z = 0$ we draw a horizontal line from ν_0 that intersects a vertical line drawn from $v_z = 0$ at point 1. Consider an clockwise wave with a frequency $\nu < \nu_0$. To interact resonantly with this wave, the atom must have a velocity in the clockwise, or $+z$, direction. A vertical line is drawn from this velocity (the hole labelled cw) so as to intersect a horizontal line drawn from ν at point 2. A line labelled cw is then drawn through points 1 and 2. Now the velocity group that interacts with any clockwise wave can be obtained by drawing a vertical line from the point of intersection between the line cw and the horizontal line from the mode frequency. For a counterclockwise wave, a similar analysis gives the line labelled ccw, where the ccw beam will interact with the atoms which have a velocity (corresponding to the hole ccw) in the anticlockwise direction.

Therefore, when the laser frequency ν is far away from the central frequency ν_0, the oppositely travelling laser modes interact with essentially different groups or velocity classes of the atoms, so that the saturation in the gain medium caused by each mode does not interfere with each other. Fig. 8.4(c) shows the dispersion changes in the gain medium caused by the ccw and cw waves separately. The total dispersion of the gain curve in this case is shown in Fig. 8.4(d). Since a hole burnt by one of the bidirectional travelling modes represents a symmetric removal of atoms about the laser frequency to first order, the hole does not have a first-order dispersive effect on the laser frequency itself (Bennett 1962).

8.3.2 Single neon isotope

Let us consider the case when a single isotope of neon only is present. When the laser frequencies of the cw and ccw wave are tuned close to the centre of the gain curve, as shown in the right side of the Fig. 8.5(a), a very strong interaction between the cw and ccw wave exists, the so–called mode competition (Aronowitz, 1972a). In this case, the holes (broken lines) induced by the the cw and ccw waves will overlap. Fig. 8.5(b) shows the individual dispersions associated with each hole

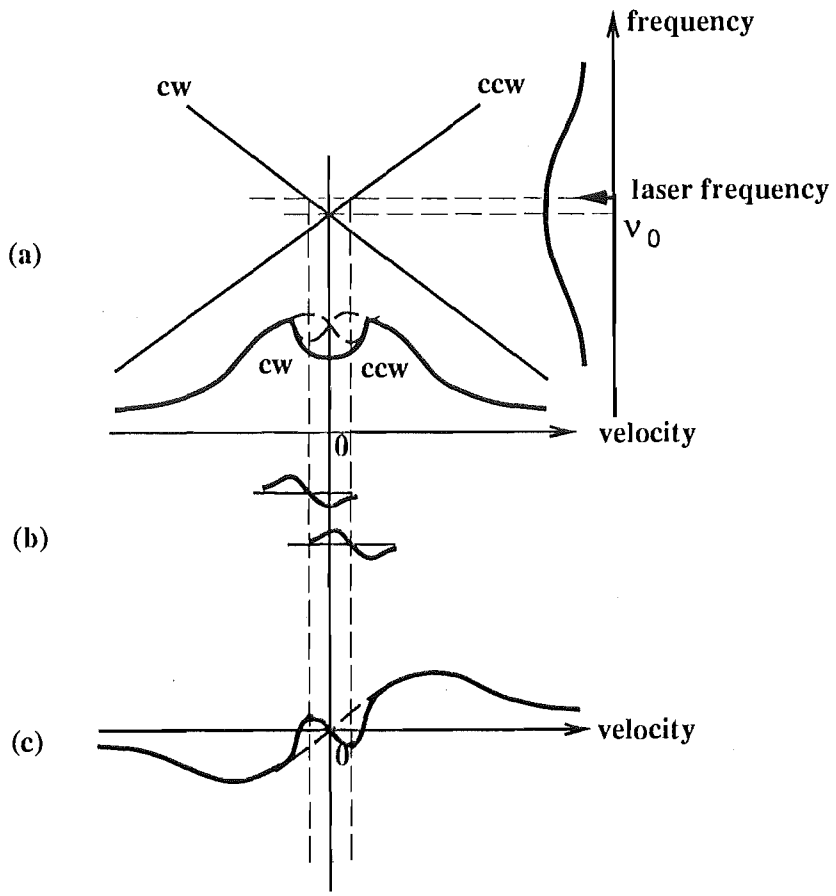

Fig. 8.5. (a) Yntema diagram for a single isotope with the laser mode oscillating close to the centre of the gain curve. In this case, the mode competition between CW and CCW waves will become strong as the two holes overlap partly. (c) and (d) show the dispersion of the gain, where the refractive index of the gain seen by a laser mode will be changed by another.

caused by the cw and ccw waves respectively. The total dispersion of the gain curve is shown in Fig. 8.5(c). In this case, the slope of the gain curve has been changed to a negative value at the portion located at the laser frequencies, and these two mode frequencies have been pushed away from each other, giving the so-called mode pushing. Therefore, the beat frequency of the ring laser will increase in this case.

8.3.3 Enriched neon isotope mixtures

When a He-Ne ring laser has the laser frequencies of the oppositely travelling modes on opposite sides of the centre of the gain curve, mode competition can be eliminated by reducing the gain medium coupling between the oppositely directed beams. This can be done by operating the laser with a mixture of isotopes of Ne^{20} and Ne^{22} (Aronowitz 1971, Statz *et al.* 1985). The centre of the atomic transition of Ne^{22} lies 875 MHz and 261 MHz higher than the centre for Ne^{20} for the 0.633 μm and 1.15 μm transitions, respectively (Aronowitz 1971). Statz *et al.* (1985) give their measurement of the isotope splitting, which is near 900 MHz for 0.633 μm, the value we use in our discussion.

Using an enriched neon isotope mixture largely overcomes the mode competition problem for a ring laser. The Yntema diagram may be extended to the case of two isotopes of Ne^{20} and Ne^{22} as shown in Fig. (8.6). In this a second diagram is superimposed upon the first. The gain curves for each isotope are displaced in frequency space. Thus, each isotope has a separate set of reflection lines cw_{2i} and ccw_{2i}, $i = 0$ or 2. Keeping the two population inversions separate allows easy determination of which isotope's holes are involved. For a proper Ne^{20}:Ne^{22} isotope mixture, the centre of the combined gain curve is approximately the average of the frequencies of the individual Ne^{20} and Ne^{22} transitions, as shown in the right side diagram of Fig.(8.6). In this case, the laser frequencies of the oppositely travelling modes of a ring laser will interact with the atoms which are separated in frequency from the central frequencies of each isotope by approximately 450 MHz (half of the isotope splitting). The clockwise wave will interact with the atoms which have the velocities $v_z < 0$ (hole cw_{20}) for the Ne^{20} isotope and $v_z > 0$ (hole cw_{22}) for the Ne^{22} isotope, respectively. On the other hand, the counter-clockwise wave will interact with the atoms which have the velocities $v_z > 0$ (hole ccw_{20}) for Ne^{20} and $v_z < 0$ (hole ccw_{22}) for the Ne^{22} isotope. For a He-Ne laser with a combined Ne^{20} and Ne^{22} mixture pressure of 2 torr, the half width of the homogeneously broadening line is about 130 MHz given by Eq. (8.2). Then, for a ring laser with an equal neon isotope mixture, the oppositely travelling waves will burn four holes in the two isotopes. These holes are well separated in the atomic velocity distribution. This means that the oppositely travelling waves interact with essentially different spectral packets, and that there is no interference between them through the gain medium. Therefore, mode competition or mode pushing effects can be negligible in a ring laser with an enriched neon isotope mixture. In this case, the dispersion of the gain medium is similar to the situation of the unsaturated gain line as shown in the right side

diagram of Fig. (8.6).

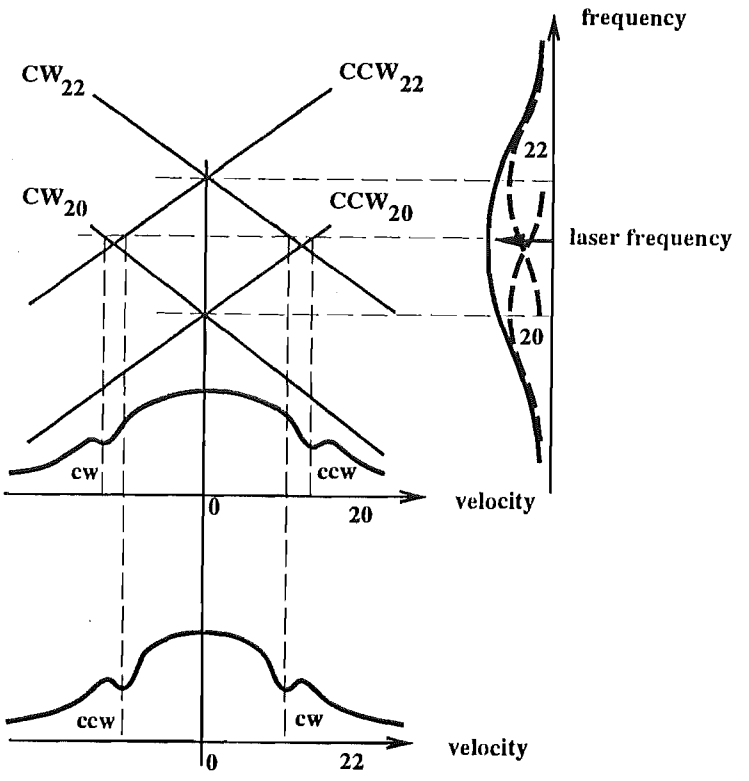

Fig. 8.6. Yntema diagram for two isotopes. This diagram allows determination of which isotope's velocity group is involved given any mode frequency. In an equal isotope mixture, the laser modes oscillate around the middle between of the two isotope transitions and then far from the each isotope's centre. Therefore, the mode competition is avoid.

8.3.4 Natural neon gas

In our experiment, natural neon gas was at first used for our laser operation. Natural neon is approximately 91% Ne^{20} and 9% Ne^{22} (Aronowitz 1972b). The beat frequency of our ring laser under earth rotation is nominally 68.68 Hz. The operating frequencies of the cw and ccw beams will be near the centre of the gain curve of the natural neon. In this case, the frequency splitting in our ring laser is observed to vary from 54 Hz to 76 Hz over a period of minutes or hours, as the excited cavity modes are tuned through the gain curve peak by thermal expansion and the change in optical path length.

Fig. (8.7) shows the case for the natural neon mixture. Since the proportion of Ne^{22} in the mixtures is only about 9%, the profile of the combination of neon isotopes will be asymmetric and the centre of the isotope mixture will be very

close to the centre of the Ne^{20} isotope distribution. The operating frequencies of the oppositely travelling waves in our ring laser are therefore near the centre of the Ne^{20} isotope distribution. In this case, though the oppositely travelling waves will still burn four holes in the two isotopes, the two holes burned in the Ne^{20} will overlap to some extent. The mode competition and mode pushing effects on the beat frequency of a ring laser are readily apparent.

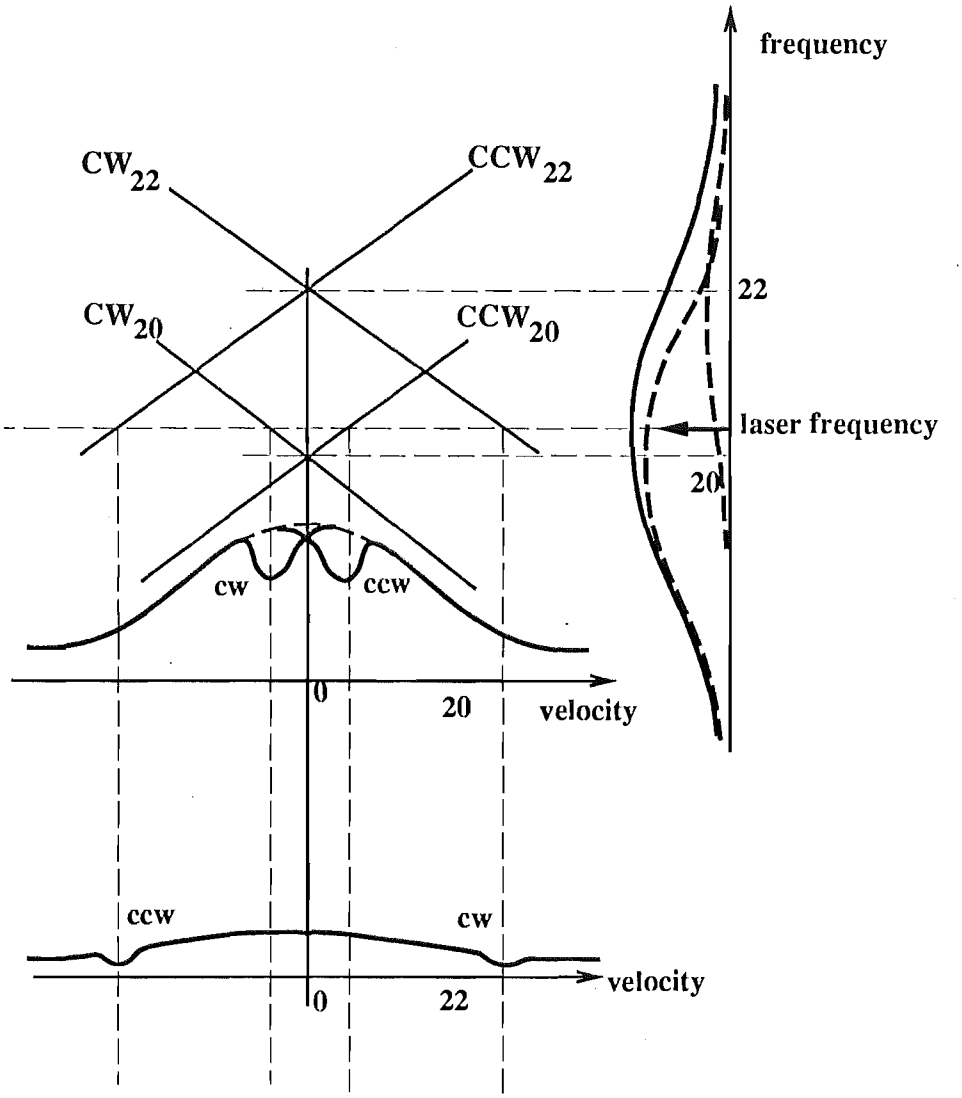

Fig. 8.7. Yntema diagram for natural neon. In this case, the two holes on the gain curve partly overlap. Therefore the mode competition between CW and CCW waves is reasonably strong, and in turn the beat frequency of the two modes varies with the cavity detuning.

8.4 Optical bias induced by multimode excitation

In our ring laser system, the free spectral range of the ring cavity (c/P, where P is the perimeter) is 86.218 MHz. This frequency difference is comparatively small compared with the FWHM of the gain curve, itself approximately 1.5 GHz and 2 GHz for the natural neon mixture and for the equal isotope mixture, respectively. In order to excite just one pair of oppositely travelling modes, the laser is driven with these modes just above the lasing threshold. When the power of the radio frequency discharge is increased, two pairs of laser modes may be excited so as to oscillate simultaneously in the cavity. In this case, the frequency splitting of the ring laser becomes higher than in the case of the single frequency oscillating the ring. In the Canterbury ring this frequency varies from 140 Hz to 300 Hz, depending on the level of the discharge and the detuning of the cavity length .

Such a phenomenon has been reported by Scully et at (1978), Anderson *et al.* (1979, 1980) and Chow *et al.* (1980) as a new method to overcome the frequency locking problem in plane ring laser gyroscopes. A theoretical analysis is given by Scully *et al.* (1978). They show that the presence of an additional pair of modes oscillating in the cavity could significantly reduce the lock-in threshold because of nonlinear coupling effects. They did not mention any drawbacks of this scheme.

As a result of our experimental work, we find that there is a fundamental problem in this method of eliminating lockin, which seriously affects the stability of the beat frequency of the ring laser. To understand the principle of this method, let us see the situation as shown in Fig. (8.8). For simplicity of discussion, we assume the laser medium is an equal mixture of Ne^{20} and Ne^{22} isotopes. We increase the gain of our ring laser so that two strong modes and two weak modes oscillate in the cavity as shown in Fig. 8.8(a). The splitting of the oppositely directed and active modes of the ring laser is so small (tens, perhaps hundreds, of hertz) that it cannot be shown in this diagram; the composite atomic gain curve is approximately 2 GHz wide. The two strong modes are numbered 1 and 2; the two weak modes are numbered 3 and 4. Modes 1 and 3 are clockwise modes, while 2 and 4 are counter-clockwise modes.

In the case of the equal isotope mixture, these four modes will burn eight holes in two isotope gain curves as shown in Fig. 8.8(b). Each mode will burn one hole in the Ne^{20} isotope gain curve and another in that for the Ne^{22} isotope. For example, mode 1 will burn the hole cw_{1-20} in the He^{20} and the hole cw_{1-22} in the He^{22} isotope curve. On the other hand, the oppositely travelling mode 2 will burn the holes ccw_{2-20} and ccw_{2-22} which are symmetrically placed with respect to the

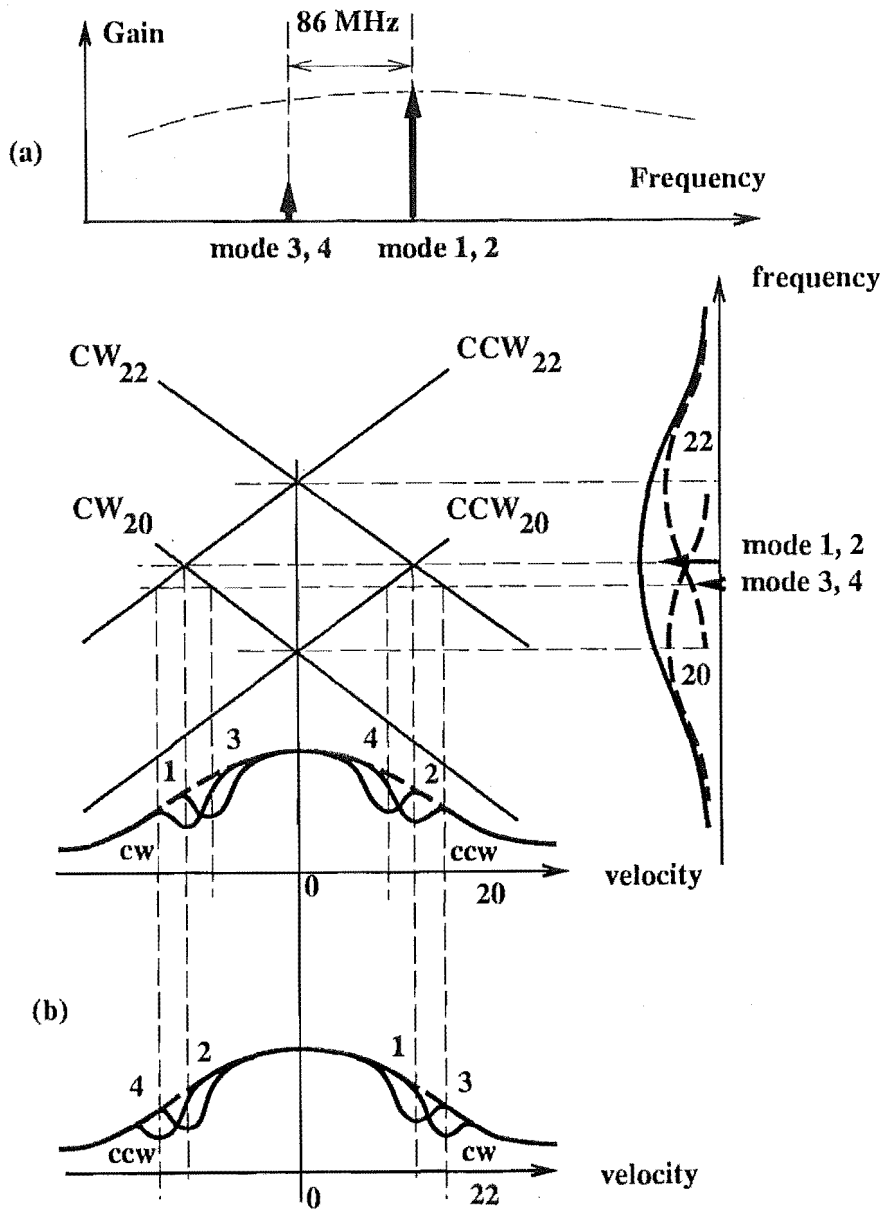

Fig. 8.8. Yntema diagram for the two longitudinal modes oscillating in a ring cavity with two isotopes. (a) This diagram shows the mode structure. For the Canterbury ring laser, the frequency difference between the two adjacent longitudinal modes is 86.218 MHz. (b) This diagram shows that the holes induced by modes 1 and 3 are overlap as well as modes 2 and 4. In this case, a bias on the beat frequency is induced by mode competition between modes 1 and 3, and modes 2 and 4.

holes cw_{1-20} and cw_{1-22} located in the Ne^{20} and Ne^{22} isotope gain curves, respectively. These four holes do not overlap. Therefore, there is no mode competition between the modes 1 and 2 through the gain medium coupling.

However, the additional modes 3 and 4 will burn another four holes cw_{3-20}, cw_{3-22}, ccw_{4-20} and ccw_{4-22}, which overlap with the holes burned by modes 1 and 2. This pair of modes changes the refractive index of the gain medium, corresponding to the holes cw_{3-20}, cw_{3-22}, ccw_{4-20} and ccw_{4-22}, and as seen by modes 1 and 2. As discussed previously, these hole overlaps will have the effect of pushing the frequencies of the oppositely travelling modes and increasing the beat frequency of the ring laser.

The major problem of this multimode unlocking method is the mode competition so induced between modes 1 and 3, and 2 and 4. This cannot be avoided; these modes will interact with the same group of atoms. For example, modes 2 and 4 will interact with the atoms which have the velocities located at holes ccw_{2-20} and ccw_{4-20} in the Ne^{20} isotope, and holes ccw_{2-22} and ccw_{4-22} in the Ne^{22} isotope gain curve. Modes 2 and 4 will interact with the same atoms because of the overlap of the holes.

When the laser modes interact with the same velocity-filtered group of atoms, significant mode coupling and competition will inevitably be present. The intensities of the modes will vary due to these mode competition. These changes in mode intensities in turn induce further changes in the refractive index of the gain medium. Therefore, mode competition again changes the frequencies of the laser modes, and adds to the variation of the frequency splitting in the ring laser. Detailed discussions about mode competition can be found in the standard textbook (Lamb 1974).

Although this optical bias method is very simple, it may not be suitable for the ring laser as a solution of the problem of the frequency locking since one cannot achieve the stability of the beat frequency based on the mechanism incorporating strong mode competition.

8.5 Transverse magnetic field effects on frequency splitting

8.5.1 Description of our findings

In our preliminary experiments, a transverse magnetic field was applied to the discharge plasma containing a natural abundance ratio for the neon isotopes. It

was then found that this induced a substantial bias in the (nonreciprocal) beat frequency which depended on the direction as well as the magnitude of this transverse magnetic field. It was also noted experimentally that such a magnetic field stabilises this beat frequency against many practically important variations e.g of the gain of the discharge and changes in the detuning associated with thermal expansion. Both of these appear to be quite novel observations, and currently lack a full explanation; partial and tentative interpretations are offered in the various subsections which follow.

In these experiments, a single permanent magnet in the shape of an annulus of diameter 6 cm was used as shown in Fig. (8.9). It provides a maximum transverse field of 0.014 T (140 Gauss) over a similar linear dimension (5 cm) when placed as close as possible to the discharge tube. This magnetic field was applied approximately perpendicular to both of the discharge tube or optical beam direction and also to the (sagittal or vertical) polarization of the laser field. When this magnetic field is oriented to point towards the geometric centre of the (square) ring cavity and the magnet itself is moved from a distance to as near the discharge tube as possible (corresponding to the maximum field of approximately 0.014 T), the beat frequency increases from 65 Hz to 135 Hz. When the direction of the magnetic field is reversed and the same procedure followed, the beat frequency of the ring laser decreases typically to 45 Hz, at roughly which point the frequencies of the two counterpropagating modes lock. The sensitivity of beat frequency to magnetic field is thus of the order of 5 kHz/T or 0.5 Hz/G in this geometry.

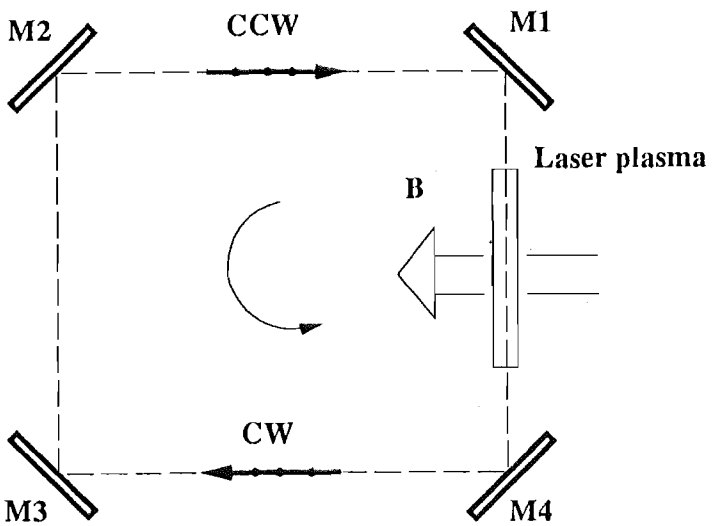

Fig. 8.9. Illustration of a ring laser experiment with a transverse magnetic field.

Fig. (8.10) show the FFT of the beat frequency and single waveform in the situation where the beat frequency has been increased by application of this field. The corresponding observation with a decrease in beat frequency is shown in Fig. (8.11).

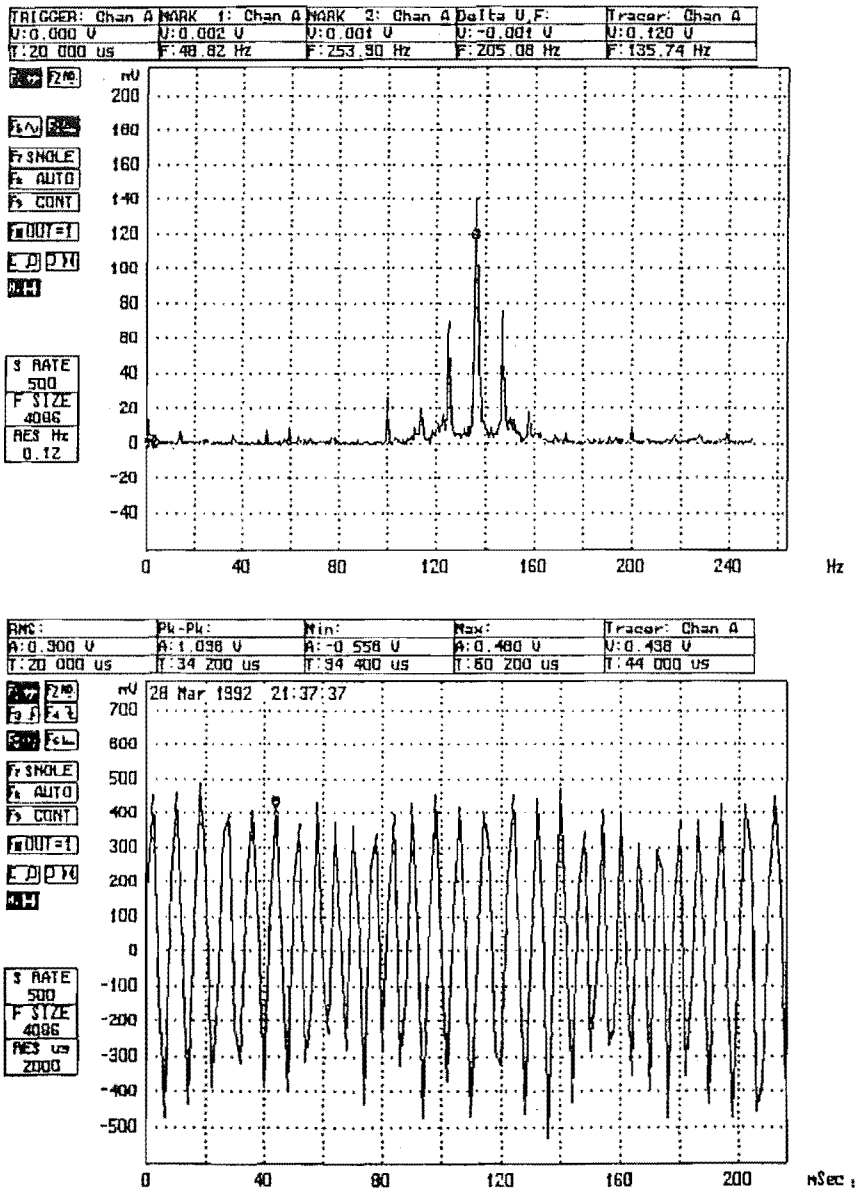

Fig. 8.10. The spectrum of the beat signal with a magnetic field (~ 0.014 T) in the direction as shown in Fig. 8.9 is given in the upper figure. The sidebands in the figure show the vibrations of the ring induced by the building vibration. The waveform of this beat signal is shown in lower figure. Note that the magnetic field has markedly increased the beat frequency.

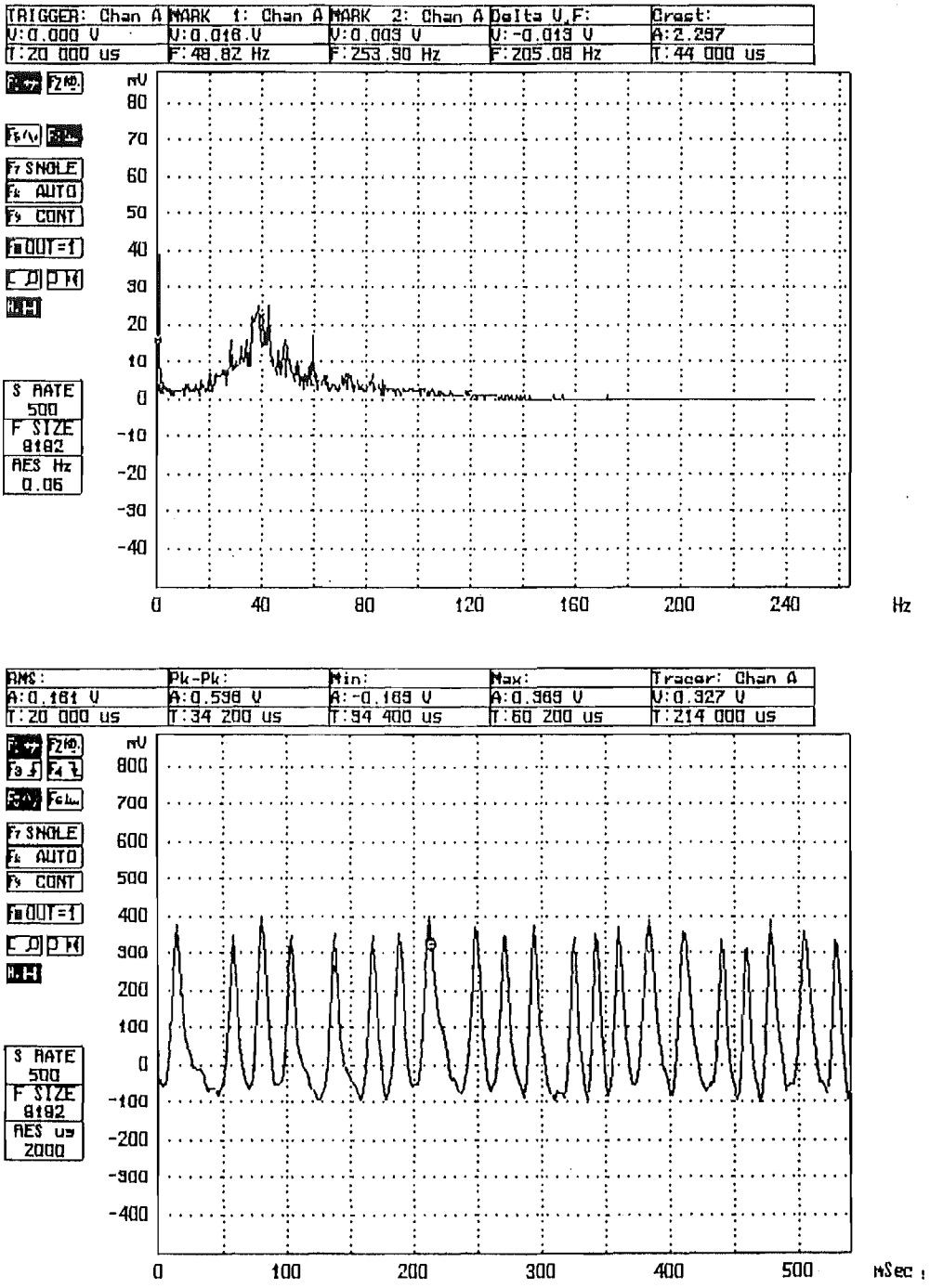

Fig. 8.11. The spectrum and waveform of the beat frequency in the same condition as Fig. 8.11, with the direction of the magnetic field reversed. Note the marked decrease in the beat frequency.

As far as we are aware, this nonreciprocal bias arising from a transverse field is an entirely novel phenomenon. It is much smaller than the Faraday effect and Zeeman splitting associated with the effects of a longitudinal or transverse magnetic field, respectively, on a He-Ne laser. For the Faraday effect in a nonplanar cavity, the nonreciprocal frequency splitting of the modes are (Statz *et al.* 1985) $\Delta F_L = (c/P)\theta_F(\lambda_L)/\pi$ and $\Delta F_R = (c/P)\theta_F(\lambda_R)/\pi$, where $=\lambda_L$ and λ_R are the frequencies of the left-hand polarized and right-hand polarized light respectively, and $\theta_F = VBl$ and is Faraday rotation, B is the longitudinal component of the magnetic field, l is the thickness of the Faraday rotator and V is the Verdet constant. Frequency splittings for typical rotator parameters are 500 kHz to 1 MHz for a small area ring laser (Statz *et al.* 1985) and for similar magnetic fields. For Zeeman effect, the frequency splitting of the two orthogonal polarization is 18.2 GHz/T (1.82 MHz/G) when a transverse magnetic field applying to the He-Ne discharge plasma (Ferguson and Morris 1978).

Fig. (8.12) shows the experimental results for the preliminary experiment for stabilizing the beat frequency by the transverse magnetic field, in which a single magnet was placed close to the discharge tube of our ring laser. The bars denote the experimental data for the beat frequency, and the broken line is the averaged beat frequency. This shows the constant bias in the beat frequency as mentioned

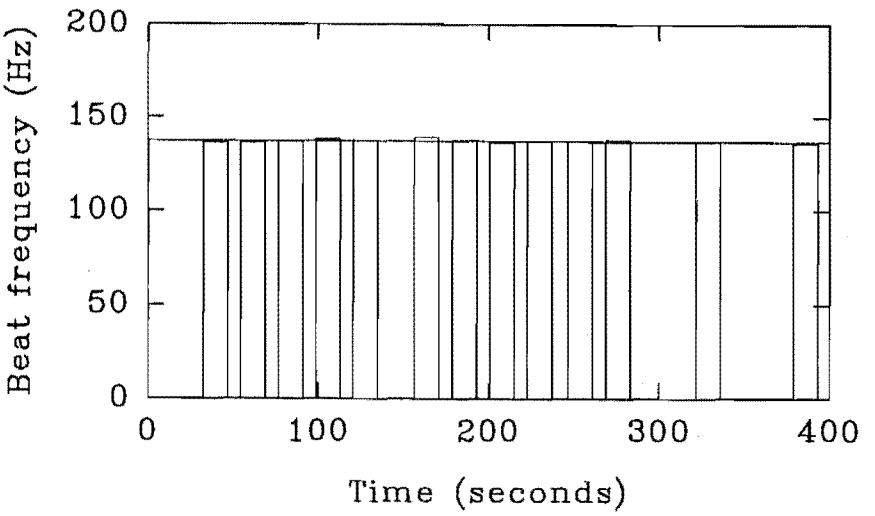

Fig. 8.12. The preliminary experimental results of the stabilization of the beat frequency by using a transverse magnetic field (~0.014 T).

previously. Now suppose that the laser frequency is tuned from a central frequency by approximately one half of the free spectral range (43 MHz for our ring laser) by changing the cavity length, which is performed by changing the voltage applied on the piezo which is bound to one mirror, the beat frequency changes from 137.81 to 139.03 Hz. Comparing the beat frequency variation from 57 to 76 Hz without applying the transverse magnetic field, the stability of the beat frequency is greatly improved by applying a transverse magnetic field. The origin of this change in beat frequency is possibly induced by the phase change of the backscattering in the ring laser, which is under investigation.

Further experiments using a Helmholtz coil for better field control are under preparation and the mechanism of this nonreciprocal effect is yet to be explored fully. We now discuss the stabilization of the beat frequency provided by the transverse magnetic field.

8.5.2 Beat frequency bias associated with the Zeeman effect of a transverse magnetic field

Let us first consider the role of Zeeman splitting of the He-Ne laser frequency in a transverse magnetic field in induced biases in the beat frequency. We shall estimate the size of this bias for our system, and show that it is necessarily insensitive to the sign of the applied transverse magnetic field, and thus cannot explain our observations.

Zeeman splitting of the He-Ne laser frequency in a transverse magnetic field has been studied by a number of authors (e.g. Keijser 1977, Ferguson and Morris 1978, Tratnik and Sipe 1986). Here we adapt the discussion given by Ferguson and Morris (1978).

When a He-Ne laser discharge plasma is placed in a transverse magnetic field, the Zeeman effect causes upper (j = 1) and lower (j = 2) level splitting. Each of the three (m = -1 0, 1) upper level atomic populations has an an associated Doppler velocity distribution, and there are three possible electric dipole transitions from each of the Zeeman split upper levels, corresponding to Δm = -1, 0, 1. When Δm = 0, the E field associated with the transition has a π polarization (parallel to the applied magnetic field); for Δm = ±1, the E field has σ polarization (perpendicular to the applied magnetic field, and for example in the sagittal direction, or perpendicular to the plane of the ring cavity). Thus, two of the transitions from each upper level will produce σ polarized E fields, while the third transition will produce a π polarization as shown in Fig. (8.13).

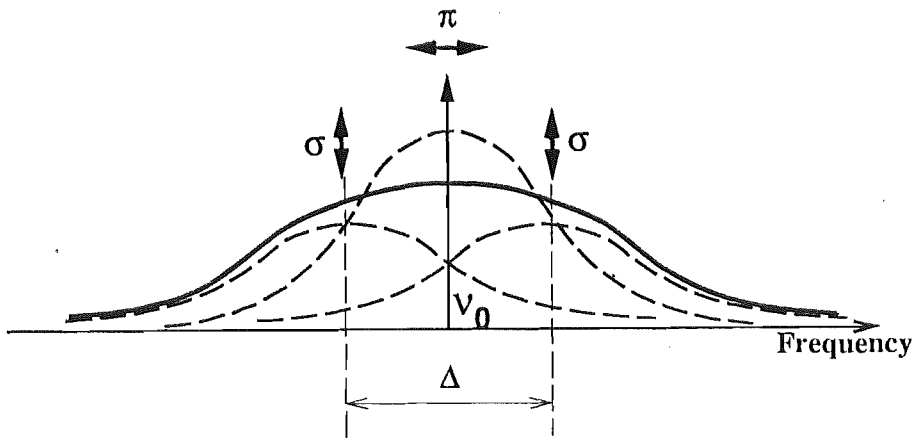

Fig. 8.13. Splitting of the gain distribution induced by a transverse magnetic field.

For a plane ring cavity, the reflection losses for a π (in-plane) polarized beam is approximately 90 times greater than that for the σ (sagittal) polarization due to the differential reflectivity of the mirrors for the two orthogonal polarization (Bilger, Stedman and Wells 1990), and the output of the active ring laser is linearly polarized in the sagittal direction. Therefore only two σ components ($\Delta m = \pm 1$) of the Zeeman splitting will interact with the laser field. In this case, because of the change of shape of the resulting overall gain curve, the Zeeman splitting has the potential to provide a similar function to the adjustment of the relative isotopic abundances afforded by using isotopically enriched neon.

As mentioned previously, the Zeeman splitting for the two orthogonal components is 18.2 GHz/T, so that the separation between the two σ components is 36.4 GHz/T. For single isotope neon^{20}, the weighting function given by Eq. (8.12) becomes

$$W(x) = (N/\Delta\nu_{20})\{\exp-[(x + g\mu_B H/h)/\Delta\nu_{20}]^2 + \exp-[(x-g\mu_B H/h)/\Delta\nu_{22}]^2\} \quad (8.12)$$

where g factor is about 1.3 (Ferguson and Morris 1978), H is the magnetic field, μ_B is the magnetic moment and h is Planck's constant.

Fig. 8.14(a) shows the variations of the gain curves with the different frequency splittings. In this calculation, we keep the discharge pumping parameter as a constant. Thus the gain at the centre of the gain curve varies with the Zeeman frequency splitting. The gain values at the centre of the gain curves are 23%, 19%, 16% and 7% for frequency splittings of 400, 500, 600 and 1000 MHz,

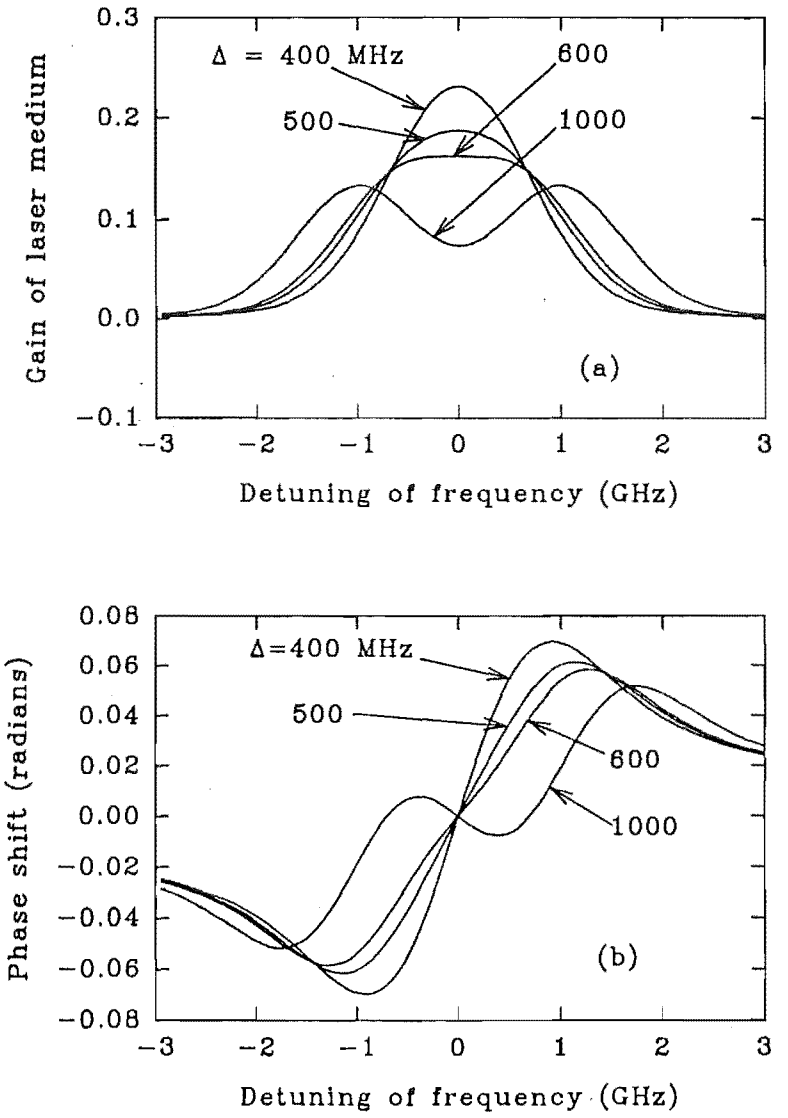

Fig. 8.14. Variation of the gain (a) and dispersion (b) versus the frequency with the different frequency splitting Δ induced by the transverse magnetic field.

respectively. These gain values are also used in the calculations for Fig. 8.14 (b), Figs. (8.15a, b) and Fig. 8.16(a). The gain shapes will be similar to the enriched neon isotope mixture when the frequency splittings are less than approximately 600 MHz. When the frequency splitting is greater than 600 MHz, the centre of the gain curve will become a dip. In this situation, the phase shifts caused by the dispersion associated with the gain curve will be different from those in the situation when the splitting is less than 600 MHz as shown in Fig. 8.15(b). Fig. 8.16(a) shows the frequency shifts of the laser modes with the detuning at these different splitting values. For a given value of the detuning, the shift in beat frequency will be a function of the magnetic field induced splitting Δ of the transition frequency, with an intercept corresponding to the residual beat frequency change at zero magnetic field as a single isotope behavior. The beat

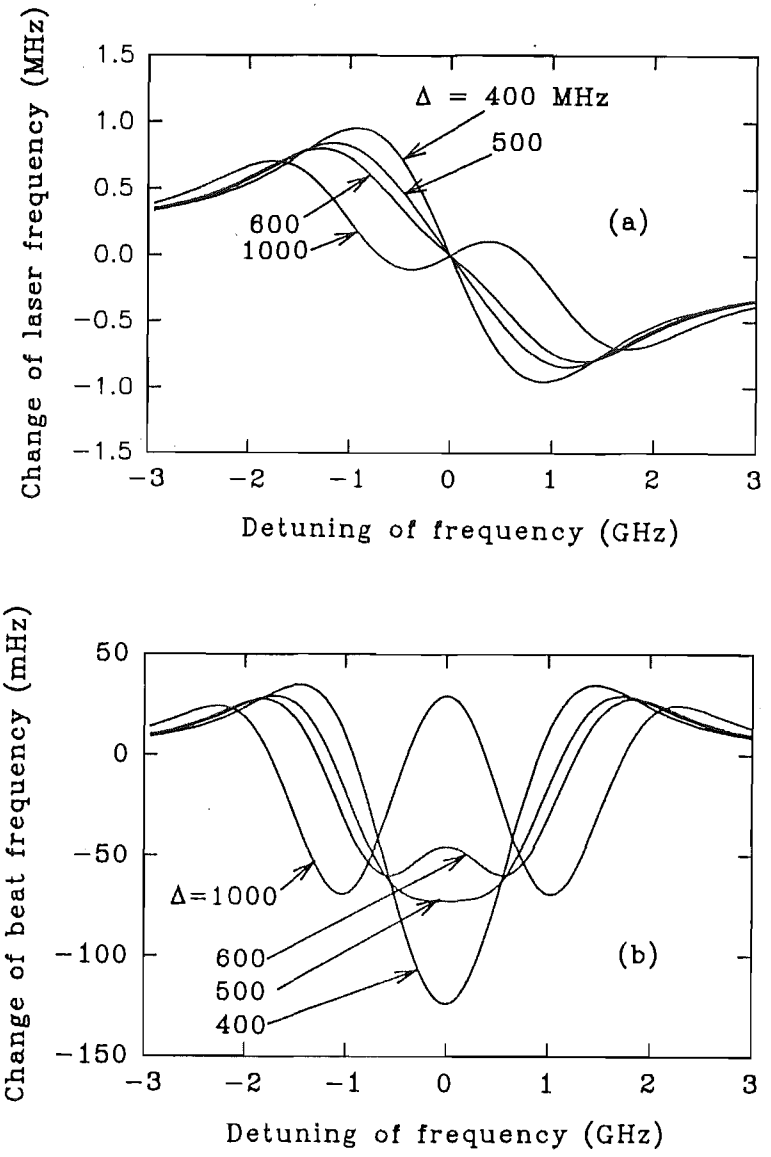

Fig. 8.15. Variation of laser frequency (a) and the beat frequency (b) versus the frequency detuning relative to the centre of the gain.

frequency shifts caused by the dispersion of the gain medium are plotted in Fig. 8.16(b) for different choices of Zeeman splitting and as a function of laser frequency detuning. This suggests the existence of a particular value of the Zeeman splitting (approximately 800 MHz in our calculation, and therefore beyond the reach of our currently available magnetic fields), at which the pulling of the beat frequency of the ring laser is zero. The existence of this residual pulling is less important than the stabilisation of the beat frequency under changes in the discharge and detuning for precision measurements.

These figures are of interest since we expect that the laser frequency can be stabilized within 1 MHz; we plan to lock the ring laser frequency to the NL-1 laser, whose long term frequency drift is 1 MHz/day. In this case the behaviour of

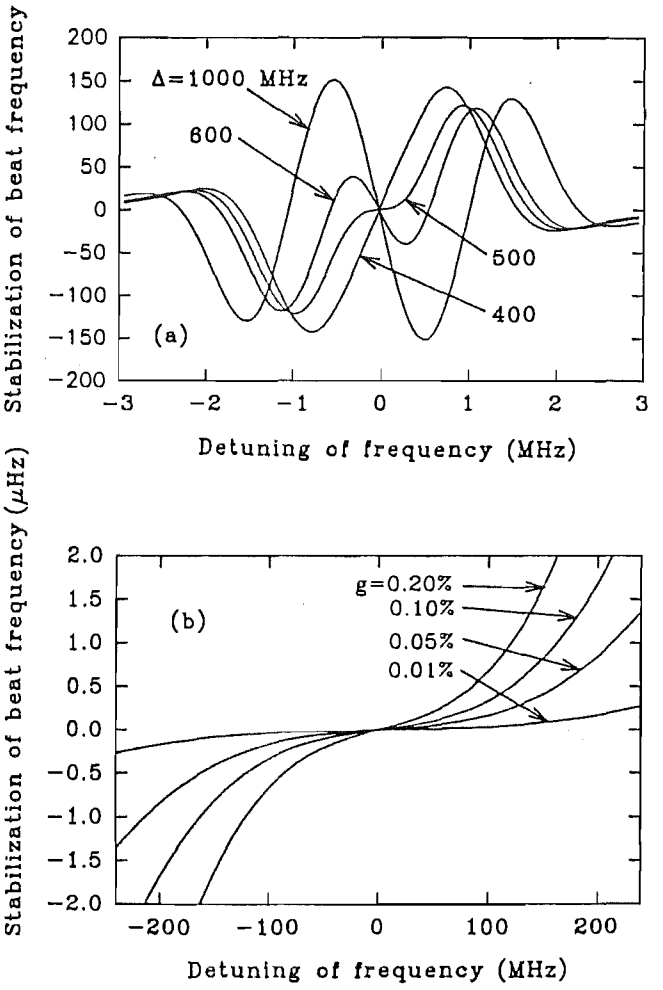

Fig. 8.16. (a) This diagram shows the stability of the beat frequency versus the frequency detuning with the different frequency splitting induced by the magnetic field. The vertical scale in (a) is μHz.

beat frequency under a change in detuning at different Zeeman splittings is of interest for possible experimental checking. These dependences are shown in Fig. 8.15(a). We notice that the curve corresponding to a Zeeman splitting of 500 MHz indicates greater stability of the beat frequency at such fields. Fig. 8.15(b) indicates the potential for stabilization of the beat frequency at different gain values, where we assume the splitting to be 500 MHz. In this case, if we tune the laser frequencies of the oppositely traveling modes close to the center of the gain curve, the precision of 0.2 μHz or better can be achieved by locking the laser frequency within 1 MHz.

We should notice that cross saturation effects (Siegman 1986) of the gain medium has not been considered here. If we further consider the dispersion change caused by the cross saturation, the laser intensity in the cavity must be

stabilized since the cross saturation effect of the gain medium is dependent on the laser intensity.

We showed in Fig. (8.13) the dependence of the gain curve on a transverse magnetic field. The induced beat frequency biases of Fig. (8.16) are, like the gain curve changes from which they are derived, insensitive to the sign of the applied magnetic field. Hence they cannot explain the linear response observed and discussed in Sec. 8.5.1. In addition, the likely frequency changes are only of the order of tens of millihertz (Fig. 8.16), very much less than is required to reproduce the data.

8.5.3 Possible mechanisms for linear and nonreciprocal optical effects from a transverse magnetic field in a ring laser

In this section I consider the category of radiation-matter interaction processes which could explain in principle our observed effect, a nonreciprocal contribution which has a linear dependence on a transverse magnetic field. I mention the range of possible optical effects which are detectable as nonreciprocal path length contributions for a ring laser. I then briefly review the selection rules of Stedman (1990, 1993b), and then apply these rules to our observation.

A ring laser gyroscope detects the nonreciprocity in the effective path lengths for the countercirculating beams. By a nonreciprocal effect, we mean (with Statz *et al.* 1985) one which reverses with the sense of propagation of the beam.

Consider a travelling electromagnetic wave in a ring laser, for which the classical electric field is proportional to the real part of $\mathbf{e}_{\mathbf{k}j}\exp i(\omega t - \mathbf{k}\cdot\mathbf{x})$; $\mathbf{e}_{\mathbf{k}j}$ (or $\mathbf{e}$ for brevity) is the polarisation vector, k the wavevector, j the polarisation, and ω the frequency of the optical mode. Reflection at an ideal mirror interchanges the handedness of a beam: right circularly polarised light converts to left, and vice versa.

A ring laser has four possible modes: ClockWise (CW), and Counter-ClockWise (CCW), and for each, two orthogonal polarisations. In a linear polarisation basis we denote these as s (sagittal or senschrit) for the out-of-plane component of electric field) and p (parallel or in-plane component); the s mode usually is excited rather than p since according to the Fresnel reflection coefficients the p reflection is inevitably more lossy for typical mirrors.

A circularly polarised basis is of interest for a square ring, as opposed to a triangular one; since a circularly polarised beam reverses its handedness upon reflection, the legs of a circularly polarised ring have alternating handedness of

polarisation, and must be even in number to sustain pure circular polarisation.

The relationship between handedness, direction and frequency itself depends on the physical mechanism inducing the nonlinear state of polarisation. A nonzero beat frequency between modes, thus giving a signal for the ring laser (as in the standard gyroscope application) $\omega_{cw} - \omega_{ccw}$ depends on having a nonreciprocal component of the optical path length: $n_{ccw} \neq n_{cw}$, and hence (from the Kramers-Kronig relations) a nonreciprocal term in the absorption or loss, not necessarily at the laser frequency.

A ring operating with strictly linearly polarised light has a beat signal dependent on *linear nonreciprocity*: an effect whose contribution $I(\mathbf{e}, \mathbf{k})$ to the intensity of absorption say in the UV, and so to refraction at the helium-neon laser wavelength, reverses in sign with $\mathbf{k}$ and satisfies the relation: $I(\mathbf{e}, \mathbf{k}) = I(\mathbf{e}^*, \mathbf{k}) = -I(\mathbf{e}, -\mathbf{k})$, the first equation since the polarisation is linear and the second since the effect reverses with the wavevector. Such a nonreciprocal contribution is inevitably time-odd; the last equation simply says that time reversing all photons reverses the observed effect. In a quantum formulation, for effects induced by interactions of the electronic states with the electromagnetic field, this implies that an odd number of time-reversal violating electronic interaction operators are involved ($\tau = -1$ in the following selection rules; see the conjugation theorem of Stedman 1990). Such a time-odd requirement certainly includes the Sagnac effect since time reversal indeed reverses all effects linearly dependent on a rotation; the rotation itself reverses. It could also include magnetic field-induced effects such as the one under discussion. This possibility will be explored further shortly.

On the other hand, a ring operating in circularly or at least nonlinearly polarised light is sensitive to any nonreciprocity induced by some medium in the effective refractive index for a circularly polarised beam, or to *circular nonreciprocity*. Since $\mathbf{e} \neq \mathbf{e}^*$, it is not so obvious that a time-odd field is either necessary or even appropriate for inducing a nonreciprocal effect. However it will certainly be useful in generating the nonlinear polarisation.

Any element of the ring which is gyrotropic, that is, exhibits circular birefringence or has a differential effect on light of different handedness, will throw a ring into nonlinear polarisation; a linearly polarised beam will inevitably be rotated on passage around a ring and can no longer be an eigenmode. In inducing image rotation a nonplanar ring also will enforce nonlinear polarisation. In the simplest analysis and for ideal mirrors any such polarisation rotation throws a four-sided ring into circular polarisation, which is an acceptable eigenmode. In practice, as shown by Bilger *et al.* (1990) in a different context, mirror nonidealities ensure that there is a finite transition region in which the polarisation

eigenmode varies continuously between linear through elliptical to circular polarisation.

There are two basic gyrotropic devices, often termed a reciprocal and a nonreciprocal polarisation rotator. (This nomenclature has nothing directly to do with the penchant of a ring laser to measure nonreciprocal effects.) The former is illustrated by the Faraday effect: a longitudinal magnetic field imparts magnetic circular birefringence. Its dependence on polarisation and direction satisfies $I(\mathbf{e}, \mathbf{k}) = -I(\mathbf{e}^*, -\mathbf{k})$ since the inducing field is time-odd, and $I(\mathbf{e}, \mathbf{k}) = -I(\mathbf{e}^*, \mathbf{k})$ since the effect is opposite for light of opposite handedness. Hence the sign of $\mathbf{k}$ is immaterial. In the jargon of the selection rules of Stedman (1993b), this rotating element is time-odd ($\tau = -1$) and gyrotropic ($\gamma = -1$). In satisfying $\tau K = \gamma$ we must require $K = +1$, so that there is no dependence of the effect on an odd power of the wavevector. As far as parity is concerned, the rule $\Pi K = 1$ for a centric system, where Π is the combined parity of external field operators, gives no restriction in this case; since $\Pi = +1$ for a magnetic field and $K = 1$ also, such an effect can be displayed by centric systems. Such a system will split CW and CCW waves of the same handedness, but not those with the same polarisation. If the rotation effect were being studied in isolation rather than through a ring, since the sign of the wavevector is immaterial a second and reversed passage through the material following a reflection will enhance the phase shift.

By contrast, a nonreciprocal rotator is an element for which the sign of the wavevector does affect the sign of the rotation, and double passage leads to cancelling contributions. This would hold for the case of natural optical activity, where $I(\mathbf{e}, \mathbf{k}) = I(\mathbf{e}^*, -\mathbf{k}) = -I(\mathbf{e}^*, \mathbf{k})$. These equations follow from its gyrotropy ($\gamma = -1$) and its time-even character ($\tau = 1$) giving in the selection rule $\tau K = \gamma$ that $K = -1$. It would therefore split copropagating waves of opposite handedness, but not counter-propagating waves of the same handedness.

Which of these three possibilities (linear nonreciprocity, a reciprocal and a nonreciprocal rotator) may prove relevant for the presently observed effect can be assessed on the basis of general arguments incorporating these and other restrictions. The effect we observe is time-odd ($\tau = -1$), since it is linear in a magnetic field.

We have not seen evidence for nonlinear polarisation when a field is applied in our experiment; I estimate from the intensity of reflection at a polarising prism, that any degree of ellipticity in the output beam, measured as the ratio of minor to major axis, is no greater than 1% when the magnetic field is present. However, polarisation effects somewhat below 1% may well be very significant for beat frequencies in our range in such a sensitive instrument.

Consider then the case that the effect is gyrotropic ($\gamma = -1$): a form of magnetic circular dichroism (MCD). In this case, $K = 1$ from the selection rule $\tau K = \gamma$, and neither interference between multipoles nor the parity restriction to an acentric system is required. In E1 (electric dipole) coupling this corresponds to the Faraday effect. For a fluid this confines us to a geometric factor of the standard MCD form $\mathbf{e} \times \mathbf{e}^* \cdot \mathbf{B}$; the triple scalar product is the only rotational invariant which can be manufactured from the three available vectors **e**, **e*** and **B**. The inclusion of higher multipoles does not change this form, since other possible invariant combinations vanish from transversality. (To see this, note that odd orders in the multipole expansion are forbidden since $K = 1$. If two more **k** vectors are included, corresponding to a second order term in the multipole expansion, the five vectors **e**, **e***, **B**, **k**, **k** may be combined into $(\mathbf{e} \times \mathbf{e}^* \cdot \mathbf{B})(\mathbf{k} \cdot \mathbf{k})$ only, since other combinations such as $(\mathbf{e} \times \mathbf{k} \cdot \mathbf{B})(\mathbf{e}^* \cdot \mathbf{k})$ vanish from transversality: $\mathbf{e} \perp \mathbf{k}$.) However $\mathbf{e} \times \mathbf{e}^* \cdot \mathbf{B}$ vanishes for a transverse field; $\mathbf{e} \times \mathbf{e}^*$ is parallel to the beam direction **k**, not to **B**. We have ignored fringing fields in this argument. For circular nonreciprocity to exist, then, our only significant remaining assumption, that of a randomly oriented fluid, has to be invalidated; we must consider seriously the existence of a minute degree of orientation of the constituent ions. This presumably arises from the only static orientational influence, the applied magnetic field. In a similar manner molecular polarisation, orientation and so electric circular dichroism at a parts-per-million level was induced by an electric field in the experiment of Buckingham and Shatwell (1980).

Before exploring this possibility, we consider the nongyrotropic case ($\gamma = +1$) or magnetic linear dichroism (MLD) in the context of both linear and circular nonreciprocity. Since $\tau = -1$, we find $K = -1$ or multipole interference is required. This breaches the parity rule for centric systems, so that for linear as well as circular nonreciprocity to exist, our assumption of randomly oriented scatterers has to be invalidated by the orientational effects of the applied magnetic field.

Oriented scatterers

In each case, then, it seems necessary to assume that the symmetry group of the scatterers is no longer the full rotation group O(3), but the subgroup C_∞ where the symmetry axis is that of the applied magnetic field. We take this to be the y axis and the beam direction to be the local z axis for definiteness. We now find what invariants under C_∞ may be constructed from the various vectors (**e**, **e***, **B**, **k**) which define the geometry at each order of multipole coupling. Such invariants must be found to ensure the feasibility of the corresponding interaction process (Stedman 1990, 1993b).

First we consider linear nonreciprocity when the process is gyrotropic and $K = -1$. The lowest order at which such contributions could arise is in E1/M1-E2 interference. Three electronic matrix elements are involved in any intensity contribution, one from the optical interaction with operator $\mathbf{e} \cdot \mathbf{p}$, one from the interaction with $[(\mathbf{e} \times \mathbf{k})^1 (\mathbf{r} \times \mathbf{p})^1]^j$ for $j = 1$ (M1) or $j = 2$ (E2) (one of these optical interactions being complex conjugated), and one from the field interaction $\mathbf{B} \cdot (\mathbf{l} + 2\mathbf{s})$. On summing over randomly oriented scatterers this then requires the external vectors $\mathbf{e}$, $\mathbf{e}^*$, $\mathbf{k}$ and $\mathbf{B}$ to be coupled multiplicatively to a C_∞ invariant, i.e. a function of y independent of x and z. $\mathbf{B}$ is already a function of y only. The polarisation vectors must be coupled symmetrically, i.e. only to rank 0 or 2; this permits the bilinear forms $\mathbf{e} \cdot \mathbf{e}^*$, $e_x e_y^* + e_y e_x^*$, $e_x e_x^*$, $e_y e_y^*$ only. In each of these cases there is no possibility of combining terms with k_z to give an invariant under rotations about y. Hence no linear nonreciprocality can occur at this order. At all higher orders for a nongyrotropic effect, we add an even number of wavevectors to the above exercise, and the same conclusion follows: in no such order can a C_∞ invariant be constructed. More formally, the C_∞ behaviour of the various vectors is given by $\mathbf{e} \sim ae^{i\Phi} + be^{-i\Phi}$ where $b = a$ under linear s polarisation, $\mathbf{k} \sim (e^{i\Phi} - e^{-i\Phi})\mathbf{i}$, $\mathbf{B} \sim$ constant. The only symmetric bilinears to be formed from $\mathbf{e}$ and $\mathbf{e}^*$ have the ϕ dependence $aa^*e^{2i\Phi}$, $bb^*e^{-2i\Phi}$, $(ab^* + ba^*)$. When combined with an odd number of $e^{\pm i\Phi}$ factors from an odd number of $\mathbf{k}$ vectors it is impossible for the ϕ dependence to cancel. We conclude that no such effect as we observe can occur within the geometrical constraints of our experiment in linear polarisation.

Now consider circular nonreciprocity. We need a gyrotropic contribution, or MCD. So far we have shown that MCD is forbidden for a fluid of randomly oriented scatterers. If now we allow for field-induced polarisation, we are committed to search for a C_∞ invariant formed from $\mathbf{e}$, $\mathbf{e}^*$, $\mathbf{B}$ and an even number of $\mathbf{k}$ vectors. This would seem to be feasible, since the various $e^{\pm i\Phi}$ factors could cancel. However $\mathbf{e}^*$ necessarily couples with $\mathbf{e}$ antisymmetrically. Therefore the product must have the spherical rank $j = 1$ and so the form $\mathbf{e} \times \mathbf{e}^*$, which is proportional to $\mathbf{k}$, in order to ensure gyrotropy. However no number of vectors parallel to z can combine to give a function of y; a product of factors each of the form $(e^{i\Phi} - e^{-i\Phi})\mathbf{i}$ cannot be independent of ϕ. As before, then, we find no possibility of such a process at any multipole of coupling even for circular birefringence.

Fringing fields

As mentioned, the above analysis ignored the longitudinal part of the

fringing field. To first order this may be expected to cancel, and further preliminary measurements with a Helmholtz coil confirm the existence of a contribution to the beat frequency which is linear in a transverse magnetic field. However in view of the strong selection rule just proved limiting effects from a transverse field, we must now take seriously the possibility that a net longitudinal component of the field is generating the observed effect. Clearly magnetic circular birefringence from this effect could induce the splitting of modes in the case on nonlinear polarisation, as in the "Zeeman laser" (Statz *et al.* 1985). It is clear that we are looking at a very highly forbidden contribution, fortunately with a very sensitive instrument. More careful measurements need to be taken to establish the true geometry of the effect, and to direct the best model for its theoretical interpretation.

Chapter 9

Discussion

In this thesis we have reached five major and novel conclusions. I list these first, and expand on each afterwards.

First, the ringing profile method provides a novel technique of measuring the losses in an optical cavity. Since these losses dictate the quantum limit of noise in ring laser measurements, such a cheap and accurate method is a valuable experimental tool.

Second, asymmetry in this profile is an unexpectedly significant characteristic when an optical cavity is scanned; both the FWHM and the asymmetry parameter of the profile cavity are defined by the normalised scanning rate.

Third, the Canterbury ring laser has reached a resolution of the beat frequency of 11 μHz, which is of the order of the quantum noise linewidth.

Fourth, a novel method for determining the parameters of frequency pulling is presented. It consists of an analysis of the waveform of the interferometric signal from a ring laser, or alternatively that of the derived instantaneous beat frequency.

Fifth, in our discussion of the dispersion effects of the laser medium on the beat frequency, a novel method is presented and demonstrated for stabilizing the beat frequency of a ring laser by using a transverse magnetic field. An associated and quite novel nonreciprocal bias of the beat frequency, which is dependent on the direction of the transverse magnetic field, is discovered and discussed.

9.1 Conclusion 1: Ringing profile method

A comparison of various measurement techniques for determining precisely the

losses in an optical cavity has been presented in Table 2.1 in this thesis. The most popular method, currently used by most manufacturers of laser gyroscopes, is the ring-down technique (Anderson *et al.* 1984). Its measurement precision of losses in an optical cavity is 5 ppm. We have demonstrated in Chapter 3 that our novel method based on the ringing in the output profile of a scanned cavity, can have a even higher precision. In our experiment, the precision of the loss measurement is 1 ppm by using the SR-130 supercavity. In addition, the ringing profile method does not need a fast optical switch, nor does the mechanical vibration of the probe cavity during the measurement affect the precision of measurement. A crucial part of the ringing profile method is the application of the relevant and (in this context) novel theory so as to give a fitting procedure, all of which has been solved in this thesis. A TurboPascal program for the parameter fitting is presented as Appendix F.

9.2 Conclusion 2: The asymmetric scanning profile of a Fabry-Perot cavity

We have showed in Chapter 4 that asymmetry in the output profile of a scanning cavity is inherent to its character. The Airy function is only the description of a limiting case of a scanning Fabry-Perot, where the scanning speed of the cavity is zero. We have demonstrated that significant (5%) asymmetry appears in an output profile for a scanning Fabry-Perot cavity even when the time interval which is required for scanning over the probe frequency is as long as 100 t_c, where t_c is the intensity decay time of the cavity. In fact, this asymmetric characteristic on the output profile of an optical cavity also degrades the measurement of the FWHM increase of the profile. Both characteristics are particularly important for the precision measurement of a spectrum by using supercavities.

9.3 Conclusion 3: The measurement resolution of the Canterbury ring laser.

A variety of ring laser gyroscopes has been discussed in Chapter 5 and a comparison of these laser gyroscope sensitivities is presented in Table 5.1. We have demonstrated in Chapter 6 that the Canterbury ring laser has a resolution of beat frequency 11 μHz, which is a fraction 2.32×10^{-20} of the He-Ne laser

frequency, and corresponds to a sensitivity of $1.6 \times 10^{-7}\ \Omega_E$, where Ω_E is the earth rotation rate. This sensitivity is of the same order as the quantum limit for the beat frequency linewidth, given the present losses of our ring laser, and is at least two orders of magnitude lower than the sensitivities of existing laser gyroscopes.

9.4 Conclusion 4: Novel methods for determination of the beat Frequency pulling and other parameters of ring lasers

Frequency pulling in a ring laser induced by backscattering has been investigated in Chapter 7. It is an important error source in our ring laser. This frequency pulling is dependent not only on the magnitudes of the CW and CCW backscattering but also on the phases of the two backscattered beams, which will themselves change with the length of each arm of the ring laser, for which no control so far exists. Therefore, it is very important to be able to abstract frequency pulling information from the beat signal. We have demonstrated that the frequency locking threshold f_l and the nominal beat frequency f (induced by the cavity rotation) can each be determined by analysis of the instantaneous beat frequency. The joint effect of laser gain, saturation and backscattering of a ring laser can be explored by the Fourier analysis of the temporal waveform of the beat signal. These novel methods are particularly important for the development of large-area ring lasers.

9.5 Novel method for stabilization of the beat frequency and the disvovery of the nonreciprocal bias by using a transverse magnetic field.

Gain-plasma induced dispersion effects on the beat frequency have been investigated in Chapter 8. We have shown following earlier work that mode competition in a ring laser will induce an increase of beat frequency, and that dispersion of the laser medium will cause a decrease of the beat frequency. We have then demonstrated that the mode competition effect, which causes the drift of the beat frequency of ring lasers, can be reduced by using a transverse magnetic field. A very interesting discovery, even more novel, is that this transverse magnetic field induces a bias on the beat frequency, which is dominated by an utterly unexpected and unexplained linear component which in particular is reversed with the direction of the magnetic field. This magnetic effect

is ~ 5 kHz/T (0.5 Hz/Gauss), and as such is very large compared to the expected effects of a transverse field on the gain curve and so on dispersion-induced shifts (~ mHz/Gauss) but is very small compared to magnetic field effects previously seen in ring lasers. It cannot be explained by presently available theories.

9.6 Goals for further study

Short-term plans

The immediate tasks facing the ring laser group are as follows:

Gas and hardware cleanliness and associated vacuum procedures are still the major problems, limiting data collection times effectively to a few minutes. The team is working to refine all aspects of mirror installation, alignment and cleaning procedures, and in particular is constructing a vacuum bakeout oven for fuller outgassing of components before assembly. Heating in situ is very difficult beyond 80-100°C on account of the presence of the piezoelectric transducer and O-ring components. The relative merits of various sizes of clean boxes and clean tents are being vigorously discussed at this time.

The effect of the transverse magnetic field (Chapter 8) requires much more accurate and quantitative study than was possible with the data obtained for this thesis. At the moment the r.f. excitation section is undergoing a major redesign so as to permit a truly Helmholtz coil configuration enclosing the active plasma.

It is hoped to stabilise the longitudinal mode in the gain curve by beating the output with our NL-1 stabilised laser and servoing with the piezoelectric transducer attached to one mirror. With the use of enriched neon, which proved only just possible in the time frame of the work reported in this thesis, this is hoped to provide very much improved stabilisation of the beat frequency, another necessary component of long-term data collection.

Time-dependent sidebands (at -40 dB) have been noticed on the earth line as also has time- and run-dependent structure at low frequencies, both in the 0.1-1 Hz range expected for microseisms. However, the microseisms as customarily measured by the linear EARSS seismographs (whose amplitude is of order 4 μm) should not appear so conspicuously, and would be expected to be several decades below this level. This is a significant puzzle, since our ring is firmly mounted in a

very stable site. We will investigate this under the sponsorship of the Foundation for Research, Science and Technology.

The intriguing conclusions in Chapter 7 regarding the measurement of pulling parameters from an interferogram waveform analysis as presented in this thesis also demand further and more accurate study. It might prove helpful to monitor the intensity of one beam only on another channel, and to incorporate an analysis of its waveform in the analysis. This may help to pin down all relevant parameters. We have been frustrated in this as in the possibility of beating with the NL-1 laser by the fact that our latest batch of mirrors proved to have unpolished backs, preventing the sampling of well-collimated exit beams. Other problems have been manifest in further work on this topic (which is not otherwise reported in this thesis) by Professor Stedman. For example the MATLAB routines for extraction of the instantaneous frequency as applied on our SUN workstations seem not always to deliver the expected results for the geometric ratios of harmonics even on test waveforms, and considerable checking of the performance of the various computer packages is also required.

Medium-term plans

The success of the quite novel design of the Canterbury ring laser has attracted further international interest. In particular Professors Stedman and Bilger have recently been contacted on behalf of a major German research programme, part of which is in need of improved methods of obtaining accurate, fast and (by German standards) relatively inexpensive data on variations in rate and orientation of earth rotation. Previous to our work, large ring lasers had been discounted as impractical. A panel of ring laser experts from Hannover (Prof. Hoch), Braunschweig (Prof. Rodloff), Techische Universitat Munich (Prof. Schneider) and Wettzell Fundamentalstation etc. meeting with our collaborator Prof. Hans Bilger in March 1993 discussed the pros and cons of various designs for a large ring; it was agreed that the feasibility study had effectively been done, and by the Canterbury ring laser. We were visited recently by Dr Ulrich Schreiber, the Manager of Fundamentalstation Wettzell where laser ranging to the moon and to satellites is routinely performed, who inspected our system.

The ultimate solution for their problem is certain to be a ring laser 4 m square crafted within a monolithic block of low-expansion ceramic. Its production, setup and operation would be an expense which we could not contemplate

within the scale of New Zealand research budgets. However it has already been decided first to build a 1 m square prototype of similar monolithic construction to circumvent the vacuum problems of our present ring and so allow truly long-term data collection. This also is beyond our means. Dr Schreiber confirmed his intention that the ring should be used initially at our site, to take advantage of our cavern which is quite unique internationally (based as it is upon a teratonne of basalt - Banks Peninsula), and difficult for the German group to reproduce. All this points to a strongly collaborative project in which this project will continue to make a significant international impact in the development of this technology for practical scientific ends.

References

Abraham, N.B. and C.O. Weiss (1988), Dynamical Frequency Shifts and Intensity Pulsations in an FIR Bidirectional Ring Laser, *Opt. Commun.* **68,** 437-441.

Abromson, D. and W.S. Bickel (1990), Probing a Standing 0.6328-μm Electromagnetic Wave in a Laser Ring Cavity, *Appl. Opt.* **29,** 1745-1748.

Adler, R. (1946), A Study of Locking Phenomena in Oscillators, *Proc. IRE* **34,** 351-357.

Anderson, D.Z., W.W. Chow, V.E. Sanders, and M.O. Scully (1979), Novel Multioscillator Approach to the Problem of Locking in Two-Mode Ring-Laser Gyro. Part II, *Appl. Opt.* **18,** 941-942.

Anderson, D.Z., W.W. Chow, M.O. Scully, V.E. Sanders (1980), Optically Biased Laser Gyro, *Appl. Opt.* **5,** 413-415.

Anderson, D.Z., J.C. Frisch, and C.S. Masser (1984), Mirror Reflectometer Based on Optical Cavity Decay Time, *Appl. Opt.* **23,** 1238-1245.

Aronowitz, F. (1965), Theory of a Traveling-Wave Optical Master, *Phys. Rev.* **139,** A635-646.

Aronowitz, F. (1966), Mode Coupling due to Backscattering in a He-Ne Traveling-Wave Ring Laser, *Appl. Phys. Lett.* **9,** 55-58.

Aronowitz, F. (1971), The Laser Gyro, In: *Laser Applications,* vol. 1, (M. Ross, ed.; Academic Press, New York) pp. 133-200.

Aronowitz, F. (1972a), Single-Isotope Laser Gyro, *Appl. Opt.* **11,** 405-412.

Aronowitz, F. (1972b), Effects of Radiation Trapping on Mode Competition and Dispersion in the Ring Laser, *Appl. Opt.* **11,** 2146-2152.

Aronowitz, F. and R.J. Collins (1966) Mode Coupling Due to Backscattering in a He-Ne Traveling-Wave Ring Laser, *Appl. Phys. Lett.* **9,** 55-58.

Aronowitz, F. and R.J. Collins (1970), Lock-In and Intensity-Phase Interaction in Ring Laser, *J. Appl. Phys.* **41,** 130-141.

Aronowitz, F., J.E. Killpatrick, S.P. Callaghan (1974), Power-Dependent Correction to the Scale Factor in the Laser Gyro, *IEEE J. Quantum Electron.,* **QE-10,** 201-208.

Aronowitz, F. and W.L. Lim (1977), Positive Scale Factor Correction in the Laser Gyro, *IEEE J. Quantum Electron.* **QE-13,** 338-343.

Aronowitz, F. and W.L. Lim (1979), Dispersion and Gas Flow Effects in the Ring Laser Gyro, *Opt. Eng.* **18,** 376-380.

Aschauer, R., A.Asebaum, and H. Gerl (1990), Fabry-Perot Interferometer with Personal Computer Control, *Appl. Opt.* **29,** 953-958.

Avenel, O., M. Rouff, D. Varoquaux and G.A. Williams (1983), Resonant Pulse Propagation of Sound in Superfluid He-*B*, *Phys. Rev. Lett.*, **50,** 1591-1594.

Balhorn, R., H. Kunzmann, and F. Lebowsky (1972), Frequency Stabilization of Internal-Mirror Helium-Neon Lasers, *Appl. Opt.*, **11,** 742-744.

Ballik, E.A. (1966), The Response of Scanning Fabry-Perot Interferometers to Atomic Transition Profiles, *Appl. Opt.* **5,** 170-172.

Barber, N.F., F. Ursell (1948), The Response of a Resonant System to a Gliding Tone. *Phil. Mag.*, **39,** 345-362.

Barber, N.F. (1949), The Optimum Performance of a Wave Analyser, *Electronic Engng.*, **21,** 175-179.

Baxter, T.D., T.T. Saito, G.L. Shaw, R.T. Evans, and R.A. Motes (1983), Mode Matching for a Passive Resonant Ring Laser Gyroscope, *Appl. Opt.* **22,** 2487-2491.

Bennett, Jr., W.R. (1962), Hole Burning Effects in a He-Ne Optical Maser, *Phys. Rev.* **126,** 580-593.

Bennett, Jr., W.R. (1977), *The Physics of Gas Lasers* (Gordon and Breach, New York). pp. 94-97.

Bennett, R.G.T. (1970), Measurement of Q of a Superconducting Cavity Using a Swept Frequency Oscillator, *Report* (PD) 70-35 *NIMROD accelerator*, 2 November.

Bergh, R.A., H.C. Lefevre, and H.J. Shaw (1981), All-Single-Mode Fiber-Optic Gyroscope, *Opt. Lett.*, **6,** 198-203.

Bergh, R.A., H.C. Lefevre, and H.J. Shaw (1984), An Overview of Fiber-Optic Gyroscopes, *J. Lightwave Technol.* **LT-2,** 91-107.

Best, G.T. (1967), Fabry-Perot Interferometers with Electronic Determination of Doppler Line Widths, *Appl. Opt.* **6,** 287-295.

Bhawalkar, D.D., L.G. Nair and S.C. Mehendale (1977), Effect of an Internal Fabry-Perot Etalon on the Modes of a Resonator, *Opt. Lett.* **23,** 427-429.

Bilger, H.R. (1992), Private correspondence with Professor G.E. Stedman.

Bilger, H.R., and M.R. Sayeh (1986), White Noise and 1/f Noise in Optical Oscillators: State-of-the-Art in Ring Lasers, in *Noise in Physical Systems and 1/f noise* (Eds. A. d'Amico and P. Mazzetti) (Elsevier: Amsterdam) pp. 293-296.

Bilger, H.R., and G.E. Stedman (1987), Stability of Ring Laser with Mirror Misalignment, *Appl. Opt.*, **36,** 3710-3716.

Bilger, H.R., and W.K. Stowell (1977), Light Drag in a Ringlaser: an Improved Determination of the Drag Coefficient, *Phys. Rev.* A **16,** 313-319.

Bilger, H.R., G.E. Stedman, M.P. Poulton, C.H. Rowe, Ziyuan Li, and P.V. Wells (1993), Ring Laser for Precision Measurement of Nonreciprocal Phenomena, *IEEE Trans. Instrum. Meas.*, **42,** 407-411.

Bilger, H.R., G.E. Stedman and P.V. Wells (1990), Geometrical Dependence of Polarisation in Near-Planar Ring Lasers, *Opt. Commun.*, **80,** 133-137.

Bilger, H.R., P.V. Wells and G.E. Stedman (1993), Fundamental Limits for Losses on Reflection at Multilayer Dielectric Mirrors, (submitted for publication).

Billardon, M., M.E. Couprie, J.M. Ortega, and M. Velghe (1991), Fabry-perot Effects in the Exponential Decay and Phase Shift Reflectivity Measurement Methods, *Appl. Opt.* **30,** 344-351.

Born, M. and E. Wolf (1980), *Principles of Optics*, 6th Ed. (Pergamon Press, London), pp. 494-499.

Buckingham, A.D., and R.A. Shatwell (1980), *Phys Rev Lett.*, **45**, 21.

Buholz, N. and Chodrow, M. (1967), Acoustic Wave Amplitude Modulation of a Miltimode Ring Laser, *IEEE J. Quantum Electron.* **QE-3,** 454-459.

Carlisle, C.B. and D.E. Cooper (1989), An Optical Isolator for Mid-Infrared Diode Lasers, *Opt. commun.*, **74,** 207-210.

Carroll, R. and J.E. Potter (1989), Backscatter and the Resonant Fiber-Optic Gyro Scale Factor, *J. Lightwave Technol.*, **7,** 1895-1900.

Chang, R., P. Meystre (1991), Instabilities of Counterpropagating beams in a Nonlinear Medium, *Phys. Rev. A* **44** 3188-3200.

Chartier, J.-M., S. Fredin-Picard and L. Robertsson (1989), Frequency-Stabilized 543 nm HeNe Laser Systems: A New Candidate for the Realization of the Metre?, *Opt. Commun.*, **74,** 87-92.

Cheng, F.C. (1991), Phase Jump and Intensity Instabilities in a Homogeneously Broadened Bidirectional Ring Laser with Backscattering, *Opt. Commun.* **82,** 45-50.

Chow, W.W., J.B. Hambenne, T.J. Hutchings, V.E. Saunders, M. Sargent III and M.O. Scully (1980), Multioscillator Laser Gyros, *IEEE J. Quantum Electron.* **QE-16,** 918-936.

Chow, W.W., J. Gea-Banacloche, and L.M. Pedrotti, V.E. Sanders, W. Schleich and M.O. Scully (1985), The Ring Laser Gyro, *Rev. Mod. Phys.* **57,** 61-104.

Christian, W.R. and L. Mandel (1986), Frequency Dependence of a Ring Laser with Backscattering, *Phys. Rev. A* **34,** 3932-3939.

Christian, W.R. and L. Mandel (1988), Investigation of Backscattering Effects on the Correlation Properties of a He-Ne Ring Laser, *J. Opt. Soc. Am.* B **5**, 1406-1411.

Christian, W.R., T.H. Chyba, E.C. Gage and L. Mandel (1988), Observation of Random π Phase Jumps in a Ring Laser with Backscattering, *Opt. Commun.* **66**, 238-244.

Christian, W.R. and M.J. Rosker (1991), Picosecond Pulsed Diode Ring-Laser Gyroscope, *Opt. Lett.* **16**, 1587-1589.

Chyba, T.H. (1990), Deterministic Solution to the Inhomogeneously Broadened Bidirectional Ring Laser Equations with Backscattering, Asymmetry, and Cavity Rotation, *Opt. Commun.* **76**, 395-405.

Cooper, V.G. (1971), Analysis of Fabry-Perot Interferograms by Means of Their Fourier Transforms, *Appl. Opt.* **10**, 525-530.

Day, R.A. (1970), Deconvolution of Fabry-Perot Profiles, *Appl. Opt.* **9**, 1213-1215.

Davis, J.L. and S. Ezekiel (1981), Closed-Loop, Low-Noise Fiber-Optic Rotation Sensor, *Opt. Lett.*, **6**, 505-507.

Dorschner, T.A., H.A. Haus, M. Holz, I.W. Smith and H. Statz (1980), Laser Gyro at Quantum Limit, *IEEE J. Quantum Electon.* **QE-16**, 1376-1379.

Elleaume, P., M. Velghe, M. Billardon, and J. M. Ortega (1985), Diagnostic Techniques and UV-Induced Degradation of the Mirrors Used in the Orsay Storage Ring Free-Electron Laser, *Appl. Opt.*, **24**, 2762-2770.

Etrich, C., P. Mandel, R. Centeno Neelen, R.J.C. Spreeuw, and J.P. Woerdman (1992), Dynamics of a Ring-Laser Gyroscope with Backscattering, *Phys. Rev. A* **46**, 525-536.

Ezekiel, S. and S.R. Balsame (1977), Passive Ring Resonator Laser Gyroscope, *Appl. Phys. Lett.*, **30**, 478-480.

Ezekiel, S., J.A. Cole, J. Harrison, and G. Sanders (1978), Passive Cavity Optical Rotation Sensor, in *Laser Inertial Rotation Sensors* (SPIE vol. 157), 68-70.

Ezekiel, S. (1984), An Overview of Passive Optical "Gyros", in *Physics of Optical Gyros* (SPIE vol. 487), 13-20.

Ferguson, J.B. and R.H. Morris (1978), Single-Mode Collapse in 6328-A He-Ne Laser, *Appl. Opt.* **17**, 2924-2929.

Freiser, M.J. (1968), A Survey of Magneto-optic Effects, *IEEE Trans. Magn.* **MAG-4**, 152-161.

Gnass, D., N.P. Ernsting, F.P. Schafer (1991), Sagnac Effect in the Colliding-Pulse-Mode-Locked Dye Ring Laser, *Appl. Phys.* B **53**, 119-120.

Gordon, E.I. (1966), A Review of Acoustooptical Deflection and Modulation Devices, *Proc. IEEE*, **54**, 1391-1401.

Greig, J.R. and J. Cooper (1968), Rapid Scanning with the Fabry-Perot Etalon, *Appl. Opt.* **7,** 2166-2170.

Haus, H.A., H. Statz and I.W. Smith (1985), Frequency Locking of Modes in a Ring Laser, *IEEE J. Quantum Electon.* **QE-21,** 78-85.

Heer, C.V. (1984), History of the Laser Gyro, in *Physics of Optical Ring Gyros* (SPIE Vol. 487), 2-12.

Herbelin, J.M., J.A. Mckay, M.A. Kwok, R.H. Ueunten, D.S. Urevig, D.J. Spencer, and D.J. Benard (1980), Sensitive Measurement of Photon Lifetime and True Reflectances in an Optical Cavity by a Phase-Shift Method, *Appl. Opt.* **19,** 144-146.

Herbelin, J.M. and J.A. McKay (1981), Development of Laser Mirrors of Very High Reflectivity Using the Cavity-Attenuated Phase-Shift Method, *Appl. Opt.* **20,** 3341-3344.

Hernandez, G. (1966), Analytical Description of a Fabry-Perot Photoelectric Spectrometer, *Appl. Opt.* **5,** 1745-1748.

Hoffer, L.M., G.L. Lippi and N.B. Abraham (1988), Phase and Frequency Jumps in a Bidirectional Ring Laser, *Opt. Commun.* **66,** 219-224.

Höling, B., G. Leuchs, H. Ruder, M. Schneider (1992), An Argon Ion Ring Laser as a Gyroscope, *Appl. Phys. B,* **55,** 46-50.

Holland, L. (1974), *Vacuum Manual,* Edited by L. Holland, W. Steckelmacher and J. Yarwood, London: Spon, 1974.

Huang, S., P.A. Nicati, K. Toyama, R.Y. Kim, and H.J. Shaw (1993), Synthetic Heterodyne Detection in a Fiber-Optic Ring-Laser Gyro, *Opt. Lett.*, **18,** 81-83.

Ioannidis, Z.K., and I.P. Giles (1988a), Nonlinear Phase Modulation in Optical Fiber Ring Resonators, *Appl. Opt.*, **27,** 3058-3059.

Ioannidis, Z.K., P.M. Radmore, and I.P. Giles (1988b), Dynamic Response of an All-Fiber Ring Resonator, *Opt. Lett.* **13,** 422-424.

Ioannidis, Z.K., R. Kadiwar, and I.P. Giles (1989), Polarization Mode Coupling in Highly Birefringent Optical-fiber Ring Resonators, *Opt. Lett.* **14,** 520-522.

Iwatsuki, K., K. Hotate, and M. Higashiguchi (1984), Effect of Rayleigh Backscattering in an Optical Passive Ring-Resonator Gyro, **23,** 3916-3924.

Iwatsuki, K., K. Hotate, and M. Higashiguchi (1986a), Eigenstate of Polarization in a Fibre Ring Resonator and Its Effect in an Optical Passive Ring-Resonator Gyro. *Appl. Opt.*, **25,** 2606-2612.

Iwatsuki, K., K. Hotate, and M. Higashiguchi (1986b), Backscattering in an Optical Passive Ring-Resonator Gyro: Experiment, *Appl. Opt.*, **25,** 4448-4451.

Iwatsuki, K., K. Hotate, and M. Higashiguchi (1986c), Kerr Effect in an Optical Passive Ring-Resonator Gyro, *J. Lightwave Technol.*, **LT-4,** 645-651.

Jin, W. and B. Culshaw (1992a), Frequency Division Multiplexing of Fibre-Optic Gyroscopes, *J. Lightwave Technol.* **10,** 1473-1480.

Jin, W. and B. Culshaw (1992b), Analysis and Observation of Backscatter-Induced Crosstalk in a 2-D FDM Fibre Gyro System, *J. Lightwave Technol.* **10,** 1481-1488.

Kadiwar, R.K. and I.P. Giles (1989), Optical Fibre Brillouin Ring Laser Gyroscope, *Electron. Lett.*, **25,** 1729-1730.

Kalb, A. (1986), Neutral Ion Beam Sputter Deposition of High-Quality Optical Films, *Optics News*, August, 13-17.

Kaplan, A.E. and P. Meystre (1981), Enhancement of the Sagnac Effect due to Nonlinearly Induced Nonreciprocity, *Opt. Lett.* **6,** 590-592.

Keijser, R.A.J. (1977), Polarization Properties of Internal Mirror He-Ne Lasers in a Strong Transverse Magnetic Field, *Opt. Commun.* **23,** 194-198.

Kim, B.Y. and Shaw, H.J. (1986), Fiber-Optic Gyroscopes, *IEEE Spectrum*. Mar., 54-60.

Korpel, A. (1981), Acousto-Optics — A Review of Fundamentals, *Proc. IEEE*, **69,** 48-53.

Krebs, J.J., W.G. Maisch, G.A. Prinz and D.W. Forester (1980), Applications of Magneto-Optics in Ring Laser Gyroscopes, *IEEE Trans. Magn.* **MAG-16,** 1179-1184.

Kwok, M.A., J.M. Herbelin, R.H. Ueunten (1982), Cavity Phase Shift Method for High Reflectance Measurements at Mid-Infrared Wavelengths, *Opt. Eng.*, **21,** 979-982.

Lamb, W.E. Jr. (1964), Theory of an Optical Maser, *Phys. Rev.* **134,** A 1429-1450.

Lamouroux, B., B. Prade, and J. Y. Vinet (1990), Kerr Effect in All-Fiber Cavity of Optical Gyros, *Appl. Opt.*, **29,** 750-753.

Lee, P.H. and J.G. Atwood (1966), 5B1-Measurement of Saturation Induced Optical Nonreciprocity in a Ring Laser Plasma, *IEEE, J. Quantum Electron.* 235-243.

Li, Z., R.G.T. Bennett and G.E. Stedman (1991), Swept-Frequency Induced Optical Cavity Ringing, *Opt. Commun.*, **86,** 51-57.

Li, Z., and G.E. Stedman (1993), Asymmetric Response Profile of a scanning Fabry-Perot Interferometer, *Opt. Commun.*, **100,** 240-246.

Loy, M.M.T. (1977), Measurement of Two-Photon Relaxation Time by Stark Switching, *Phys. Rev. Lett.* **39,** 187-190.

Macek, W.M., and D.T.M. Davis, Jr. (1963), Rotation Rate Sensing with Traveling-Wave Ring Lasers, *Appl. Phys. Lett.* **2,** 67-68.

Macek, W.M, J.R. Schneider, and R.M. Salamon (1964), Measurement of Fresnel Drag with the Ring Laser, *J. Appl. Phys.*, **35,** 2556.

Mackintosh, J.H., and B. Culshaw (1989), Analysis and Observation of Coupling Ratio Dependence of Rayleigh Backscattering Noise in a Fiber Optic Gyroscope, *J. Lightwave Technol.*, **7,** 1323-1328.

Martin, G.J. (1986), Gyroscopes May Cease Spinning, *IEEE Spectrum*, February, 48-53.

McGregor, A. (1992), Ring Laser Signal Processing, (Undergraduate project report, No. 1992-10).

McNamara, B., K. Wiesenfeld & R. Roy (1988), Observation of Stochastic Resonance in a Ring Laser, *Phys. Rev. Lett.* **60,** 2626-2629.

Merkle, D., and F. Kaiser (1991), Dynamics of the Passive Optical Ring Resonator: Stability Analysis and the Onset of Self-Pulsing, *Phys. Lett. A* **153** 95-100.

Meyer, R.E., S. Ezekiel, D.W. Stowe, and V.J. Tekippe (1983), Passive Fibre-Optic Ring Resonator for Rotation Sensing, *Opt. Lett.*, **8,** 644-646.

Milovsky, N.D., and A.M. Tkachyov (1993), Polarization Instability of RIng Lasers, *Opt. Commun.* **95,** 127-140.

Moeller, R.P. , W.K. Burns, and N.J. Frigo (1989), Open-Loop Output and Scale Factor Stability in a Fibre-Optic Gyroscope, *J. Lightwave Technol.* **7,** 262-269.

Niebauer, T.M., J.E. Faller, H.M. Godwin, J.L. Hall, and R.L. Barger (1988), Frequency Stability Measurements on Polarization-Stabilized He-Ne Lasers, *Appl. Opt.*, **27,** 1285-1289.

Ohtsu, M. and S. Araki (1987), Using a 1.5-μm DFB InGaAsP Laser in a Passive Ring Cavity-Type Fiber Gyroscope, *Appl. Opt.*, **26,** 464-470.

Olesen, H and G. Jacobsen (1982), A Theory and Experimental Analysis of Modulated Laser Fields and Power Spectra, *IEEE J. Quantum. Electron.* **QE-18,** 2069-2080.

O'Keefe, A. and D.A.G. Deacon (1988), Cavity Ring-Down Optical Spectrometer for Absorption Measurements Using Pulsed Laser Sources, *Rev. Sci. Instrum.* **59,** 2544-2551.

Ono, K. Y. Nishiura, and M. Nishikawa (1991), Phase-Modulated Fiber Optic Gyroscope with Wide Dynamic Range and Linear Scale Factor, *Appl. Opt.*, **30,** 1070-1073.

Pesquera, L and R. Blanco (1989), Analysis of the Intensity Correlation Function of Gas Ring Lasers with Backscattering, *Opt. Commun.* **74,** 102-106.

Pesquera, L., R. Blanco, and M. A. Rodriguez (1989), Statistical Properties of Gas Ring Lasers with Backscattering, *Phys. Rev. A* **39,** 5777-5784.

Podgorski, T.J. and F. Aronowitz (1968), Langmuir Flow Effects in the Laser Gyro, *IEEE J. Quantum Electron.* **QE-4,** 11-18.

Post, E.J. (1967), Sagnac Effect, *Rev. Mod. Phys.* **25,** 475-493.

Ramponi, A.J., F.P. Milanovich, T. Kan, and D. Deacon (1988), High Sensitivity Atmospheric Transmission Measurements Using a Cavity Ringdown Technique, *Appl. Opt.* **27,** 4606-4608.

Rodloff, R. (1989), ELSY — Design for a Laser Gyro of Highest Precision, *Laser und Optoelektonik,* **21,** 33-42.

Rothenberg, J.E. and D. Grischkowsky (1985), Measurement of the Phase of a Frequency-Swept Ultrashort Optical Pulse, *J. Opt. Soc. Am.* B **2,** 626-633.

Rothenberg, J.E. (1986), Self-Induced Heterodyne: The Interaction of a Frequency-Swept Pulse with a Resonant System, *IEEE Quantum Electron.* **QE-22,** 174-181.

Rotge, J. R., B.J. Simmons, D.J. Stech, G.T. Kroncke (1986), Optical Rotation Sensors Final Report, FJSRL-TR-86-0002, USAF Academy.

Rowe. C.H., and H.R. Bilger (1992), Thermo-Dynamics of Cave, (report, 1 september, 1992).

Salomon, Ch., D. Hils, and J.L. Hall (1988), Laser Stabilization at millihertz Level, *J. Opt. Soc. AM. B* **5,** 1576-1587.

Sanders, V. (1977), High-Precision Reflectivity Measurement Technique for Low-Loss laser Mirrors, *Appl. Opt.* **16,** 19-20.

Sanders, G.A., M.G. Prentiss, and S. Ezekiel (1981), Passive Ring Resonator Method for Sensitive Inertial Rotation Measurements in Geophysics and Relativity, *Opt. Lett.* **6,** 569-571.

Scully, M.O., V. Sanders, M. Sargent III (1978), Novel Multioscillator Approach to the Problem of Locking in Two-Mode Ring Laser Gyros, *Opt. Lett.*, **3,** 43-45.

Shelby, R.M., M.D. Levenson, and S.H. Perlmutter (1988), Bistability and Other Effects in a Nonlinear Fiber-Optic Ring Resonator, *J. Opt. Soc. B* **5,** 347-357.

Siegman, A.E. (1986), *Lasers,* University Science Books, Mill Valley, California, pp. 331-334, 1130-1170.

Simpson, R.R. (1988), Ring Laser Gyro Geometry and Size, (paper presented at the AGARD meeting, 1988).

Smith, R.G. (1973), Use of the Acoustooptic Light Deflector as an Optical Isolator, IEEE J. Quantum Electron., **9**, 545-546.

Spielman, S., K. Fesler, C.B. Eom, T.H. Geballe, M.M. Fejer, and A. Kapitulnik, *Phys. Rev. Lett.* **65**, 123-6 (1990).

Statz, H., T.A. Doeschner, M. Holtz and I.W. Smith (1985), The miltioscillator Ring Laser Gyroscope, in *Laser Handbook*, Vol. 4 (M.L. Stitch and M. Bass ed., Elsevier Science Publishers B.V., 1985), pp. 231-332.

Stedman, G.E. (1985), Ring Interferometric Test of Classical and Quantum Gravity, *Contemp. Phys*, **26**, 311-332.

Stedman, G.E. (1990), *Diagram Techniques in Group Theory*, Cambridge University Press, Cambridge U.K.

Stedman, G.R. (1993a), General Manual on Canterbury Ring, Particularly the Data Significance and Processing.

Stedman, G.E. (1993b), Selection Rules for Coherent and Incoherent Nonlinear Optical Processes, in *modern Nonlinear Optics Part 2: Adv. Chem Phys.* **65***B*, eds. S. Kielich and M W Evans (Wiley, New York, 1993).

Stedman, G.E., and H.R. Bilger (1992), Ringlaser, an Ultrahigh-Resolution Detector of Optical Nonreciprocities, *Digital Signal Proc.*, **2**, 105-109.

Stedman, G.E., H.R. Bilger, Li Ziyuan, M.P. Poulton, C.H. Rowe, I. Vetharniam and P.V. Wells (1993), Canterbury Ring Laser and Test for Nonreciprocal Phenomena, *Aust. J. Phys.*, **46**, 87-101.

Stone, J. and W. Stulz (1990), Shuttle Pulse Measurement of the Reflectance of Mirrors Deposited on Fiber Ends, *Appl. Opt.* **29**, 1720-1722.

Storey, R.O., J.K. Grierson (1958), Time-Symmetric Filters (Part 2): Response to Gliding Tones, *Electronic Engng.*, **30**, 648-653.

Stowell, W.K., R.W. McAdory, C.R. Ziernicki (1978), Air Force Applications for Optical Rotation Rate Sensors, in *Laser Inertial Rotation Sensor* (SPIE vol. 157), 166-171).

Stowell, W.K (1984), Damage Effects Identified by Scatter Evaluation of Supersmooth Surfaces, in *Physics of Optical Ring Gyros* (SPIE vol. 487), 58-77.

Takahashi, M., S. Tai, and K Kyuma (1990), Effect of Reflections on the Drift Characteristics of a Fiber-Optic Passive Ring-Resonator Gyroscope, *J. Lightwave Technol.*, **8**, 811-816.

Takiguchi, K. and K. Hotate (1992), Bias of an Optical Passive Ring-Resonator Gyro Caused by the Misalignment of the Polarization Axis in the Polarization-Maintaining Fiber Resonator, *J. Lightwave Technol.*, **10,** 514-522.

Thomas, N.L. (1978), Low-Scatter, Low-Loss Mirrors for Laser Gyros, *SPIE*, **157,** *Laser Inertial Rotation Sensors*, 41-48.

Thomas, P.J., Van Driel, H.M., and Stegman, G.I.A. (1980), Possibility of using an optical fibre Brillouin ring laser for inertial sensing, *Appl. Opt.*, **19,** 1906-1908.

Tratnik, M.V., and J.E. Sipe (1986), Polarization Eigenstates of a Zeeman Laser, *J. Opt. Soc. Am. B.* **3,** 1127-1137.

Vali, V. and Shorthill, R.W. (1977), Passive Ring Resonator Laser Gyroscope, *Appl. Opt.* **15,** 1099-1100.

Vaughan, J.M. (1989), The Fabry-Perot Interferometer, *Hilger, Bristol*, p. 471-473.

Verdeyen, J.T. (1989), *Laser Electronics*, 2d. ed. Prentice Hall, New Jersey, pp. 50-51.

Wang, L.J. and L. Mandel (1988), Reduction of the Effects of Backscattering in a HeNe Ring Laser by Increased Loss and Gain, *Opt. Commun.* **68,** 357-360.

Wax, S.I. (1972), Phase Modulation of a Ring-Laser Gyro - Part I: Theory, *IEEE J. Quantum Electron.* **QE-8,** 343-352.

Wax, S.I. and Chodrow, M (1972), Phase Modulation of a Ring-Laser Gyro - Part II: Experimental Results, *IEEE J. Quantum Electron.* **QE-8,** 352-361.

Zeghlache, H., P.Mandel, N.B. Abraham, L.M. Hoffer, G.L. Lippi, and T. Mello (1988), Bidirectional Ring Laser: Stability Analysis and Time-Dependent Solutions, *Phys. Rev A* **37** 470-497.

Zipoy, D.M. (1988), Fabry-Perot Inversion Algorithm, *Appl. Opt.* **18,** 1988-1995.

Appendix A LI ET AL. 1991

Ziyuan Li, R.G.T. Bennett and G.E.Stedman (1991), Swept-frequency induced optical cavity ringing, *Opt. Commun.*, **86.** 51-57.

Optics Communications 86 (1991) 51–57
North-Holland

OPTICS
COMMUNICATIONS

Swept-frequency induced optical cavity ringing

Ziyuan Li, R.G.T. Bennett and G.E. Stedman
Department of Physics, University of Canterbury, Christchurch 1, New Zealand

Received 25 March 1991

A characteristic ringing has been observed when a high finesse ring cavity is excited by an external laser source. It is caused by the beating between the laser frequency and the cavity mode frequency when either is swept in time. The temporal waveform is analysed theoretically, extending similar analyses of ocean waves and of superconducting cavities to the optical case, and can be brought into good agreement with the experimental waveforms provided the effects of nonlinearities in the relative frequency scanning rate and of the finite laser linewidth are included. This gives a novel determination of the finesse F of supercavities (where $F \sim 10^4$), and permits the determination of a laser linewidth less than that of the cavity resonance.

1. Introduction

The ringing of a resonant system under swept frequency excitation has been investigated and applied in a wide variety of problems, wherever the frequency of a signal and the resonant frequency of the system cross over in time. Observations of such phenomena have been used to perform a frequency analysis of ocean waves by Barber [1,2] and Storey [3], and to measure the quality factor of a superconducting cavity by Bennett [4]. They have been noted in acoustic waves by Avenel [5]. Rothenberg [6,7] sent a frequency-swept ultrashort optical pulse through a resonant vapour, determining from the observed ringing the time-dependent phase of the ultrashort pulse. Loy [8] observed ringing in a Stark-switching optical experiment when the resonant frequency of the medium was swept rather than the pulse frequency. Loannidis et al. [9,10] observed ringing in an optical fibre ring resonator, a phase modulation being induced by a piezoelectric cylinder around which was wrapped a length of optical fibre.

In any experiment displaying these phenomena, the system must be linear, the input frequency must sweep through the system resonance in a time which is much smaller than the decay time of the resonant system, and the coherence length of the source must be long compared to the temporal width of the ringing pulse.

We report analogous optical ringing phenomena when the beam from a Newport NL-1 HeNe frequency-stabilised laser is injected through an acousto-optic modulator (AOM) as isolator and a matching lens into each of two passive supercavities: firstly a Newport SR-130 supercavity with a free spectral range of 6 GHz and with a finesse which is quoted as greater than 20000, and secondly (fig. 1) a square ring cavity with a perimeter of 4 m and whose supermirrors have reflectance of approximately 99.9985%, giving a free spectral range of 75 MHz and also a finesse $\sim 10^4$. Our use of an AOM as isolator (a precedent is in ref. [11]) relies on the doubled frequency shift (140 MHz) in the retroreflected beam moving its frequency outside the cavity profile (of width ~ 1 MHz) of the NL-1 laser; the attendant beam deflection (approximately 14 mrad) varies less than 0.5 μrad during the ringing, so that injection alignment is not affected. Direct monitoring with the SR-130 indicates that the laser frequency fluctuates over about 100 kHz in the short term (5 ms), itself at a frequency of the order of 50–100 kHz; this work shows that a rather lesser frequency excursion is found over the smaller time scales probed by this experiment.

While the TEM_{00} mode of the NL-1 laser was matched to each cavity by a conventional lens, there

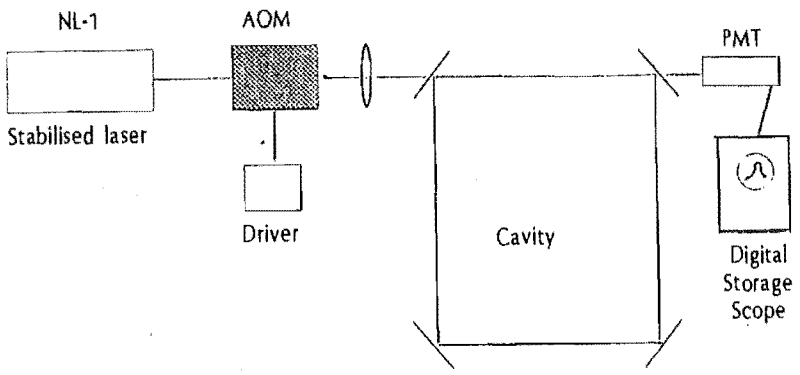

Fig. 1. Experimental setup for inducing ringing profiles for the ring supercavity.

is no locking loop between the two cavities, so that relative frequency variations also arise from variations in the passive cavity, including controlled scanning in the case of the Newport SR-130, and atmospheric microturbulence in the case of the ring cavity. In each case these variations induce observable ringing, the output taking the form of a partly random series of pulses each with a temporal width of about 3 μs. The PMT detectors have a much faster response, and it was checked that system response was not the limiting factor by bypassing the cavity with mirrors, when no ringing signals were seen. These pulses are captured on a digital storage oscilloscope. Each pulse is asymmetrical, the leading edge rising smoothly, but the trailing edge having a pronounced oscillatory envelope with the characteristic of a chirp with ascending frequency.

We show that this waveform depends significantly and characteristically on each of three considerations: the quality factor of the probe cavity, the functional form of the relative frequency scanning, and the laser linewidth. Each of these may then be deduced from experiment. Oversimplifying somewhat, we can separate the role of each parameter as follows. The ratio of the cavity resonance width to the (linear part of the) scanning rate determines, and so can be estimated from, the overall ringing pulse width. Several orders of nonlinear terms in the scanning rate may be estimated from the temporal distribution of the interference maxima; the random variations in the nonlinear coefficients cause the difference in waveforms between pulses. The linewidth of the laser line can be estimated from the visibility of the ringing oscillations.

Although the Airy function, or filter function for intensities, is used in standard theoretical studies of the scanning Fabry-Perot interferometer [12–18], it is inadequate for the analysis of ringing. It is vital to include the phase shift information in the amplitude response, since ringing is a consequence of interference between the instantaneous laser amplitude and the cavity amplitude response function. Our analysis therefore avoids the Airy function description of an optical cavity response.

2. Theory of the ringing profile

Let $A_i(t)$ be the incident complex wave amplitude for one choice of linear polarisation of the beam incident on an optical cavity. Its Fourier transform will be written $\mathscr{A}_i(\omega)$.

In the simplest approximation of a wave with constant amplitude, $A_i(t)=A_0\exp[i\omega(t)t]$. The effect of residual laser jitter needs inclusion; we use a stochastic model for phase noise and write the input field at time t as

$$A_i(t)=A_0\exp[i\omega(t)t]\exp(-|t|/\tau_s)\,, \qquad (1)$$

where τ_s is an effective decay time, and $\omega(t)$ is the instantaneous angular frequency. A derivation is

given in the appendix. The angular frequency can be expanded in a Taylor series: $\omega(t)=\omega_0+\omega_0' t+\frac{1}{2}\omega_0'' t^2+\frac{1}{6}\omega_0''' t^3$, where the expansion coefficients are ω_0, the injected frequency at $t=0$, ω_0', the (linear approximation to the) relative scanning rate, and ω_0'', ω_0''' representing nonlinearities in the relative scanning rate. $\omega(t)-\omega_0$ is to be interpreted as the instantaneous difference between the laser frequency and the cavity resonance, arising from scanning of the SR-130 and from microturbulence of the air and motion of the cavity mirrors for the ring cavity, after taking a short-time (sub-millisecond) average over jitter. Over the microsecond timescale of the experiment we may expect the linear term ω_0' to dominate, so that the response of either the SR-130 scanning Fabry-Perot cavity or the 1 m² ring cavity to a monochromatic wave will be similar to the response of a stable cavity to a wave with linear FM. We shall attempt to determine the quadratic and cubic terms ω_0'', ω_0''' as well as the linear term ω_0' applicable in any particular run, together with the effective laser linewidth and the cavity finesse, from the profile of the system response.

The transfer function of the optical cavity is $H(\omega)=T/[1-R\exp(-\mathrm{i}\delta)]$. T is the equivalent transmissivity of the cavity mirrors, and R their reflectance; typically $T\sim 4$ ppm, $1-R\sim 15$ ppm, the difference representing the effects of absorption and scattering in the multilayer dielectric coatings [19]. The round-trip optical phase shift $\delta=(\omega-\omega_c)L/c$ where ω_c is the resonant frequency of the cavity, L is its optical path length and c is the speed of light.

In such a supercavity with finesse F of order 10^4, δ will be of order 10^{-4} modulo 2π when the transmitted field $\mathscr{A}_t(\omega)=\mathscr{A}_i(\omega)\,H(\omega)$ is significant. Hence [20] we may expand the exponential in $H(\omega)$, and retain only the linear term: $H(\omega)=B/[\gamma_c+\mathrm{i}(\omega-\omega_c)]$ where $B\equiv cT/RL$ and the cavity width $\gamma_c\equiv c(1-R)/RL$. We work in the time domain, where the transmitted amplitude $A_t(t)$ is the convolution of $A_i(t)$ and the impulse response $h(t)$, the inverse Fourier transform of $H(\omega)$, so that

$$h(t)=BS(t)\exp(-\gamma_c t)\exp(\mathrm{i}\omega_c t)\,, \tag{2}$$

where $S(t)$ is Heaviside's unit step function [21]: $S(t)=0$ for $t\leqslant 0$ and $S(t)=1$ for $t>0$. Then:

$$A_t(t)=\int_{-\infty}^{\infty}\mathrm{d}t'\,A_i(t')\,h(t-t')$$

$$=\int_{-\infty}^{t}\mathrm{d}t'\,A_i(t')\,h(t-t')\,. \tag{3}$$

We choose the origin of time so that $\omega_0=\omega_c$ and obtain from the above equations, with the change of variables $\tau\equiv\gamma_c t'$, $\bar{t}\equiv\gamma_c t$, $b\equiv 1/(\gamma_c\tau_s)$, $a_1\equiv\omega_0'/\gamma_c^2$, $a_2\equiv\frac{1}{2}\omega_0''/\gamma_c^3$, $a_3\equiv\frac{1}{6}\omega_0'''/\gamma_c^4$, $C=A_0B/\gamma_c$:

$$A_t(t)=C\exp(-\bar{t})\exp(\mathrm{i}\omega_c t)\int_{-\infty}^{\bar{t}}\mathrm{d}\tau\exp(\tau-b|\tau|)$$

$$\times\exp\{\mathrm{i}[\tau^2(a_1+a_2\tau+a_3\tau^2)]\}\,. \tag{4}$$

This equation encapsulates the ringing phenomenon. The simplistic discussion of section 1 may be justified as follows. The final complex exponential (sinusoidal) factor represents the beating of the amplitudes (particularly for $\tau>0$, i.e. $t>0$ and so the decay of the pulse, since the accompanying exponential factor then enhances the contribution), its nonlinear form characterising the spacing of interference maxima; the resulting oscillations are damped by the term involving b, and the overall envelope is provided by the remaining real exponential terms. We perform a least squares fit of the model parameters a_1, b, a_2 and a_3 to the experimental pulse waveform, and in doing so find this parametrisation to be both adequate and informative.

This is demonstrated by the curves (a), (b), (c) of fig. 2, which give the predictions of eq. (4) when each of b, a_2 and a respectively are varied over a certain range. A comparison of these figures gives further emphasis to our earlier qualitative discussion. The major effect of the (renormalised) effective laser width parameter b is on the visibility of the ringing. The nonlinear coefficients a_2, a_3 squeeze the oscillations on the tail, as observed experimentally, but their variation affects ringing in the precursor (i.e. the profile for times prior to the main peak), some evidence of which can be seen in the experimental profile.

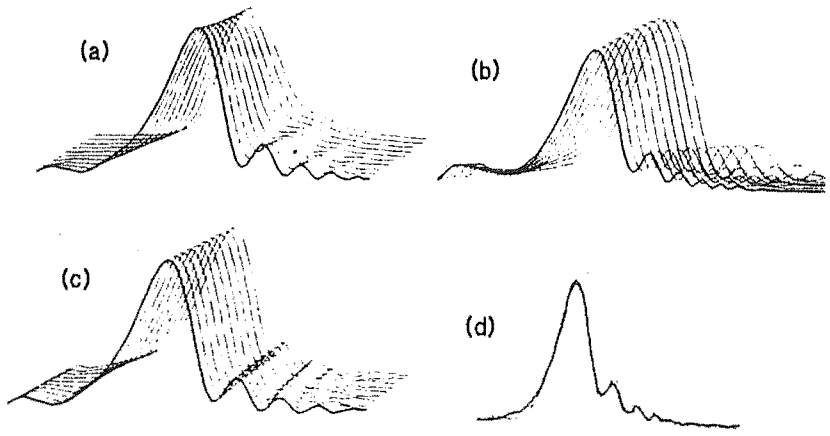

Fig. 2. (a), (b), (c): the predictions of eq. (5) when each of the laser linewidth parameter b, and the nonlinear scanning rate parameters a_2 and a_3 are varied. Unless otherwise stated, a_1 (where $a_1 \equiv \omega_0'/\gamma_c^2$) is set to 4.0, while b ($b \equiv \Delta\nu_L/\Delta\nu_{1/2}$) and the nonlinear parameters a_2 ($a_2 \equiv \frac{1}{2}\omega_0''/\gamma_c^3$) and a_3 ($a_3 \equiv \omega_0'''/6\gamma_c^4$) are set to zero. In (a), b ranges from 0.0 (heavy line) to 2.0; in (b), a_2 ranges from -0.8 to $+0.8$; in (c), a_3 ranges from -0.2 to $+0.8$. (d) A typical fit to experiment. The theoretical curve is repeated with a displacement to show its form more clearly.

3. Analysis of experimental fits

3.1. Introduction and general features

In fig. 2d, a comparison is given of a typical experimental profile obtained from the SR-130 supercavity with a fitted theoretical curve from eq. (4), the latter is also reproduced with a displacement so as to show its shape more clearly. The success of our model is apparent in that a judicious combination of the fitting coefficients reproduces all the main features of the pulse. Without this judicious combination, it is very difficult for example to position the first fringe maximum in the tail of the profile sufficiently close to the main peak. The limitations of the model are also apparent; it is hard to force the theory also into keeping the visibility of the interference pattern as high in the tail as the experiment indicates.

3.2. SR-130 supercavity

Data from three experimental runs, together with theoretical fits using eq. (4), are given in fig. 3. The fitting parameters and derived constants are listed in table 1.

First we comment on the run-dependent parameters. The value for the linear scan rate ω_0' varies between runs even in this case because of scanning range variations imposed on the SR-130. Except for the relatively poor fit of fig. 3c these run-dependent parameters can be estimated for each run from the fit to an accuracy of 2%. The nonlinear terms ω_0'', ω_0''' are particularly affected by the data, and also the quality of the fit, for the tail of the ringing waveform. They are consequently much more sensitive to the details of the fit, such as choice of starting point and number of iterations, and relative weighting of peak and tail data points. The effective laser width $\Delta\nu_L$ is markedly less than that inferred by direct observation of transmission through the SR-130 Fabry-Perot on a standard oscilloscope (see section 1), presumably because of the shorter time scale of this experiment. In principle, these various parameters contain information on the phase jitter in the laser, and it is noteworthy in view of the relative stability of the SR-130 cavity that these parameters vary significantly between runs. However more accurate results would be needed for worthwhile deductions to be possible. This is a possibility for future work.

The averaged finesse estimate from these runs is 85000 ± 4000. Such a value exceeds the specifications ($F \sim 40000$ at centre wavelength) for the SR-130, corresponding to a resolution of the order of 0.6 μÅ. This is consistent with the (undoubtedly conservative) estimate of 3 μÅ quoted by Boero [22].

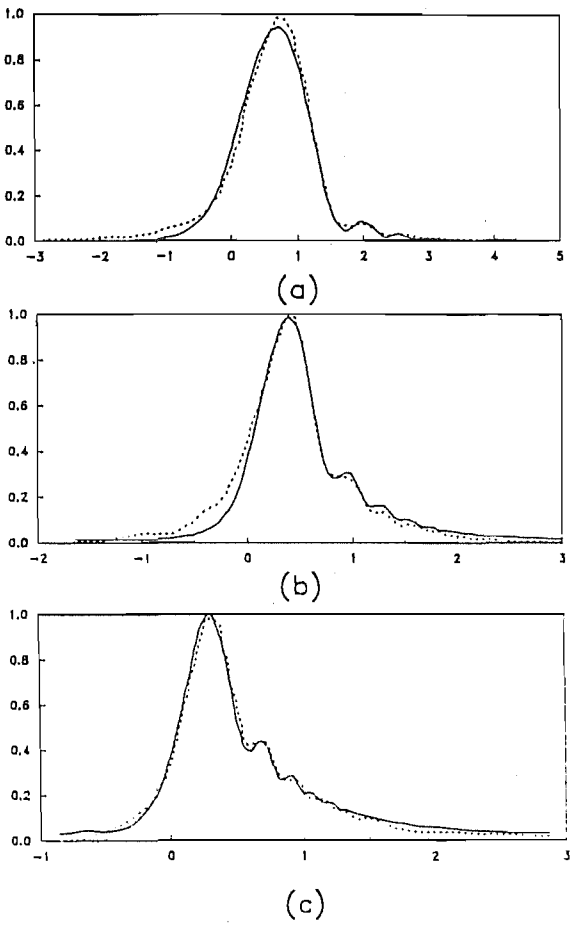

Fig. 3. Experimental results and theoretical fits for three runs using the Newport SR-130 supercavity.

The quoted error in F is associated with calibration of the time axis and is itself readily capable of improvement: the mutual consistency of our various estimates of the finesse is 1.5%.

3.3. Square ring cavity

A similar set of results, now for the setup of fig. 1, is given in fig. 4. The derived fitting parameters are given in table 2.

It is gratifying that similar values are obtained to those in table 1 for the laser effective linewidth parameter. The relatively low values obtained for Q, despite the use of supermirrors, and their variations between runs, may be attributed to difficulties in matching the injected beam to the cavity mode.

Table 1
Fitting parameters for the theoretical plots in figs. 3a-c for the SR-130 scanning Fabry-Perot supercavity. Estimated errors in the last decimal place from calibration errors and from variation between different fits in the case of the run-dependent parameters ω_0', ω_0'', ω_0''' are quoted in square brackets. The mirrors have a separation L of 25.3 mm, giving a free spectral range $\Delta\nu_{FSR}$ ($=c/2L$) equal to 6.0 GHz. Of the two run-independent fitting parameters, one parameter is variously expressed as the quality factor Q, the corresponding frequency resolution $\Delta\nu_{1/2}$ (the full width at half-power, equal to γ_c/π) given by $\Delta\nu_{1/2}=\nu/Q$, and the corresponding finesse $F=Q\Delta\nu_{FSR}/\nu$, where ν is the optical frequency of 474 THz. The other parameter is the effective laser linewidth $\Delta\nu_L$ given by $\Delta\nu_L=1/\pi\tau_s$.

	Run			
	(a)	(b)	(c)	Units
Q	6.79	6.73	6.61	10^9
$\Delta\nu_{1/2}$	6.98	7.04	7.17	10^4 Hz
F	8.60	8.52	8.37	10^4
$\Delta\nu_L$	3.1	8.6	9.5	10^4 Hz
ω_0'	0.115 [5]	0.387 [5]	0.718	$(\text{MHz})^2$
ω_0''	0.0017 [2]	0.000 [4]	0.0072	$(\text{MHz})^3$
ω_0'''	0.0005 [5]	0.0000 [1]	0.0001	$(\text{MHz})^4$

Acknowledgements

We acknowledge gratefully the help of C. Rowe for much invaluable technical assistance, also Professors F.V. Kowalski and H.R. Bilger for comments and for several relevant references.

Appendix 1

Phase noise model for laser width

We model the optical field emitted by the NL-1 laser as a quasimonochromatic amplitude-stabilized field undergoing a phase fluctuation [23]

$$E(t)=E_0\exp\{i[\omega_0 t+\phi(t)]\}, \qquad (A1)$$

where ω_0 is the mean optical frequency and $\phi(t)$ the random phase fluctuation from those stochastic processes leading to the frequency jitter and spectral broadening of the laser line; it is assumed that the gain tube makes amplitude fluctuations relatively less

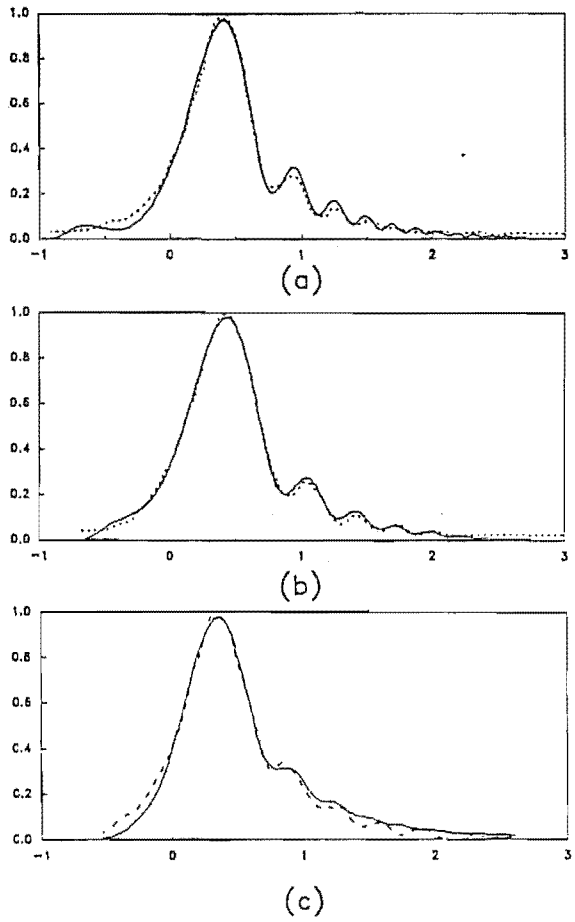

Fig. 4. Experimental results and theoretical fits for three runs using the ring supercavity.

Table 2
Fitting parameters for the theoretical plots in figs. 4a-c for the ring supercavity. Notation is as for table 1. The ring has a perimeter of 4.0 m, giving a free spectral range of 75 MHz.

	Run			
	(a)	(b)	(c)	Units
Q	9.4	8.4	7.5	10^9
$\Delta\nu_{1/2}$	5.0	5.7	6.4	10^4 Hz
F	1.5	1.3	1.2	10^3
$\Delta\nu_L$	1.6	4.1	7.2	10^4 Hz
ω_0'	0.215 [3]	0.248 [4]	0.43 [4]	$(\mathrm{MHz})^2$
ω_0''	−0.0039 [8]	0.007 [8]	0.01 [1]	$(\mathrm{MHz})^3$
ω_0'''	0.000 [1]	0.0007 [7]	0.003 [3]	$(\mathrm{MHz})^4$

important [24]. The autocorrelation function defined as

$$G_E^{(1)}(\tau) = \langle E^*(t)\, E(t+\tau)\rangle$$
$$= \langle \exp[\mathrm{i}\Delta\phi(t,\tau)]\rangle \exp(\mathrm{i}\omega_0\tau)\,, \qquad (A2)$$

where $\Delta\phi(t,\phi)$ is the phase jitter, i.e. the random phase change between time t and $t+\tau$. $\Delta\phi(t,\tau)$ is assumed to be a non-zero stationary gaussian probability distribution. The ensemble average can be rewritten using the relation [25]:

$$\langle \exp[\mathrm{i}\Delta\phi(t,\tau)]\rangle = \exp[-\tfrac{1}{2}\langle\Delta\phi^2(\tau)\rangle]\,. \qquad (A3)$$

The instantaneous frequency fluctuation spectrum is taken to be flat [26], leading to a linear time dependence of the mean-square phase jitter. This results in a lorentzian line shape. $\langle\Delta\phi^2(\tau)\rangle$ can be expressed as [27]

$$\langle\Delta\phi^2(\tau)\rangle = 2\gamma_s|\tau|\,, \qquad (A4)$$

where $2\gamma_s$ is the angular full line width at half maximum of the lorentzian spectrum of the laser field. Using (A1)–(A4) and changing the variables $\gamma_s = 1/\tau_s$ and $\tau = t$, we obtain eq. (1).

References

[1] N.F. Barber and F. Ursell, Phil. Mag. 39 (1948) 345.
[2] N.F. Barber, Electronic Engineering 21 (1949) 175.
[3] L.R.O. Storey and J.K. Grierson, Electronic Engineering 30 (1958) 648.
[4] R.G.T. Bennett, Measurement of Q of a superconducting cavity using a swept frequency oscillator, Report (PD)70-35 NIMROD accelerator, 2 November 1970.
[5] O. Avenel, M. Rouff, D. Varoquaux and G.A. Williams, Phys. Rev. Lett. 50 (1983) 1591.
[6] J.E. Rothenberg and D. Grischkowsky, J. Opt. Soc. Am. B 2 (1985) 626.
[7] J.E. Rothenberg, IEEE J. Quantum Electron. QE-22 (1986) 174.
[8] M.M.T. Loy, Phys. Rev. Lett. 39 (1977) 187.
[9] Z.K. Loannidis and I.P. Giles, Appl. Optics 27 (1988) 3058.
[10] Z.K. Loannidis, P.M. Radmore and I.P. Giles, Optics Lett. 13 (1988) 423.
[11] D. Hils and J.L. Hall, Phys. Rev. Lett. 64 (1990) 1697.
[12] E.A. Ballik, Appl. Optics 5 (1966) 170.
[13] G. Hernandez, Appl. Optics 5 (1966) 1745.
[14] G.T. Best, Appl. Optics 6 (1967) 287.
[15] R.A. Day, Appl. Optics 9 (1970) 1213.
[16] V.G. Cooper, Appl. Optics 10 (1971) 525.
[17] W.R. Bennett Jr., Appl. Optics 17 (1978) 3344.

[18] D.M. Zipoy, Appl. Optics 18 (1979) 1988.
[19] H.R. Bilger, G.E. Stedman and P.V. Wells, Optics Comm. 80 (1990) 133.
[20] D.Z. Anderson, J.C. Frisch and C.S. Masser, Appl. Optics 23 (1984) 1238.
[21] R.N. Bracewell, The Fourier transform and its applications (New York, McCraw-Hill, 1965) p. 363.
[22] F. Boero, Laser Focus/Electro-Optics (March 1988) p. 120.
[23] A. Yariv and W.M. Caton, IEEE J. Quantum Electron. QE-10 (1974) 509.
[24] P.W. Milonni and J.H. Eberly, Lasers (Wiley, New York, 1988) p. 342.
[25] H.E. Rowe, Signal and noise in communication systems (Van Nostrand, Princeton, 1965).
[26] A. Yariv, Quantum electronics (2nd Ed., Wiley, New York, 1975).
[27] P.B. Gallion and G. Debarage, IEEE J. Quantum Electron. QE-20 (1984) 343.

Appendix B BILGER ET AL. 1993

H.B. Bilger, G.E. Stedman, M.P. Poulton, C.H. Rowe, Ziyuan Li, P.V. Wells (1993), Ring Laser for precision measurement of nonreciprocal phenomena, *IEEE Trans. Instrum. Meas. (special issue for CPEM/92: Conference on Precision* Electromagnetic Measurements, Paris, June 9-12, 1992), **42,** 407-411.

Ring Laser for Precision Measurement of Nonreciprocal Phenomena

Hans R. Bilger, G. E. Stedman, M. P. Poulton, C. H. Rowe, Ziyuan Li, and P. V. Wells

Abstract—We constructed a 0.75 m^2, square-ring laser operating at the helium–neon wavelength 633 nm (474 THz), for precision experiments in applied sciences as well as for fundamental experiments in the physics of nonreciprocal optical and other phenomena. High-quality mirrors and the absence of media, except for the He–Ne gas mixture in the beam, insure a high-quality factor of the cavity and low lock-in frequency. The Sagnac effect by the earth rotation sufficed to unlock the countercirculating modes, without the need to restore to dither, or other means of biasing, thus providing a very stable bias with a stability of the order of 1 part in 10^9. Once the ring is unlocked by this means and is in single mode excitation, the response is extremely linear in any additional frequency, whether induced mechanically or via electromagnetic fields; in the Fourier domain, all lines are equally affected by frequency pulling and by susceptibility changes. As a result, their relative positions are not affected, and their absolute frequencies may be calibrated from the earth rotational frequency. We observed a net line width of 32 ± 2 MHz. The center of the earth line is determined with a precision of about 1 mHz, that is, with a fractional precision of 1 MHz/474 THz ≈ 2×10^{-18}, which outclasses Mössbauer [1] and maser [2] lines by several orders of magnitude. This implies that it is now possible to obtain *accuracies* of such additional effects of the order of millihertz. We intend to exploit this extraordinarily high resolution in seismography, in particular shear waves, as well as in a number of physics experiments such as Fresnel drag.

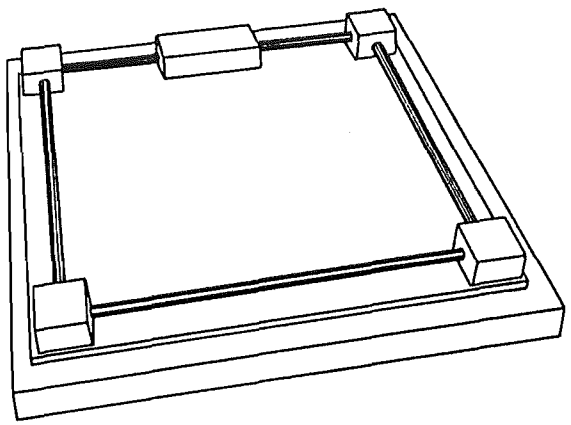

Fig. 1. Schematic of the square ring laser with four corner boxes containing highly reflective multilayer dielectric mirrors. The ring is based on a 2.54 cm thick Zerodur plate that in turn is placed on a leveled granite block of about 10 cm thickness. The upper side contains the RF excitation of the helium–neon gas. The interferometer is placed at the output of the mirror at the upper right corner. The laser beams travel inside the pyrex tubes, with no interfaces. Before filling the ring with the gas of adjustable mixing ratio and total pressure, it is evacuated to about 10^{-3} to 10^{-5} Pa.

I. Introduction

In a ring laser (Fig. 1) at least two counterrotating laser beams are created in a cavity with perimeter P and area vector $\vec{A}$ (in our case $P = 3.48\ m$, and $|\vec{A}| = 0.748\ m^2$ respectively). The theory and operation have been dealt with in various publications [3]–[5]. As the beams travel in exactly the same path, any change in geometry, for example, due to temperature changes, stress of the support, and so on, affects both beams equally, and the counterrotating beam frequencies are split only by nonreciprocal phenomena. This stability has enabled the measurement of fundamental noise limits [6], [7] and has enabled us in the past to perform precision measurements of Fresnel drag [8].

Given a frequency-splitting phenomenon, the resulting frequency difference can easily be obtained by combining the two beams at some mirror output, where an interferometer produces a running fringe pattern such that a corotating detector observes precisely the beat frequency.

Ring lasers thus act as differential sensors for effects that influence the two counterrotating beams differently. No external reference is in principle needed, and frequency differences in the microhertz range can be established with suitable measuring time lengths. As this is done with optical frequencies of the order of 10^{15} Hz, the achievable sensitivities for such phenomena as Faraday effect, Fresnel drag, magnetic-field induced changes of the index or refraction [9], mechanical rotation, and so on are correspondingly high.

II. Construction of Ring Laser and First Results

The ring laser has a nearly square, plane geometry. The ring geometry is defined by highly reflecting multilayer dielectric mirrors with original reflectance of 99.9985%

Manuscript received June 12, 1992; revised October 13, 1992. H. R. Bilger was supported in part by the NSF. This work was also supported by the US-NZ Cooperative Science Program, two Erskine Fellowships given by Canterbury University, and the Prince of Wales Foundation.

H. R. Bilger is with the School of Electrical and Computer Engineering, Oklahoma State University, Stillwater, OK 74078-0321.

G. E. Stedman, M. P. Poulton, C. H. Rowe, Z. Li, and P. V. Wells, are with the Department of Physics and Astronomy, University of Canterbury, Christchurch 1, New Zealand.

IEEE Log Number 9206480.

for s-reflection as measured in a ring-down cavity. Ultra-high vacuum coated SiO_2-TiO_2 $\lambda/4$ layers give losses of 4 ppm due to scattering (TIS), 4 ppm from transmission and absorption (by difference) of 7 ppm, approaching that of the bulk materials. For further mechanical and thermal stability the mirrors are mounted in superinvar holders resting on a 1 × 1 m^2 Zerodur plate, itself on a granite base. The stainless steel corner boxes avoid mechanical contact with the mirrors; their bottoms are open and are sealed by Viton O-rings against the Zerodur plate. The corners are connected with each other by pyrex tubes (see Fig. 1) which also contain the helium–neon mixture. The beams can easily be accessed with electric and magnetic fields. To insert material media into the beams, Brewster or antireflection windows have to be introduced.

High-frequency (RF) excitation for the HeNe plasma amplifier is chosen at various frequencies between 10 and 50 MHz. This mode of excitation has the advantage of easy adjustability; it avoids biasing effects like Langmuir flow [5], and it obviates the need for internal electrodes. The ring presents no interfaces to the beam; that is, the beam travels through the HeNe mixture only. The mixture ratio and the total pressure are variable. The present results below are obtained with a natural isotope mixture, although we intend to use an isotope mix Ne^{20}:Ne^{22} = 54:46 [5] in the future, for better control on the composite gain curve.

All data were taken while the ring operated in single longitudinal gaussian mode, as observed on a high-resolution Fabry–Perot with a free spectral range of 6 GHz and an observed finesse ≃ 60000 (NL-1 from Newport). Starving out all but one mode proved to be surprisingly easy, despite the relatively small longitudinal mode spacing of 86 MHz. Our applications require small bandwidths—typically less than 1 Hz—and therefore need only low beam power for an adequate signal/noise ratio. We had previously estimated that reducing the gain to the point when the output beam power was approximately 30 nW would suffice to starve out all but one mode; the measured output beam power under single mode operation was typically 16 nW.

The ring-down decay time is τ = 15 μs, which translates into a quality factor $Q = \omega\tau = 4.5 \times 10^{10}$. This value is substantially lower than that given through the reflectivity of the mirrors above because of contamination.

After several (up to eight) hours of operation, the locking frequency increases noticeably, and ultimately the ring locks. This is due to contamination of the gas; the prototype uses Viton O-rings for ease of assembly. Fortunately, the ring may be regenerated essentially to its previous level of performance by thorough pump-down and a gas refill. It seems that this contamination is associated with the O-rings. It affects the gas much more than the mirrors. A next generation ring now under design avoids O-rings altogether. Independently of this, we also observed slowly increasing mirror damage, which could only partially be restored by special cleaning and annealing by the manufacturer. This appears to be related to our initial use of an oil-diffusion pump, albeit with a liquid nitrogen cold trap; a turbomolecular pump and mass spectrometric leak detector system are presently being installed.

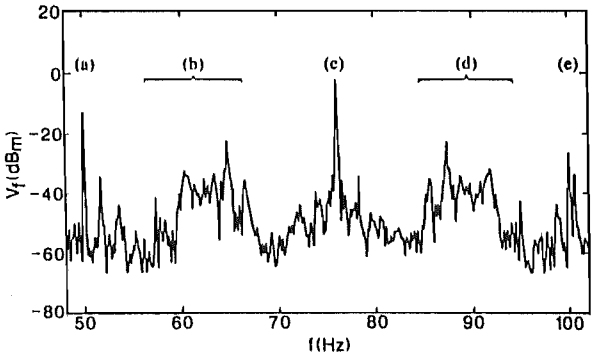

Fig. 2. Spectral analysis of the ring laser output in the frequency range 48 Hz–102 Hz. Identification of lines: a) 50 Hz for vibration due to fundamental power line frequency, b) lower sideband with prominent peaks at 11.306 Hz below and above the earth line. This is due to torsional oscillations of the ring laser base, c) earth line, d) upper sideband, symmetric to lower sideband b, due to the same causes, e) 100 Hz harmonic of power line frequency. Not shown are the harmonics of the earth line at 152 Hz and 228 Hz (analyzed in [16]), larger satellite frequencies of the 50 Hz sideband, and the fundamental frequencies of the rotation of the ring laser base in the frequency range 9–25 Hz.

For an initial demonstration of the operation of our ring we observed the frequency splitting due to the earth rotation. The beat frequency between the counterrotating beams of a ring operating at wavelength λ, that is subjected to a rotation $\vec{\Omega}$, is given by the Sagnac equation

$$\Delta f = 4\vec{\Omega} \cdot \vec{A}/(\lambda P). \quad (1)$$

The ring is placed level. At Christchurch (latitude 43° 29'), where the ring is working, we expect a beat frequency of 68.5 Hz. Fig. 2 shows one of the spectra obtained from ring output for a duration of T = 16.384 s, with a sampling rate of 500 s^{-1}. It may be emphasized again that no extra frequency splitting was introduced; the ring is free-running, subject only to the earth rotation. The ring laser output was prefiltered with a simple low-pass filter of bandwidth 500 Hz.

We observe several characteristic features. The peak at 76 Hz is due to the earth rotation (the next two harmonics have been observed as well). The noise power spectral density is approximately 32 dB below the observed peak and constant in the observed frequency range of 0.2–250 Hz. The peaks at 50 Hz and at 100 Hz are most probably due to residual power line hum, that is, modulation of the RF-excitation power by the electricity mains supply. Symmetric sidebands to the earth rotation-induced peak appear in the frequency range 50–76 Hz, and 76–99 Hz. These sidebands are due to the various mechanical resonances of the ring base which are excited by motion of the building. For an analysis, see Section III.

With a filter whose bandwidth (full width at half maximum) is 164 MHz to suppress sidelobes in the frequency domain, we observe the data in Table I for the three earth

TABLE I
EXAMPLE OF EVALUATION OF ONE RUN

	Earthline	Double Line	Triple Earthline
Center frequency (Hz)	76.1238 ± 0.0011	152.2474 ± 0.0020	228.3698 ± 0.0026
Base frequency (Hz)	76.1238 ± 0.0011	76.1237 ± 0.0010	76.1233 ± 0.0009
Linewidth (FWHM)			
With window (Hz)	0.1649 ± 0.0027	0.1740 ± 0.0048	0.1830 ± 0.0074
Without window (Hz)	0.0684 ± 0.0015	0.0831 ± 0.0040	0.1151 ± 0.010

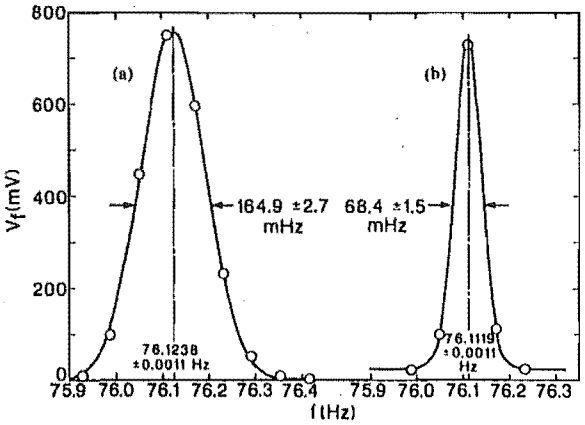

Fig. 3. Fit of Gaussians (continuous lines) to the measured Fourier components of the earthline (circles). 3(a) From a run that was prefiltered to avoid sidelobes. 3(b) Without prefiltering. The best-fitted parameters (full-width-at-half-maximum (FWHM) and center-of-line are given, together with their errors.

lines (see also Fig. 3(a)). The equivalent base frequencies are the same within 1 MHz, while the errors given show that the evaluations are compatible.

Without filtering, the linewidths are much smaller, see Fig. 3(b). The harmonics are no longer dominated by the time window; the net ring laser linewidth is in this run thus determined by deconvolution as 32 ± 2 MHz in [10], together with further details of the statistical analysis of the prototype output.

The precision of the determination of line position, 1 MHz, is a fraction 2.3×10^{-18} of the laser frequency at 474 THz. As a fraction of the earth rotation peak (76 Hz in Fig. 2), the relative precision is 1 MHz/76 Hz = 1.3×10^{-5}.

Under simplified conditions we expect noncorrelated white noise in the beams. If observed through a square window in time (duration T), the rms frequency fluctuation of the beat frequency is expected to be

$$\Delta f_{\text{rms}} = [2hf_0^3/Q^2P_0T]^{1/2}. \quad (2)$$

With a measured decay time of $\tau = 15\ \mu s$ ($Q = 4.5 \times 10^{10}$), a measurement duration of $T = 16.384$ s, and an estimated power loss of $P_0 = 1\ \mu W$ (the latter is difficult to ascertain), we calculate $\Delta f_{\text{rms}} \sim 2$ MHz due to quantum noise. A few estimates of the sensitivity of the instrument for various planned experiments are given in Section IV.

III. Calibration of Ring Laser Output

It is of considerable importance to know the properties of the ring laser as a transducer for measuring nonreciprocal effects. To this end, we report here an analysis of the satellite frequencies ("sidebands") b and d in Fig. 2, in particular those due to the prominent lines arising from the ring laser base resonance (which was also directly measured) at $f_T = 11.306 \pm 0.009$ Hz, with the relatively high quality factor $Q = 34$.

This ring laser base resonance was determined to generate a peak-to-peak angular motion of 1.1 μrad, which produced satellites whose relative amplitudes agree with standard frequency-modulation theory, four being above the noise. The latter also predicts that these sidelobes should have an equidistant frequency separation of f_T. Their center frequencies are plotted in Fig. 4 (filled circles) versus the order of the sidelobe, where zero corresponds to the earth line itself. A straight line in Fig. 4 verifies this; it has a slope of 11.300 ± 0.010 Hz. The agreement between the values of this slope and of f_T demonstrate the linearity of the ring laser as a transducer. The sidelobes cover the frequency range of 53 to 98 Hz.

A much larger frequency range is covered by the 50 Hz sidelobes, namely from 26 Hz to 226 Hz. The four analysed sidelobe frequencies are plotted in Fig. 4 as hollow dotted circles. The fitted straight line has a slope of 50.0162 Hz, compared to a measured 50 Hz line center of 50.0155 ± 0.0010 Hz. This fit is particularly good, the residuals in this case having an rms value of 6.3 mHz.

We would like to include a word of caution; while the table resonance satellites at 11.306 Hz stem clearly from a mechanical frequency modulation of the earth line and suffice to show the extreme linearity of the device, the 50 Hz satellites may not necessarily have the same cause; as already suggested above, the satellites could be partly due to the effects of hum at the international power line frequency of 50 Hz and its harmonics, giving rise to amplitude modulation of the optical beam through the RF excitation.

This result is exceedingly simple: Any additional oscillatory effect such as an oscillatory rotation will produce sidelines to the earth rotation line at a spacing given precisely by their oscillation frequency, even if (as in our case) the earth rotation line itself suffers systematic shifts (up to several hertz) from the value given by (1). The situation is equivalent to frequency modulation with a drifting carrier frequency (which in our case is the Sagnac

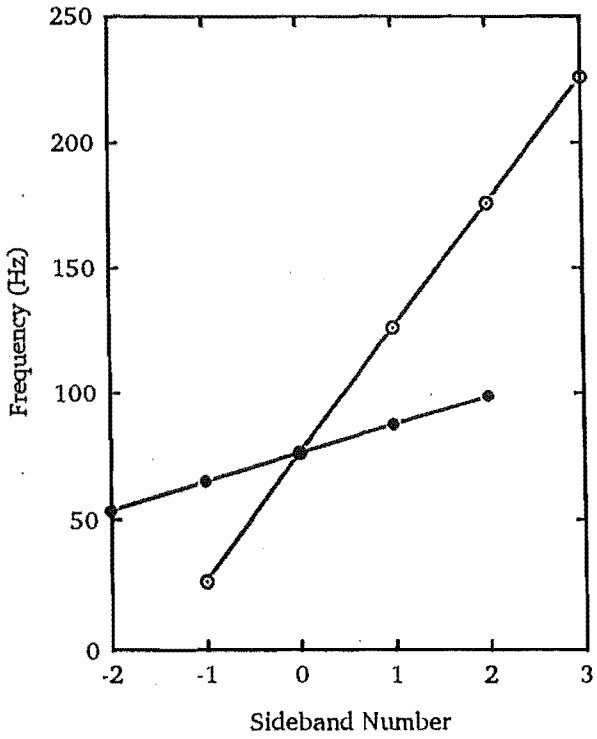

Fig. 4. Calibration of the spectrum. The frequency differences of the satellites to the earth line are plotted versus their order. The solid circles represent positions of the satellite frequencies to the earth line due to the 11,306 Hz mechanical resonance of the ring laser support; the open circles are from the 50 Hz vibrations. The vertical error bars are all less than 15 MHz rms and therefore are not visible. The slopes, in hertz, equal the two basic sideband frequencies.

frequency of the earth line). The relative positions of the modulation frequencies are not thereby affected.

IV. Future Applications of Ring Lasers

A. Seismography

The ring will sense rotation of the base on which it is mounted, or generally the curl of the absolute velocity. For example, if a horizontal shear wave from seismic activity moves the base, the ring output will show side bands to the earth's rotation, whose amplitudes are proportional to the linear amplitude of the seismic wave. Expressed as a limit of sensitivity to rotation, the results above give at present $(10^{-3}\ \text{Hz}/68\ \text{Hz}) \times (2\pi/\text{day}) \simeq 1 \times 10^{-9}$ rad/s. From [11], we estimate a level of microseisms that is within the reach of such rings.

The sensitivity to additional rotation of the ring base is seen in Fig. 1 where sidebands to the earth line of up to about 50 Hz are created. We independently verified with motion detectors that the mounting base of the ring has torsional resonances in that range, with a quality factor of $Q = 34$. Such torsional resonances are excited by building vibrations: It was found impossible to get good spectra during business hours, or even at night under windy conditions; the ring was on the sixth floor of a nine-story building when the data presented in Figs. 1–4 were taken. At present, the ring is being transferred into a cave on Banks Peninsula near Christchurch, New Zealand, where it will be mounted on a concrete socket directly to the granite of an 11 million-year-old volcano. One of the uses is the detection of secondary shear waves, or any waves with a curl of ground velocity. The site is 131 km off the very active Indian–Pacific tectonic plate boundary and 5.8 km from the Pacific ocean. Thus we will be in a good position to evaluate the ring's potential as a seismographic detector of a novel kind.

It is complementary to methods like very-long-baseline interferometry [12], [13] which are sensitive to translation only. As opposed to classic seismographs the ring needs no external reference, nor a virtual reference, since it is an indicator of absolute rotation. Seismic activity will be observed as a time-dependent frequency (or phase) deviation from the average earth rate. For example, the seismometer installed at the present site of the ring laser shows as a predominant feature a background at 0.2 Hz, with 4 μm peak-to-peak displacement which originates from interaction of the air mass with oceans, and is observed at all coastal stations within several hundred kilometers from the coastline. As an early application we will attempt to measure the curl of this ground motion; it should appear as side lobes to the earth line at ± 0.2 Hz, etc.

B. Nonreciprocal Optical Pathlength Variations

A rough estimate of the minimum required nonreciprocal change along the beam path for an observable signal is $(n^+ - n^-) \simeq \Delta f/f \simeq 0.001/474 \times 10^{12} \sim 2 \times 10^{-18}$ which improves presently known measurement limits of such effects by several orders of magnitude [14].

Any phenomenon that influences the effective optical path of the ring in this way can be considered a candidate for a ring laser experiment. This includes searches for various conceivable nonlinear field-induced properties of vacuum and of material media, for example all types of Fresnel drag. In this latter case, the confirmation of the role of Lorentz and Laub drag by earlier precision experiments [8], [15] is still incomplete, since in these cases either the residual discrepancies in the experiment were greater than the statistical errors, or else the theoretical analysis was insufficiently refined compared to the capabilities of modern experiments such as the present ring. These and other applications are discussed in more detail in Stedman *et al.* [16], where the potential of this ring for a wide-ranging set of applications in fundamental physics is analysed and a first upper bound for a novel special-relativity-violating parameter is estimated.

V. Conclusion

The 0.75 m^2 area of our ring laser is sufficient for it to be unlocked by the Sagnac effect arising from the very stable earth rotation alone and with no other means of biassing. The lines in the Fourier transform of the ring interferometer output had a width of 32 Hz convolved

with the width due to the finite observation time of 16 s. The net width is approximately an order of magnitude above the estimated quantum noise limit. We observed pulling and pushing of the earth line of up to several hertz due to Adler pulling and susceptibility changes. We are currently seeking to include a frequency stabilization of one of the counterrotating beams with an external iodine cell to reduce the drift associated with susceptibility changes. Calibration of additional oscillatory phenomena is however both simple and precise, since they give rise to sidebands which are placed very precisely at the appropriate frequencies (see Section III). Harmonics of the earth rotation line which are produced by the nonlinearity of the laser gain medium were used to evaluate the frequency resolution of the line centers as being approximately 1 MHz. The accuracy with which the relative frequency of the sidebands may be determined is better than 10 MHz over a frequency range of 26–226 Hz. The extreme linearity will allow us to determine easily the lock-in threshold frequency, since the lines can be shifted by applying a transverse magnetic field to the plasma. A sensitivity of 10^4 Hz/T has been observed for such shifts.

Acknowledgment

The authors thank A. W. Louderback of Ojai Research, Ojai, CA, for his generous supply of our project with mirrors. The authors especially wish to thank B. G. Wybourne, the former Head of the Physics Department at the University of Canterbury for his unflagging support of the experiment, and F. V. Kowalski, School of Mines, Golden, CO, for substantial help during the construction phase of the ring.

References

[1] R. V. Pound and J. L. Snider, "Effect of gravity on gamma radiation," *Phys. Rev.*, vol. 140, pp. B788–B803, 1965.
[2] J. Vanier, "The active hydrogen maser: state of the art and forecast," *Metrologia 18*, pp. 173–186, 1982; Hellwig, H. W., *Proc. IEEE* 63, "Atomic frequency standards: a survey," pp. 212–229, 1975.
[3] E. J. Post, "Sagnac effect," *Rev. Mod. Phys.*, vol. 39, pp. 475–493, 1967.
[4] W. W. Chow, J. Gea-Banacloche, L. M. Pedrotti, V. E. Sanders, W. Schleich, and M. O. Scully, "The ring laser gyro," *Rev. Mod. Phys.*, vol. 57, pp. 61–104, 1985.
[5] H. Statz, T. A. Dorschner, M. Holtz, and I. W. Smith, *The Multioscillator Ring Laser Gyroscope*, M. L. Stitch and M. Bass, eds. pp. 229–332, Laser Handbook vol. 4, (North-Holland, 1985).
[6] T. A. Dorschner, H. A. Haus, M. Holtz, I. W. Smith, and H. Statz, "Laser gyro at quantum limit," *IEEE J. Quantum Electron.*, QE-16, pp. 1376–1379, 1980.
[7] M. R. Snyeh and H. R. Bilger, "Flicker noise in frequency fluctuations of lasers," *Phys. Rev. Lett.*, vol. 55, pp. 700–702, 1985.
[8] H. R. Bilger and W. K. Stowell, "Light drag in a ring laser: An improved determination of the drag coefficient," *Phys. Rev.*, vol. A16, pp. 313–319, 1977.
[9] G. E. Stedman, *Diagram Techniques in Group Theory*. Cambridge, UK: Cambridge University Press, 1990.
[10] G. E. Stedman and H. R. Bilger, "Ringlaser, an ultrahigh-resolution detector of optical nonreciprocities," *Digital Signal Processing*, vol. 2, pp. 105–109, 1992.
[11] A. Giazotto, "Interferometric detection of gravitational waves," *Phys. Rep.*, vol. 182, pp. 365–424, 1989.
[12] D. S. Robertson, "Geophysical applications of very-long-baseline interferometry," *Rev. Mod. Phys.*, vol. 63, pp. 899–918, 1991.
[13] U. Schreiber, Fundamentalstation Wettzell, Germany, private communication.
[14] E. Iacopini *et al.*, "On a sensitive ellipsometer to detect the vacuum polarization induced by a magnetic field," Nuovo Cimento, vol. 61B, pp. 21–37, 1981.
[15] G. A. Sanders and S. Ezekiel, "Measurement of Fresnel drag in moving media using a ring resonator technique," *J. Opt. Soc. Am.*, vol. B5, pp. 674–678, 1988.
[16] G. E. Stedman, H. R. Bilger, Li Ziyuan, M. P. Poulton, C. H. Rowe, I. Vetharaniam, and P. V. Wells, "Canterbury ring laser and tests for nonreciprocal phenomena," *Austral. J. Phys.*, vol. 46, pp. 87–102, 1993.

Appendix C STEDMAN ET AL. 1993

G.E. Stedman, H.R. Bilger, Li Ziyuan, M.P. Poulton, C.H. Rowe, I. Vetharaniam and P.V. Wells (1993), Canterbury ring laser and test for nonreciprocal phenomena, *Aust. J. Phys.*, **46**, 87-101.

Aust. J. Phys., 1993, 46, 87–101

Canterbury Ring Laser and Tests for Nonreciprocal Phenomena*

G. E. Stedman, H. R. Bilger,[A] *Li Ziyuan, M. P. Poulton, C. H. Rowe, I. Vetharaniam and P. V. Wells*

Department of Physics, University of Canterbury, Christchurch 1, New Zealand.
[A] School of Electrical and Computer Engineering, Oklahoma State University, Stillwater, OK 74078–0321, U.S.A.

Abstract

An historic and simple experiment has been revitalised through the availability of supercavity mirrors and also through a heightened interest in interferometry as a test of physical theory. We describe our helium–neon ring laser, and present results demonstrating a fractional frequency resolution of $2{\cdot}1\times10^{-18}$ (1·0 mHz in 474 THz). The rotation of the earth unlocks the counterrotating beams. A new field of spectroscopy becomes possible, with possible applications to geophysical measurements such as seismic events and earth tides, improved measurements of Fresnel drag, detection of ultraweak nonlinear optical properties of matter, and also searches for preferred frame effects in gravitation and for pseudoscalar particles.

1. Introduction

A few years after the advent of the laser, Macek and Davis (1963) demonstrated the first ring laser, and also its unique potential as a rotation detector via the Sagnac effect. The optical lengths of the closed paths for the counterpropagating beams are made unequal by rotation of the whole device. In an active device the frequencies adapt to this, the corotating beam becoming more red and the counterrotating beam more blue (Heer 1964). Both beams take essentially the same path within the cavity, so that when the beams transmitted at any mirror interfere, the resulting beat frequency δf reflects only the difference in optical path length, and not any common-mode effects such as frequency jitter. The beat frequency depends on the angular frequency Ω of rotation with respect to the local inertial frame, the area $\mathbf{A}$ and perimeter P of the ring, and the optical wavelength λ (Post 1967; Anandan 1981; Chow *et al.* 1985; Stedman 1985*a*):

$$\delta f = \frac{4\mathbf{A}\,.\,\Omega}{\lambda P}. \qquad (1)$$

Any nonreciprocal effect, i.e. one which distinguishes the optical path lengths of the counterpropagating beams, will give rise to a frequency shift, making the ring laser more versatile than merely a rotation sensor.

Macek and Davis (1963) (see also Macek *et al.* 1963, 1964) used a 1 m^2 square helium–neon ring laser at 1·15 μm to measure beat frequencies down to 5 kHz;

* Paper presented at the Tenth AIP Congress, University of Melbourne, February 1992.

0004-9506/93/010087$05.00

backscattering from the 16 beam interfaces (the Brewster windows on the four gain tubes) and the corner mirrors caused the two counterpropagating modes to lock at 2 kHz (for discussions of locking, see Aronowitz 1971, Statz *et al.* 1985). If we assume a Rayleigh or $1/\lambda^4$ variation of backscattering with wavelength, the equivalent locking threshold at 633 nm is 22 kHz.

In effect, we have repeated the Macek *et al.* experiment, and on a ring of similar shape and size. The key experimental differences are the use of supercavity mirrors, whose reflectances approach 99·999% — an ultimate, since it demands surface preparation which is smooth over atomic dimensions — and the complete absence of interfaces. This reduces the locking threshold to the point where the beat frequency induced by earth rotation (at 68 Hz) unlocks the ring without the need for any other biassing or dithering systems.

The development of supercavity mirrors has been vigorously driven by the potential for their application as ring gyros, now used for aviation inertial guidance systems in aircraft (e.g. the Airbus 320), and in various missiles (e.g. the Patriot system). An optical gyro with an area of the order of square decimetres has a sensitivity to rotation rates of order $10^{-4}\Omega_E$, where Ω_E is the earth rotation rate. Recently supercavity mirrors have been incorporated in such commercial items as the Newport SR-130 spectrum analyser. The scientific applications of the resolution enhancement inherent in these mirrors have not been fully explored.

2. Theoretical Aspects

(2a) Introduction

At the time of the Macek *et al.* experiment, only the application as a rotation sensor was demonstrated. This itself takes on a new interest with the increase in precision achieved over the intervening years. Some theoretical revitalisation is illustrated by the papers of Forder (1985), Scorgie (1990, 1991), Dieks and Nienhuis (1990) and Hendriks and Nienhuis (1990).

Less obvious physical effects could also generate a nonreciprocal effect in a ring laser (Macek *et al.* 1964; Bilger and Stowell 1977). There has been a renaissance of interest in interferometric tests of fundamental physical theory; the SQUID in the 1960s, the neutron interferometer in the 1970s and 1980s, and more recently atomic interferometry (Levi 1991) have spawned a variety of demonstrations and tests of quantum theory, relativity and related topics. These various interferometers are largely complementary, as discussed by Stedman (1985*a*, 1986) and Bilger *et al.* (1990), although atomic interferometry has much untapped potential (Clauser 1988; Levi 1991) and has demonstrated the Sagnac effect (Riehle *et al.* 1991; see Al'tshuler 1992). It is therefore appropriate to re-evaluate any unique potential that ring lasers may have as probes for old and new physics.

This potential rests partly in the geometry of the closed, as opposed to an open, interferometer, and partly in the unique characteristics of photons as the workhorse of the ring laser (Post 1972; Stedman *et al.* 1991), an electromagnetic system with the capability of detecting a parity-violating effect, in the sense that any frequency difference must be reversed by mirror reflection. Indeed effects which are detectable uniquely in a ring laser are not necessarily chiral (or gyrotropic, Stedman 1991) in the sense used in chemical physics; the relationship

depends on the configuration of the ring laser (Stedman 1992). There has been considerable interest over the last decade or so in setting experimental limits on possible parity-violating effects within relativity or gravitation theory on the one hand, and quantum field theory and particle theory on the other.

(2b) Rotation Sensing and Seismology

Since the earth rotation unlocks the Canterbury ring, it is a free device, sensing absolute rotation without the need of any external bias or dither (tricks whose absence prevented the first ring laser from showing the earth rotation, and which are otherwise universally applied for ring lasers). It becomes possible to sense seismic events and earth tides as they affect the observed earth rate, at a precision better than 10 ppm. A ring-laser-based seismometer would measure information on any rotational effects, associated for example with horizontal shear, in seismic waves which would complement that derived from the traditional linear accelerometers, and at comparable precision; the rotation detection sensitivity of 10^{-9} rad/s or $0{\cdot}01$ rad/yr demonstrated in this paper is quite enough for detecting microseisms according to the data of Giazotto (1989); see Robertson (1991). The cave in which our ring is due to be installed is built into an 11 million year old volcanic basalt, 131 km off the very active Indian–Pacific tectonic plate boundary.

In collaboration with Ojai Research, we have shown the possibility of using the polarisation state of a square ring laser to measure mirror tilt with an accuracy of the order of picoradians. This suggests a new technique for linear seismometry (Bilger *et al.* 1990).

According to general relativity, the local Lorentz frame itself can rotate with respect to the fixed stars, or be 'dragged', by a nearby rotating object such as the earth. This Lense-Thirring field exemplifies the gravitomagnetic effects in general relativity which so far have been tested only indirectly (Nordtvedt 1988). An experiment to detect this frame dragging, based on mechanical gyros, is due to be put into orbit by the Space Shuttle in 1996. Scully *et al.* (1981) have considered the possibility of their detection by a land-based experiment using a ring laser. Since such effects arise at $10^{-10}\Omega_E$, rather than the 10^{-5}–$10^{-7}\Omega_E$ sensitivity of the present ring, rings of a larger area/perimeter ratio are required.

(2c) Acceleration in Dispersive Media

Equation (1) for the response of a ring laser to rotation is sufficiently general to hold under linear and angular acceleration to very high precision. However, there has been some interest recently in examining the validity of (1), especially in the presence of dispersive dielectric media, under rotational and linear acceleration (Post 1972; Kuriyagawa and Mori 1979; Takahashi 1985; Fabri and Picasso 1989; Scorgie 1990, 1991; Kowalski *et al.* 1992). We mention also the increasing development of fibre optic gyro systems, e.g. Dennis *et al* (1991); however we consider the lack of solid material in our basic ring to be a potential advantage in reducing field- and stress-induced biases, as well as error and noise sources.

(2d) Fresnel Drag and Special Relativity

A popular application of ring laser precision is in tests of special relativistic effects in the dragging of the speed of light in moving media. The classic

experiments of Zeeman (1920) have now been considerably improved by Bilger and Stowell (1977) and by Sanders and Ezekiel (1988), although in each case the analysis and comparison with theory has left something to be desired. In the former case there is a residual small discrepancy between the theoretical estimate and the experimental value. In the latter case some questionable assumptions in the theory need examination, for example the use of the refractive index of the sample with respect to air in lieu of that in vacuo, and various problems of nonreciprocity of beam path in view of the use of nonperpendicular moving medium boundaries. The presence of counterrotating beams which may physically coincide makes the ring laser an ideal instrument for Fizeau-type drag experiments, with greatly increased precision and accuracy. Further experiments of this type would be one obvious test for a ring laser with increased precision.

(2e) Tests of Preferred-frame Theories

Ring interferometry *per se* has a long history in tests of relativity, going back at least to the 1851 experiments of Fizeau on Fresnel drag, but still has a confused status. Stedman (1972, 1973) and Anderson and Stedman (1977, 1992) pointed out some misconceptions arising from a neglect of the logically distinct role of ring interferometry in the kinematical development of special relativity. Tests of relativity have often been motivated at this kinematic level. The test theory of Mansouri and Sexl (1977) has been widely used to motivate Michelson–Morley-like and other experiments with linear lasers (see for example Riis *et al.* 1988; Will 1992*a*,*b*), albeit still in a form which is flawed by the claim of permitting one-way measurements (Vetharaniam and Stedman 1991, 1992). In the same vein one might well motivate searches for violations of special relativity in the conjugate ring geometry (Post 1972; Stedman *et al.* 1991) by postulating a parity-violating preferred-frame test theory.

For example, let us suppose that a boost, induced by the rotation of the earth carrying the ring laser into a new frame which is approximately inertial, generates a gravitomagnetic field $\mathbf{h}$ ($h_i = g_{0i}$) which is proportional to the velocity $\mathbf{v}$ relative to the preferred frame. It is customary but not necessary to identify the preferred frame as that in which the microwave background is isotropic. Let the proportionality constant be a parameter σ :

$$\nabla \times \mathbf{h} = \sigma \mathbf{v} . \tag{2}$$

From equation (1) in its general relativistic form (Post 1967; Anandan 1981), as applied to the earth-rotation-induced beat frequency in the Canterbury ring laser, we would have a (sidereal) diurnal variation in the beat frequency given by $\delta f = \delta[2f_0 \mathbf{A} \cdot \nabla \times \mathbf{h}/P] = 2f_0 A\sigma v \delta(\cos\theta)/P$, where $\delta(\cos\theta)$ is the maximum diurnal change in the projection $\cos\theta$ of the direction of the ring area $\hat{\mathbf{A}}$ on the direction $\hat{\mathbf{v}}$ of the velocity with respect to the preferred frame, on the assumption that the magnitude v of this velocity is much greater than its diurnal variation. We take the magnitude and declination of the preferred frame velocity from Narlikar *et al.* (1991) as $v \approx 6{\times}10^5$ m s^{-1} and $\delta \approx -26°$ so that, at the latitude of Christchurch ($\lambda \approx -43°.5$), $\delta(\cos\theta) = \cos(\lambda - \delta) - \cos(\pi - \lambda - \delta) = 1{\cdot}30$. Hence $\delta f/\sigma \approx 1{\cdot}6 \times 10^{20}$ m^2 s^{-2} and an experiment searching for a variation in the

Canterbury ring laser beat frequency with the Fourier period of one sidereal day and amplitude $\Delta\omega$ would give an estimate of σ as

$$\sigma \approx P\delta f/2\cdot 6 f_0 A v; \qquad \sigma(\mathrm{s/m^2}) \sim 6\times 10^{-21}\delta f\ (\mathrm{Hz}). \tag{3}$$

Equation (3) shows that at a beat frequency precision of 1 mHz we may set a bound on σ to an accuracy of the order of 10^{-23} s/m^2.

Why might we do such a test? While a purely kinematic postulate of such a gross assumption in flat spacetime and in the absence of matter has little appeal, the Mansouri–Sexl (1977) test theory was equally kinematic in motivation, but has still proved useful. One could argue, as did Okun (1988), on the possibility of testing the exclusion principle (whose possible violation, as Okun was concerned to show, is even less credible), that 'in fundamental physics if something can be tested it should be tested.' Franklin (1986) has emphasised, and recent stirring events in condensed matter verify, that novel experiments do not require a supporting theory; physics is an experimental science. Telegdi (1990) has emphasised such points in the context of a warm tribute to the skill of Michelson and Gale (1925) in their historic interferometric measurement of the Sagnac effect from earth rotation.

However, most physicists prefer to have a dynamic model, for example a Lorentz-invariance-violating term in the Lagrangian underpinning any test theory to motivate an experiment. The kinematic approach of Mansouri and Sexl (1977) for linear tests of special relativity has often been replaced (Will 1992*b*) with the dynamic model of the $TH\epsilon\mu$ theory. In this the assumption is made that Lorentz invariance may be broken by differentiating the speed of light and the limiting speed of matter. This still permits an elegant classical Lagrangian formulation and most importantly a quantised form which enables the use of high-precision atomic spectroscopy to place more accurate bounds on the parameters (Will 1992*b*).

Parity-violating models of gravitation have been of renewed interest (Gibbons 1992). Possible effects from a gravitational anomaly have been discussed by Dolgov *et al.* (1988, 1990). Ni (1977) has proposed, and Ritter *et al.* (1990) have tested, an alternative and parity-violating gravity theory in which a postulated constitutive tensor density, dependent in part on a scalar function of the gravitational fields, gives rise to anomalous torques on electromagnetically interacting and polarised bodies. The possible effects of spacetime torsion have been discussed by a number of authors such as Hojman *et al.* (1980) who showed that with torsion, gravitational theories admit a parity-violating term in the action. Hehl *et al.* (1976, 1992) considered the Einstein–Cartan theory of gravity whose non-zero torsion tensor is proportional to the antisymmetric part of the connection, and which gives rise to a non-propagating torsion inside matter. Hojman *et al.* (1978, 1979) developed a theory using Cartan's torsion tensor but departed from the Einstein–Cartan theory by modifying the concepts of gauge invariance and minimal coupling, thus obtaining a propagating torsion even within a vacuum. Propagating torsion was also discussed by Hammond (1990). Moffat (1989, 1990) considered the physical consequences of his nonsymmetric gravitation theory in which the fundamental geometric object is the nonsymmetric connection compatible with a complex, nonsymmetric metric. Others (Mashhoon 1975, 1988, 1989; Gabriel *et al.* 1991)

have discussed the electromagnetic effects of gravitational coupling to the rotation of the earth.

Dynamic support for an effect related to that of equation (2) was illustrated within the parametrised post-Newtonian (PPN) formalism by Scully *et al.* (1981). A variation in the apparent earth rotation rate with the period of one sidereal day could be interpreted in terms of a nonvanishing value for the preferred-frame PPN parameter α, which vanishes in general relativity. Presently α is bounded to vanish to 1 part in 10^4 (Will 1992*b*).

Other derivations of equation (2) from the rather more drastic parity-violating modifications referenced above can be expected to yield models that will also justify a search for bounds on the parameter σ.

(2f) Small Material Nonreciprocities

Nonreciprocal physical effects giving absolute phase shifts of 10^{-10} rad between counterrotating beams should be detectable (Stedman 1985; Ross *et al.* 1989; Stedman 1992). This would allow sensitive tests of nonlinear optical effects in gases associated with the chiral effects of electric and magnetic fields. Field-induced magnetic linear dichroism in gases is one obvious candidate. In chemical physics, absolute measurements of such parameters are often very difficult, and the determinations of the hyperpolarisabilities of helium by Buckingham and Dunmur (1968) and the quadrupole moment of CO_2 by Buckingham and Disch (1963) (see also Buckingham 1968) have stood unimproved for many years. Such devices as the ring laser give hope of new results in these directions. Finally, rotation could itself make an atomic gas optically active at a very low level (Silverman 1989; Stedman 1990).

(2g) Anomalous Interaction with Pseudoscalars

The anomaly or triangle diagram occurring in the quantum electrodynamics of pseudoscalar particles has been the focus of an extended literature. Since it is concerned with a parity-violating effect, a ring laser detection system has some relevance.

There has been speculation that even within QED, triangle diagrams provide physically detectable effects (Stedman and Bilger 1987). We are now convinced that such speculation is not well founded (Ross and Stedman 1988; we may note in passing that the work of Maiani *et al.* 1986 is not thereby compromised as Ross and Stedman suggested, since their ϕ does not correspond to measurement of optical activity). However, as discussed above, a novel experiment is worth doing whether or not theorists are sufficiently inventive to get a plausible test theory to justify it.

One can search for upper bounds on electric and/or magnetic field-induced optical properties of the vacuum. The Canterbury ring could set sensitive bounds on such effects. Like the above-mentioned special relativity test, these are particularly clean experiments, requiring no medium and consequently no degradation of cavity finesse. In many respects the vacuum behaves as a nonlinear medium for quantum optical experiments. It can be squeezed, in that some field amplitude fluctuations can be reduced below the levels suggested by the

uncertainty principle, at the expense of others. According to QED, the most well-tested of all physical theories, the vacuum is predicted to permit nonlinear processes such as light–light scattering, but at levels below detection by our present ring, although Ni *et al.* (1991) have proposed an interferometric technique for achieving the required sensitivity of 10^{-25} in a refractive index measurement.

The triangle diagram has noncontroversial application when the anomaly is external, and the pseudoscalar particle exists in nature, as for example in the analysis of $\pi^0 \rightarrow \gamma\gamma$ decay. Various candidates for new neutral pseudoscalar particles have been proposed, including the axion (e.g. Sikivie 1992), the arion and the majoron (Fischler 1991). In principle, these if they exist will interact by the axial anomaly or triangle diagram to couple with two photons. Searches have been conducted for axions, in which one photon is that of a magnetic field, and an optical effect is sought to reveal the otherwise invisible particle. The coupling strength is set through the mass of the pseudoscalar. If (as for Hagmann *et al.* 1990) a tunable microwave cavity were included in the ring laser optical path, it would be possible in principle to detect the effects of circularly polarised 633 nm photons created through the anomaly coupling with incoming pseudoscalars. The microwave magnetic field tunability of say 4 GHz is admittedly only a few ppm of the laser photon energy, 2·0 eV, an energy range which nevertheless is not covered by present axion searches (Sikivie 1992).

3. Canterbury Ring Design and Performance

(3a) Noise Limits

The fundamental limits on the resolution attainable with a ring laser are determined by quantum noise (Dorschner *et al.* 1980; Hellwig 1975) and $1/f$ noise. The transition between these two noise sources is clearly evident in the earlier work of Bilger and Sayeh (1983), and when $1/f$ noise takes over, further time averaging does not improve the data. However, both of these are reduced by a factor of order $1/P^n$, where P is the perimeter and $n \sim 2$–3, by using larger rings through the increasing finesse and the decreasing solid angle in backscatter. When this is done, as in our present ring, $1/f$ noise is essentially eliminated in that the ultimate resolution is restricted by other considerations such as laser stability. Methods such as quantum nondemolition measurement, which extend the resolution of optical systems to break the barrier imposed by quantum noise, are not of prime interest in this application at least at this stage; our strategy is to lower, rather than breach, the standard quantum noise limit itself. The introduction of squeezed light, say by introducing a nonlinear optical element into the cavity, while an exciting theoretical possibility, could in practice risk the very quality of cavity finesse that led to the lowering of the standard quantum limit. Our success in this direction, without resorting to squeezing etc., again illustrates that the potential of the ring laser for precision measurements is still quite underdeveloped.

In confirmation of these comments, we write the power spectral density of the beat frequency fluctuations as $S_{\delta f} = h_0 + h_{-1}/f$, where f is the Fourier frequency. The coefficient for quantum noise is given by $h_0 = 2hf_0^3 3/P_0Q^2$ with the value $h_0 = 3 \times 10^{-6}$ Hz^2/Hz for a total optical power loss $P_0 = 0{\cdot}1\ \mu$W and the ideal cavity quality factor Q; f_0 is the laser frequency of 474 THz;

$h_{-1} = 8f_0^2/Q^4$ (this is an empirical relation, for which see Sayeh and Bilger 1987). With a measurement time T, the rms frequency fluctuation of the beat frequency is then

$$\Delta f_{rms} = [2hf_0^3/Q^2P_0T]^{\frac{1}{2}} . \tag{4}$$

The analysis leading to equation (4) assumes that the cw and ccw beams are uncorrelated; while methods for inducing and exploiting a correlation for noise reduction are now well discussed and physically demonstrated, there is no immediate prospect of using this in systems such as ours. With the above specifications and $T = 1$ h, a frequency fluctuation of 20 μHz can be achieved in principle, corresponding to a frequency resolution $\Delta f/f_0 = 4 \times 10^{-20}$. Other interferometric techniques have been proposed (Ni *et al.* 1991) which could improve on this figure, and which would correspond to the performance that we may expect of a ring laser with an area of say 50 m^2 (as in Scully *et al.* 1981). From this viewpoint, even the earlier ring lasers have already outclassed (Bilger and Sayeh 1986) other precision tools such as the Mössbauer effect (Pound and Snider 1965) and the maser (Vanier 1982).

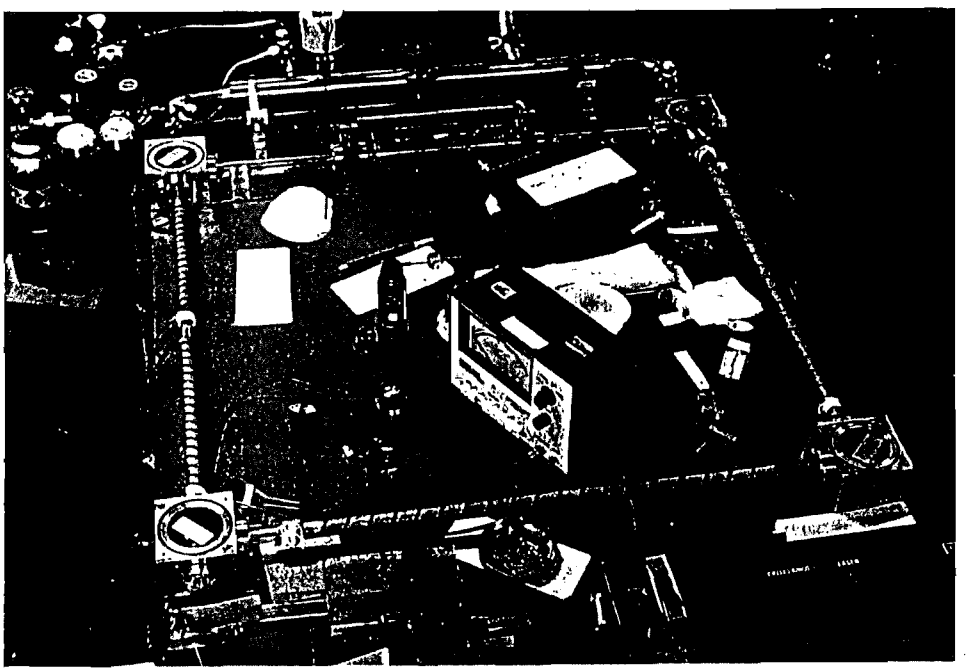

Fig. 1. The Canterbury ring laser. The RF excitation section is in the topmost leg, and the superinvar mirror mounts are visible through the glass lids of the corner boxes. The green helium–neon laser for alignment is in the foreground.

(3b) Construction

The Canterbury ring laser (Fig. 1) is designed to realise the potential of the recent advances. So that the cavity finesse is maximised, the beam paths are

entirely in the helium–neon gas; the Rayleigh scattering of neutral neon gas at 300 Pa has a negligible effect on the quality factor. Neither do the beams intersect any interface, although for some applications Brewster windows will be both necessary and tolerable. Supermirror coatings were generously provided by Ojai Research. Zerodur blanks were used which have 0·1 nm rms surface roughness (i.e. smoothness to atomic dimensions), achieved through ion beam milling with argon and nitrogen beams. Ultrahigh vacuum coated SiO_2/TiO_2 $\lambda/4$ layers give losses of 4 ppm due to scattering (TIS), 4 ppm from transmission, and absorption (by difference) of 7 ppm, approaching that of the bulk materials. The observed total reduction in reflection is then 15 ppm, corresponding to a reflectivity of 99·9985%. After extended use in our environment the total losses increased significantly.

The radio frequency excitation mechanism is novel, involving a magnetic coupling at 50 MHz. The laser gas is 7:1 He:Ne with a nominal total pressure of 2·3 Torr (300 Pa); however the latter can successfully be varied over an order of magnitude. A natural mixture of neon isotopes (Ne^{20}:Ne^{22} = 9:1) and natural helium is used at present.

For further mechanical and thermal stability the mirrors are mounted in superinvar holders resting on a 1×1 m^2 Zerodur plate, itself on a granite base. The stainless steel corner boxes avoid mechanical contact with the mirrors; their bottoms are open, and are sealed by Viton O-rings against the Zerodur plate.

A triangular ring was used in earlier lasers such as that of Bilger and Stowell (1977). We have used a square ring primarily to optimise the parameter $G = A/PN$, where A is the area, P the perimeter and N the number of mirrors. From earlier equations, together with the dependence of Q on mirror losses, G is proportional to the signal/noise ratio of the system. Since there is an odd number of reflections, each of which reverses handedness of the beam, a triangular ring cannot be put in circularly polarised mode. A square ring could be put in circularly polarised mode, should applications require it, for example by introducing nonplanarity (Bilger *et al.* 1990), another impossibility with a triangle. The increase in angle of incidence means that backscatter is reduced; indeed, Lambert backscatter formally vanishes at 45° incidence. Together these measures help to avoid locking.

Partly to preserve the advantages sought from a simple open design with mechanical and thermal isolation for the mirrors, and partly on account of cost, no feedthroughs are installed at this stage in the corner boxes. Hence alignment to 20 arcsec in angle and 10 μm in position has to be achieved before adding vacuum sealed covers to the corner boxes, pumping down, gas handling and initiating the lasing. Mirror holders were machined to locate the poles to this precision. A green helium–neon laser beam was overlaid with that of a standard red laser to preserve alignments under a sequence of operations where the mirrors were rotated from retroreflecting configurations, in which tilt about a horizontal axis was adjusted and from which mirrors were rotated about a vertical axis to reach the final positions. The output interferometer was mounted on top of the glass cover for one corner box. Its components were aligned to overlay the emergent beams to a precision of 0·3 mrad.

This device will shortly be taken to an underground cavern giving further thermal and mechanical stability. The results reported here are therefore only preliminary.

(3c) Results

The Canterbury ring generates a nominal beat frequency δf of 68·826 Hz, given the latitude of 43° 29′ South, (vacuum) wavelength $\lambda = 633{\cdot}0$ nm, perimeter $P = 3477{\cdot}1 \pm 0{\cdot}1$ mm (measured from the free spectral range of 86·218 MHz determined from the beat frequency between neighbouring longitudinal modes) and area $A = 0{\cdot}748$ m^2 (given with lesser accuracy from the two sides of 898 mm, 837 mm). Since the gain curve for natural neon has a width of order 1 GHz, several longitudinal modes could readily be excited, and of course the intermediate transverse modes. A fused silica tube of length 30 cm and 4 mm internal diameter served both as RF-excited amplifier and as an aperture. Our design aimed to achieve single mode operation by reducing the gain so that (thanks to the variation of gain with wavelength) all longitudinal modes except one would be starved. In principle this required output power reduction to the manageable level of 30 nW. In practice, we were pleasantly surprised at the ease at which such gain control achieved single mode excitation of the ring. Typical RF powers for single mode excitation were 5–7 W, and output beam powers were then indeed of the order of 30 nW. For higher excitation power, say 30 W, output beam powers reached 2 μW, which corresponds (since mirror transmission is 4 ppm) to a circulating power of 0·5 W. Although high circulating powers reduce quantum shot noise, they induce nonlinear effects in mirror media, and as noted by Chow *et al.* (1985) multimode rings give new branches in the beat-frequency–rotation-rate plot. Mode structure was monitored with a Newport SR-130 scanning Fabry–Perot.

The ringdown decay time of the ring was measured to be approximately $\tau = 15$ μs by monitoring lasing output as the RF is turned off using a digital storage oscilloscope. This translates into a quality factor $Q = \omega\tau = 4{\cdot}5 \times 10^{10}$, noticeably below the ideal. The causes of this long-term contamination of mirror coatings have been identified, and within our limited budget we are working towards their elimination.

The interference fringes on detection were processed by a Strobes Acquisition-PC data collection system (equivalent to Rapid Systems R380), which permitted runs of 16·384 s with a 2 ms sampling time. A spectrum obtained is given in Fig. 2.

While the 50 Hz signal from mechanical motion induced at the frequency of the New Zealand mains power supply, together with its harmonics, is conspicuous, the spectrum is dominated by the line associated with earth rotation in the region 67–78 Hz. Even the subsidiary features of the spectrum are sharp; the mechanical resonances of the ring support system (at 15 and 19 Hz for example), which appear at those frequencies and as sidebands to the main features, reflect their relatively high mechanical quality factor (measured to be 34 ± 1). Indeed in our current site on the sixth level of a multi-storey building facing the prevailing wind, data of the quality of Fig. 2 can only be obtained under relatively wind-free conditions and late at night, when other uses of the building are minimal.

The earth-rotation-induced signal is almost as sharp as the mains frequency line. Its width is dominated by the windowing resolution of up to 160 mHz (Fig. 3). However, a careful analysis (Stedman and Bilger 1992) has shown that the net optical line width of the beat frequency may be extracted by deconvolution, and by using the second and third harmonics of the earth-rotation-induced signal

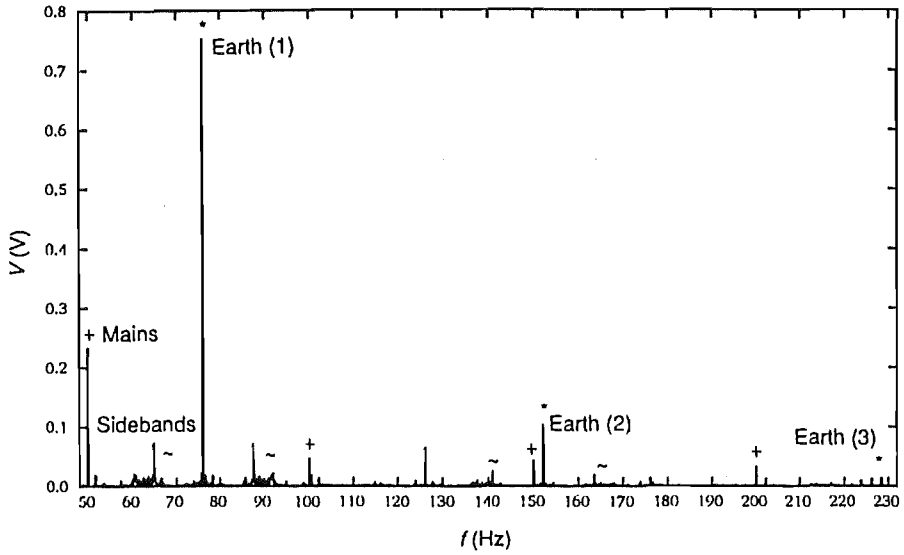

Fig. 2. A spectrum from the Canterbury ring. The beat signal from earth rotation, together with its two higher harmonics, are marked by an asterisk. Sidebands arising from the mechanical resonance of the support are marked by a tilde, and mechanical rotation from the AC mains with its harmonics by a plus sign.

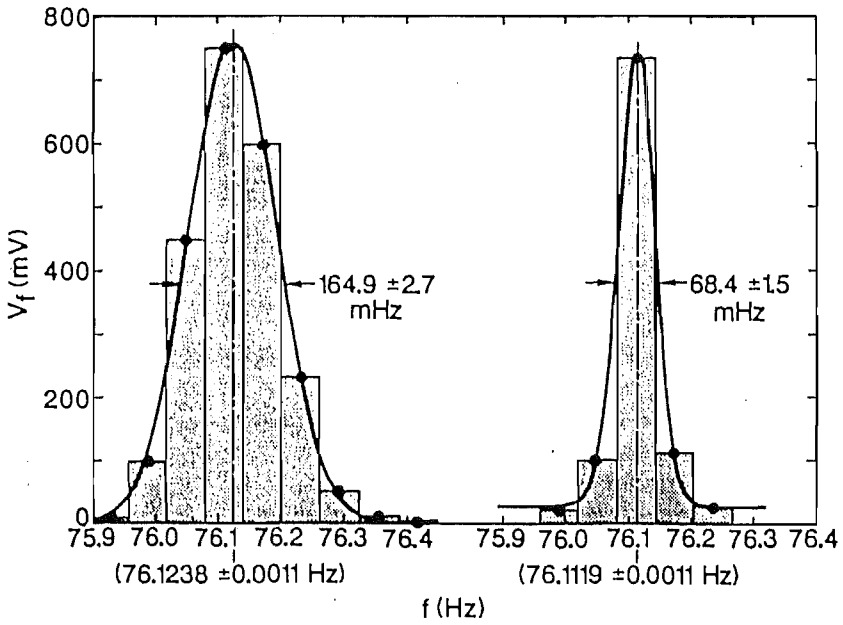

Fig. 3. The effect of windowing on the raw data for the fundamental earth rotation line in Fig. 2; on the left is a Nuttall window (Stedman and Bilger 1992), and on the right a square window corresponding to the time gate of 16·384 s.

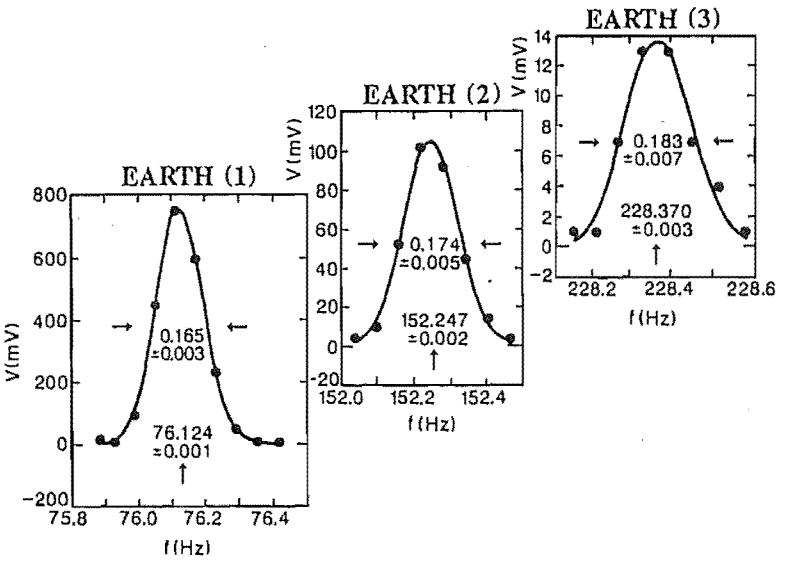

Fig. 4. A comparison of the widths of the raw data for all harmonics in Fig. 2. The fitted curve is a convolution of the known window function and a net laser line shape function, whose width is thus determined consistently to be 33 mHz. As noted in Fig. 3 and in the text, the line positions may thus be determined to 1·0 mHz, or $2{\cdot}1\times10^{-18}$ of the laser frequency.

(Fig. 4) it is possible to check the consistency of this procedure, and obtain at present a laser beat frequency full width at half maximum (FWHM) of 32·7±1·7 mHz for the runs of 16·384 s duration. This is an order of magnitude larger than the expected quantum noise limit. Most importantly, the line profile can be fitted to a Gaussian and the position of the centre of the line obtained to a precision of 1·0 mHz; this estimate also was reduced by a comparison of harmonics. This justifies our claim for a fractional frequency resolution capability of $2{\cdot}1\times10^{-18}$. The earth-rotation-induced line position in our as yet unstabilised ring drifts typically by several hertz in a few minutes. Such drift during the sampling time explains the difference between the observed line width and the quantum noise limit. Shorter sampling times lead to wider windows, and to no improvement in resolution; at this stage our maximum data collection time is (fortuitously) optimal.

We attribute this drift to the well-known effects of the susceptibility variation over the composite neon gain curve when the path length, and with it the resonance frequency, varies, compounded by saturation effects (Aronowitz 1971; Sargent *et al.* 1974; Siegman 1986). Thermal expansion effects even in Zerodur would induce shifts of the cavity modes within the gain curve by several per cent of the free spectral range per Celsius degree, and the counterpropagating waves sample the gain curve at different frequencies. The difference in optical path length for these modes itself depends on the position within the gain curve. We are therefore deferring the proposed test of relativity suggested earlier in this paper until present work on stabilising the cavity modes within the gain curve via feedback is completed. The forthcoming transfer to the cavern will also markedly help reduce drifts and mechanical interference.

The cavity parameters appropriate for the original mirrors and for the results given above are given in Table 1, together with comparative figures for the Newport SR-130 supercavity.

Table 1. Ring parameters

We give the performance limit obtainable in principle given supercavity mirror parameters as measured by the manufacturer, the performance actually attained in our environment, and for comparison the corresponding figures for the Newport SR-130 scanning Fabry–Perot supercavity (Li *et al.* 1990). In all cavities, the quality factor is $Q = f_0/\Delta f_{\frac{1}{2}} = \omega\tau$, where $f_0 = \omega/2\pi = 474$ THz; the finesse is $F = S/\Delta f_{\frac{1}{2}} = Q\lambda/P$, where the free spectral range (FSR) is $S = c/P$, P is the round trip length and $\Delta f_{\frac{1}{2}}$ is the power FWHM of the cavity response. In a Fabry–Perot, $TF = \pi$ where the mirror power transmittance $T = 1 - R$, and $\Delta f_{\frac{1}{2}} = cT/\pi P$; in a four-mirror ring, $TF = \pi/2$ and $\Delta f_{\frac{1}{2}} = 2cT/\pi P$. The nonreciprocal refractive index and rotational velocity limits are estimated as in Stedman *et al.* (1987)

	Ring laser		Fabry–Perot
	Design	Achieved	SR-130
Perimeter P (mm)	3477·1		50·6
FSR S (GHz)	0·086218		6·0
Cavity finesse F	~200 000	30 000	85 000
FWHM $\Delta f_{\frac{1}{2}}$ (kHz)	~0·5	10·6	70
Quality factor Q	$\sim 10^{12}$	4×10^{10}	7×10^{9}
Resolution δf	~20 μHz	1·0 mHz	70 kHz
averaging time	1 h	16 s	
relative $\delta\nu/\nu$	$\sim 4\times10^{-20}$	$2\cdot1\times10^{-18}$	
rotation (rad/s)	10^{-10}		
refractive index	10^{-20}		

At this stage we estimate the beat frequency to be stable to the order of Hz over a time scale of hours, and that σ in equation (3) vanishes to a precision of the order of 10^{-19} s/m^2. It is hoped to improve this bound significantly in the future. This interferometric determination of the earth rotation rate already makes an interesting comparison with the historic interferometric measurements of Michelson and Gale (1925) using light and Werner *et al.* (1979) using neutrons.

Acknowledgments

We are most grateful to Tony Louderback of Ojai Research, Ojai, California, for providing the supercavity mirror coatings and for much advice; also Professors B.G. Wybourne for enthusiastic support and F.V. Kowalski for discussions and for substantial help in the construction of the ring, notably the output beam interferometer. H.R.B. acknowledges partial support by the US National Science Foundation under the US–NZ Cooperative Science scheme, the Royal Society of New Zealand by a Prince and Princess of Wales Science Award, and the University of Canterbury by two Erskine Fellowship awards. G.E.S. thanks Professors A. D. Buckingham, P. West and Dr B. Rosenstein for discussions and correspondence.

References

Al'tshuler, V. (1992). *Phys. Today* **45** (Feb.), 13.
Anandan, J. (1981). *Phys. Rev.* D **24**, 338.
Anderson, R., and Stedman, G, E. (1977). *Found. Phys.* **7**, 29.
Anderson, R., and Stedman, G. E. (1992). *Found. Phys. Lett.* **5**, 199.

Aronowitz, F. (1971). *In* 'Laser Applications' (Ed. M. Ross) 1, pp. 133, 169 (Academic: New York).
Bilger, H. R., and Sayeh, M. R. (1983). *In* 'Noise in Physical Systems and $1/f$ Noise' (Eds M. Savelli *et al.*), pp. 325–8 (Elsevier: Amsterdam).
Bilger, H. R., and Sayeh, M. R. (1986). *In* 'Noise in Physical Systems and $1/f$ Noise' (Eds A. d'Amico and P. Mazzetti), pp. 293–6 (Elsevier: Amsterdam).
Bilger, H. R., and Stowell, W. K. (1977). *Phys. Rev.* A **16**, 313.
Bilger, H. R., Stedman, G. E., and Wells, P. V. (1990). *Opt. Commun.* **80**, 133.
Buckingham, A. D. (1968). *J. Chem. Phys.* **48**, 3827.
Buckingham, A. D., and Disch, R. L. (1963). *Proc. R. Soc. London* **273**, 275.
Buckingham, A. D., and Dunmur, D. A. (1968). *Trans. Farad. Soc.* **64**, 1776.
Chow, W. W., Gea-Banacloche, J., Pedrotti, L. M., Sanders, V. E., Schleich, W., and Scully, M. O. (1985). *Rev. Mod. Phys.* **57**, 61.
Clauser, J. F. (1988). *Physica* B **151**, 262.
Dennis, M. L., Diels, J.-C., and Lai, M. (1991). *Opt. Lett.* **16**, 529.
Dieks, D., and Nienhuis, G. (1990). *Am. J. Phys.* **58**, 650.
Dolgov, A. D., Kriplovich, I. B., and Zakharov, V. I. (1988). *Nucl. Phys.* B **309**, 591.
Dolgov, A. D., Kriplovich, I. B., Vainshtein, A. I., and Zakharov, V. I. (1990). *Nucl. Phys.* B **315**, 138.
Dorschner, T. A., Haus, H. A., Holtz, M., Smith, I. W., and Statz, H. (1980). *IEEE J. Quant. Electr.* QE-16, 1376.
Fabri, E., and Picasso, L. E. (1989). *Phys. Rev.* A **39**, 4641.
Fischler, W. (1991). *Phys. Lett.* B **266**, 408.
Forder, P. W. (1985). *J. Phys.* A **18**, 3343.
Franklin, A. (1986). 'The Neglect of Experiment' (Cambridge Univ. Press).
Gabriel, M. D., Haugan, M. P., Mann, R. B., and Palmer, J. H. (1991). *Phys. Rev. Lett.* **67**, 2123.
Giazotto, A. (1989). *Phys. Reports* **182**, 365.
Gibbons, G. W. (1992). Comments on long range parity violating forces. DAMPT R-91/17.
Hagmann, C., Sikivie, P., Sullivan, M. S., and Tanner, D. B. (1990). *Phys. Rev.* D **42**, 1297.
Hammond, R. T. (1990). *Gen. Rel. Gravitat.* **20**, 813.
Heer, C. V. (1964). *Phys. Rev.* **134**, A799.
Hehl, F. W., Lemke, J., and Mielke, E. W. (1992). *In* 'Bad Honnef Lectures' (Eds J. Debrus and A. C. Hirshfeld) (Springer: Berlin).
Hehl, F. W., von der Hyde, P., Kerlick, G. D., and Nester, J. M. (1976). *Rev. Mod. Phys.* **8**, 393.
Hellwig, H. W. (1975). *Proc. IEEE* **63**, 212.
Hendriks, B. H. W., and Nienhuis, G. (1990). *Quant. Optics* **2**, 13.
Hojman, R., Mukku, C., and Sayed, W. H. (1980). *Phys. Rev.* D **22**, 1915.
Hojman, S., Rosenbaum, M., Ryan, M. P., and Shepley, L. C. (1978). *Phys. Rev.* D **17**, 3141.
Hojman, S., Rosenbaum, M., and Ryan, M. P. (1979). *Phys. Rev.* D **19**, 430.
Kowalski, F. V., Murray, J., and Head, A. (1992). Interaction of light with an accelerating dielectric (submitted for publication).
Kuriyagawa, A., and Mori, S. (1979). *Phys. Rev.* D **20**, 1290.
Levi, B. G. (1991). *Phys. Today* **44** (July), 17.
Li, Z., Bennett, R. G. T., and Stedman, G. E. (1991). *Opt. Commun.* **86**, 51.
Macek, W. M., and Davis, D. T. M. Jr. (1963). *Appl. Phys. Lett.* **2**, 67.
Macek, W. M., Davis, D. T. M., Jr., Olthius, R. W., Schneider, J. R., and White, G. R. (1963). 'Symposium on Optical Masers', p. 199 (Polytechnic Press: New York).
Macek, W. M., Schneider, J. R., and Salamon, R. M. (1964). *J. Appl. Phys.* **35**, 2556.
Maiani, L., Petronzio, R., and Zavattini, E. (1986). *Phys. Lett.* B **175**, 359.
Mansouri, R., and Sexl, R. U. (1977). *Gen. Rel. Gravitat.* **8**, 497, 505, 819.
Mashhoon, B. (1975). *Phys. Rev.* D **11**, 2679.
Mashhoon, B. (1988). *Phys. Rev. Lett.* **61**, 2639.
Mashhoon, B. (1989). *Phys. Lett.* A **139**, 103.
Michelson, A. A., and Gale, H. G. (1925). *Astrophys. J.* **61**, 140.
Moffat, J. W. (1989). *Phys. Rev.* D **39**, 474.

Moffat, J. W. (1990). Review of the nonsymmetric gravitation theory, Lectures given at the Summer Institute on Gravitation, Banff, Alberta
Narlikar, J. V., Pecker, J. C., and Vigier, J. P. (1991). *Phys. Lett.* A **154**, 203.
Ni, W.-T. (1977). *Phys. Rev. Lett.* **38**, 301.
Ni, W. T., Tsubono, K., Mio, N., Narihara, K., Chen, S-C., King, S-K., and Pan, S-S. (1991). *Mod. Phys. Lett.* A **6**, 3671.
Nordtvedt, K. (1988). *Phys. Rev. Lett.* **61**, 2647.
Okun, L. B. (1988). *Comments Nucl. Part. Phys.* **19**, 99.
Post, E. J. (1967). *Rev. Mod. Phys.* **39**, 475.
Post, E. J. (1972). *J. Opt. Soc. Am.* **62**, 234.
Pound, R. V., and Snider, J. L., (1965). *Phys. Rev.* **140**, B788.
Riehle, F., Kisters, Th., Witte, A., and Helmcke, J. M. (1991). *Phys. Rev. Lett.* **67**, 177.
Riis, E., Andersen, L.-U. A., Bjerre, N., Poulsen, O., Lee, S. A., and Hall, J. H. (1988). *Phys. Rev. Lett.* **60**, 842.
Ritter, R. C., Goldblum, C. E., Ni, W.-T., Gillies, G. C., and Speaker, C. G. (1990). *Phys. Rev.* D **42**, 977.
Robertson, D. S. (1991). *Rev. Mod. Phys.* **63**, 899.
Ross, H. J., and Stedman, G. E. (1988). *Phys. Lett.* A **132**, 229.
Ross, H. J., Sherborne, B. S., and Stedman, G. E. (1989). *J. Phys.* B **22**, 459.
Sanders, G. A., and Ezekiel, S. (1988). *J. Opt. Soc. Am.* B **5**, 674.
Sargent, M. III, Scully, M. O., and Lamb, W. E. Jr. (1974). 'Laser Physics', Ch. 10 (Addison–Wesley: New York).
Sayeh, M. R., and Bilger, H. R. (1985) *Phys. Rev. Lett.* **55**, 700.
Scorgie, G. C. (1990). *J. Phys.* A **23**, 5169.
Scorgie, G. C. (1991). *Eur. J. Phys.* **12**, 64.
Scully, M. O., Zubairy, M. S., and Haugan, M. P. (1981). *Phys. Rev.* A **24**, 2009.
Siegman, A. E. (1986). 'Lasers', pp. 1193ff (University Science Books: Mill Valley).
Sikivie, R. (1992). Axion searches. UFIFT-HEP-91-29.
Silverman, M. P. (1989). *Europhys. Lett.* **9**, 95.
Statz, H., Dorschner, T. A., Holtz, M., and Smith, I. W. (1985). *In* 'Laser Handbook', Vol. 4 (Eds M. L. Stitch and M. Bass), p. 229 (North Holland: Amsterdam).
Stedman, G. E. (1972). *Am. J. Phys.* **40**, 782.
Stedman, G. E. (1973). *Am. J. Phys.* **41**, 1300.
Stedman, G. E. (1985*a*). *Contemp. Phys.* **26**, 311.
Stedman, G. E. (1985*b*). *Adv. Phys.* **34**, 513.
Stedman, G. E. (1986). *In* 'Quantum Optics IV' (Eds J. D. Harvey and D. F. Walls), pp. 259–66 (Springer: Berlin).
Stedman, G. E. (1990). *Phys. World* **3**, 23.
Stedman, G. E. (1991). *Phys. Lett.* A **152**, 19.
Stedman, G. E. (1993). *In* 'Modern Nonlinear Optics, Part 2' (Eds S. Kielich and M. W. Evans) (Wiley: New York).
Stedman, G. E., and Bilger, H. R. (1987). *Phys. Lett.* A **122**, 289.
Stedman, G. E., and Bilger, H. R. (1992). *Digital Signal Proc.* **2**, 105.
Stedman, G. E., Bilger, H. R., and Kowalski, F. V. (1991). *Aust. & N.Z. Physicist* **28**, 16.
Takahashi, Y. (1985). *Phys. Lett.* A **113**, 5.
Telegdi, V. L. (1990). Mind over matter: the intellectual content of experimental physics. CALTECH ERN-90-09.
Vanier, J. (1982). *Metrologia* **18**, 173.
Vetharaniam, I., and Stedman, G. E. (1991). *Found. Phys. Lett.* **4**, 275.
Vetharaniam, I., and Stedman, G. E. (1992). Significance of precision tests of special relativity (submitted for publication).
Werner, S. A., Staudenmann, J-L., and Colella, R. (1979). *Phys. Rev. Lett.* **42**, 1103.
Will, C. M. (1992*a*). *Phys. Rev.* A **45**, 403.
Will, C. M. (1992*b*). The confrontation between general relativity and experiment: a 1992 update. *Int. J. Mod. Phys.* A (to be published).
Zeeman, H. (1920). *Proc. R. Acad. Sci. (Amsterdam)* **22**, 462, 512.

Manuscript received 30 March, accepted 25 June 1992

Appendix D LI ET AL. 1993

Ziyuan Li, G.E. Stedman and H.R. Bilger (1993), Asymmetric response profile of a scanning Fabry-Perot interferometer, *Opt. Commun.*, **100**, 240-246.

Optics Communications 100 (1993) 240–246
North-Holland

OPTICS
COMMUNICATIONS

Full length article

Asymmetric response profile of a scanning Fabry–Pérot interferometer

Ziyuan Li, G.E. Stedman
Department of Physics, University of Canterbury, Christchurch 1, New Zealand

and

H.R. Bilger
School of Electrical and Computer Engineering, Oklahoma State University, Stillwater, OK 74078-0321, USA

Received 10 November 1992; revised manuscript received 26 January 1993

The finite scanning speed of a scanning Fabry–Pérot interferometer induces asymmetry in the response profile to a monochromatic input beam. The amplitude of this profile is mathematically that of a fixed interferometer subjected to an input beam with suitable frequency scanning, and is related to the complex error function. The extent of the asymmetry thus depends on a single parameter, $\eta=\beta t_c^2$, where β is the frequency scanning rate and t_c is the power decay time of the interferometer. To obtain an asymmetry less than 5% in the profile obtained from scanning a monochromatic beam requires a scanning time as much as 100 times of the decay time of the interferometer. Experimental data are in good agreement with our calculations.

1. Introduction

In high resolution spectroscopy with a Fabry–Pérot interferometer, the extraction of the input spectrum from the output profile is of great importance. Most of the literature on this subject uses the symmetric Airy function in the deconvolution algorithm [1–3]. However, the Airy function for the intensity distribution in the fringe pattern is strictly valid only for a source of constant brightness and spectral distribution and for a non-scanning interferometer. For a scanning interferometer, the limitations on rapid scanning were discussed by Greig and Cooper [4]. They estimated a time to establish the interference pattern as approximately $1.4F\tau$, where F is the finesse and τ is the round trip time of the interferometer. We can rewrite this expression as $1.4F\tau = 2.8\pi t_c$ since $F=S/\Delta f_{1/2}$ and $\tau=1/S$, where S is the free spectral range of the interferometer and $\Delta f_{1/2}$ is its power fwhm in frequency; $\Delta f_{1/2}=1/2\pi t_c$ where t_c is the decay time of the power in the cavity. However, their analysis was based on the Lummer–Gehrcke plate [5], and is relevant only for the steady-state multiple-beam interferometer. Optical ringing [6] occurs when the input frequency sweeps through an interferometer in a time which is not large compared to t_c. The ringing profile is caused by the beating between the input frequency and the cavity mode frequency when either is swept in time.

We find that the asymmetry in fringe profiles can occur in a scanning interferometer even when the time interval which is required for scanning over the probe frequency is as large as $100t_c$. This is particularly important for spectral measurements using a supercavity interferometer. In using the Newport SR-130 supercavity (whose free spectral range is 6 GHz and finesse ~ 60000 [6]) to measure the mode spectrum in our 1 m^2 ring laser, we can see the asymmetry of the fringe profiles of the interferometer output over a large range of interferometer scanning rates, from 3–50 GHz/s. When we further increase the scanning rate of the interferometer, the ringing profile discussed earlier [6] becomes conspicuous. We will present an analysis of this asymmetric fringe

profile of a scanning interferometer in sec. 2. Generally, the response of a scanning interferometer can be expressed as a series in the intracavity field amplitudes. The asymmetry of the fringe profiles might be expected to depend on the three parameters: the reflectivity R of the mirrors, the round trip optical path L of the reflected beams in the interferometer and the scanning rate of the interferometer. While the influences of the three parameters on the asymmetric line profile could be determined by numerical calculations, its physical significance would be obscured. We will prove that the response of a scanning interferometer to a signal of constant frequency is equivalent to the response of a fixed interferometer to a frequency which is scanned in a certain linear manner. The asymmetry of the profiles will then depend on the single parameter η where $\eta \equiv \beta t_c^2$. The experimental results and discussion will be given in sec. 3.

2. Response of scanning Fabry–Pérot

Let us consider a monochromatic wave $A_{in}(t, z) = A_0 \exp i(k_0 z - \omega_0 t)$ to be injected into a scanning interferometer (fig. 1). The mirrors are separated by a length l; one of these mirrors is moving at a constant speed v so as to increase l. The frequency of the transmitted wavelet $A_n(t, z)$ will be Doppler shifted on each reflection; after the nth reflection, the wave has a frequency $\omega_n = \omega_0(1 - 2nv/c)$ and wavevector $k_n = \omega_n/c$ to first order, where c is the speed of light. The output of the scanning interferometer is the sum of the waves $A_n(t, z)$. Although the cavity length is modified by $\Delta l = v\tau$ within one round trip of a light pulse, we take a snapshot picture of the infinite wave trains at the given time t when the moving mirror is at $z = 0$, and demand only that the boundary conditions be satisfied at each reflection in order to determine the phases of the components. We relegate the essential mathematical development to the appendices. Applying the boundary conditions for reflection and transmission in each mirror rest frame, and Lorentz transforming where necessary to the laboratory frame, we obtain the transmitted field given by eq. (A.1):

$$A_{out}(t, z) = A_{in}(t, z)(1 - R) \sum_{n=0}^{\infty} R^n \exp(i\Phi_n), \quad (1)$$

where

$$\Phi_n = \omega_0\{n[B_0 + (B_1 t + B_2)v/c] + n^2 Cv/c\}, \quad (2)$$

and $B_0 = -C = 2l/c \equiv \tau$, $B_1 = 2$, $B_2 = -2(z + l)/c$.

B_0 represents the phase shift from repeated internal reflections with a stationary mirror, and would in isolation lead to the Airy function. B_1 arises from a combination of effects associated with the Doppler shift, including both its direct effect on the phases of the emerging partial waves and its indirect effects on the phase shift accumulated in internal reflections. On its own B_1 simply modifies the effective cavity length by a velocity-dependent amount, without affecting the symmetry of the Airy profile. Part of the indirect effect of the Doppler shift is to induce a term in the exponent which is quadratic in n (the term C) since on the nth bounce the frequency is shifted by n steps; it is this term which will induce asymmetry in the interferometer profile.

Now the response of a fixed interferometer to a signal whose frequency is scanned at a rate β has a modulus of the form of eqs. (1) and (2) (see eq. (B.2)) in which v/c is replaced by $\beta\tau/2\omega_0$ and the same values are obtained for B_0, C, B_1 and (to within a change of time origin) B_2. This proves the formal equivalence of the two problems: we can express the output of a scanning interferometer as that for a interferometer with a frequency scanned input beam.

Neither eq. (1) nor its counterpart (eq. (B.2)) for the fixed interferometer is easily solved; a series of the form $\sum_n a^n b^{n^2}$ is involved. Instead, we use the equivalence described above to derive an alternative solution. Details are given in appendix C. The ratio of the outgoing and incoming intensities I_{out} ($|A_{out}|^2$), I_0 ($|A_0|^2$) is then given by

$$I_{out}/I_0 = (\pi/8\eta)\,|w(\zeta)|^2, \quad (3)$$

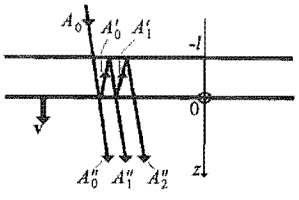

Fig. 1. The scanning Fabry–Pérot interferometer. Details are discussed in appendix A.

where $w(\zeta)$ is given in eq. (C.4) and is related to the error function.

Figure 2 shows this calculated intensity response (solid line) of a scanning interferometer for three values of the normalized scanning rate: $\eta=0.5$, 0.1, and 0.01. The dashed line and the dotted line in fig. 2a represent the real and imaginary parts respectively of the transmitted amplitude. The definitions of the characteristic parameters of an asymmetric transmission profile as shown in fig. 2b; δ is the deviation of the profile peak from the ideal case. Δ_l and Δ_r describe the half-width of the intensity profile on the left and right side, respectively. For convenience of discussion, we define the deviation parameter $\delta_c=2\delta/\Delta f_{1/2}$ and the asymmetry parameter in the frequency domain of $\Delta_a=2(\Delta_l-\Delta_r)/\Delta f_{1/2}$. For the case $\eta=1\%$ as shown in fig. 2c, the corresponding scanning time over the probe frequency is 100 times the decay time of the interferometer, and the asymmetry parameter Δ_a is less than 5%. As the normalized scanning rate increases, the profile of the transmitted intensity of the scanning interferometer varies in four ways: the asymmetry and the peak shift of the profile change, the relative fwhm increases, and the transmitted intensity decreases. Figure 3 shows numerical calculations of the variations in the intensity ratio I_{out}/I_0 at the peak and the peak deviation δ with the normalized scanning rate η. An analytic approximation to the integral in eq. (3) is derived in appendix D, with the result

$$I_{out}/I_0=\exp[-(2\eta)^{3/2}t']/[1+\tfrac{1}{4}\eta t'^2+\sqrt{8}t'\eta^{3/2}]\,. \tag{4}$$

A comparison in the case $\eta=1\%$ of the results of eqs. (3) and (4) shows that even for this relatively large parameter value eq. (4) is accurate to $\sim 10\%$. The asymmetry parameter is given from eq. (4) by a weighted average of the solutions $T_\pm$ of $I_{out}/I_0=\frac{1}{2}$; on using a linear expansion of the exponent we find (appendix D)

$$\Delta_a=4[2\eta^3/(72\eta^3+\eta)]^{1/2}\,. \tag{5}$$

This equation (to be plotted in fig. 7) shows that η values of 1%, 5% and 10% translate into asymmetry parameters of approximately 6%, 26% and 43%, respectively.

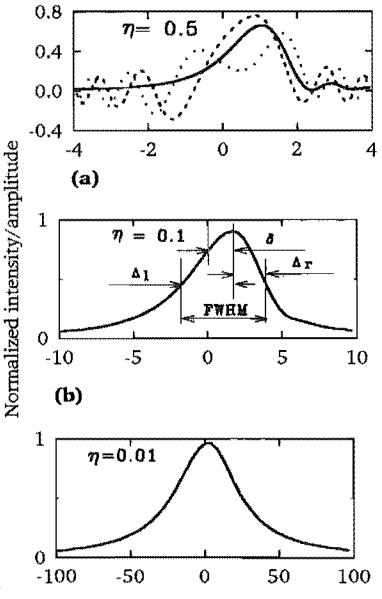

Fig. 2. Amplitude and intensity profiles from numerical evaluation of eqs. (C.7) and (3) at various normalized scanning rates η: (a) $\eta=0.5$, (b) $\eta=0.1$ and (c) $\eta=0.01$. Throughout, the solid line represents the intensity profile, and in (a) the broken and dotted lines represent the real and imaginary parts of the amplitude. Here and in following figures the normalized time t' is related to real time t by $t'=\Gamma_c t$.

3. Experiment and discussion

The experiment setup is shown in fig. 4. A Newport NL-1 HeNe frequency-stabilised laser is used as

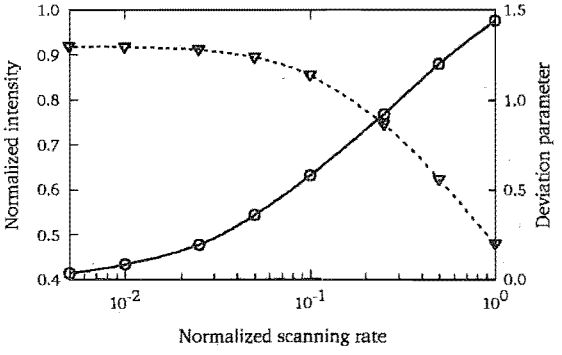

Fig. 3. The variation of the output intensity ratio I_{out}/I_0 (broken line) and the peak deviation δ (solid line) with the normalized scanning rate η from numerical calculation of eq. (3).

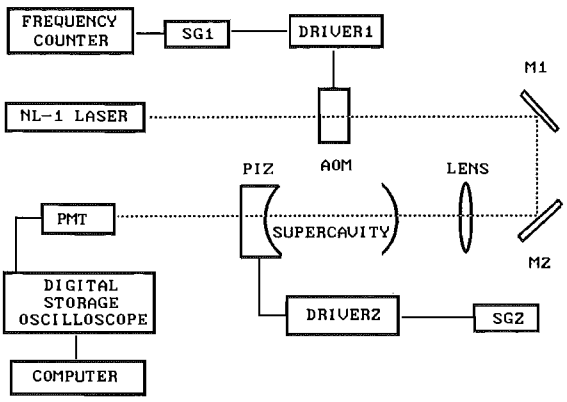

Fig. 4. Experimental setup for measurement of the asymmetry in the response of a scanning Fabry–Pérot interferometer.

a light source. Its rms frequency fluctuations are 100 kHz in short term (5 ms) and 5 kHz in medium term (100's), respectively. An acousto-optic modulator (Newport N24080) inserted between the HeNe Laser and the scanning interferometer (Newport SR-130 supercavity spectrum analyzer) has two functions. First it is an optical isolator to reduce the influence of the feedback of reflection from the interferometer mirror [6]; we observed that the intensity of the NL-1 laser output could have low frequency (a few Hz) fluctuations in the absence of the acousto-optic modulator. Secondly it supplies a frequency scanning calibration since the relation between voltage and expansion of the piezoelectric material is in general not exactly linear [8]. In principle, we could use an AM or FM calibration of the scanning rate. Since the nonlinearity of the frequency sweeps of the driver of the acousto-optic modulator for FM is 15%, we chose the AM modulation in our experiment. A modulation signal of 1.5 MHz is used as input to the modulator driver and a frequency counter with a fractional precision of 10^{-7} (1 Hz in 10 MHz) is used to monitor the modulation frequency. The laser beam passing through the optical modulator is injected into the scanning interferometer with TEM_{00} mode matching by a conventional lens. Fringes from the scanning interferometer are detected by a photomultiplier (Thorn EMI 9214) with a bandwidth of 100 MHz and its output is sent to a digital storage oscilloscope (Hitachi Denshi Models VC-6275) with a maximum sampling rate of 200 million samples per second and a fractional precision of time scale reading of 10^{-4}.

Frequency jitter in the output of the NL-1 frequency-stabilized laser is evident when the resonance of the interferometer is scanned over this probe frequency. The effect of this frequency jitter on the calibration of the scanning rate increases as the scanning rate slows down. We averaged runs to reduce this error. A single run with a scanning rate of 3.25 GHz/s gives sidebands whose fwhm is approximately that of the carrier. Figures 5a and 5b shows profiles from the average of 64 runs with the scanning rates 9.29 GHz/s and 3.46 GHz/s. The variation of the fwhm of the sidebands reflects the frequency jitter of the NL-1. Figure 6 gives an extreme example of the effect of jitter for a very low scanning rate; the separations of the side bands from the central peak differ by more than 20%.

The experimental data on profile asymmetry is compared with numerical calculations, both on the full and approximate models of eqs. (3) and (5), in fig. 7. Scales have been chosen for best fit, and this with the value of the known absolute frequency scanning rate β gives a fwhm $\Delta f_{1/2} = (1/2\pi)(\beta/\eta)^{1/2}$ for

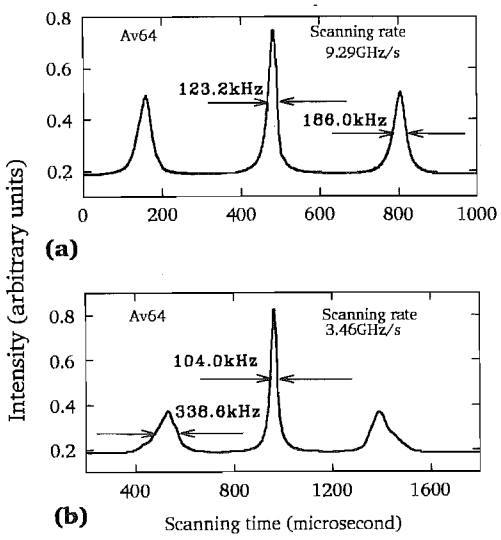

Fig. 5. Joint effect on the profile of probe frequency jitter and frequency scanning rate. The averages of 64 runs at scanning rates of 9.29 GHz/s (a) and 3.46 GHz/s (b), with the oscilloscope triggering on the central peak. The larger width of the side peaks reveals the variation in scanning rate and so averaging of non-coincident peaks.

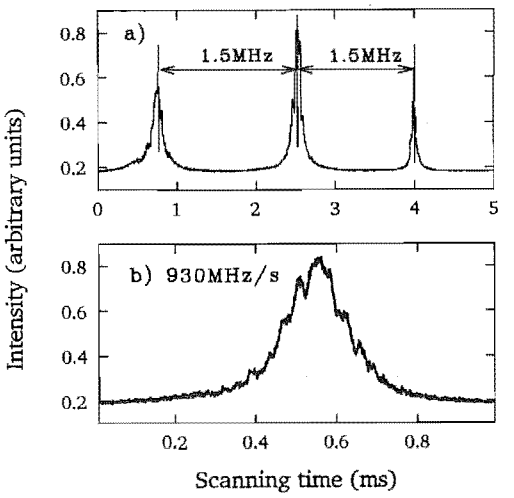

Fig. 6. A profile obtained at very low scanning rate (0.93 GHz/s). (a) Unequal spacing of sidebands caused by jitter during collection of the profile. (b) Ragged shape of the profile for one such peak, reflecting shorter-term frequency jitter of the NL-1 laser.

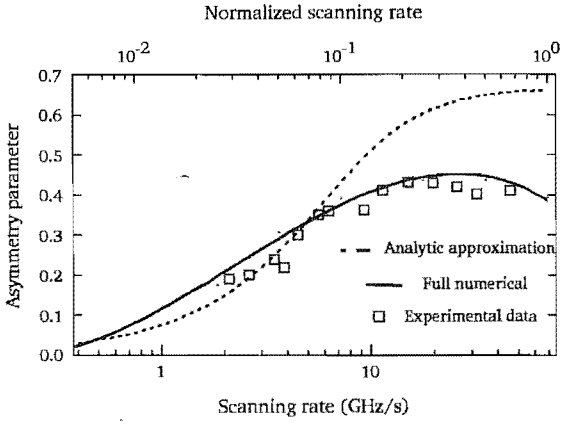

Fig. 7. Variation of the asymmetry A_a of the profile with the scanning rate (the normalized rate η used in the calculation being plotted on the upper axis, and the absolute value β for the experiment on the lower). The solid (broken) line is the numerical prediction from the full (approximate) theory (eqs. (3) and (5), respectively).

the SR-130 supercavity interferometer. Figure 8 shows the variation of the observed fwhm with the scanning rate. The squares represent the experimental data, the fwhm being determined by $\Delta f_{1/2} = 3\Delta t_{1/2}/\Delta t$ (MHz), where Δt is the time interval between the two sidebands and $\Delta t_{1/2}$ is the fwhm in the

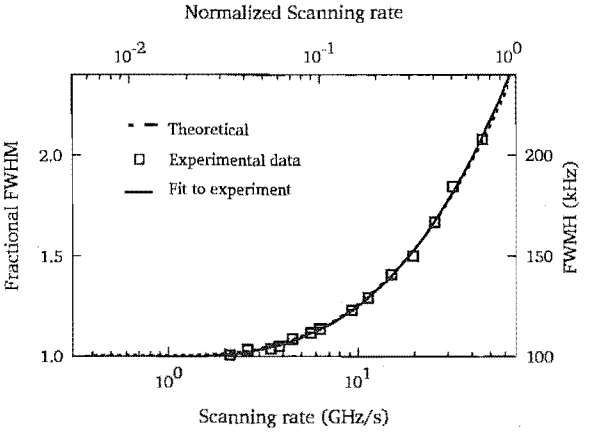

Fig. 8. The increase of the full width at half maximum (fwhm) of the profile with the scanning rate. The broken line is the theoretical prediction and the solid line is a fit to the experimental data.

time domain. The experimental data are in excellent agreement with the numerical calculation from eq. (3).

Acknowledgements

We acknowledge gratefully the help of C. Rowe for much invaluable technical assistance and Ziyuan Li would like to thank P. Wells for much help in computing.

Appendix A
Response of a scanning Fabry–Pérot interferometer to a monochromatic field

The wave $A_0 \exp[i(k_0 z - \omega_0 t)]$ is incident on the back, stationary mirror of a scanning Fabry–Pérot interferometer (fig. 1). Within the interferometer the waves reflected from the front (and moving) mirror have the form

$$A_0' = A_0 rq \exp[-i(k_1 z + \omega_1 t)],$$

$$A_1' = A_0 r^3 q \exp[-i(k_2 z + \omega_2 t - 2k_1 l)], \text{ etc.}$$

The transmitted wave has the components

$$A_0'' = A_0 q^2 \exp[i(k_0 z - \omega_0 t)],$$

$$A_1'' = A_0 r^2 q^2 \exp[\mathrm{i}(k_1 z - \omega_1 t + 2k_1 l)] ,$$

$$A_2'' = A_0 r^4 q^2 \exp\{\mathrm{i}[k_2 z - \omega_2 t + 2(k_1 + k_2)]\}, \text{ etc.} ,$$

where q is the transmission coefficient of the wave amplitude at each reflection.

These give rise to a total transmitted amplitude of

$$\begin{aligned} A_{\mathrm{out}}(t, z) &= A_{\mathrm{in}}(t, z)(1-R)\{1 + R\exp\{\mathrm{i}[(k_1 - k_0)z \\ &\quad - (\omega_1 - \omega_0)t + 2k_1 l]\} + R^2 \exp\{\mathrm{i}[(k_2 - k_0)z \\ &\quad - (\omega_2 - \omega_0)t + 2k_1 l + 2k_2 l]\} + \ldots\} \\ &= A_{\mathrm{in}}(t, z)(1-R)\sum_{n=0}^{\infty} R^n \exp(\mathrm{i}\Phi_n) \qquad (A.1) \end{aligned}$$

(using $\sum_0^n m = n(n-1)/2$) in agreement with eqs. (1) and (2).

Appendix B
Response of a steady-state Fabry–Pérot to a frequency modulation field

The amplitude transfer function of a fixed interferometer for a beam $A_0 \exp[\mathrm{i}(k_0 z - \omega_0 t)]$ has the form $H(\omega) = (1-R)/(1-R\exp \mathrm{i}\delta)$, where $\delta = (\omega - \omega_0)\tau$ is the phase delay in a round trip of the injected wave in the interferometer relative to that (a multiple of 2π: $\omega_0 = 2\pi N/\tau$, $N\lambda = 2l$) for exact resonance, and as before $\tau = 2l/c$. $H(\omega) = (1-R)\sum_n R^n \exp \mathrm{i}n\omega\tau$, and its Fourier transform is given by $h(t) = (1-R)\sum_n R^n \delta(t - n\tau)$ where δ is the Dirac delta function. For small detuning: $\omega \approx \omega_0$ [6], this may be approximated by $H(\omega) = [1 - 2\mathrm{i}(\omega - \omega_0)/\Gamma_c]^{-1}$, where the power rate of decay in the cavity is $\Gamma_c = 1/t_c = 2\pi\Delta f_{1/2}$; note that Γ_c is twice the amplitude rate of decay γ_c used in ref. [6]. The quality factor $Q = \omega t_c$, the free spectral range (FSR) is $c/2l$, the finesse is $F = \pi R/(1-R) = Q\lambda/2l$, and the power full width at half maximum $\Delta f_{1/2} = f_0/Q = c(1-R)/2\pi l R$.

Let us consider an input field which is ramped in frequency:

$$A_{\mathrm{in}}(t, z) = A_0 \exp\{-\mathrm{i}[\omega_0 + \tfrac{1}{2}\beta(t - z/c)](t - z/c)\} . \qquad (B.1)$$

β is the frequency scanning rate; the instantaneous frequency $\omega = \omega_0 + \beta(t - z/c)$ and is related to the time derivative of the phase [9], and because of the dependence on t and z through $(t - z/c)$ the above form satisfies the wave equation with $k = \omega/c$. The output of the interferometer is given by the convolution of the input field and the impulse response of the cavity:

$$\begin{aligned} A_{\mathrm{out}}(t, z) &= (1-R)\sum_n R^n A_{\mathrm{in}}(t - n\tau) \\ &= (1-R)A_0 \exp[\mathrm{i}(k_0 z - \omega_0 t + \beta t z/c - \tfrac{1}{2}\beta t^2 \\ &\quad - \beta z^2/2c^2)] \sum_n R^n \exp(\mathrm{i}\Phi_n) , \qquad (B.2) \end{aligned}$$

where

$$\begin{aligned} \Phi_n &= \omega_0\{n[B_0 + (\beta\tau/2\omega_0)(B_1 t + B_2)] \\ &\quad + n^2 \beta\tau C/2\omega_0\} . \qquad (B.3) \end{aligned}$$

Apart from the complex factor, which does not affect the magnitude of the temporal profile, this has the form of eq. (2) for the scanning interferometer under constant excitation, where $(\beta\tau/2\omega_0)$ now plays the role of v/c and as before the parameters $B_0 = -C = \tau$, $B_1 = 2$. $B_2 = -2z/c$ and is now different to that for the scanning interferometer case; however this difference amounts merely to a change in the origin of time. Hence the cases of a linearly scanned interferometer with fixed input frequency and a fixed interferometer with a linearly ramped input frequency give indistinguishable intensity profiles at the output.

Appendix C
Solution for the temporal profile

We use the solution from appendix B for the scanning interferometer to solve for the cases of both appendices A and B. The input field $A_{\mathrm{in}}(t, z)$ has the Fourier transform

$$\begin{aligned} A_{\mathrm{in}}(\omega, z) &= A_0 \exp[\mathrm{i}(k_0 z - \beta z^2/c^2)] \\ &\quad \times \int_{-\infty}^{\infty} \mathrm{d}t \exp\{\mathrm{i}[(\omega - \omega_0 + \beta z/c)t - \tfrac{1}{2}\beta t^2]\} \qquad (C.1) \end{aligned}$$

and with the change of variable $t \to u = (\beta/2)^{1/2}[t - (\omega - \omega_0)/\beta - z/c]$, this gives

$$\begin{aligned} A_{\mathrm{in}}(\omega, z) &= A_0(2/\beta)^{1/2} \exp\{\mathrm{i}[k_0 z + (\omega - \omega_0)^2/2\beta \\ &\quad + (\omega - \omega_0)z/c]\} I , \qquad (C.2) \end{aligned}$$

where

$$I=\int_{-\infty}^{\infty} \mathrm{d}u \exp(-\mathrm{i}u^2)=\pi^{1/2}\exp(-\mathrm{i}\pi/4)\,.$$

Multiplying this by the response function of the fixed interferometer (see appendix B; $\Gamma_c=1/t_c$) and Fourier transforming, we obtain

$$A_{\mathrm{out}}(t,z)=\frac{1}{2\pi}\int_{-\infty}^{\infty}\mathrm{d}\omega\exp(-\mathrm{i}\omega t)\,A_{\mathrm{in}}(\omega,z)\,H(\omega)$$

$$=A_0/(2\pi\beta)^{1/2}\int_{-\infty}^{\infty}\mathrm{d}\omega\frac{1}{1-2\mathrm{i}(\omega-\omega_0)/\Gamma_c}$$

$$\times\exp\{\mathrm{i}[(\omega-\omega_0)^2/2\beta+(\omega-\omega_0)(z/c-t)$$

$$-\omega_0 t+k_0 z-\pi/4]\}\,. \qquad (C.3)$$

This can be cast into closed form using the complex error function in the form [7]

$$w(\zeta)=\frac{\mathrm{i}}{\pi}\int_{-\infty}^{\infty}\mathrm{d}v\frac{\exp(-v^2)}{\zeta-v}$$

$$=\exp(-\zeta^2)\,\mathrm{erfc}(-\mathrm{i}\zeta)\quad(\mathrm{Im}\,\zeta>0)\,. \qquad (C.4)$$

To this end we now change variable $\omega\to v$ where

$$v\equiv G\exp(-\mathrm{i}\pi/4)[(\omega-\omega_0)/(2\beta)^{1/2}$$

$$+(\beta/2)^{1/2}(z'/c-t')]\,, \qquad (C.5)$$

and the sign factor $G\equiv-\mathrm{sgn}[1+(\eta/2)^{1/2}(z'/c-t')]$, where $z'=\Gamma_c z$, $t'=\Gamma_c t$, $\eta=\beta/\Gamma_c^2$; this is chosen so that the expression

$$\zeta\equiv G(1/8\eta)^{1/2}[-\exp(\mathrm{i}\pi/4)$$

$$+\exp(-\mathrm{i}\pi/4)(\eta/2)^{1/2}(z/c-t)] \qquad (C.6)$$

always has a positive imaginary part. We then have the closed form for the resultant amplitude:

$$A_{\mathrm{out}}(t,z)=-G\exp(-\mathrm{i}\pi/4)\,(\pi/8\eta)^{1/2}A_0$$

$$\times\exp\{\mathrm{i}[k_0 z-\omega_0 t-\tfrac{1}{2}\beta(z/c-t)^2]\}\,w(\zeta)\,. \qquad (C.7)$$

Hence the corresponding intensity ratio I_{out} ($|A_{\mathrm{out}}|^2$), I_0 ($|A_0|^2$) of the outgoing and incoming beams is given by eq. (3).

Appendix D
Analytical formulae for limiting cases

We expand eq. (3) for small normalized scanning speed η. In the limit that the scanning rate β (and therefore η) tens to zero, and omitting an unobservable overall phase,

$$A_{\mathrm{out}}/A_0=\left(\frac{\pi}{8\eta}\right)^{1/2}w(\zeta)=\frac{\mathrm{i}}{(8\pi)^{1/2}}\int_{-\infty}^{\infty}\frac{\mathrm{d}v\exp(-v^2)}{\xi-\sqrt{\eta}v}$$

where $\xi=\sqrt{\eta}\,\zeta$. The denominator factor may be rewritten as $\exp(\sqrt{\eta}v/\xi+\frac{1}{2}\eta v^2/\xi^2)$ to $O(\eta v^2)$, and on completing the square of the gaussian integral and expanding the result to $O(\eta v^2)$ we obtain

$$A_{\mathrm{out}}/A_0=\frac{\mathrm{i}}{(8a)^{1/2}\xi}\exp(b^2/a)\,,$$

$$a=1-\eta/2\xi^2\,,\quad b=\sqrt{\eta}/\xi\,,$$

$$I_{\mathrm{out}}/I_0=|A_{\mathrm{out}}/A_0|^2$$

$$=\exp[-(2\eta)^{3/2}t']/[1+\tfrac{1}{4}\eta t'^2+\sqrt{8}t'\eta^{3/2}]\,.$$

In the time domain the asymmetry parameter $A_a=2(2T_0-T_+-T_-)/(T_+-T_-)$, where the maximum of I_{out} is at $t'=T_0\equiv-8(2\eta)^{1/2}$, and the half-powers points are the solutions $T_\pm$ of $I_{\mathrm{out}}=\frac{1}{2}I_0$, giving $\frac{1}{4}\eta T_\pm^2+3(2\eta)^{3/2}T_\pm-1=0$. Hence $T_++T_-=-12(8\eta)^{1/2}$, $(2T_0-T_+-T_-)=8(2\eta)^{1/2}$, and $T_+-T_-=4(72\eta^3+\eta)^{1/2}/\eta$. We obtain $A_a=4[2\eta^3/(72\eta^3+\eta)]^{1/2}$, whose form is plotted in fig. 7.

References

[1] G. Hernandez, Appl. Optics 5 (1966) 1745.
[2] D.M. Zipoy, Appl. Optics 18 (1979) 1988.
[3] J.M. Vaughan, The Fabry–Pérot interferometer (Hilger, Bristol, 1989) pp. 471–473.
[4] J.R. Greig and J. Cooper, Appl. Optics 7 (1968) 2166.
[5] M. Born and E. Wolf, Principles of optics (Pergamon, Oxford, 1964) p. 346.
[6] Z. Li, R.G.T. Bennett and G.E. Stedman, Optics Comm. 86 (1991) 51.
[7] M.A. Abramowitz and I.A. Stegun, eds., Handbook of mathematical functions (Dover, New York, 1965).
[8] R. Aschauer, A. Asenbaum and H. Gerl, Appl. Optics 29 (1990) 953.
[9] A.E. Siegman, Lasers (Univ. Science, Mill Valley, CA, 1986) p. 332.

Appendix E

Experimental records of the ringing profiles

A series of ringing profiles using the SR-130 supercavity with the frequency scanning range from 185.8 GHz/s down to 16.90 GHz/s are presented.

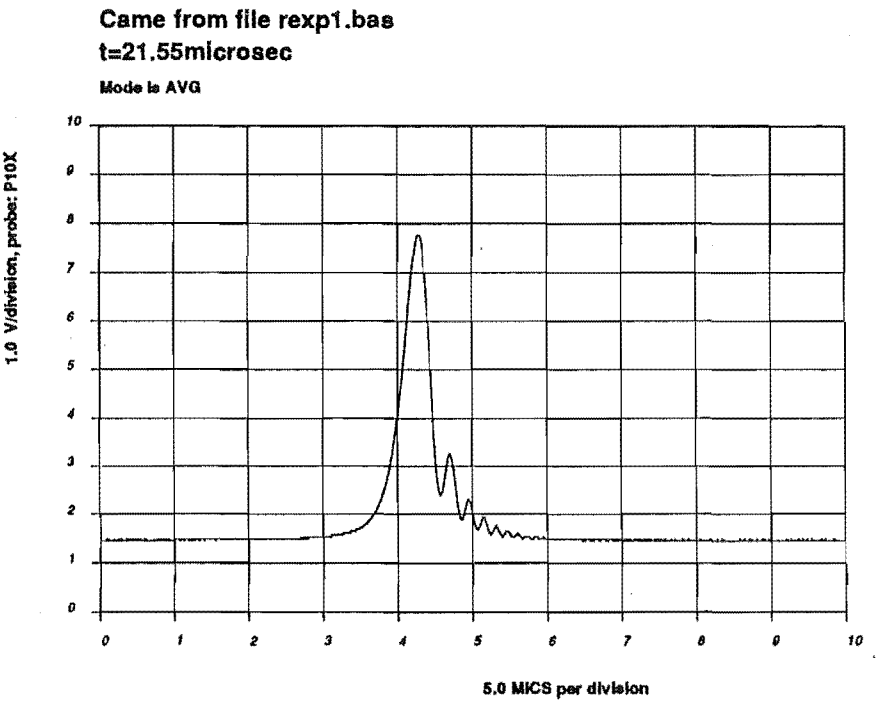

Figure 1: The frequency scanning rate is 185.8 GHz.

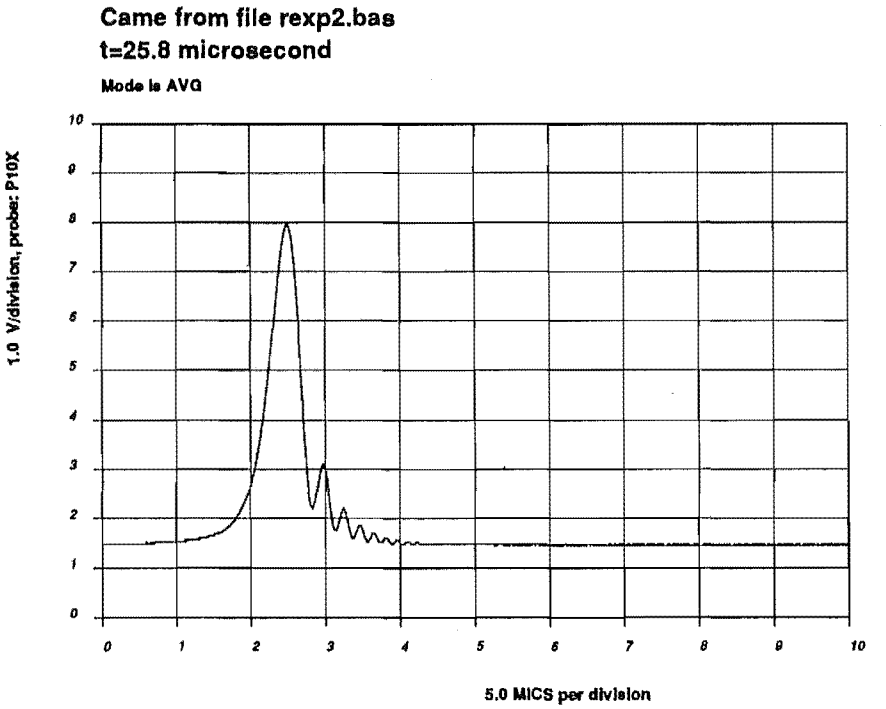

Figure 2: The frequency scanning rate is 152.2 GHz.

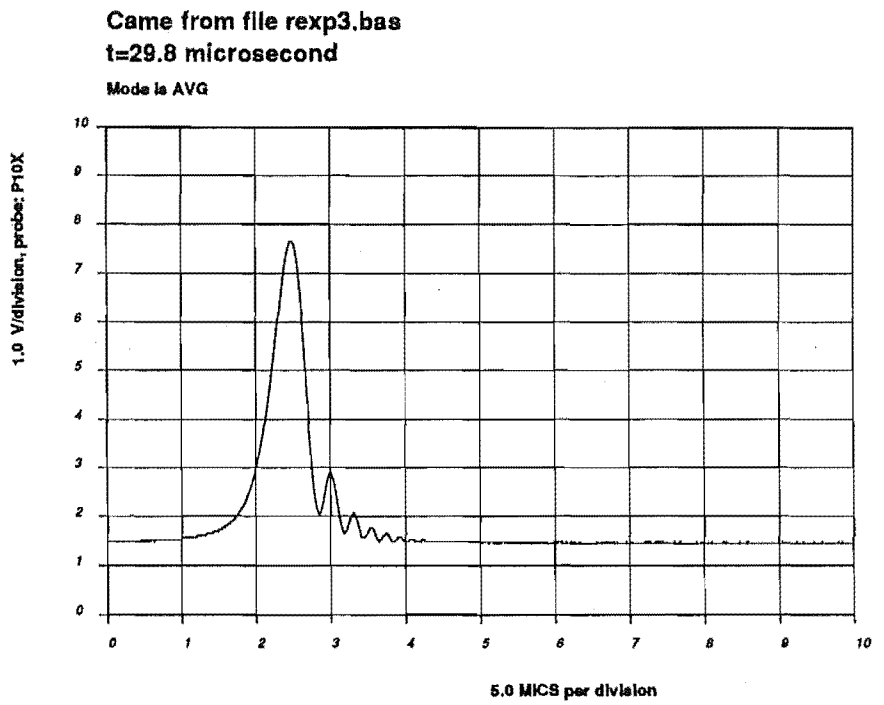

Figure 3: The frequency scanning rate is 134.4 GHz.

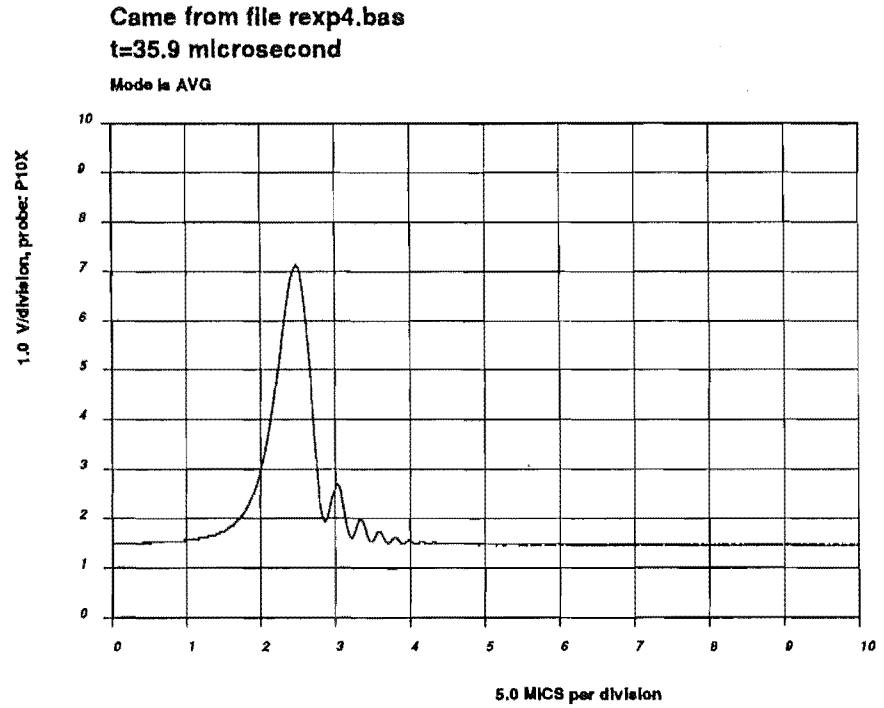

Figure 4: The frequency scanning rate is 111.5 Ghz.

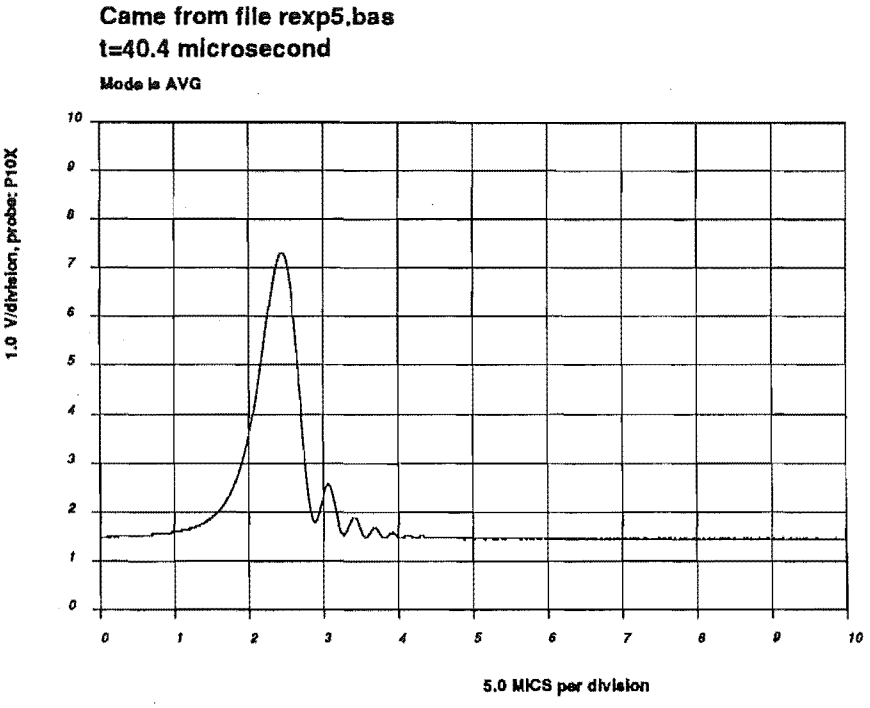

Figure 5: The frequency scanning rate is 99.11 GHz.

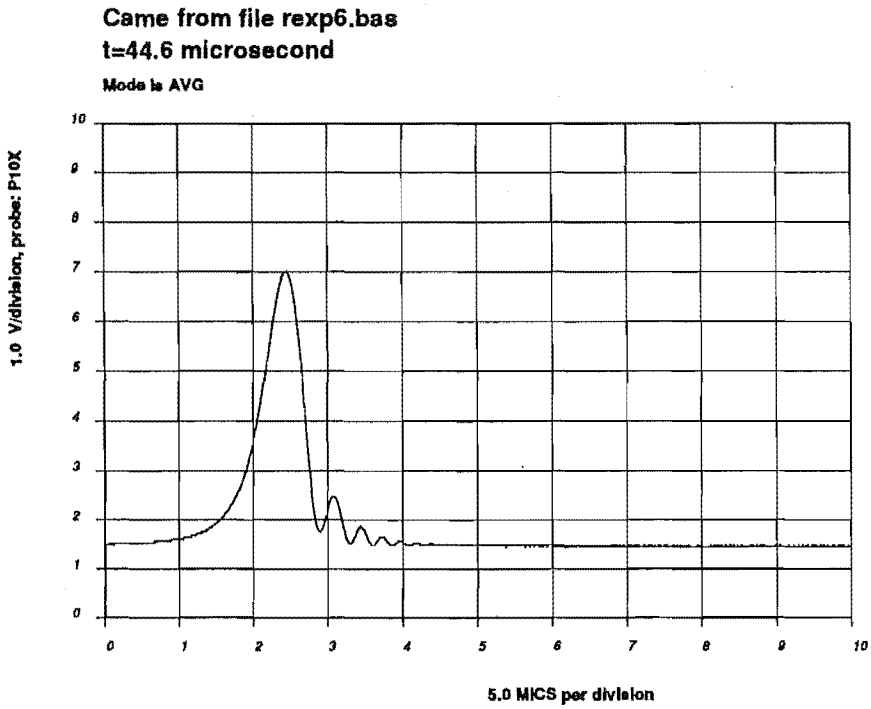

Figure 6: The frequency scanning rate is 90.88 GHz.

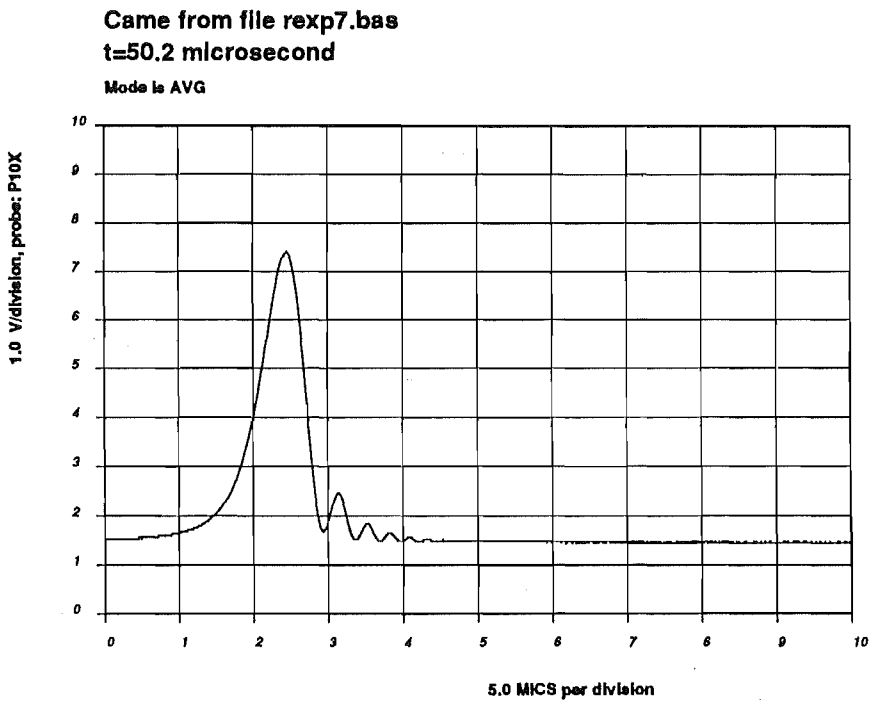

Figure 7: The frequency scanning rate is 79.76 GHz.

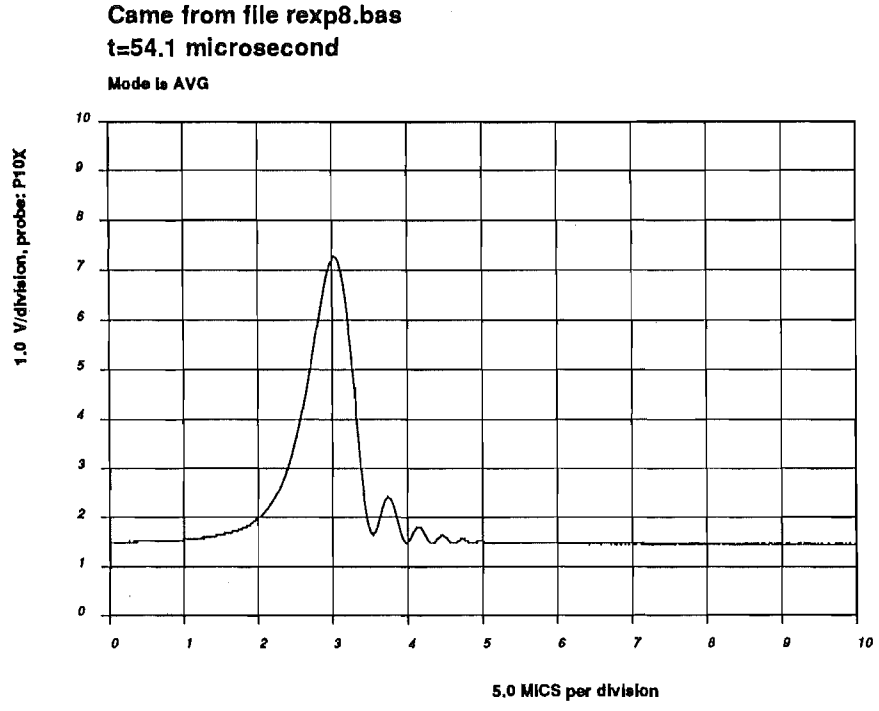

Figure 8: The frequency scanning rate is 74.01 GHz.

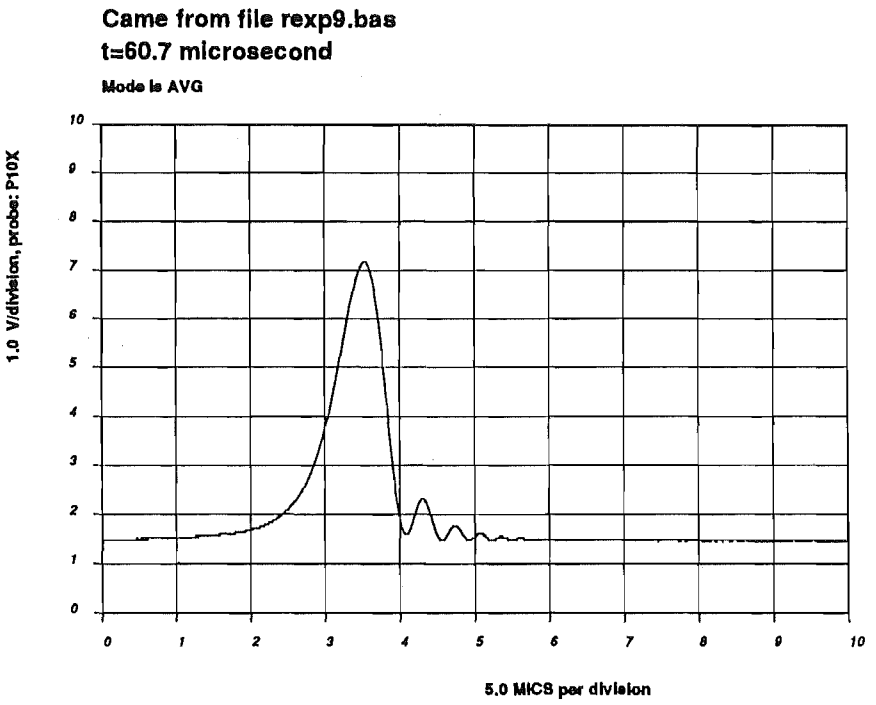

Figure 9: The frequency scanning rate is 65.96 GHz.

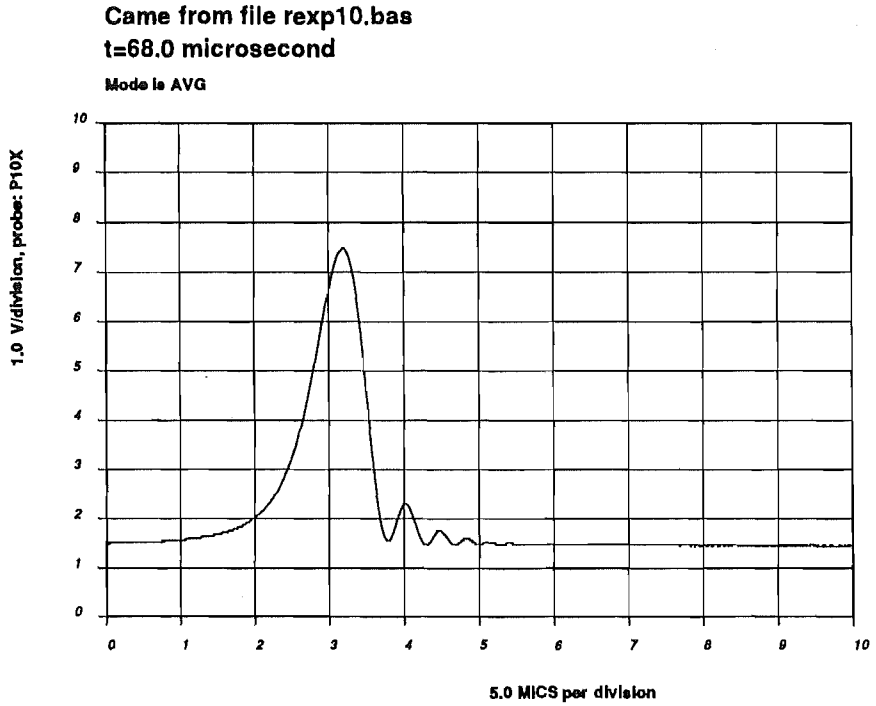

Figure 10: The frequency scanning rate is 58.88 GHz.

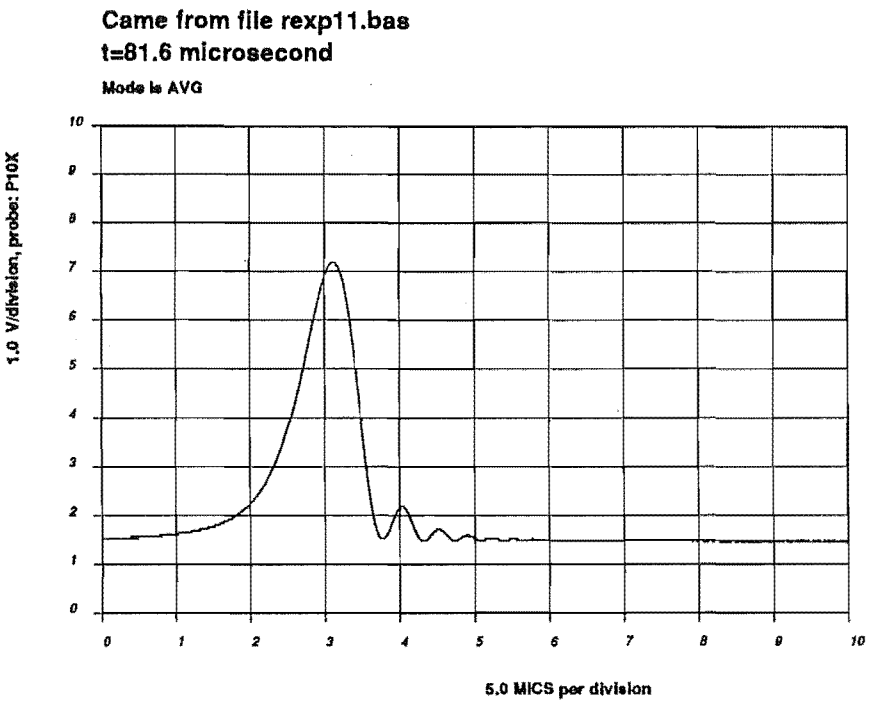

Figure 11: The frequency scanning rate is 49.07 GHz.

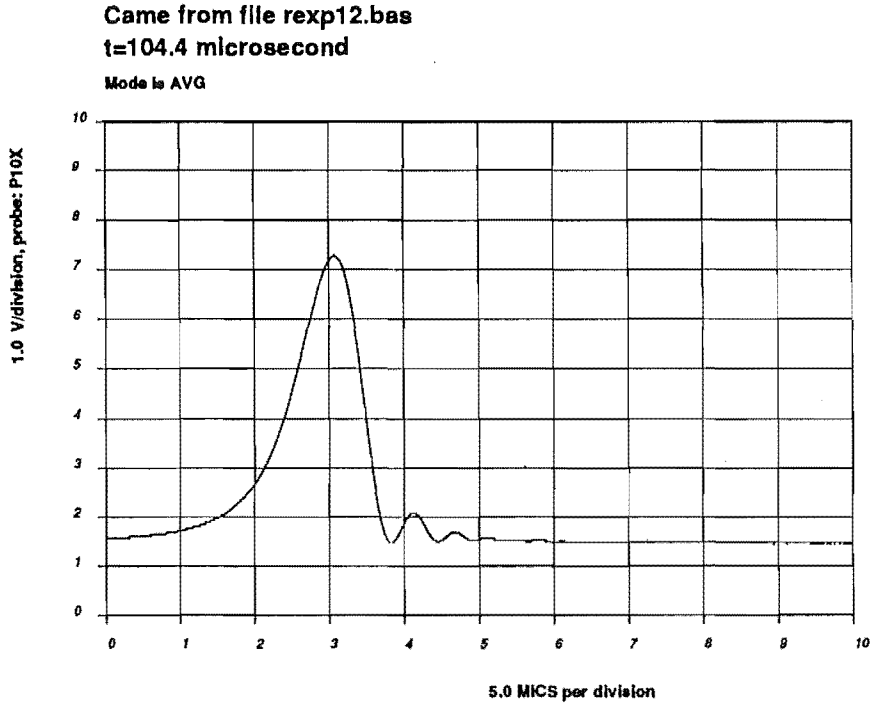

Figure 12: The frequency scanning rate is 35.35 GHz.

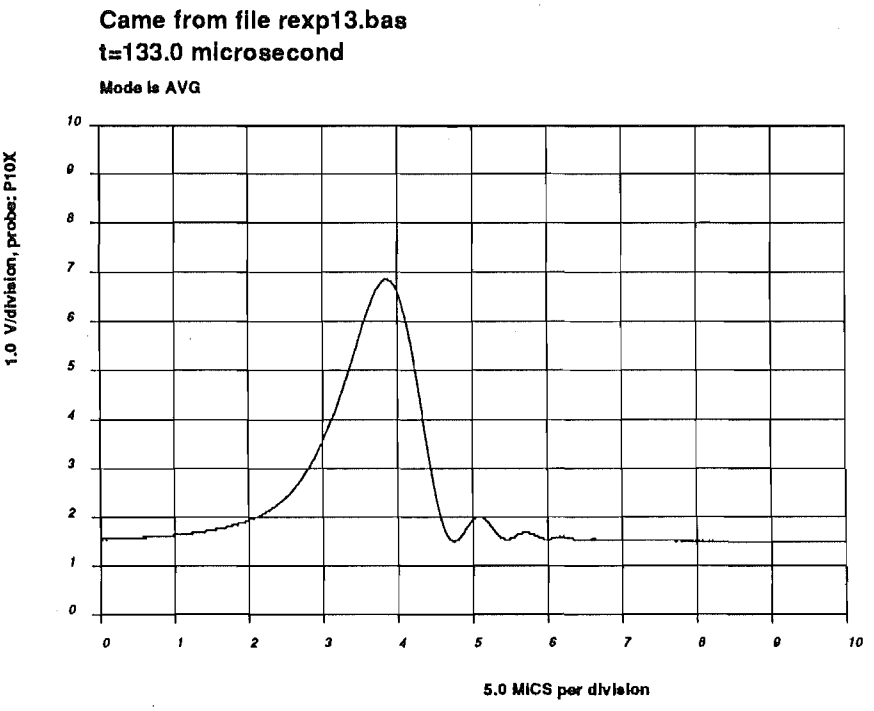

Figure 13: The frequency scanning rate is 30.11 GHz.

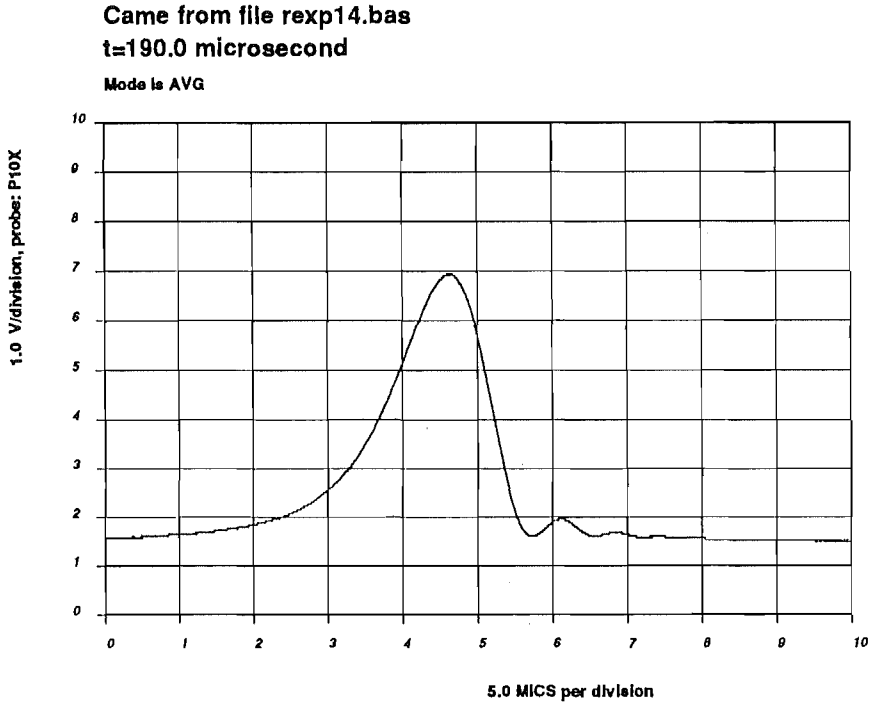

Figure 14: The frequency scanning rate is 21.07 GHz.

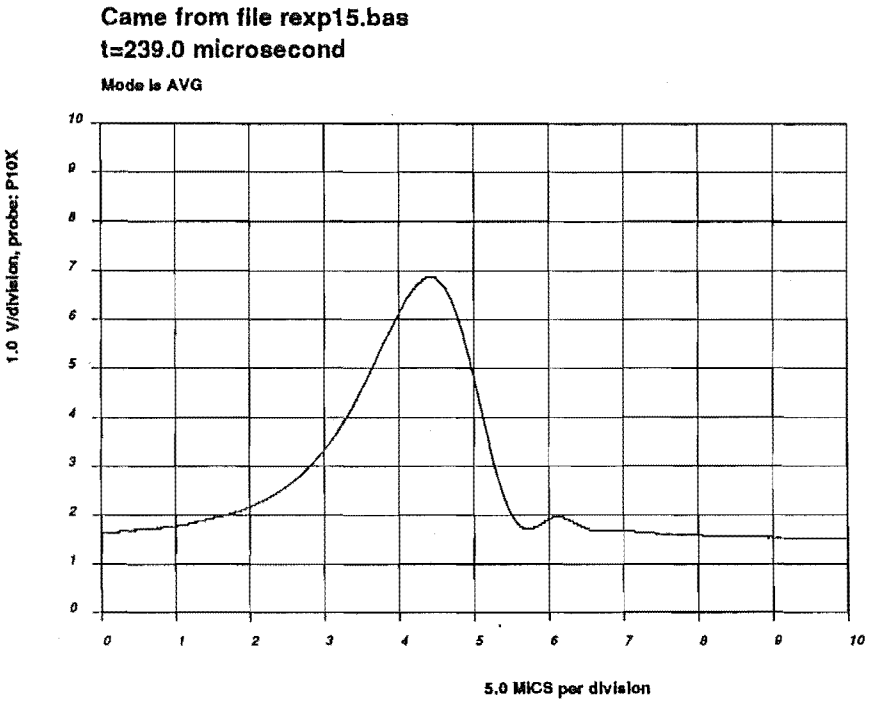

Figure 15: The frequency scanning rate is 16.75 GHz.

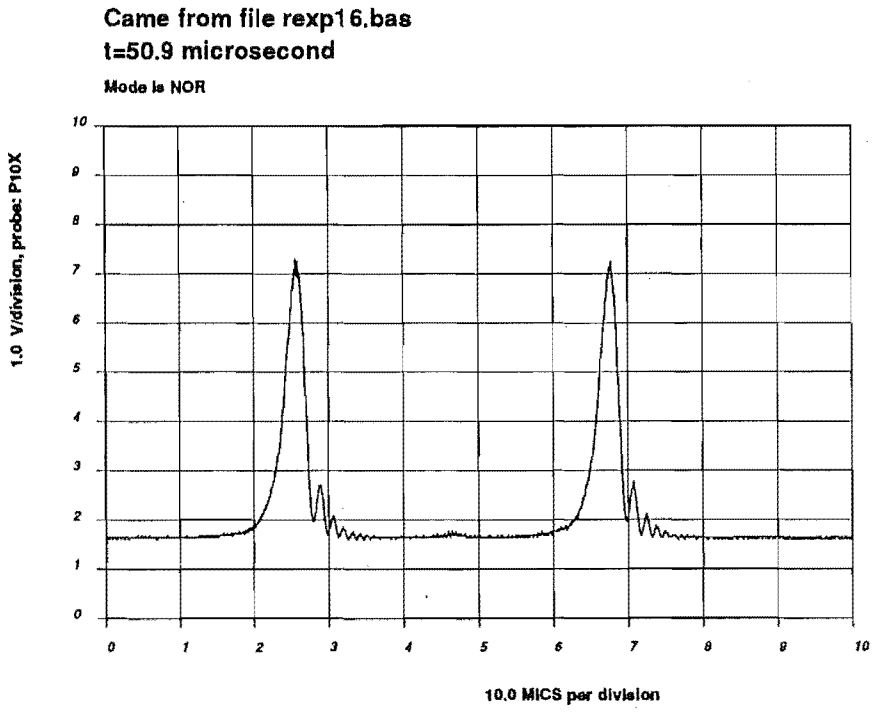

Figure 16: The time interval between the two sidebands is 50.9 microseconds, the modulation frequency is 4.004 MHz, then we obtain the frequency scanning rate of 78.66 GHz.

Appendix F

TurboPascal program for theoretical fitting

In this program, 600 experimental data points are read in from each ringing profile which have been recorded by the digital storage oscilloscope (Hitachi Denshi Model VC-6275). These data are then rescaled for the theoretical fits, and plotted on the computer screen for comparison with the theoretical fits.

Six parameters are needed for the fit to each ringing profile: two ringing-dependent parameters a_1 and b, and four scale parameters V_0, V_s, H_0 and H_s where V_0 and V_s are the origin and scale of the vertical axis, and H_0 and H_s are similar parameters for the horizontal axis.

```
{$N+,R+}

program Datafitting;
{fitting the theoretical curve to the experiment data}
uses crt, graph, dos, printer;
const
      Vhight=500;
      Maxstep=600;
      maxtime=600;
      Hrang=10.0;
      c=14;
      alpha=1;
      gamma=2;
      beta=0.5;
      itmax=100;
      ndim=6;
      mp=7;
      np=6;
      ftol=0.001;
      total=900;
type
      glmpnp =array [1..mp, 1..np] of real;
      glmp =array [1..mp] of real;
      glnp =array [1..np] of real;
      Edata= array [1..total, 1..2] of integer;
      Tdata= array [1..maxtime, 1..2] of integer;
      Odata= array [1..total, 1..2] of real;
var
  a2,a3,hwidth,tau,time,tstep,step,p1,p2,p3,p4,p5,p6,s1,s2,
  dy,yprr,ypr,rtol,x1,x2,x3,x4,y1,y2,y3,y4,y5,z1,z2,z3,z4:real;
  int1,int2,intmod:array [0..800] of real;
  points,iter,mpts,inhi,ilo,ihi,i,i1,i2,i3,i4,i5,j,j1,j2,j3,j4,j5,
  r1,r2,r3,m,n,gd,gg:integer;
  ye1:Odata;
  buffer:Tdata;
  y:glmp;
  ye,yt,dye:Edata;
  pr,prr,pbar,pmeter: glnp;
  p:glmpnp;
Lst : Text;
{------------------------------------------------------------------}

procedure readdata;
{reading the experimental data of ringing profile}
var
    filein: text;
    fileout1:text;
label 10;
begin
    assign (filein,'out.txt');
    reset (filein);
    assign (fileout1, 'a:Edatout1.pas');
    rewrite(fileout1);
    for i1:= 1 to total do
  begin
    readln (filein,ye1[i1,1],ye1[i1,2]);
    points:=i1;
    ye[i1,1]:=trunc((ye1[i1,1])*1.2);
    Hwidth:=ye[i1,1]-ye[1,1];
    ye[i1,2]:=trunc(300-1.5*ye1[i1,2]);
    writeln(fileout1,ye[i1,1],'        ',300-ye[i1,2]);
    if eof(filein) then goto 10;
  end;
  10:
  close (fileout1);
end;
```

```
  {-------------------------------------------------------------------------}

procedure plotdata;
{plotting the exprimental curve on the screen for comparison}
label 20;
begin
    readdata;
    gd:=0;
 {
    initgraph(gd,gg,'\tp');
 }
    setlinestyle(0,gd,1);
    drawpoly(points, ye);
end;

  {-------------------------------------------------------------------------}

procedure  compute (var polypts:tdata;a1,ho,vo,hs,vs,a:real);
{calculating the theoretical data for ringing profile}
begin
    a2:=0;
    a3:=0;
    x1:=0;
    x2:=0;
    step:=10/maxstep;
    tau:=  -c;
    for i2:=1 to maxstep do begin
        tau:= tau+step;
        x3:=exp(tau-a*abs(tau))*cos(((a2+a3*tau)*tau+a1)*sqr(tau))*step;
        x4:=exp(tau-a*abs(tau))*sin(((a2+a3*tau)*tau+a1)*sqr(tau))*step;
        x1:=x1+x3;
        x2:=x2+x4;
      { writeln(tau,x1,x2); }
    end;
    tstep:=Hrang/maxtime;
    y1:=x1;
    y2:=x2;
    time:=-(c-10);
    for j2:= 1 to maxtime do
    begin
        time:=time+tstep;
        y3:=exp(time-a*abs(time))*cos(((a2+a3*time)*time+a1)*time*time)*tstep;
        y4:=exp(time-a*abs(time))*sin(((a2+a3*time)*time+a1)*time*time)*tstep;
        y1:=y1+y3;
        y2:=y2+y4;
        int1[j2]:=exp(-time)*y1;
        int2[j2]:=exp(-time)*y2;
        intmod[j2]:=(int1[j2]*int1[j2]+int2[j2]*int2[j2]);

        {H-scale}
        z1:= Hwidth/maxtime;
        z2:=j2;
        z3:=z1*z2;
        z4:= Ho + Hs*z3;
        polypts[j2,1] :=Trunc(z4);

        {V-scale}
        y5:= Vs*Vhight*intmod[j2];
        polypts[j2,2] :=Trunc(vo-y5);
    end;
end;

  {-------------------------------------------------------------------------}
```

```
function func(parameter:glnp):real;
(least squar calculation)
Var
   lsqr : Real;
begin
    p1:=parameter[1];
    p2:=parameter[2];
    p3:=parameter[3];
    p4:=parameter[4];
    p5:=parameter[5];
    p6:=parameter[6];
    compute(buffer,p1,p2,p3,p4,p5,p6);
    lsqr:=0;

    for i3:= 1 to points do begin
        r1:=ye[i3,1];
        for j3:=1 to maxstep do   begin
            r2:=buffer[j3,1];
            if (r2=r1) then   begin
                r3:=buffer[j3,2];
            end;
        yt[i3,1]:=ye[i3,1];
        yt[i3,2]:= r3;
        end;
{
        writeln(i3:2,' ','yt1:, ',yt[i3,1],' ','yt2: ',yt[i3,2],' ',
                'ye1: ',ye[i3,1],' ','ye2: ',ye[i3,2]);
}
        dy:= yt[i3,2]-ye[i3,2];
        lsqr:= lsqr + sqr(dy);
        func:=lsqr;
{
        writeln(i3,'  ',dy,'  ',lsqr);
}
    end;
end;
  {-------------------------------------------------------------------------}

procedure matrix ;
(producing the paramter matrix for fitting)
var
   filedata: text;
begin

   assign (filedata, 'datain.pas');
   reset (filedata);
   for i4:= 1 to mp do
   begin
       writeln ('point ', i4 ,'    ','a1? ','Ho? ','Vo? ','Hs? ','Vs? ','a? ');
       for j4:= 1 to np do
       begin
           read (filedata, pmeter[j4]);
           read(pmeter[j4]);
           p[i4,j4]:= pmeter[j4];
        end;
   Writeln ('data input ...');
   y[i4]:=func(pmeter);
   writeln ('         ',i4:2,'  ', P[i4,1]:5:2,'  ',p[i4,2]:5:2,'  ',
                p[i4,3]:5:2,'  ', p[i4,4]:5:2, '  ',p[i4,5]:5:2,'  ',
                p[i4,6]:5:2,'  ',y[i4]:5:2);
   writeln (Lst,'         ',i4:2,'  ', P[i4,1]:5:2,'  ',p[i4,2]:5:2,'  ',
                p[i4,3]:5:2,'  ', p[i4,4]:5:2, '  ',p[i4,5]:5:2,'  ',
                p[i4,6]:5:2,'  ',y[i4]:5:2);
  end;
end;
```

```
{-------------------------------------------------------------------------}

procedure amoeba;
{six dimension fitting}
label 99;
begin
    mpts := ndim+1;
    iter :=0;
    while true do begin
        ilo :=1;
        if (y[1]>y[2]) then begin
            ihi := 1; inhi :=2 end
        else begin
            ihi :=2; inhi :=1 end;
        for i:=1 to mpts do begin
            if (y[i] < y[ilo]) then ilo :=i;
            if (y[i] > y[ihi]) then begin
                inhi :=ihi; ihi:=i end
            else if (y[i]>y[inhi]) then
                if(i <> ihi) then inhi:=i
        end;
        rtol :=2.0*abs(y[ihi] - y[ilo])/(abs(y[ihi]) + abs(y[ilo]));
        writeln('rtol:', rtol);

        writeln(Lst,'rtol:', rtol);

        if (rtol < ftol) then goto 99;
        if (iter =itmax) then begin
            writeln('pause in amoeba - too many iteration'); readln
        end;
        iter :=iter + 1;
        for j:=1 to ndim do pbar[j]:=0.0;
        for i:=1 to mpts do
            if (i <> ihi) then for j:=1 to ndim do pbar[j]:=pbar[j]+p[i,j];
        for j:=1 to ndim do begin
            pbar[j] :=pbar[j]/ndim;
            pr[j] :=(1.0+alpha)*pbar[j]-alpha*p[ihi,j] end;

        writeln ('a1:  ',pr[1], '  Ho:  ',pr[2],'  Vo:  ',pr[3]);
        writeln ('Hs:  ',pr[4], '  Vs:  ',pr[5],'  a:   ',pr[6]);
        writeln (Lst,'a1:  ',pr[1], '  Ho:  ',pr[2],'  Vo:  ',pr[3]);
        writeln (Lst,'Hs:  ',pr[4], '  Vs:  ',pr[5],'  a:   ',pr[6]);

        ypr :=func(pr);
        writeln ('func:  ',ypr);
        writeln (Lst,'func:  ',ypr);
        if(ypr <= y[ilo] )then begin
            for j :=1 to ndim do prr[j] :=gamma*pr[j]+(1.0-gamma)*pbar[j];
            yprr:=func(prr);
            if (yprr <y[ilo]) then begin
                for j :=1 to ndim do p[ihi,j] :=prr[j];
                y[ihi] :=yprr end
            else begin
                for j :=1 to ndim do p[ihi,j] :=pr[j];
                y[ihi] :=ypr end end
            else if (ypr >= y[inhi]) then begin
                if (ypr < y[ihi]) then begin
                    for j:=1 to ndim do p[ihi,j]:= pr[j];
                    y[ihi] :=ypr end;
                for j:= 1 to ndim do prr[j] :=beta*p[ihi,j]+(1.0-beta)*pbar[j];
                yprr:=func(prr);
                if (yprr < y[ihi]) then begin
                    for j:=1 to ndim do p[ihi,j] := prr[j];
                    y[ihi] :=yprr end
```

```
                else begin
                    for i:=1 to mpts do
                        if (i <>ilo) then begin
                            for j:=1 to ndim do begin
                                pr[j]:=0.5*(p[i,j]+p[ilo,j]);
                                p[i,j] :=pr[j]
                            end;
                            y[i] :=func(pr) end end end
            else begin
                for j:= 1 to ndim do p[ihi,j] :=pr[j];
                y[ihi]:=ypr end end;
99: End;

  {--------------------------------------------------------------------------}


procedure determine;
{output theoretical data and plotting the theoretical carve}
var
fileout2:text;

begin
    gd:=0;
    writeln ('determine  ','a1?  ','Ho?  ','Vo?  ','Hs?  ','Vs?  ','a?  ');
    readln (p1,p2,p3,p4,p5,p6);
    compute(buffer,p1,p2,p3,p4,p5,p6);
    Assign (fileout2, 'a:Tdatout2.pas');
    rewrite(fileout2);
    for i5:= 1 to maxtime do begin
    writeln(fileout2, buffer[i5,1],'     ',300-buffer[i5,2]);
    end;
    close (fileout2);
    initgraph(gd,gg,'\tp');
    setlinestyle(0,gd,1);
    drawpoly(maxtime, buffer);

end;
   {--------------------------------------------------------------------------}

{Main program}

begin
    Assign(Lst,'LPT1');
    rewrite(Lst);
    readdata;
    determine;    {only for output data of the theoretical carve}
    plotdata;
    matrix;
    amoeba;
    Close(Lst);
end.
```

Appendix G

Theoretical fittings to the experimental data

Five experimental results and theoretical fits for the ringing profiles using the SR-130 supercavity are presented. For investigating the tiny differences between the experimental results and the theoretical predictions given by Eq. (3.4), we have magnified these diagram by a factor of 3 in the vertical scale. Of these pictures, Figs. *G*1, 3 and 5 are duplicates of (a), (b) and (c) of Fig. (3.4), except for the magnified scale.

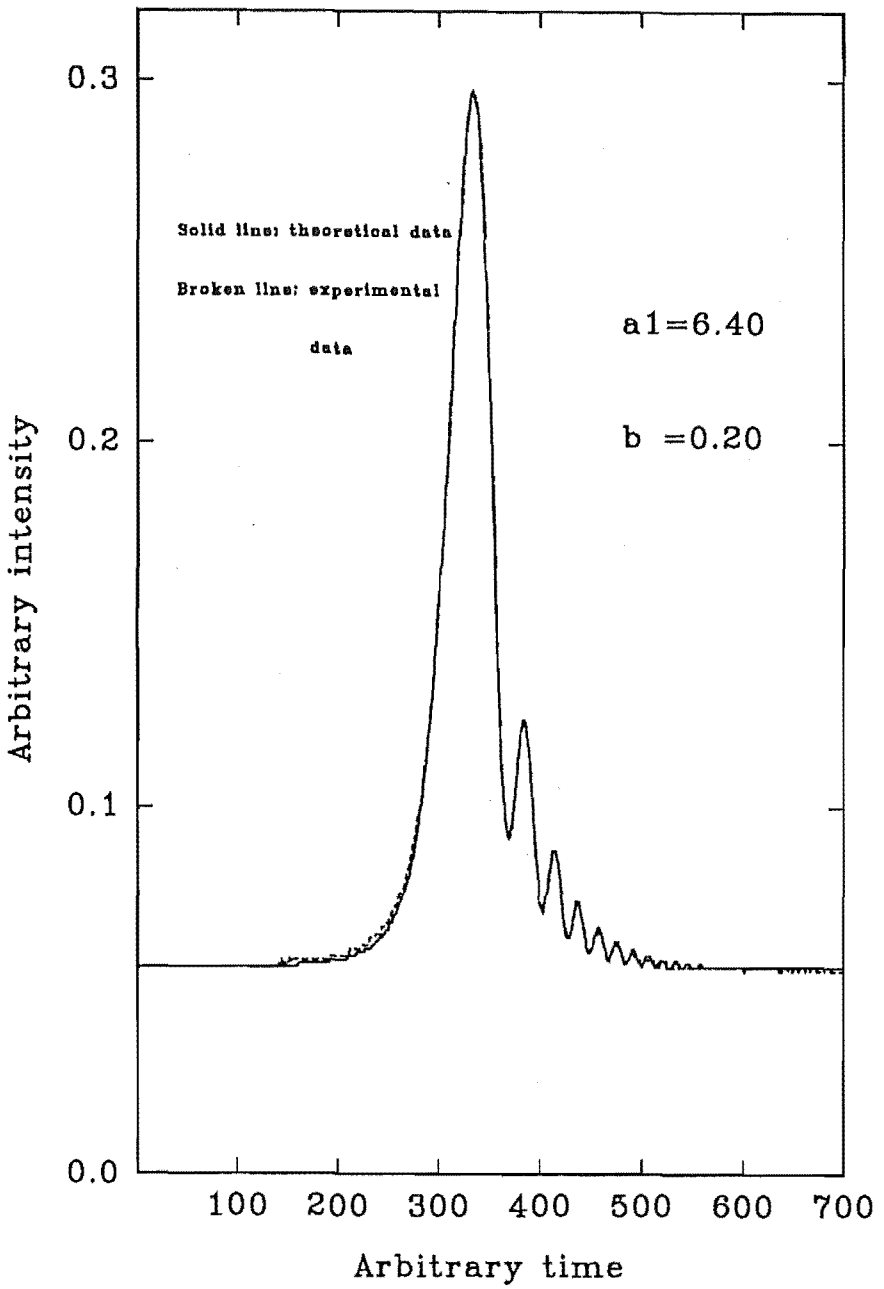
0.3
0.2
0.1
0.0
Arbitrary intensity
Solid line: theoretical data
Broken line: experimental data
a1=6.40
b =0.20
100
200
300
400
500
600
700
Arbitrary time

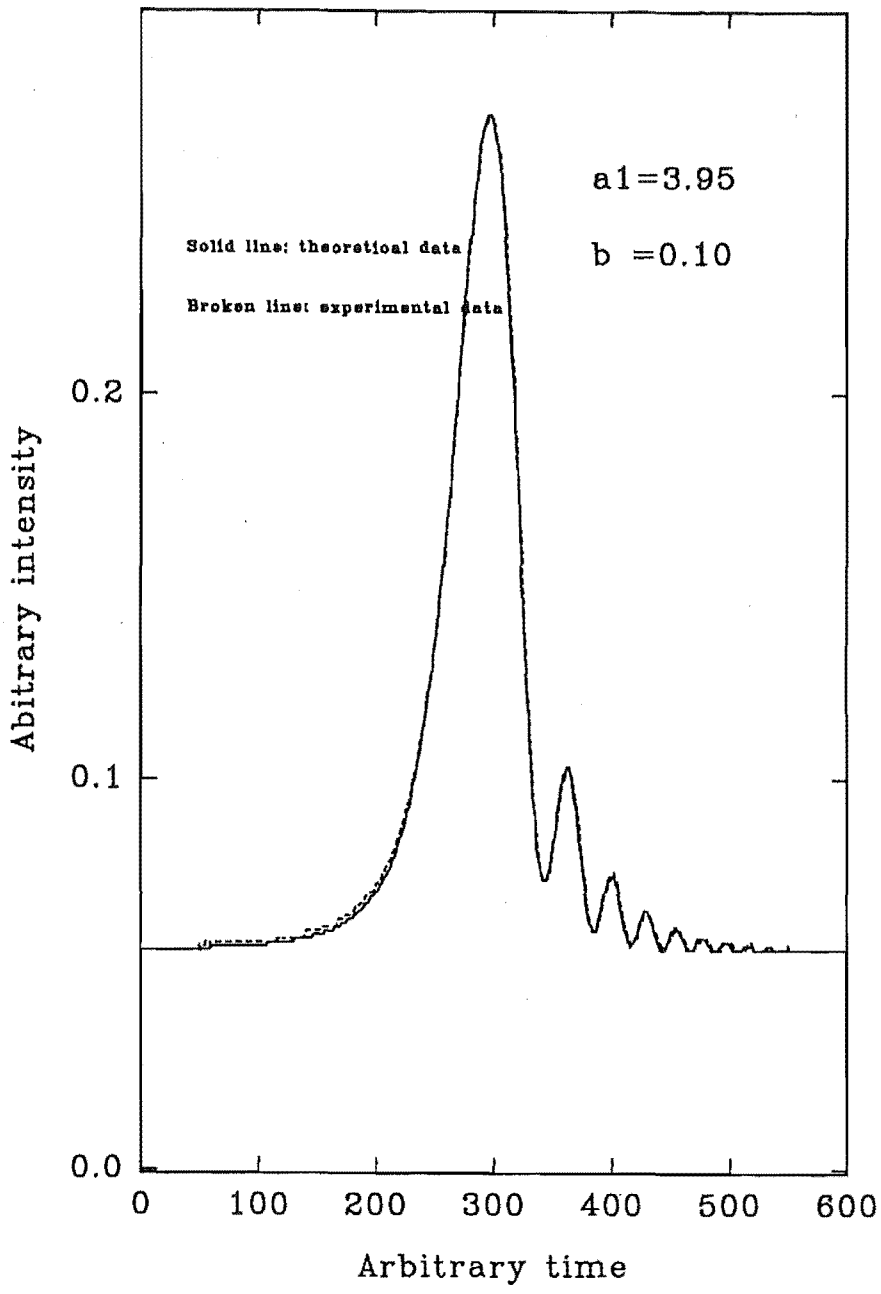
a1=3.95
b =0.10
Solid line: theoretical data
Broken line: experimental data
Abitrary intensity
0.0
0.1
0.2
0
100
200
300
400
500
600
Arbitrary time

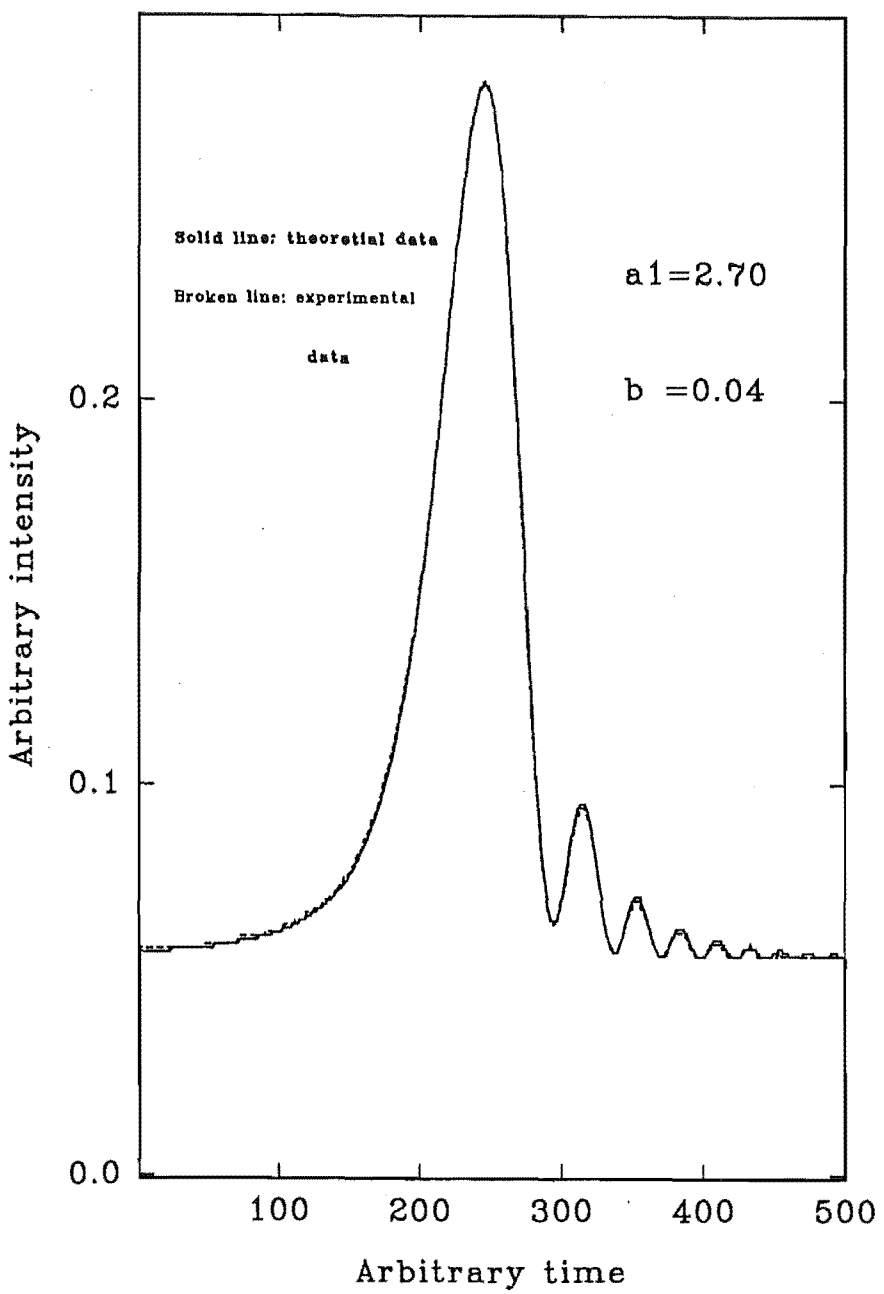
Solid line: theoretial data
Broken line: experimental data
a1=2.70
b =0.04
Arbitrary intensity
0.0
0.1
0.2
100
200
300
400
500
Arbitrary time

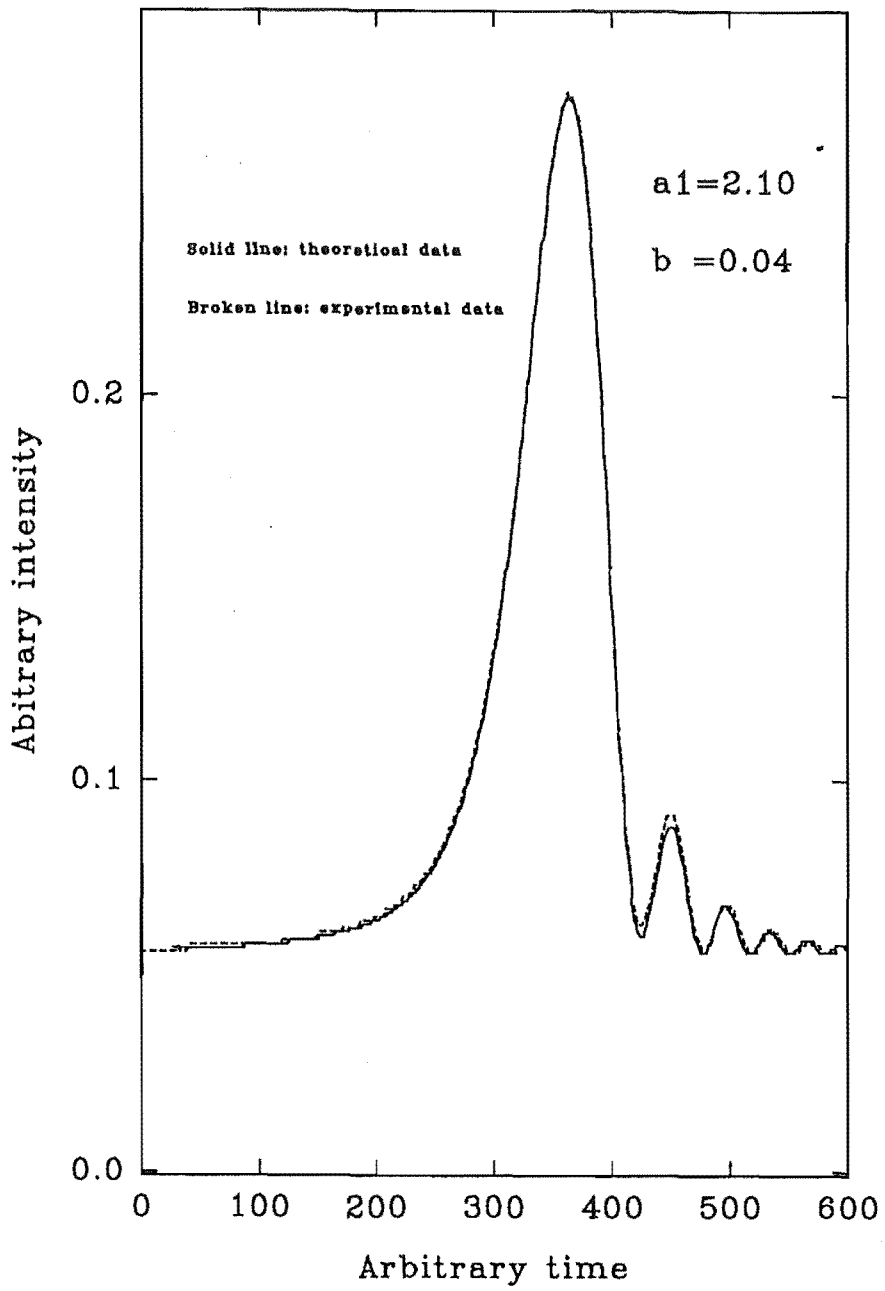
a1=2.10
b =0.04
Solid line: theoretical data
Broken line: experimental data
Abitrary intensity
0.0
0.1
0.2
0
100
200
300
400
500
600
Arbitrary time

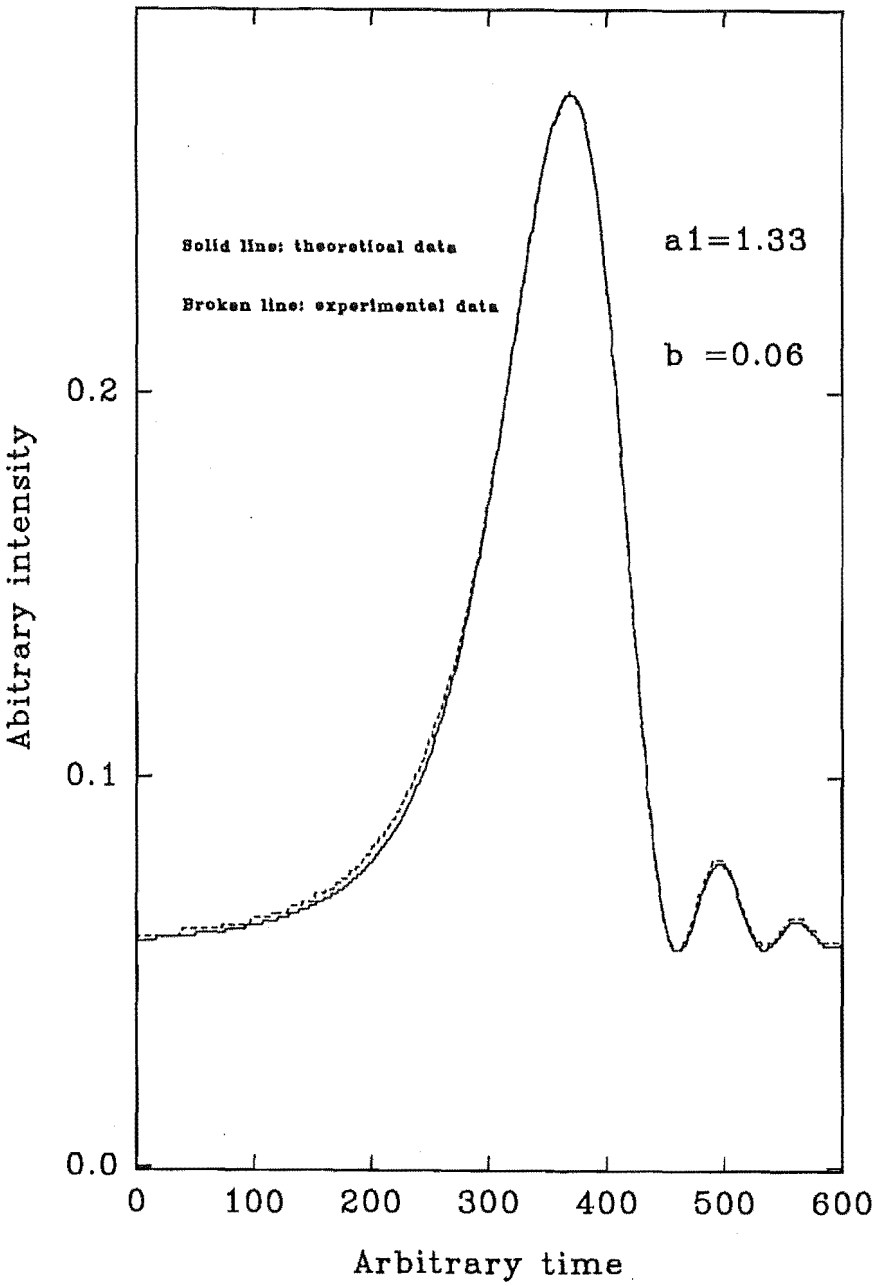
Solid line: theoretical data
Broken line: experimental data
a1=1.33
b =0.06
Abitrary intensity
0.0
0.1
0.2
0
100
200
300
400
500
600
Arbitrary time